AO-08 White Book of *Insight*-HXMT

Institute of high energy physics, CAS

Apr. 15, 2025

Contents

1 Overview 1

1.1 Introduction 1

1.2 Dates and Deadlines 2

1.3 Observation Time Allocation and Data Rights 2

1.4 Useful Links 4

2 Science Programs and Core Science Team 6

2.1 *Insight*-HXMT Science Programs 6

2.2 *Insight*-HXMT Core Science Team 6

2.3 *Insight*-HXMT team members 7

2.4 Domestic members 7

2.5 International members 8

3 *Insight*-HXMT Satellite and Telescopes 10

3.1 Overview 10

3.2 High energy X-ray Telescope (HE) 15

3.2.1 Introduction 15

3.2.2 Gain Modes 18

3.2.3 Observation Scenarios of HE 19

3.3 Medium energy X-ray telescope (ME) 28

3.4 Low energy X-ray telescope (LE) 34

3.5 Space environmental monitor (SEM) 39

3.6 Characteristics of *Insight*-HXMT telescopes 41

4 Core Sciences 45

4.1 Introduction 45

4.2 Main topics of *Insight*-HXMT scientific study 45

4.2.1 Galactic plane scanning survey and source monitoring 45

4.2.2 High cadence monitoring of accreting BH and NS binaries 54

4.2.3 High statistic observation of BH and NS systems 89

4.2.4 Space- and ground-based coordination and follow-up observations 102

5 Observation Modes 107

5.1 Introduction 107

5.2 Pointing observation mode 107

5.3 Small sky area scan mode 108

6 Background 110

6.1 Background Estimation Method 110

6.2 Background components 110

6.3 In-orbit background analysis 113

6.4 In-orbit background model 115

7 Detector response 119

7.1 In-orbit gain and energy resolution calibration 119

7.2 Calibration of the effective areas 126

7.3 Calibration of PSF 128

7.4 Calibration of the time accuracy 129

8 Ground Segment 131

8.1 Introduction 131

8.2 User Support and Service 132

8.3 Observation Planning 133

9 Proposals Collection and Observation Plans 134

9.1 Proposal Classification 134

9.2 Proposal Collection 135

9.3 Proposal Evaluation 135

10 Proposal Tools 140

10.1 Basic requirements for *Insight*-HXMT observation proposals 140

10.2 Target Visibility Predictor 141
10.3 Observation Time Estimator 142
10.4 Bright source warning tool 143
10.5 Simulate the target source energy spectrum for given exposure time. 144
10.6 Proposal Submission Tool 149
10.6.1 Proposal collection website 149
10.6.2 Account management and permission 149
10.6.3 Proposal submission 150
11 References 152
12 *Insight*-HXMT Publications 158
12.1 Published papers 158
12.2 Special Issue in SCPMA 192
12.3 Special issue in JHEAp 193
12.4 Special issue in RDTM 196
13 Summary of AO-07 Observations 197

Abbreviations

ACD: Anti-Coincidence Detector, also called HVT

ARF: Ancillary Response File

ASIC: Application Specific Integrated Circuit

Atel: Astronomy Telegram

AXP: Abnormal X-ray Pulsar

CALDB: Calibration database

CCD: Charge Coupled Device

CRP_D: Cosmic Ray Protons induced Delayed background

CRP_P: Cosmic Ray Protons induced Prompt background

CsI: Cesium Iodide, short form for CsI(Na)

CXB: Cosmic X-ray Background

CXB_A: CXB induced Aperture background

CXB_N: CXB-induced Non-aperture background

FOV: Field of View

FWHM: Full Width at Half Maximum

GCN: The Gamma-ray Coordinates Network

Geant4: GEometry ANd Tracking

GPS: Global Positioning System

GRB: Gamma-Ray Burst

GW: Gravitational Wave

GWEM: Gravitational Wave Electromagnetic counterpart

HE: High Energy X-ray Telescope

HDPC: HXMT high level Data Production Processing and Calibration Center

HMXB: High Mass X-ray Binary

HSOC: HXMT Science Operation Center

HSSC: HXMT Science Support Center

HSUC: HXMT Science User Center

HVT: HE Veto detector, also called ACD

HXMT: Hard X-ray Modulation Telescope

Insight-HXMT: *Insight*-Hard X-ray Modulation Telescope

LE: Low Energy X-ray Telescope

LMXB: Low Mass X-ray Binary

LVDS: Low-Voltage Differential Signaling

ME: Medium Energy X-ray Telescope

NaI: Sodium Iodide, short form for NaI(Tl)

PHA: Pulse Height Amplitude

PI: Pulse Invariant

PM: Particle Monitor

PMT: Photo-Multiplier Tube

PSD: Pulse Shape Discrimination

PSF: Point Spread Function

PV: Performance Verification

QPO: Quasi-Periodic Oscillation

RMF: Redistribution Matrix File

RMS: Root Mean Square

SAA: South Atlantic Anomaly

SCD: Swept Charge Device

SEM: Space Environment Monitor

SFXT: Supergiant Fast X-ray Transients

SGR: Soft Gamma-ray Repeater

TGF: Terrestrial Gamma-ray Flash

TOA: Time of Arrival

ToO: Target of Opportunity

1 Overview

1.1 Introduction

Insight-Hard X-ray Modulation Telescope (*Insight*-HXMT) is China's first X-ray astronomy satellite. It was launched on 15th June 2017 and is currently in service smoothly (Zhang et al. 2020). There are three main payloads onboard *Insight*-HXMT, the high energy X-ray telescope (20–250 keV, 5100 cm^2) (Liu et al. 2020), the medium energy X-ray telescope (8–35 keV, 952 cm^2) (Cao et al. 2020), and the low energy X-ray telescope (1–12 keV, 384 cm^2) (Chen et al. 2020). The main scientific objectives of *Insight*-HXMT are:

(1) to scan the Galactic Plane to find new transient sources and monitor the known variable sources;

(2) to observe X-ray binaries to study the dynamics and emission mechanism in the strong gravitational or magnetic fields;

(3) to monitor and study the Gamma-Ray Bursts (GRBs) and Gravitational Wave Electromagnetic counterparts (GWEM).

The *Insight*-HXMT Data Analysis Software (HXMTDAS, V2.06) and the CALDB have been frequently updated and the latest version (V2.07) has been released in December of 2023. In this software version, some bugs have been fixed and some other useful modules have been provided. The new update notes are available on the portal (http://hxmten.ihep.ac.cn/documents/850.jhtml). To facilitate the analysis of the GRB data, the *Insight*-HXMT GRB Data Analysis software (version: beta 1.4) has been released.

Users can download Level-1 data products from the *Insight*-HXMT official website (http://archive.hxmt.cn/proposal). Members of core science team can apply for the core observation data within the proprietary period; the PI of each guest observation can download the corresponding data; the data beyond the proprietary period or ad hoc ToO observation data are open to the public. Up to Mar 31, 2025, 4263 data product and 536 GRB data have been publicly released.

AO-07 will be finished on Aug. 31st, 2025 and a summary of the proposals is given in Chapter 13. This is the eighth Cycle of Announcement of Opportunity (AO-08).

1.2 Dates and Deadlines

Important dates for Cycle 8 Announcement (in Beijing Time, UTC+8):

Proposals Submissions Open time: Apr. 21, 2025
Proposals Due: June 15, 2025
Announcement of accepted proposals: Aug. 30, 2025
Start time of the AO-08 Observations: Sept. 1, 2025
End time of the AO-08 Observations: Aug. 31, 2026

1.3 Observation Time Allocation and Data Rights

(1) Approximately 47 Ms of exposure time (also called effective observation time; for 50% observation efficiency, the actual observation time is two times longer) will be available in the observing period, in which the ratio for core proposals and guest proposals is 2:3, as shown in Table 1-1. Up to 12 Ms of exposure time will be assigned for non-ToO observations (quiescent or persistent sources) and up to 35 Ms of exposure time would be assigned for ToO observations (transient sources, for whom the probability of the outbursts is approximately 10%). Accepted proposals will be awarded with priority A, B, and C targets, respectively, and priority C targets will be observed depending on the available time allocation. In addition, up to 2 Ms of exposure time will be reserved for the ad hoc observations, such as not pre-approved ToO or calibration observations.

Table 1-1 The assignment of exposure time for different types of proposals.

Type	Exposure time for Non-ToO observations (Ms)	Exposure time for ToO observations (Ms)	Total exposure time (Ms)
Core Proposals	4 (2.5 for galactic plane survey)	14	18
Guest Proposals	6	21	27
Calibration Proposals	2	0	2

(2) The core proposals can ONLY be submitted by the core science group leaders, which will be reviewed and selected by the core science group. Data rights will be shared within the core science group members during the data proprietary period.

(3) The core science group members can submit the guest proposals, and follow the data policy of guest proposals.

(4) Proposals for the Galactic Plane scan, background observations and calibration observations are ONLY open to the core science groups now.

(5) Joint proposals are open to coordinated observations with other ground- or space-based observatories. If accepted, the proposers should secure the requested observations of other observatories before requesting trigger to *Insight*-HXMT and coordinate all observations.

(6) The data proprietary periods for this AO are one year for approved non-ToO observations and three months for approved ToO observations, if not specified and approved otherwise.

(7) “PhD Research Program”: Up to 20% of the data from the regular observations can be made for exclusive-use for PhD research. The PhD supervisors from the core science groups can apply for data protection in the proposals. If approved, the data will be protected during the proprietary periods.

(8) Data protection can also be applied to Ad Hoc ToO observations. If approved, the data proprietary period will be three months. Otherwise, Ad Hoc ToO data will be released immediately.

(9) Approved but not yet fully executed Priority A non-ToO observations from AO-7 will be moved to AO-8automatically; the other approved but not yet fully executed AO-7observations need to be re-proposed with scientific justifications.

1.4 Useful Links

Submit via the website (registration required): http://proposal.ihep.ac.cn/proposal.jspx

Guide for proposal submission: http://enghxmt.ihep.ac.cn/doc/170.jhtml

Observation time estimator: http://proposal.ihep.ac.cn/calc/calc.jsp

Target Visibility Predictor: http://proposal.ihep.ac.cn/TargetVisibilityPredictor/

Bright source warning tool: http://proposal.ihep.ac.cn/soft/soft2.jspx

Spectrum simulation tool: http://proposal.ihep.ac.cn/soft/user_spec.zip

Instructions for proposal submission: http://enghxmt.ihep.ac.cn/doc/170.jhtml

Proposal forms download: http://enghxmt.ihep.ac.cn/doc/282.jhtml

List of Sources observed: http://hxmten.ihep.ac.cn/ObsSrcList.jhtml

---

Data Policy: http://enghxmt.ihep.ac.cn/policy/174.jhtml

Insight-HXMT core team composition and paper authorship rules:

http://hxmten.ihep.ac.cn/policy/173.jhtml

Insight-HXMT publications: http://hxmten.ihep.ac.cn/papers.jhtml

2 Science Programs and Core Science Team

2.1 *Insight*-HXMT Science Programs

Similar to most of the astronomical space telescopes in the international community, there are two major science programs for *Insight*-HXMT in terms of scientific observation, data analysis and associated research.

1) *Insight* -HXMT Core Science Program

Insight-HXMT Core Science Program aims at taking full advantages of *Insight*-HXMT with high cadence and long duration observations which may have strong international competitiveness and high scientific value. The Core Science Program is formulated by *Insight*-HXMT core science team members.

2) *Insight*-HXMT Guest Science Program

Insight-HXMT Guest Science Program is made of observations not yet included in the Core Science Program, which can be proposed by individuals or teams from both domestic and international astronomy communities, and will be selected by the dedicated peer review panel. *Insight*-HXMT Guest Science Program is open to the whole international scientific community without any condition.

2.2 *Insight*-HXMT Core Science Team

The *Insight*-HXMT Core Science Team consists of three types of members:

1) *Insight*-HXMT team members, including the proposers of *Insight*-HXMT, members of *Insight*-HXMT payloads and *Insight*-HXMT Science Center.

2) Domestic members, domestic scientists who are interested in contributing to the *Insight*-HXMT core scientific research.

3) International members, international scientists who have either made significant contributions to *Insight*-HXMT or recommended by cooperation organizations that contributed to *Insight*-HXMT.

A brief description of the responsibilities and rights of the three types of *Insight*-HXMT Core Science Team members is given below.

2.3 *Insight*-HXMT team members

Major responsibilities:

1) Complete the payload development and performance tests.

2) Study the space environment's impacts on payload performance.

3) Participate in the payload calibration.

4) Participate in the *Insight*-HXMT in-orbit operation organized by HSDC.

Major rights:

1) Claim authorship in all scientific publications coming out of the *Insight*-HXMT Core Program observations during the data proprietary period. The order of authorship is classified in the Appendix.

2) Participate in/quit from any Core Science Group once approved by *Insight*-HXMT principal investigator (PI).

2.4 Domestic members

Domestic members are scientists who are the leading researchers in the related field and are interested in contributing to *Insight*-HXMT core scientific research, and are divided into several Core Science Objectives Groups. Proposals for *Insight*-HXMT Core Science Objectives are solicited among domestic astronomy community, while the submitted proposals will be reviewed and selected by a peer review committee composed of domestic and international experts. The peer review committee determines the Core Science Objectives and the constitution of the corresponding proposal groups, as well as the observation time for each Core Science Objective. Subsequently, the *Insight*-HXMT HSDC will formulate the corresponding observation schedules for these Core Science Objectives.

Major responsibilities:

1) Justification of the Core Science Objectives, including scientific value, observation simulation, observation time estimation and observation schedule.
2) Complete the *Insight*-HXMT white papers for proposed objectives and publish it as key elements of the *Insight*-HXMT user manual or scientific publications.
3) Cooperate with HSDC on scheduling observations for the approved Core Science Objectives.
4) Accomplish the data analysis of the proposed Core Science Objectives in high quality and manage to publish the results.
5) The retrieved data can ONLY be accessed by authorized groups/members during the data proprietary period.
6) Collaboration with a third-party organization/scientist is ONLY allowed once permitted by a peer review committee or PI during the data proprietary period.
7) Apply all kinds of resources required to accomplish the requirements listed above, including funding and computation support.

Major rights:

1) Use the data from the Core Program observations during the data proprietary period, including possible collaboration with a third-party organization/scientist with an approval from a peer review committee or PI.
2) Participate in all kinds of major scientific research projects organized by PI, with funding support.
3) Apply scientific research projects based on *Insight*-HXMT Core Science Objectives, with funding support.

2.5 International members

International scientists who have made significant contributions to *Insight*-HXMT or been recommended from cooperation organizations can either apply to join a specific *Insight*-HXMT Core Science Group proposed by domestic members or submit new

Insight-HXMT Core Science Objectives proposals to be reviewed by a peer review committee led by PI. The peer review committee will oversee the following review and approval. International members shall have the same rights as domestic *Insight*-HXMT core science members once the proposals are approved by the peer review committee.

International collaborations are very welcome and foreseen to stipulate the scientific research of *Insight*-HXMT. International scientists who have NOT made direct contribution to *Insight*-HXMT are encouraged to participate in the collaboration groups of the *Insight*-HXMT Core Science Objectives. Application for collaborating with *Insight*-HXMT core science groups/members is required and shall be submit to the associated Core Science Group leader (the application forms are available online http://hxmtweb.ihep.ac.cn/policy/85.jhtml) and the PI. Once approved, they can access the data during the data proprietary period.

3 *Insight*-HXMT Satellite and Telescopes

3.1 Overview

The overview of *Insight*-HXMT mission is taken from Zhang et al. (2020). Fig. 3-1 shows the schematic view of the *Insight*-HXMT satellite in-orbit. The satellite consists of two cabins, the payload cabin and the platform cabin. All telescopes are installed in the payload cabin, which is on the top of the satellite. The total weight of *Insight*-HXMT satellite is about 2, 700 kg, and its designed lifetime is four years. *Insight*-HXMT is operating in Low Earth Orbit with an altitude of 550 km and an inclination angle of 43°. The pointing accuracy, attitude measurement accuracy and attitude stability are 0.1° (3σ), 0.01° (3σ) and of 0.005°/s, respectively.

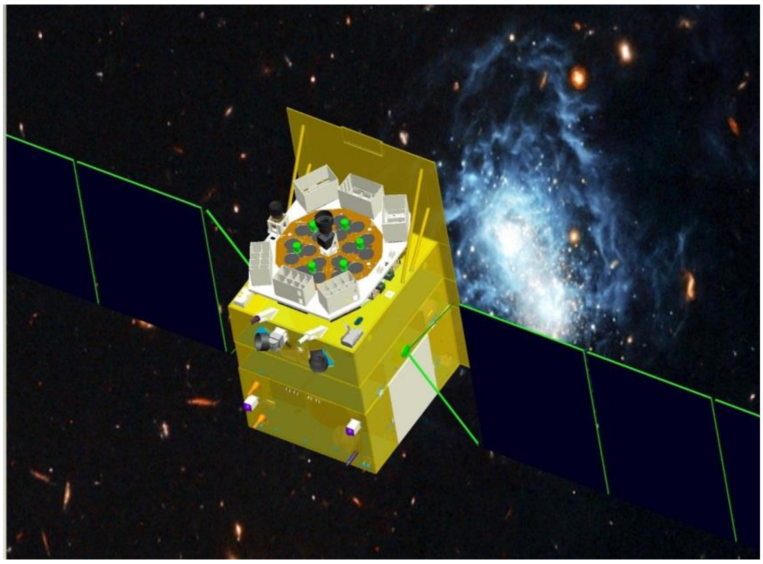

Fig. 3-1 A cartoon of *Insight*-HXMT.

There are three main payloads onboard *Insight*-HXMT, the High Energy X-ray telescope (HE), the Medium Energy X-ray telescope (ME) and the Low Energy X-ray telescope (LE). The supplementary instrument named Space Environment Monitor (SEM) is also installed on the satellite to monitor the particle environment of the satellite. Each payload contains several devices showing distinct functions, as described in Table 3-1. Fig. 3-3 shows the details of the collimators in the three X-ray telescopes onboard *Insight*-HXMT. Table 3-2 lists the FOVs and orientations of these collimators.

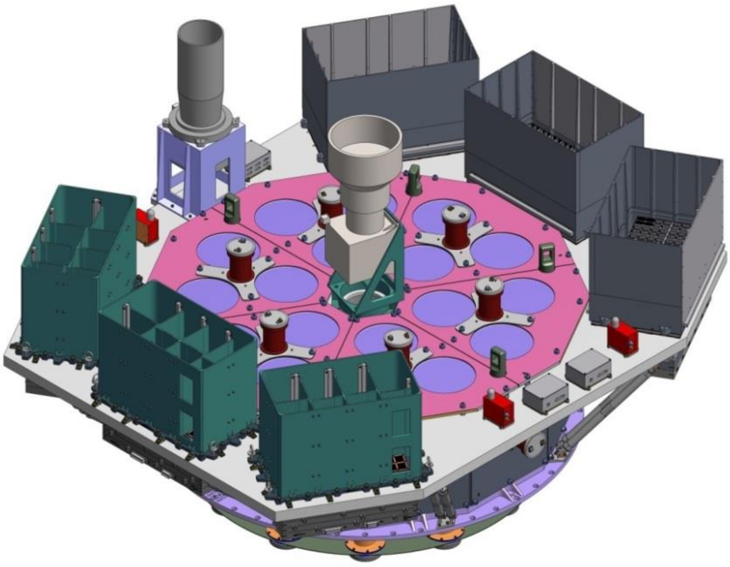

Fig. 3-2 Layout of main instruments onboard the *Insight*-HXMT satellite.

LE consists of three detector boxes marked dark green color in the left bottom panel; HE consists of eighteen detectors in the middle panel; ME consists of three detectors boxes with gray color. Two star-sensors are also mounted onboard *Insight*-HXMT and located in the center and left side in this figure. The colors in the figure are adopted to show different devices, rather than the real ones.

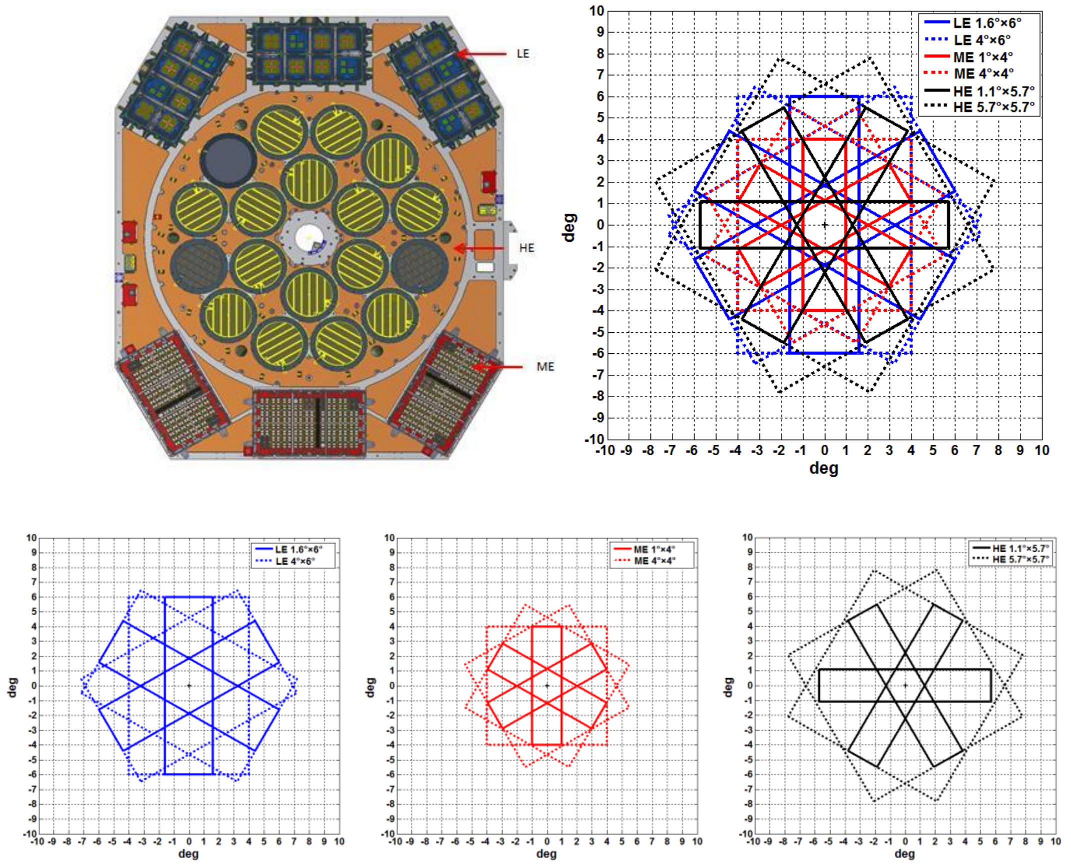

LE ME HE

Fig. 3-3 Top left panel: Collimators of the three X-ray telescopes of *Insight*-HXMT. Top right and bottom panels: FOVs of HE, ME and LE.

Table 3-1 Sub-systems and functions of each telescope and payload onboard *Insight*-HXMT

No.	Detectors	Devices	Functions
1	HE	Main detectors	With 18 NaI/CsI detectors, to observe the sources in the FoV defined by collimators in the energy band of 20–250 keV by using NaI, and to monitor the all-sky un-occulted by the Earth in gamma-ray band (0.2–3 MeV) by using CsI.
		Collimators	To define the Field of View for HE Main detectors. It consists of 18 collimators.16 collimators are narrow-FOV of 1.1°×5.7°. 2 collimators are wide-FOV of 5.7°×5.7°.
		Anti-coincidence detectors	By detecting the penetrated charged particles, it provides anti-coincidence signals to the main detectors to eliminate the background signals in

			main detectors induced by these charged particles.
		Particle detectors	Three identical devices, which continuously detect the flux of high energy particles in space.
		In-orbit calibration detectors	Based on the hard X-ray photons at 59.5 keV from the radioactive source ^{241}Am, they can adjust AGC of the main detectors, and tag the typical arriving times of these event photons.
		HE power-controller boxes	Control-centers of HE sub-systems, which are used to monitor the in-orbit status of the detector, collect, package and deliver the data.
		HE power-supply boxes	Supply power for the detectors and execute the remote control-instructions.
2	ME	ME detectors	Consists of 3 detector boxes. Each box is composed of Si-PIN detector-array, read-out electronics, collimators and shading covers. Energy range is 5–30 keV.
		Collimators	To define the Field of View for ME detectors. It consists of 54 collimators. 48 collimators are narrow-FOV of 1.0°×4.0°. 6 collimators are wide-FOV of 4.0°×4.0°.
		ME electronic controllers	Control the data-management of the sub-systems, and execute the remote control-instruction, and supply power for ME devices.
3	LE	LE detectors	Consists of 3 detector boxes. Each box is composed of SCD detector-arrays, read-out electronics, collimators and filtering film. Energy range is 1–15 keV.
		Collimators	To define the Field of View for LE detectors. It consists of 90 collimators. 63 collimators are narrow-FOV of 1.6°×6.0°. 21 collimators are wide-FOV of 4.0°×6.0°. 6 collimators are wide-FOV of 60.0°×2.5°.
		LE electronic controllers	Control the data-management of sub-systems, and execute the remote-control instruction, and supply power for LE devices.
4	SEM	SEM	Detect the flux of the charged particles, and to some precise it discerns the direction of particles, protons/electrons. SEM supplies spectrum with low resolution.
5	Supporting structure (SS)	Main structure	Provide the platform for the sub-systems installation of these payloads, fulfilling the requirements of the installation and mechanism.

Table 3-2 FOVs and orientations of HE, ME and LE Collimators

Payload	Numbers. of Collimators	FOVs	Orientations
HE	5	1.1°×5.7°	0°
	5	1.1°×5.7°	60°
	5	1.1°×5.7°	-60°
	1	5.7°×5.7°	-60°
	1	5.7°×5.7°	60°
	1	1.1°×5.7° (blocked)	0°
ME	15	1°×4°	90°
	15	1°×4°	30°
	15	1°×4°	-30°
	2	4°×4°	90°
	2	4°×4°	30°
	2	4°×4°	-30°
	1	1°×4° (blocked)	90°
	1	1°×4° (blocked)	30°
	1	1°×4° (blocked)	-30°
LE	20	1.6°×6°	90°
	20	1.6°×6°	30°
	20	1.6°×6°	-30°
	6	4°×6°	90°
	6	4°×6°	30°
	6	4°×6°	-30°
	2	1.6°×6°, 4°×6° (blocked)	90°
	2	1.6°×6°, 4°×6° (blocked)	30°
	2	1.6°×6°, 4°×6° (blocked)	-30°
	2 (Large)	60°×2.5°	90°
	2 (Large)	60°×2.5°	30°
	2 (Large)	60°×2.5°	-30°

3.2 High energy X-ray Telescope (HE)

3.2.1 Introduction

The overview of *Insight*-HXMT/HE is taken from Liu et al. (2020). HE is composed of eighteen groups of detector units. Each detector unit consists of a NaI(Tl)/CsI(Na) crystals phoswich detector and a collimator. In addition, HE contains in-orbit calibration detectors and switch boxes, anti-coincidence detectors, particle-monitors (PM) and corresponding mechanical structure, as described in Fig. 3-4.

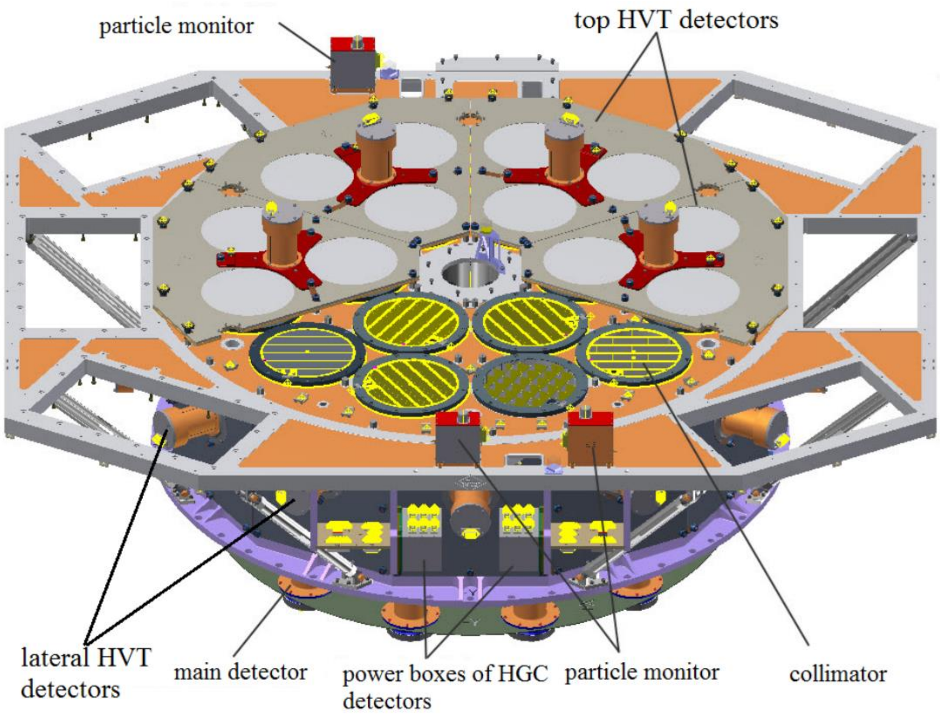

Fig. 3-4 (Left) HE Main Detector array. (Right) Illustration of a HE main detector.

HE detector performs in hard X-ray band 20–250 keV. To supply space modulation for the direct demodulation imaging, the FOVs of eighteen collimators are mounted in three different directions; in-orbit calibration detectors are used for gain-control and spectral calibration; to decrease the particle background, the anti-coincidence detectors are adopted to shield the charged particles in space. The particle detectors are utilized to monitor the particle flux to protect the main detectors and anti-coincidence detectors with high voltage when the particle flux is too high.

Each HE detector unit is composed of a cylindrical NaI(Tl)/CsI(Na) phoswich scintillation detector with a diameter of 19 cm (i.e., geometrical area of 283.5 cm^2) and the total geometrical area is 5100 cm^2. Because of the photoelectric effect in the NaI(Tl), the X-ray photons could deposit energy, which is used to measure the energy spectra and arrival times of the hard X-ray events. The latter CsI(Na) is primarily used as an active shielding detector to reject background events incident from the backside within the solid angle of 2π. The scintillation signals of these two types of crystals can be read out by a shared Photomultiplier Tube (PMT) and selected by Pulse Shape Discrimination (PSD) technique for selecting good events, during which energy is deposited only in the NaI(Tl) scintillator rather than in CsI(Na). To eliminate the side-effect of the evolving temperature on the detector, HE detector adopts the active temperature-control to maintain the temperature at 18±2℃.

There are 18 collimators, designed for the 18 detectors accordingly. The FOVs of fifteen collimators are set to 1.1°×5.7° and two collimators are set to 5.7°×5.7°. Specifically, one collimator with a FOV of 1.1°×5.7° is covered by a 2 mm-thick tantalum lid, which is used to measure the local background of HE and is called a blocked detector. All 18 collimators are divided into three groups and separated with orientation of 60° in the payload, which form the FOV of 5.7°×5.7°. The collimator allows the access of photons from special direction. The collimator is grid structure,which is made of material with strong X-ray absorption. The size of the grid determines the FOV of the collimator, e.g., the FOV of 1.1°×5.7° is made of grids with 6 mm × 30 mm × 300 mm (width × length × height). The distribution of 18 HE main detectors and 18 collimators is shown in Fig. 3-5. The top is the collimator, the middle is the NaI(Tl)/CsI(Na) phoswich crystal, and the bottom is the PMT reading out the fluorescence produced during the interaction between X-ray photons and the crystal.

The function of the in-orbit calibration detector depends on radioactive source ^{241}Am and plastic scintillator. ^{241}Am with radioactivity of about 200 Bq is embedded into a small plastic scintillator, which is installed in the grid close to the injection window of the corresponding detector. The calibration source emits the 59.5 keV photons and the 5.5 MeV α particle detected by the main detector and the plastic scintillator, respectively. If these two signals are detected simultaneously, the signal is tagged as calibration events. Based on the variation of calibration events (the good events produced by the 59.5 keV photons in the detector), HE power-control box adjusts the high-voltage of the PMT of the main detector to stabilize the gain of the main detector.

The particle-monitor (PM) is used to measure the flux of the high energy protons and electrons. When the flux is higher than a critical value, the PMTs in the main detectors and the anti-coincidence detectors would be closed to protect the tubes. There are three PMs mounted in HE payload. A PM is composed of a plastic scintillator, a photomultiplier tube, a high voltage unit and an electronic circuit. The plastic scintillator is designed as a cylinder with height of 10 mm and diameter of 10 mm, the top and side surface of which are painted with reflection material. The above system is packaged with Teflon, plastic hat and 1 mm aluminum sheets. The lower energy threshold of PM is 1 MeV (20 MeV) for electrons (protons). The fluorescence could be produced by the collision of the charged particles with the plastic scintillator. The fluorescence signal detected by PMT (0.5 inch) is processed in HE power-control box. HE main detector cannot perform the scientific observation when the environment is filled with many charged particles (e.g., in SAA) with the protection of the PM.

Anti-coincidence detector (ACD) is embedded into the front of the main detector, and consists of 6 top detectors and 12 side-surface detectors. ACD is designed as an active veto detector, i.e., screening the background event produced by the injected charged particles within the solid angle in the main detector. The ACD output signal is processed in HE power-control box. In the good event data of each main detector, 18 digits of BOOL type strings define the signal in the 18 ACD when the event appears. We can manually choose suitable anti-coincidence events during the offline data reduction.

HE power-control box manages the signal processing and control of all detectors, and exchanges data with the data-manage system of the satellite via LVDS and 1553B. To assure the accuracy of times, HE power-control box receives the synchronized time signal from the satellite and 5 MHz time signal at the same time.

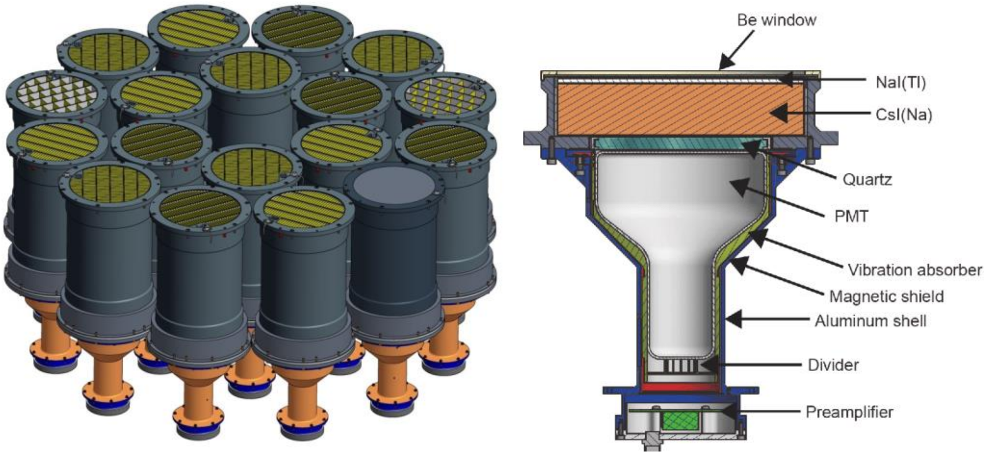

Fig. 3-5 (Left) HE Main Detector array. (Right) Illustration of a HE main detector

3.2.2 Gain Modes

The gain of NaI/CsI detector is mainly controlled by the High Voltage of the PMT which converts the scintillation light produced by NaI/CsI crystals to the electric signals. To meet various observation requirements, two gain modes are designed for the HE NaI/CsI detectors: NOrmal Mode (NOM) and Low Gain Mode (LGM). The measured energy ranges for NaI and CsI are different in these two gain modes, as listed in Table 3-3.

Change of gain mode must be implemented by telemetry commands. Please note that, gain mode will affect the energy range of both NaI and CsI detectors of HE, thus the gain mode (either NOM or LGM) should be specified explicitly in any proposal that uses HE telescope.

Table 3-3 Two gain modes for HE main detectors. The LGM is primary used to monitor the gamma-ray sources such as GRB, thus this mode is used to call GRB mode. Cited from Liu et al.

(2020)

Gain Mode	NaI Energy Range (keV)	CsI Energy Range (keV)	Notes
NOrmal Mode (NOM)	20–250	40–600	Normal HV for PMT. Enable the auto-gain control.
Low Gain Mode (LGM)	100–1250	200–3000	Reduced HV for PMT. Disable the auto-gain control.

3.2.3 Observation Scenarios of HE

HE can observe the sky with two observation scenarios:

(1) Pointed or scan observation: By using NaI/CsI detectors, HE can detect hard X-ray emission in 20–250 keV from the celestial sources within the FOV defined by collimators. HE can do pointed observation to a specific source, or scan observation to a small sky area.

(2) Gamma-ray all-sky monitoring: Gamma-ray photons with energy higher than ~200 keV from all directions can penetrate the spacecraft and be detected by the CsI detectors. CsI can monitor the gamma-ray all-sky with the only exception of the occulted region by the Earth. This gamma-ray all-sky monitoring is an extended capability for HE and inapplicable for ME or LE.

Please note that these two scenarios can work simultaneously.

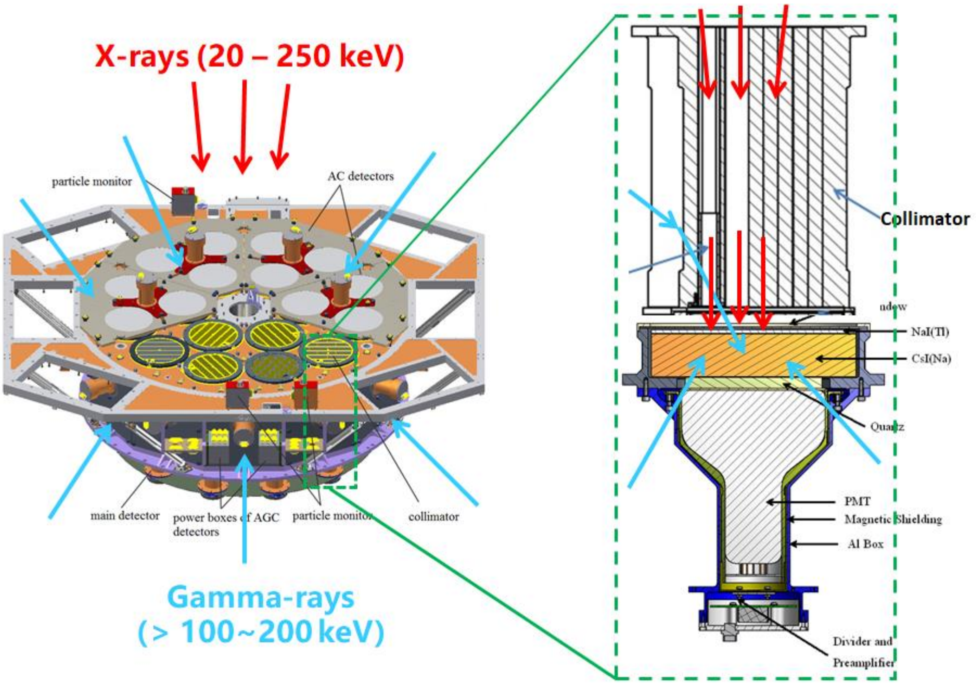

Fig. 3-6 Illustration of HE observation scenarios. Red arrows depict x-ray photons incident within the FOV of collimator while cyan arrows represent gamma-rays that can penetrate the satellite structure. These two observation scenarios can work simultaneously.

3.2.3.1 Pointed or scan observation

The primary observation scenario of HE is the pointed observation mode or scan observation mode, both of them use the NaI as the main detector and detect sources within the FOV of collimator in 20–250 keV. The CsI detectors mainly act as the anti-coincidence and shielding to reduce the background of NaI.

Fig. 3-7 shows the detection efficiency of HE detectors, and Fig. 3-8 shows the energy-dependent energy resolution.

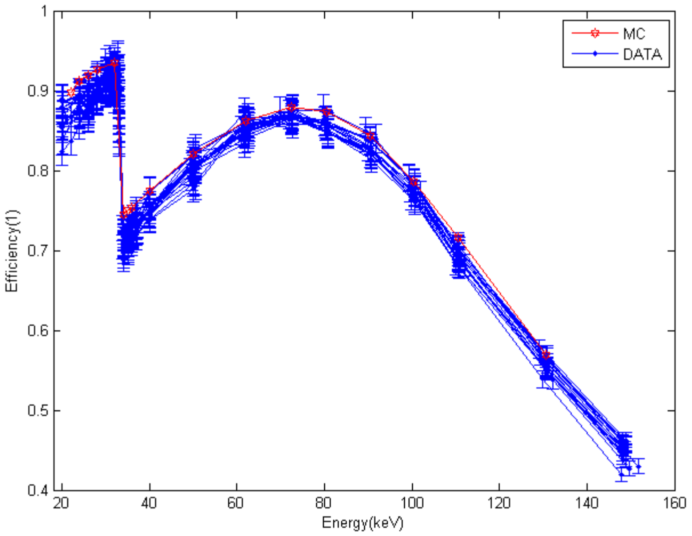

Fig. 3-7 the detection efficiency of 18 HE detectors in the whole energy range. The blue data points are obtained from the calibration experiments, and the red from the simulations (Liu et al. 2020).

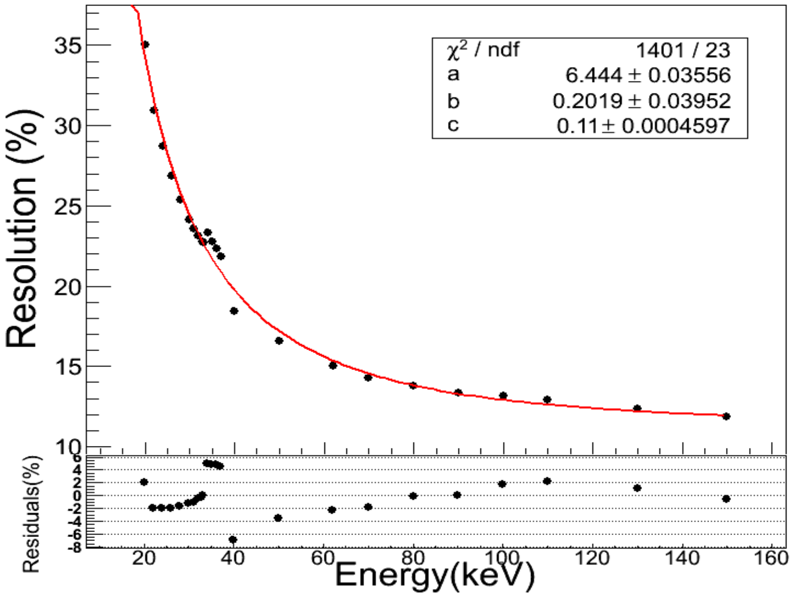

Fig. 3-8 the energy resolution of HE. The black points are obtained from the calibration experiments and the red line is the fitted line.

3.2.3.2 Gamma-ray all-sky monitoring

Apart from the observation of hard X-ray photons incident within the FOV of collimator, HE can detect the gamma-ray photons with energy higher than ~200 keV from all directions, which can penetrate the spacecraft, experience complicate processes and leave energy deposition in the CsI detectors. The FOV of this gamma-ray all-sky monitoring is all sky un-occulted by the Earth.

To improve the energy range of CsI for gamma-ray all-sky monitoring, HE main detector will switch to the Low Gain Mode by tele-command during the observation periods when the NaI measurement in 20–250 keV is not needed.

As shown in Fig. 3-9, the payload coordinate is used to define the incident angle (zenith angle θ and azimuthal angle φ) of gamma-ray source.

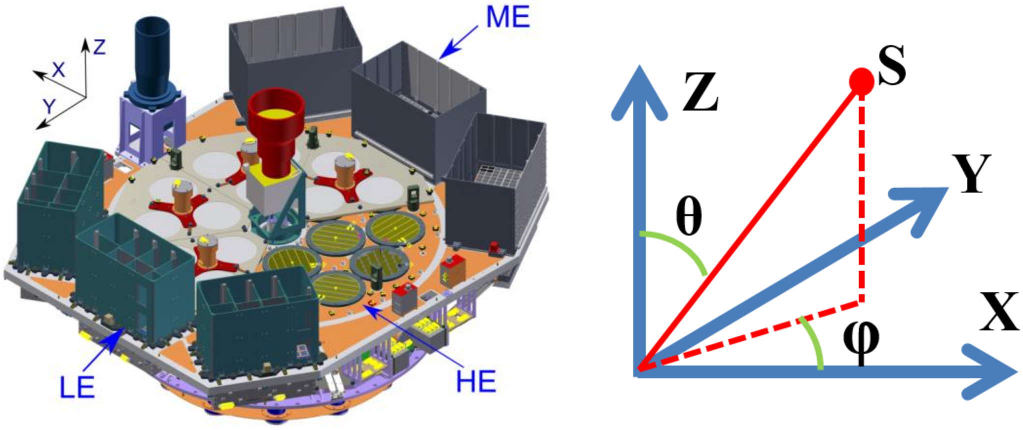

Fig. 3-9 (Left) Definition of the payload coordinate. (Right) Illustration of the incident angle (zenith angle θ and azimuthal angle φ) of gamma-ray sources (S) in the payload coordinate.

There are 18 CsI detectors in HE, denoted as HED-0, HED-1, …, HED-17 respectively. The dependence of the total effective area on the energy and incident angle of gamma-rays is shown in Fig. 3-10. Because the effective area mainly varies with the zenith angle θ and has little dependence on the azimuthal angle φ, the effective area curve for each θ is calculated by averaging over the φ in 0–360 deg.

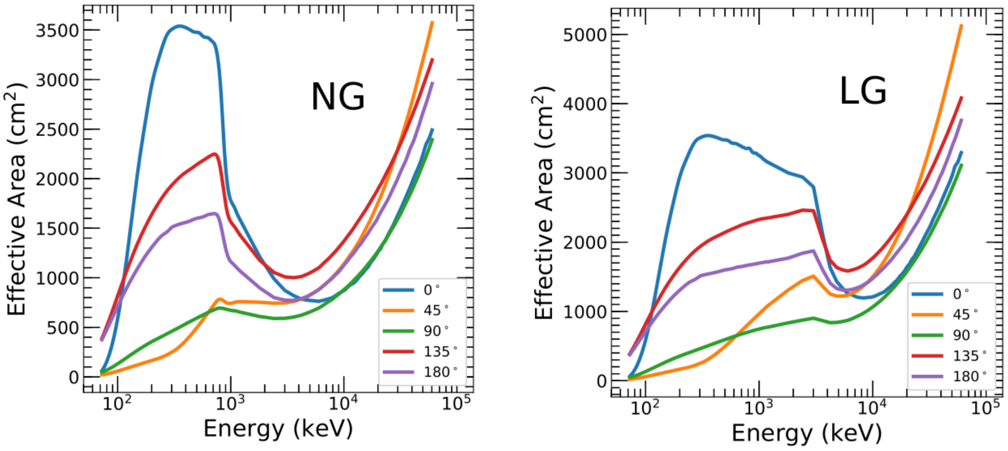

Fig. 3-10 Effective area of the CsI detectors to the gamma-rays. Normal mode and Low Gain Mode are shown in Left and Right panels, respectively. Each line represents the effective area for different zenith angle θ (shown in the legend) averaged within azimuthal angle φ from 0 deg to 360 deg (Q Luo et al. 2020).

Shown in Fig. 3-11 is a comparison of effective area between *Insight*-HXMT/CsI and other gamma-ray monitors in operation.

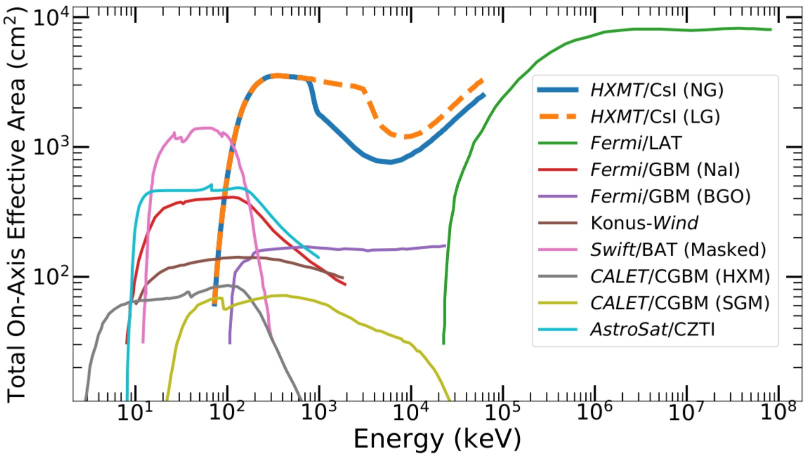

Fig. 3-11 Effective areas of *Insight*-HXMT/CsI and other gamma-ray monitors in operation. An averaged effective area over the unocculted sky is plotted for *Fermi*/GBM (NaI) (Luo et al. 2020).

Since CsI can detect gamma-rays from all incident angles, the FOV of the gamma-ray monitoring is the all-sky unocculted by the Earth, as shown in Fig. 3-12.

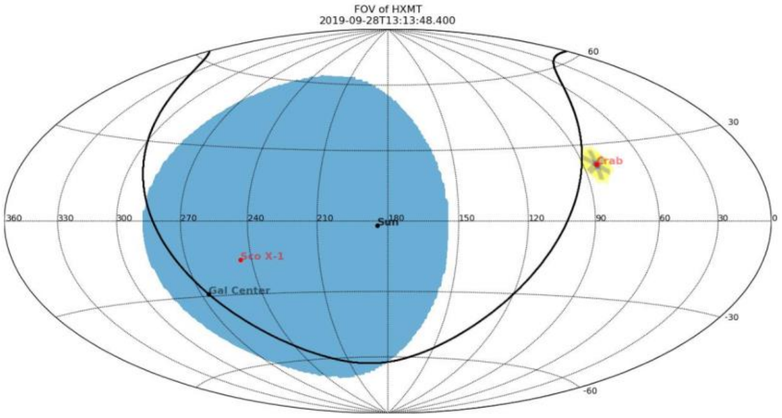

Fig. 3-12 the FOV of *Insight*-HXMT as a gamma-ray all-sky monitor at 2019-09-28T13:13:48.400. The blue region represents the occulted sky by the Earth that changes with time, while the yellow region is the FOV of HE collimator.

Energy resolution of all 18 CsI detectors and energy response of a CsI detector (HED-0) are shown in Fig. 3-13 and Fig. 3-14, respectively.

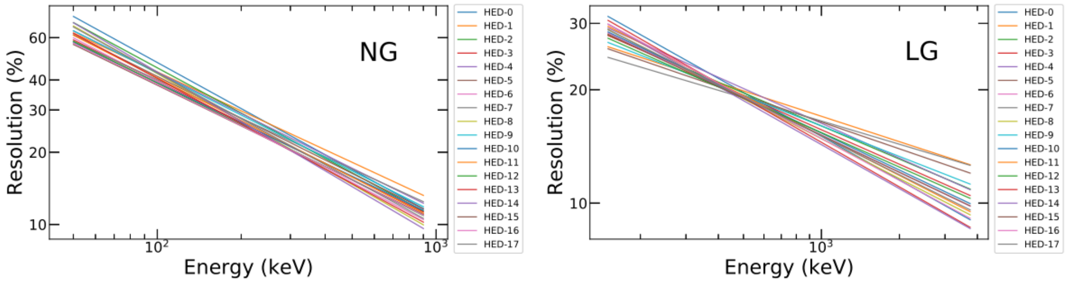

Fig. 3-13 Energy response of HE CsI detector in NOrmal Mode (Left) and Low Gain Mode (Right) (Luo et al. 2020).

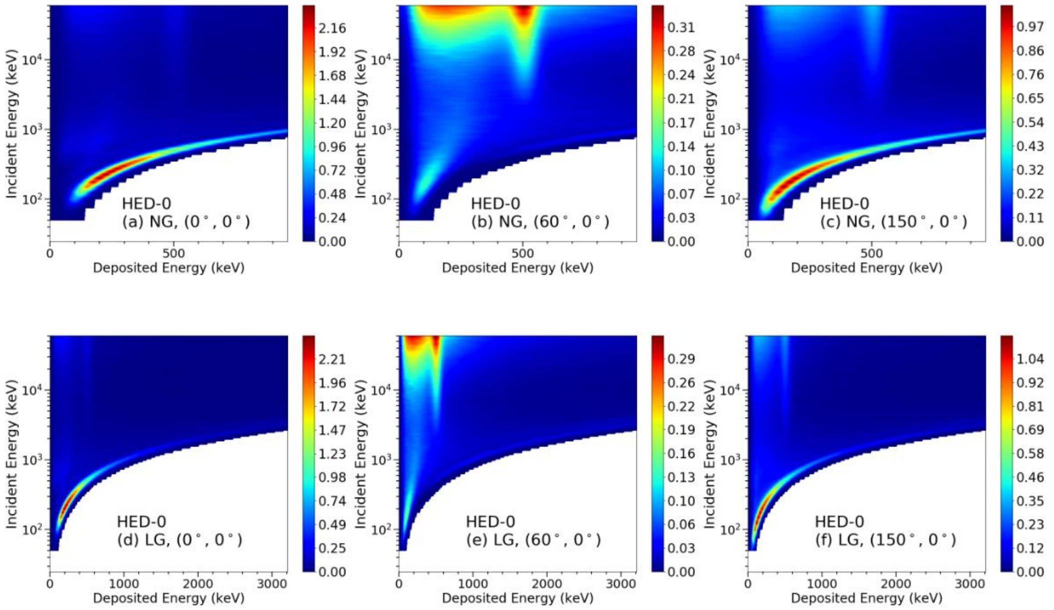

Fig. 3-14 Energy response of HE CsI detector (HED-0 as an example) in NOrmal Mode (up panels) and Low Gain Mode (bottom panels). Incident angles in the format of (θ, φ) are shown in the legend (Luo et al. 2020).

The total background rate of 18 CsI detectors varies from 5000 to 12000 counts/s, depending on the geolocation of the satellite, the solar activity and geomagnetic activity. Low Gain Mode has lower background than NOrmal Mode. Since the effective area also depends on the incident angle, the GRB detection sensitivity of CsI is determined by the incident angle of GRB, the geolocation of satellite and the gain mode of the NaI/CsI detector.

Since *Insight*-HXMT does not have in-flight trigger and real-time downlink, all GRBs are found by the ground search from the CsI event data. Both blind search and targeted search have been implemented in the GRB processing pipeline. By using a much finer search parameter, targeted search could find weaker GRBs than blind search. In general, the *Insight*-HXMT detection sensitivity to GRB prompt emission (in 0.2–3 MeV) could reach ~8×10^{-8} erg/cm^2 (10–1000 keV), as shown in Fig. 3-15.

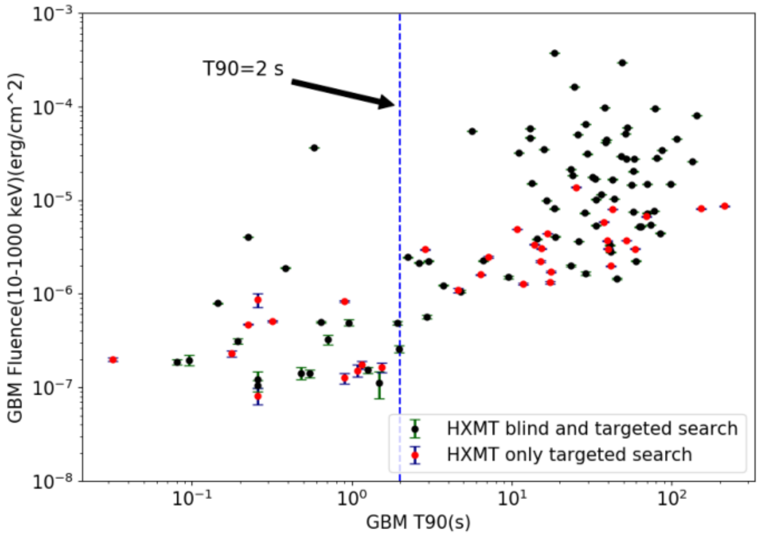

Fig. 3-15 GRBs jointly detected by *Insight*-HXMT and *Fermi*/GBM. Those GRBs in green could be found by both blind search and targeted search, while red ones are only revealed by targeted search (C. Cai et al. 2020).

Since event data is recorded for CsI detector, the time accuracy of gamma-ray monitoring data is about few microseconds. CsI detector has an effective area of thousands square centimeters, which allows CsI to measure the fine temporal features of GRBs in MeV band. Fig. 3-16 gives the Light curve of GRB170904A detected by *Insight*-HXMT/HE CsI detector.

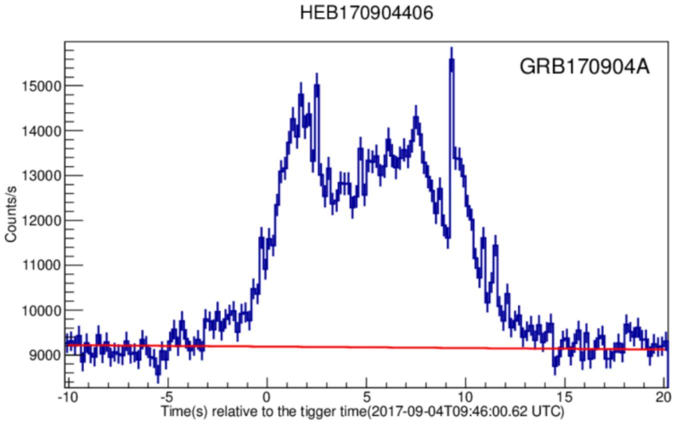

Fig. 3-16 Light curve of GRB170904A detected by *Insight*-HXMT/HE CsI detector. Fine temporal features (e.g. spikes) are seen with high statistics.

Insight-HXMT can also monitor the MeV pulsars with the gamma-ray all-sky monitoring observation scenario. Especially, gamma-ray emission from the Sun and the Earth could be monitored as well, including Solar Flares and Terrestrial Gamma-ray Flash (TGF).

TGF is a very short period (~0.1 ms) of gamma-ray emission produced in the lightning process. *Insight*-HXMT can detect about 100 TGFs/year. Observation data of a typical TGF is shown in Fig. 3-17. Fig. 3-18 shows the distribution of sub-satellite points of *Insight*-HXMT when TGFs are detected. Most TGFs are produced in the active region of lightning.

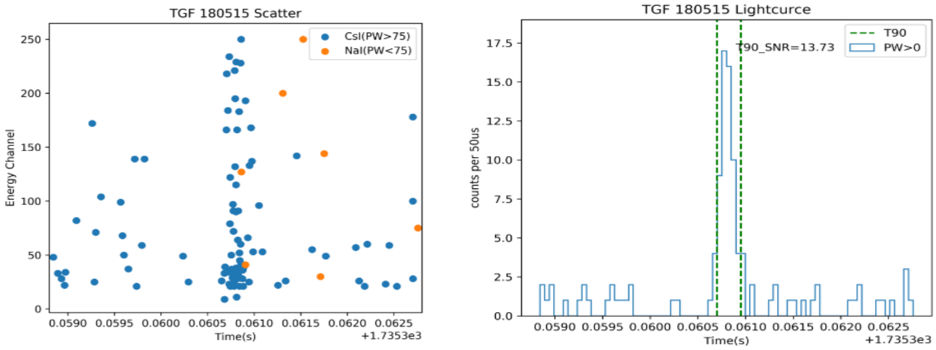

Fig. 3-17 Observation data of TGF180515. (Left) scatter plot of event data. (Right) Light curve of the TGF. Dashed green lines indicate the time interval of T90.

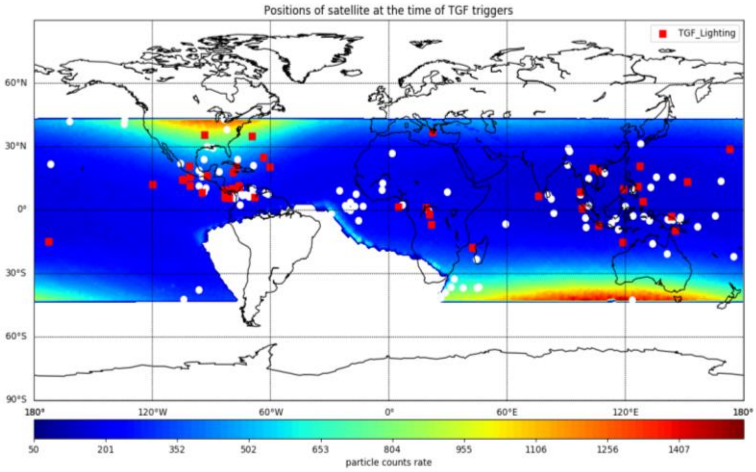

Fig. 3-18 Distribution of sub-satellite points of *Insight*-HXMT when TGFs are detected. Red are TGFs with lightning association while white are without lightning association.

3.3 Medium energy X-ray telescope (ME)

The overview of *Insight*-HXMT/ME is taken from Cao et al (2020). ME is designed to study the radiation properties of X-ray sources in the medium X-ray band. It covers 5–30 keV energy band and has energy resolution of about 3 keV, a total geometrical area of 952 cm^2, and a main FOV of 1°×4° (FWHM).

ME consists of three detector boxes (MED1,MED2,MED3) and a power-control box (MEB). Fig. 3-2 and Fig. 3-3 show the layout of these detectors (installed on one side of HE) and the directions of their long sides are separated by 60°. Power-control box locates inside the payload of the satellite. ME detectors consist of Si-PIN arrays divided into nine independent detector-units, with three units constituting one detector box. The collimator is installed on the top of the detector. A detector unit is further divided into six detector modules, with each of which contains 32 Si-PIN detectors. To obtain high energy resolution with lower noise, Si-PIN detectors should work in low temperature. The in-orbit shade cover serves as a heat conductor, in order to transmit the detector heat to the radiative surface to ensure the detector temperature lower than -10℃.

Fig. 3-19 shows the structure of ME detector, including the radiative cooling panel, collimator and some plug-in components.

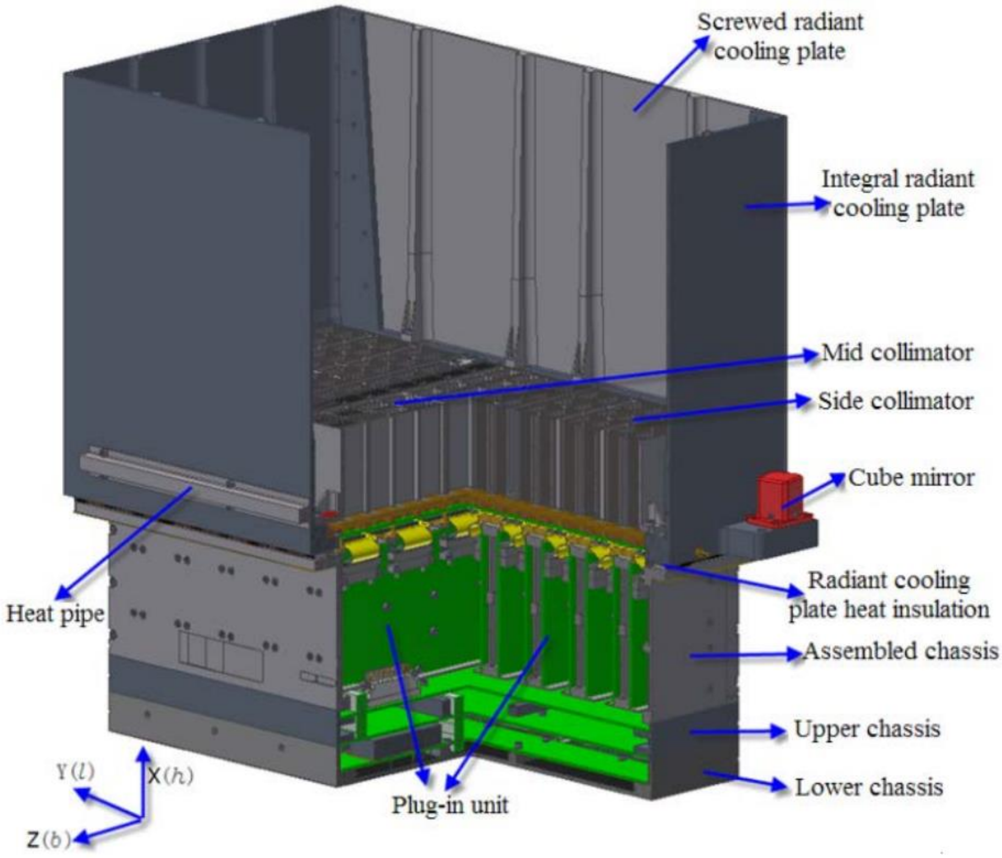

Fig. 3-19 the structure of the ME detector case.

The radiative cooling panel, contacting with the detector-component, can transmit the detector heat to the radiative surface to ensure the detector temperature ranging from -40 to -10℃. The Si-PIN detector is designed with the thickness of about 1 mm, and pixel scale of 56 mm^2. When X-ray photons reach the detector base, X-ray photons lose all or part energies through photoelectric and Compton processes, which induces the formation of the electron-vacancy pair. Due to the existence of the inner electric field, these electron-vacancy pairs would be collected by the electrodes, accordingly forming the electric signal. The energy resolution (FWHM) is ≤3 keV@20 keV in working temperature ranging from -40 to -10℃.

The collimator is designed to set a limit on the FOV of the telescope. ME collimators perform with large and small FOVs, which facilitate the background analyses. There are 54 detector modules, 45 of which are covered by collimators with a FOV of 1°×4°. A detector with a small FOV shows high spatial resolution and low probability of source contamination, and is applicable to observe point sources and diffuse sources with a small scale; especially in the scanning observations, the detector displays the same observation advantage. Six modules adopt collimators with a large FOV of 4°×4°, displaying large FOV area, which is helpful to search for and observe diffuse sources. The other three modules are equipped with blocked collimators, which can measure the background events of the leaked sources and charged particles. Fig. 3-20 shows one unit of ME collimator.

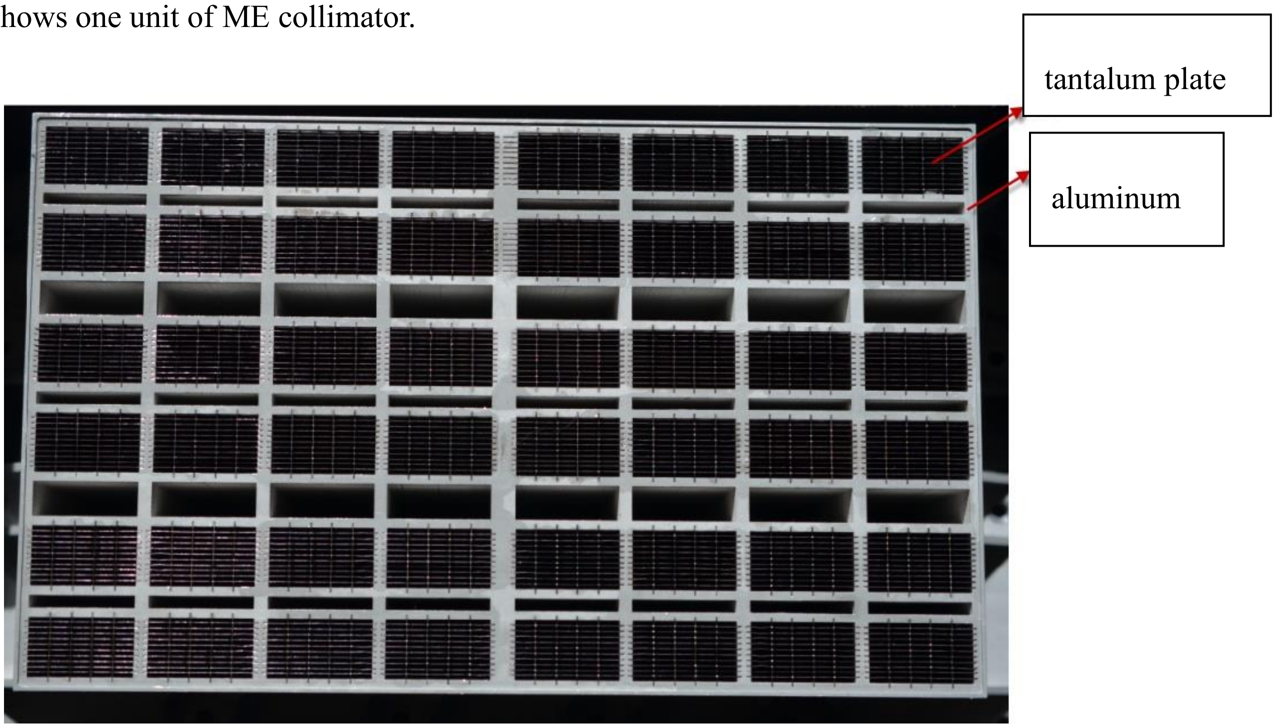

Fig. 3-20 One unit of ME collimator.

The pixel area of a Si-PIN detector is positively correlated with electric capacity that is positively correlated with the noise of the electric charge amplifier. In order to maintain the energy resolution of the system, the area of the detector should be smaller than certain value. However, due to the physical requirement, the area of a single-pixel detector should be larger than a value to avoid the complexity of the readout electronic circuit and high power-consumption o the system. Consequently, the scale of the pixel is set as about 50 mm^2, i.e., 12.5 mm × 4.5 mm (56.25 mm^2) after many trials. At present, there are 54 ME modules, and 32 detector pixels in each module, all of which are readout by one VA32-TA6 chip. In total, there are 1728 Si-PIN detector pixels with the area of 952 cm^2. In each ME box, there is a collimator installed with the radioactive source, which is applied for calibrating the energy resolution and signal amplitude of the in-orbit calibration detector. In the detection energy range of ME sub-system (5–30 keV), the in-orbit calibration adopts the radioactive source ^{241}Am. That is, based on the radiation at 17.8 keV, the count rate should be 16, and the activity of radioactive source is 1 μCi.

Each ME detector box has 9 independent plug-in components, while each component possesses two independent modules. There are 16 Si-PIN detector packages, in which each of them contains 4 Si-PIN pixels, adhered to the plug-in copper plate. The shell of the detector is ceramics, with its top covering with an aluminum alloy frame with tantalum foils inserted inside and Be windows.

Fig. 3-21 shows the ME plug-in component.

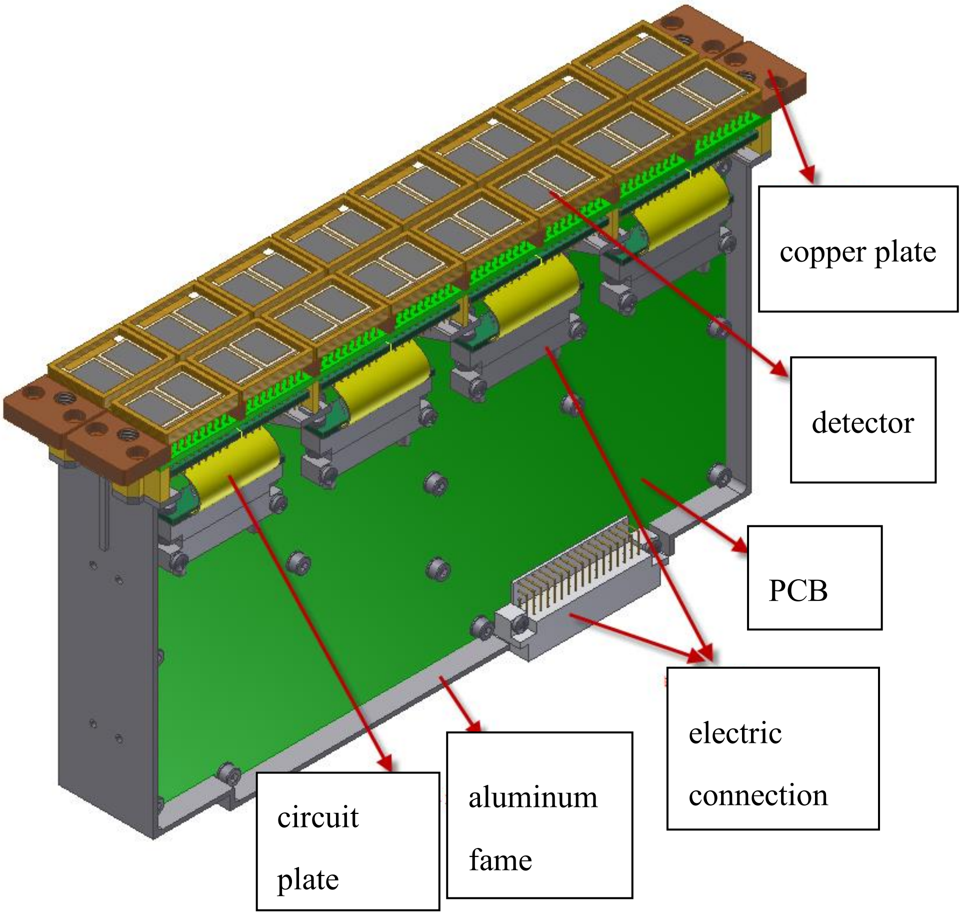

Fig. 3-21 the structure of one MED plug-in component

Fig. 3-22 shows the detection efficiency of ME telescope. Here the decay of the efficiency below 13 keV is caused by the trigger threshold of the readout ASIC chip. Fig. 3-23 shows the measured spectrum of the radioactive source Am-241, with the energy resolution of about 3 keV@17.8 keV.

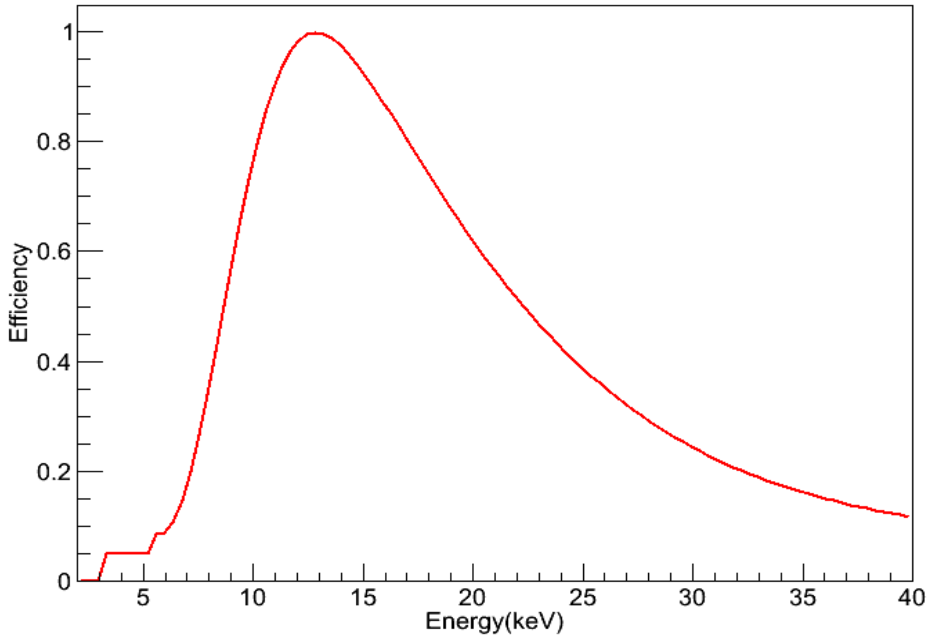

Fig. 3-22 the detection efficiency of *Insight*-HXMT/ME. The duty-cycle of the collimator is considered, and the area of the collimator is smaller than 850 cm^2.

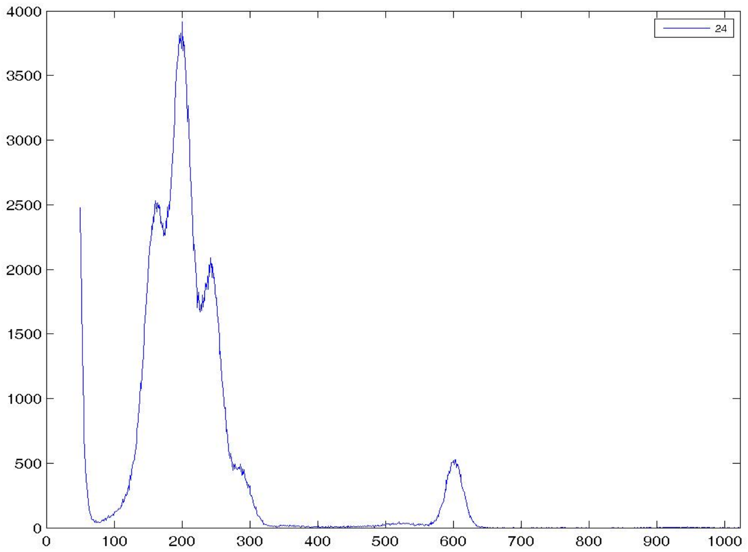

Fig. 3-23 the energy spectrum of Am-241 detected by *Insight*-HXMT/ME. The three peaks in the low energy band locate at 13.9, 17.8 and 21 keV, respectively, and the one in the high energy band at 59.5 keV.

3.4 Low energy X-ray telescope (LE)

The overview of *Insight*-HXMT/LE is taken from Chen et al (2020). LE mainly performs observations with high energy resolution (150 eV@5.9 keV) and high time resolution (1 ms) in 1–15 keV. LE contains 3 independent detector boxes, controlled by a power-control module. Each box includes 8 detector modules, while each module has 4 CCD236. The area of each box is 128 cm^2, hence the total area is 384 cm^2, as described in Fig. 3-24.

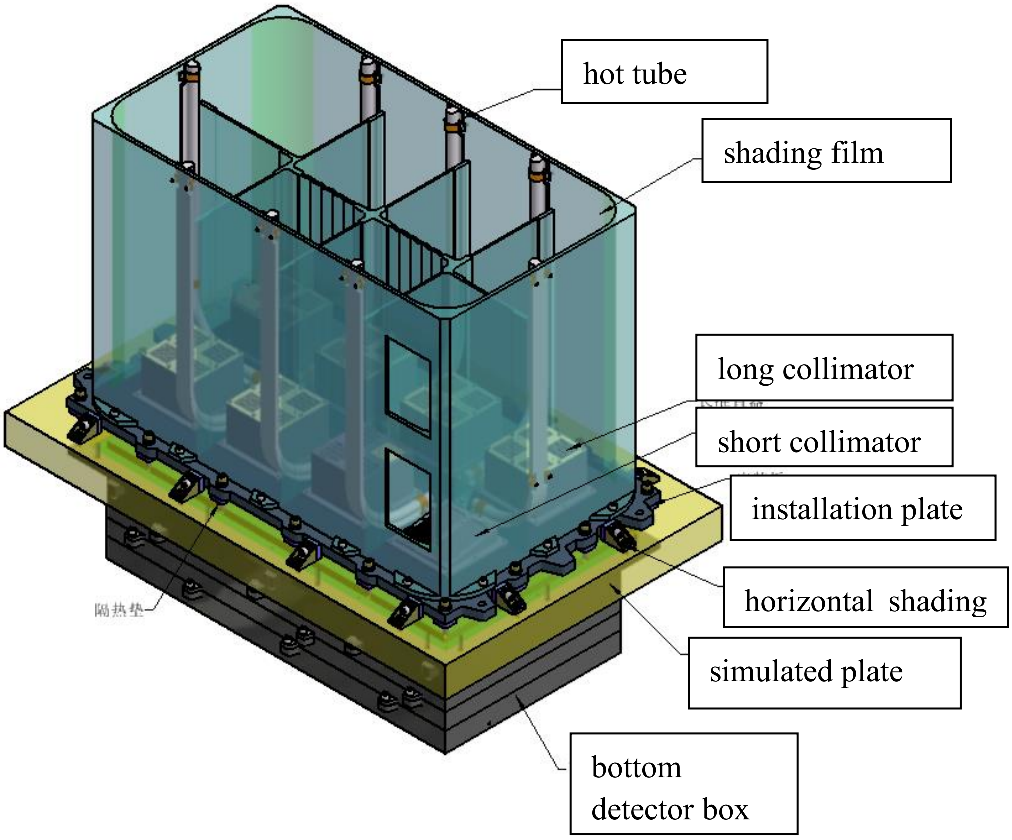

Fig. 3-24 the structure of one LE detector box. The top gray part is the collimator, and the semi-transparent part is the block cover.

There are eight collimators in each LE detector box, including seven long collimators and a short collimator. Each long collimator contains 4 collimation units, and each short one has 2 units, i.e., a total of 30 collimation units. The height of the long collimator is 53.5 cm, including three FOVs of 1.6°×6.0° and one FOV of 4.0°×6.0°. Every LE detector unit contains two blocked long collimators, i.e., those with FOV of 1.6°×6.0° and 4.0°×6.0°. The height of the short collimator is 27.5 cm, including two units with FOVs of 50~60°×2~6°.

In total, according to the classification of the FOV unit, the FOVs of three boxes of the LE collimator involve 60 FOVs of 1.6°×6.0°, 18 FOVs of 4.0°×6.0°, 6 blocked FOVs, and 6 all-sky monitors FOVs of 50~60°×2~6°.

Fig. 3-25 describes the layout of FOV units of distinct collimators in the same detector box.

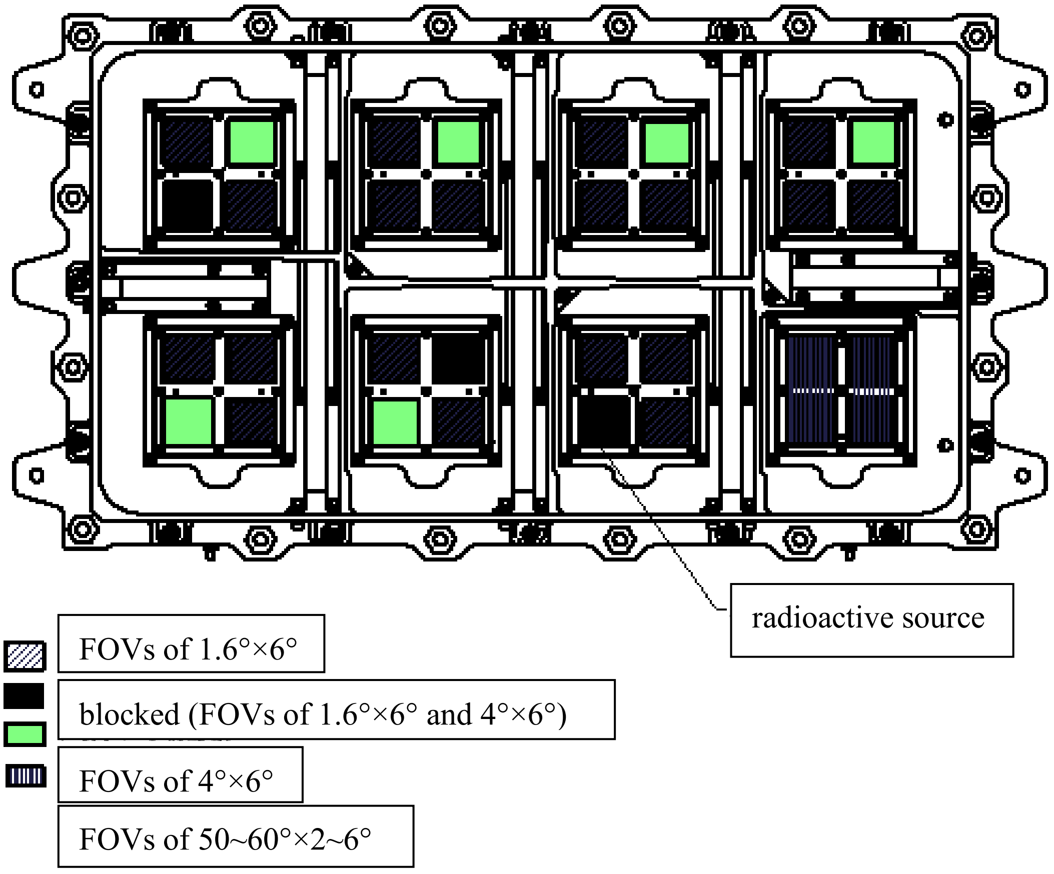

Fig. 3-25 the layout of LE collimator FOV units.

LE collimator is produced by the integrated wire cutting process, its bottom flange connects with the installation plate, and the optical blocking filters (OBFs) mechanically strengthened by Ni frames fixed on the top of the collimator. With the protection of special-shaped ventilation holes distributed on the top of the collimators, the optical blocking filters can survive the severe airflow impact during the satellite launch. To avoid possible material disturbing the function of the CCD, the bottom of the collimator is packaged by the dustcover. The normal collimators are attached around with 0.2 mm thick tantalum plates to reduce the background induced by gamma-rays and charged particles in space. The tantalum plates are also pegged by screws. Fig. 3-26 describes the structure of the long collimator, shade cover and dustcover.

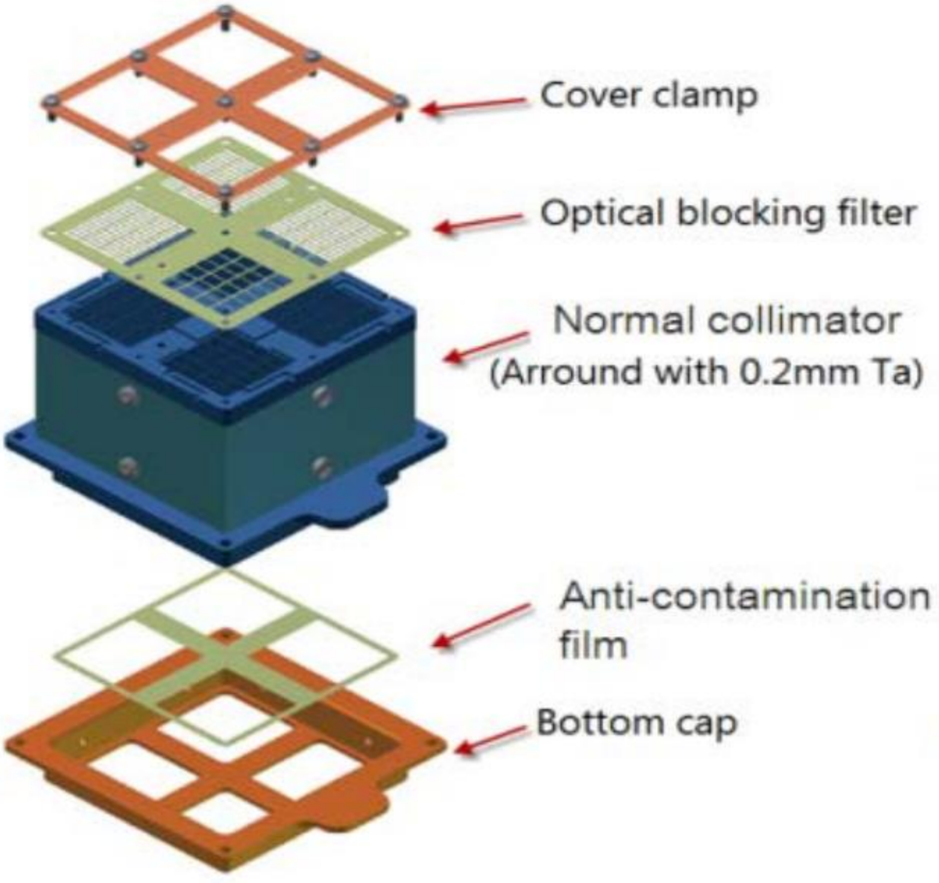

Fig. 3-26 the structure of the long collimator, shade cover and dustcover in LE.

The short collimator (see Fig. 3-27) is pegged with transverse tapered stiffener with the taper of 15°, bottom width of 8 mm and height of 18 mm. Whereas the stiffener blocks partial injected light, decreasing the theoretical FOV of the collimator

(50~60°×2~6°). Thus, the top surface of the collimator is designed as a bevel to offset the partially blocked light. The maximal height of the short collimator is 27.5 mm, and the minimal height is 16 mm. This kind of collimator can supply a large FOV to monitor the bright source in the large sky-area. The collimator is also packaged in the shade cover and dustcover.

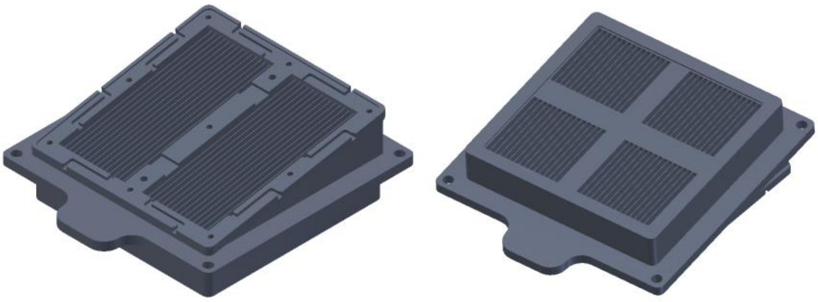

Fig. 3-27 the front face and the backside of the short collimator in LE.

The soft X-ray filtering film allows the penetration of the soft X-ray radiation, and screens the optical and ultra-violet light to LE's CCD, which can effectively decrease the noise of the observation. In order to resist the vibration during satellite launch and the background noise, the filtering film should not only satisfy the mechanical strength and radiation resistance, but also allow the penetration of the soft X-ray radiation as much as possible. Thus, the filtering film is composed of aluminum shell, polyimide shell and Ni frame. Here the aluminum shell (with thickness of 200 nm) can inhibit the optical radiation, polyimide shell (with thickness of 400 nm) can strengthen the mechanical performance of the film, and the Ni frame can supply the stability of the whole film.

The swept charge device (SCD) is adopted as the detector of LE. SCD is a kind of special CCD, which can quickly output the information of the injected X-ray photons by discarding the position information, with time resolution of 1 ms. Due to small dark current, low electric capacity, and low noise, SCD displays good energy and time resolution, with lower detection energy threshold down to 1 keV. CCD236 is a SCD detector jointly developed by IHEP and e2v-company (see Fig. 3-28), applying virtual/real output to reduce common mode noise, and the chip area of each detector is 4 cm^2. In the CCD236, there are many small electrodes, which collect the electrons produced during the low energy X-ray photons (1–15 keV) injecting the CCD236. The number of the electrons is positively correlated with energy deposition of the incident X-ray photons. The electrons can reach the output point, and can be converted into the voltage signal via the interior front end charge sensitivity amplifier.

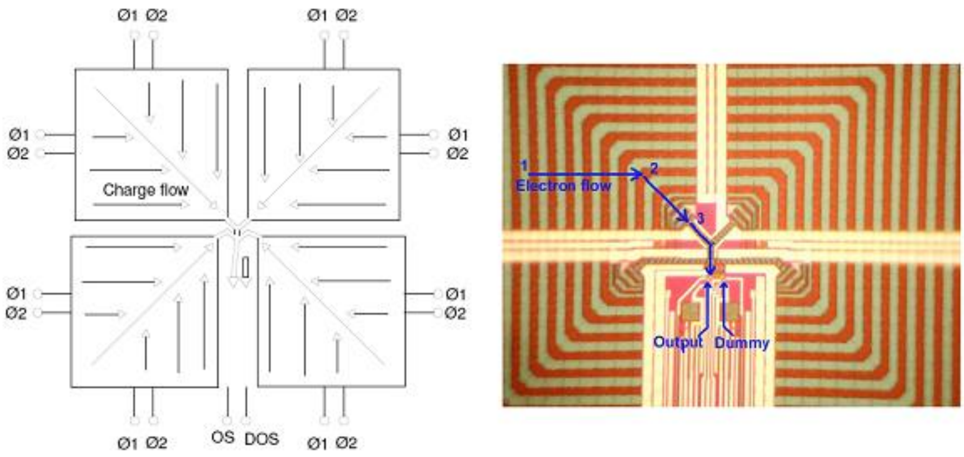

Fig. 3-28 the structure of CCD236 and its readout (installed in the center of the detector).

SCD may amplify its dark current due to the damage caused by the radiation from the charged particles in space. In order to control its noise within 4 years, SCD should work at a very low temperature of -80℃~-30℃. Thus, the detector should be separated from the electronic part, and the heat produced by the detector should be transported to the filtering film via the heat tube and further radiates to space. According to the radiation examination, the energy resolution of LE detector would deteriorate from 140 eV@5.9 keV@-50℃ to 220 eV@5.9 keV@-50℃ finally, due to the illumination of the charged particles. In Fig. 3-29 the detection efficiency of LE is plotted, and the temperature-dependent energy resolution is measured in Fig. 3-30.

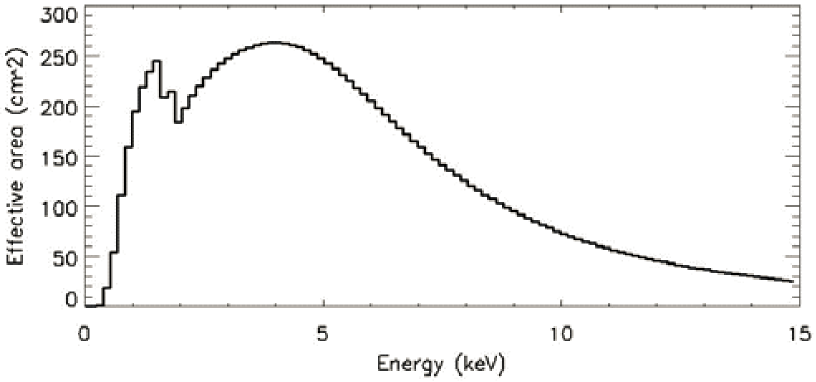

Fig. 3-29 the detection efficiency of LE. The horizontal axis is in units of keV (Li X.B. et al. 2020).

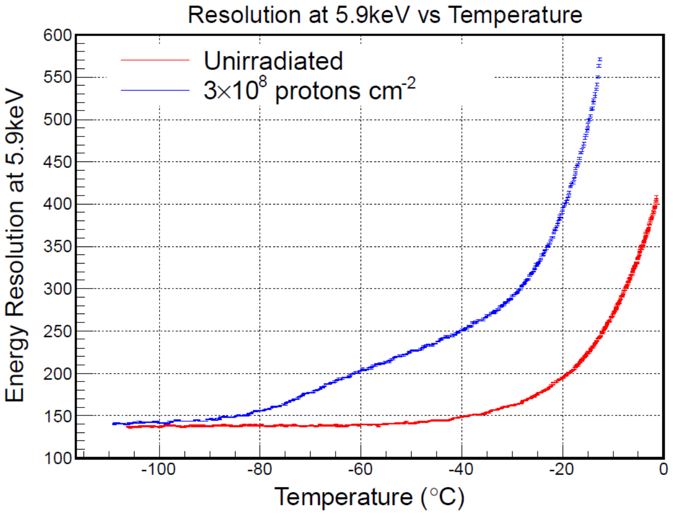

Fig. 3-30 the energy resolution of LE. The red curve is the profile without radiation, and the blue is that considering proton radiation with the dose for 4 years.

3.5 Space environmental monitor (SEM)

The overview of *Insight*-HXMT/SEM is taken from Zhang et al (2020). The Space Environment Monitor (SEM) is to monitor the charged particle environment of the satellite, which can be used in the estimation of the in-orbit background of the telescopes. SEM has 18 individual detector units, among which one is to measure the spectrum of electrons in 0.4 to 1.5 MeV, one to measure the spectrum of protons in 3 to 150 MeV, and the other 16 units to measure the particle fluxes in different directions, as described in Fig. 3-31. Both the electron spectrometer and the proton spectrometer have seven energy channels.

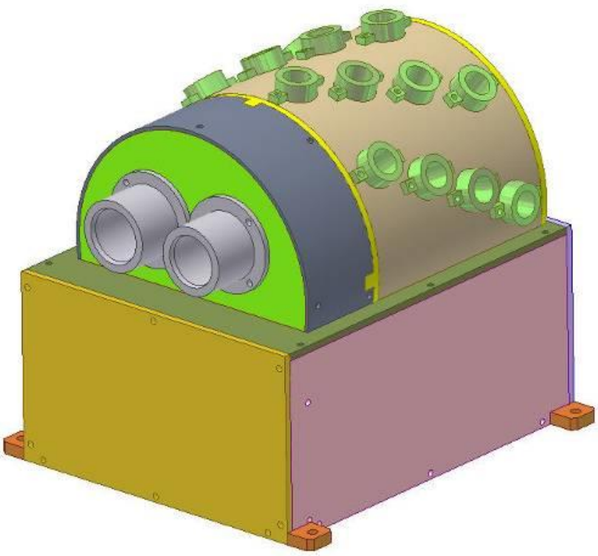

Fig. 3-31 the structure of SEM. The two detectors in grey color are the electron spectrometer (left) and the proton spectrometer (right), and all others measure particle fluxes from different directions.

More details about SEM are summarized as Table 3-4.

Table 3-4 the main technique parameters of SEM

	Particle direction detector	Electron spectrometer	Proton spectrometer
Numbers	16	1	1
FOV(FWHM)	180°×15°	30°	40°
Energy band (FWHM)	⩾200 keV (electron) 1.5–200 MeV (proton)	0.4–1.5 MeV (6 channels) ＞1.5 MeV (1 channel)	3–150 MeV (6 channels) ＞150 MeV (1 channel)
Time resolution	1 s		

3.6 Characteristics of *Insight*-HXMT telescopes

The main parameters of all three telescopes are listed in Table 3-5. The effective areas of the three X-ray telescopes are shown in Fig. 3-32, the background spectrum in Fig. 3-33, and sensitivities in Fig. 3-34 and Fig. 3-35, respectively.

Table 3-5 Characteristics of *Insight*-HXMT telescopes

Payloads	HE	ME	LE
Detectors	NaI/CsI	Si-PIN	SCD
Detector area (cm^2)	~5100	952	384
Energy band (keV)	Normal mode: 20–250 (NaI) 40–600 (CsI) Low Gain mode: 100–1250 (NaI) 200–3000 (CsI)	8–35	1–12
FOV (FWHM)	Pointed or scan observation: 18 collimators, including 16 FOVs of 1.1°×5.7° (one blocked), 2 FOVs of 5.7°×5.7° Gamma-ray monitoring: all-sky unocculted by the Earth	3 detector boxes, each of which contains 16 FOVs of 1°×4° (one blocked), 2 FOVs of 4°×4°	3 detector boxes, each of which contains 21 FOVs of 1.6°×6° (one blocked), 7 FOVs of 4°×6° (one blocked), and 2 FOVs of 50~60°×2~6°
Energy resolution (FWHM)	⩽17%@60 keV	15%@20 keV	2.5%@6 keV
Point source resolution (20σ)	1' (1σ)		
Time resolution	4 μs	240 μs	1 ms

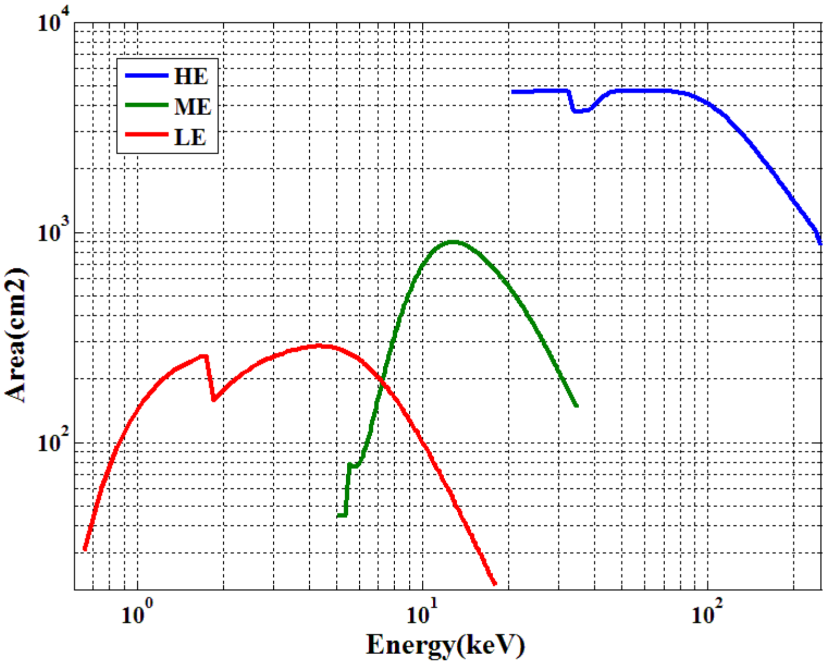

Fig. 3-32 the effective areas of the three telescopes (HE, ME and LE) of *Insight*-HXMT (Zhang S.N. et al. 2020).

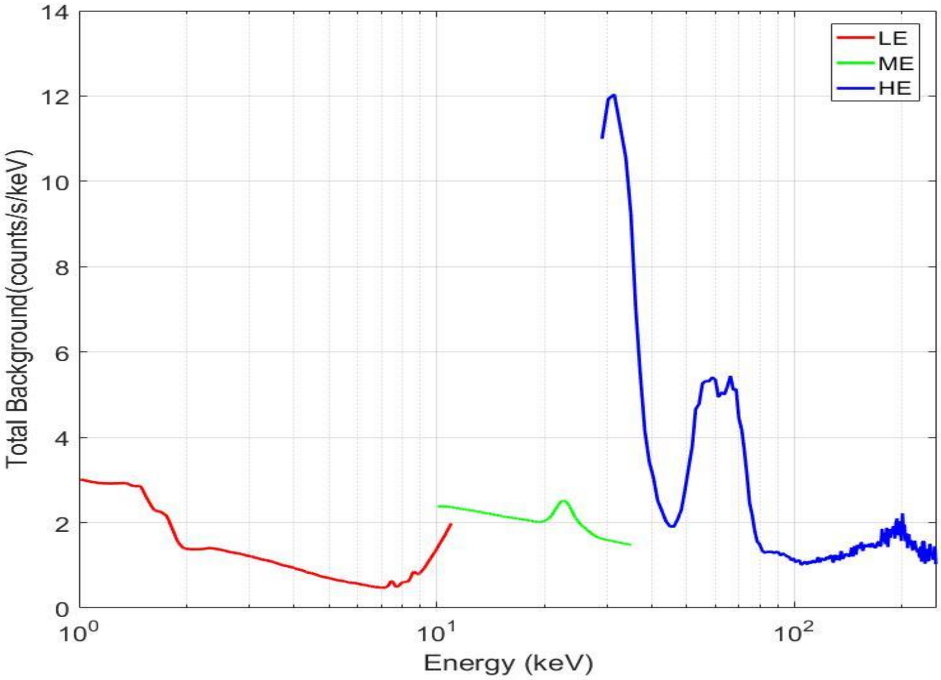

Fig. 3-33 the background spectrum of *Insight*-HXMT detectors.

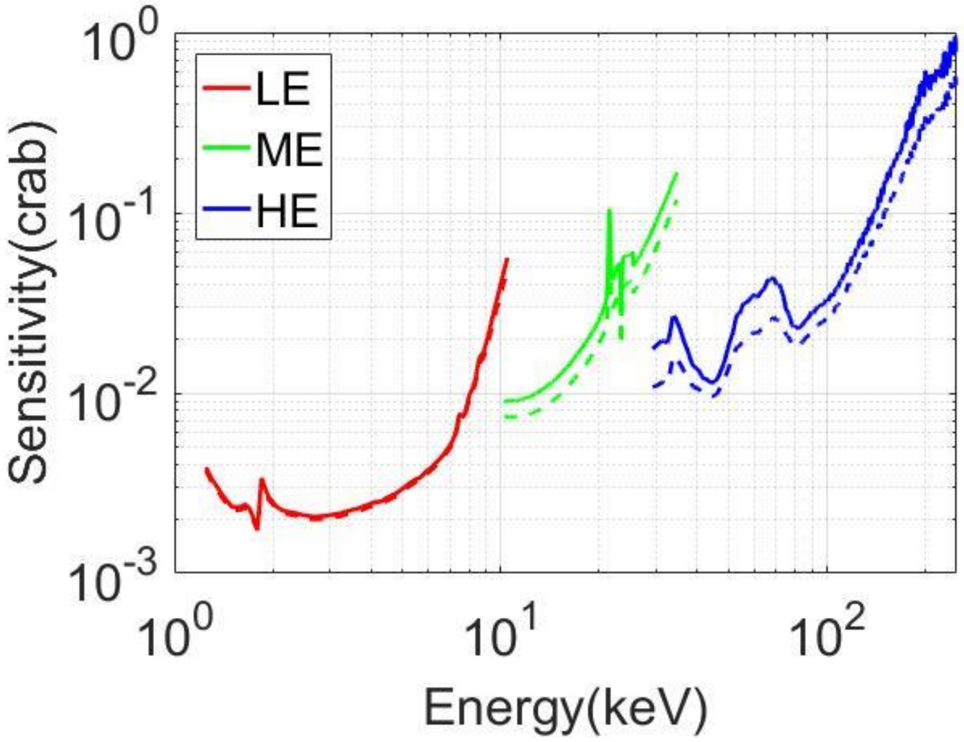

Fig. 3-34 Sensitivity of pointing observations of the three *Insight*-HXMT detectors (100 s, 3σ). The dashed line is the estimation considering only the statistical fluctuations, and the solid line is that including systematic errors of the background (the systematic errors of HE, ME and LE are 1%, 2% and 2% of their backgrounds, respectively).

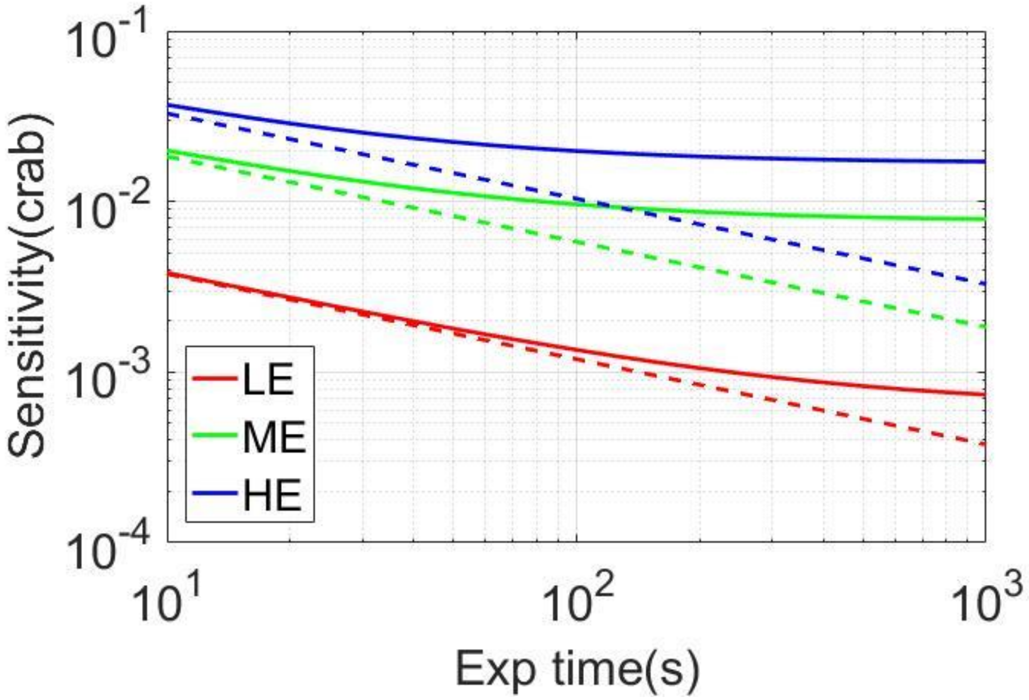

Fig. 3-35 the time-dependent sensitivity of pointing observations of the three *Insight*-HXMT detectors (3σ). The energy ranges of LE, ME and HE are 1–6 keV, 10–20 keV, and 30–100 keV, respectively. The dashed lines are the estimation considering only the statistical fluctuations, and the solid lines are that including the systematic errors of the background (the systematic errors of HE, ME and LE are 1%, 2% and 2% of their backgrounds, respectively).

4 Core Sciences

4.1 Introduction

Thanks to its large effective area and narrow field of view in hard X-ray band, *Insight*-HXMT has better capability in sky survey for weak and variable sources than other hard X-ray telescopes. *Insight*-HXMT will survey the Galactic plane frequently. It will perform deep and high cadence Galactic survey, produce catalog that encloses new transients or reveals new phenomenon. *Insight*-HXMT has a very wide energy band (1–250 keV) that covers both soft and hard bands of X-ray binaries. HE (20–250 keV) has the largest effective area among the space telescopes with narrow field of view (FOV), which is an advantage in observing the X-ray binary outbursts and evolution in low/hard spectral state. Its soft X-ray band reaches the energy as low as 1 keV and has adequate energy and time resolution. It can avoid the problem of detector saturation (photon pile-up) when observing bright sources, and has advantages in observing bright sources in soft X-ray energy band and outbursting sources in high/soft spectral state. Overall, *Insight*-HXMT will bring broad-band and high statistical observations for bright and outbursting sources in 1–250 keV. Such results can be used to systematically study the outburst evolution of an X-ray binary, such as the low/hard state and high/soft state, to study the basic properties of a BH, i.e., the accretion disk behavior near its horizon and the measurement of BH spin. It will also help us to understand the basic characteristics of NSs, to study the magnetospheric characteristics and measure the magnetic field strength of NSs surface. For the overview on the mission and early scientific researches refer to Zhang et al. (2020).

4.2 Main topics of *Insight*-HXMT scientific study

4.2.1 Galactic plane scanning survey and source monitoring

4.2.1.1 Scientific objectives

X-ray binaries containing NSs or BHs mostly distribute in the Galactic plane and the Galactic center, and are active at different time scale in the X-ray band. Each sky survey and monitor of the Galactic plane and center in history have found new activities of known sources and new transient sources. There have been intensive observation campaigns with international multi-wavelength, observatories and space-ground coordination. *Insight*-HXMT expects to find new activities of known sources, organize joint observations in multi-wavelength with multiple observatories, and study the diversity of the activities of high energy sources. It also aims at discovering new transient high energy sources, triggering follow-up identification and studies, further understanding the diversity of high energy sources.

Based on the sky survey of *INTEGRAL* and *Swift*, it has been found that many hard X-ray sources in the Galaxy are transients which are mainly populated in X-ray binaries. The source catalogue given by *INTEGRAL*/ISGRI up to December 2019, lists 939 sources (Bird et al. 2016), among which about 39% (369 sources) are AGNs, and 32% are X-ray binaries including 129 HMXBs, 116 LMXBs and 56 cataclysmic sources. The 70-month sky survey in hard X-ray energy band by *Swift*/BAT results in 1171 sources (4.8σ) detected (14–195 keV) from December 2014 to September 2019 (Baumgartner et al. 2013). These sources are classified into 711 AGNs including 261 obscured AGNs, and 281 Galactic sources including 186 X-ray binaries. The detector area of ISGRI (1000 cm^2) is smaller than that of BAT (5243 cm^2), but its FOV is smaller (50% encoded, 361 deg^2 for ISGRI and 3800 deg^2 for BAT). Thus, the former has a better sensitivity, which mainly focuses on Galactic survey.

The characteristics of having large detection area and small FOV allow *Insight*-HXMT to survey the Galactic plane. The simultaneously observations from HE, ME and LE cover an energy range of 1-250 keV, with non-pileup issue, better energy resolution, and a sensitivity of about 3 mCrab.

Some new types of hard X-ray sources have also been found through the Galactic plane survey by present hard X-ray telescopes, e.g., *INTEGRAL* found anomalous X-ray pulsars and magnetar outbursts. One of the main scientific objectives of *Insight*-

HXMT is to find new types of hard X-ray sources or outbursts. The potential new types of hard X-ray sources or outbursts include: (1) X-ray binaries might have relatively weak X-ray radiation at short time scale, which cannot be detected by the previous hard X-ray detectors due to their low sensitivity at short time scales. (2) Some hard X-ray sources do have normal outbursts with increasing accretion in many cases, or even cannot reach the accretion due to failed outbursts. Their hard X-ray emission might be weak, which is normally generated by up-scattering soft X-ray photons in the corona or jet. Their time scale might be short and the energy released by the accreted material cannot produce bright X-ray outbursts. Since many of the present detectors have large FOV, high background and low sensitivity, it is highly possible that those sources have not yet been detected. The detection and follow-up study of such sources might become an important scientific objective of the *Insight*-HXMT Galactic plane survey.

4.2.1.2 Observation strategy

The Galactic plane survey is primarily carried out with the small sky area scan mode, in which the whole Galactic plane is divided into many small patches and scanned patch by patch. At the beginning of the Insight-HXMT's operation, the entire Galactic plane (including the Galactic bulge) was divided into 22 patches with a radius of 10 deg. Based on the experience gained from the scanning observations in the first two years, the scanning strategy was adjusted to enhance the limit sensitivity of Insight-HXMT. During the operation from 2019 to 2023, the entire Galactic plane (including the Galactic bulge) was re-divided into 50 patches with a radius of 7 deg. Following 2023, as the LEIA and EP satellites commenced their operations, the scanning strategy of Insight-HXMT was modified once again. In the new scanning strategy, Insight-HXMT will align its observations with the EP’s plan, conducting simultaneous scanning observations of the Galactic plane. This approach will facilitate the localization of new source candidates and the study of short timescale variable sources across a broad energy range. Considering that the angle between the satellite's pointing and the sun must be greater than 70 deg, the visibility time for each zone is approximately six months per year. The visibility and visibility efficiency of different positions on the Galactic plane are shown in Fig. 4-1. When formulating the weekly scanning plan, priority will be given to regions with high cooperative observation efficiency between Insight-HXMT and EP/WXT.

The scanning mode of *Insight*-HXMT can be set via adopting the parameters of scanning radius (7 and 10 deg), step (0.1, 0.4 and 0.8 deg) and speed (0.01 deg/s, 0.03 deg/s and 0.06 deg/s). Cooking with these parameters can organize the scanning observations to meet a variety of scientific requirements.

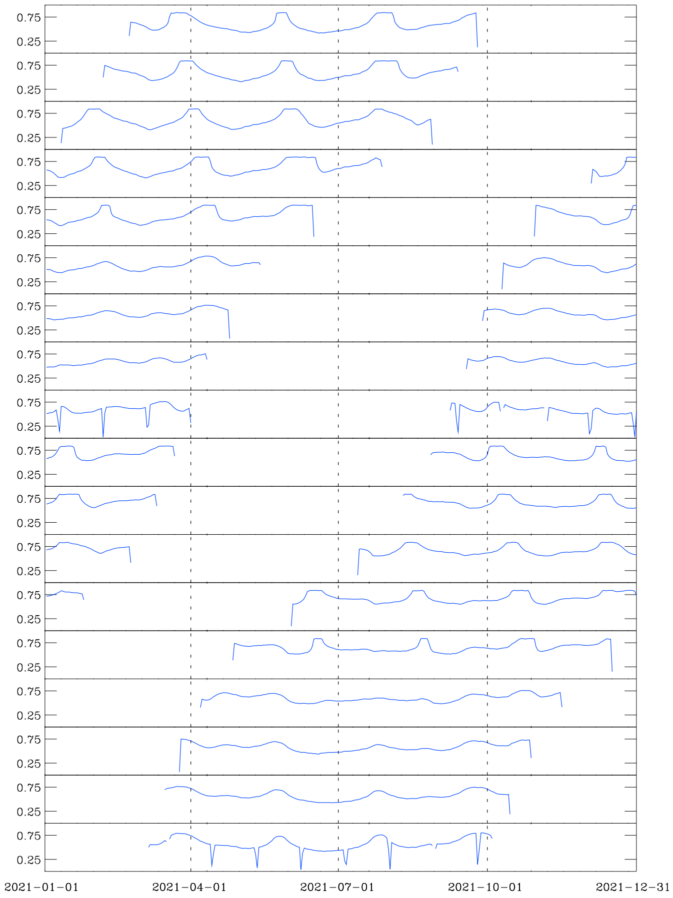

Fig. 4-1 visibility and visible efficiency of 18 zones on the Galactic plane. All 18 zones have $b =$ $0°$ and $= 0°, 20°, 40°, \dots 340°$ from bottom to top.

4.2.1.3 Recent results

Up to March 31th, 2023, *Insight*-HXMT has carried out 3533 small sky area scanning survey, which has fully covered the Galactic plane (Fig. 4-2). Data from each small sky area scan is analyzed with the data analysis software, while both sky maps and light curves of the sources being monitored are produced. The sky map can also be produced by taking a revised direct demodulation method developed by Guan et al. (2020) after launch. Fig. 4-3 shows the result of an individual scanning observation, in which the left one is the reconstructed sky map and the right one is the comparison between the observed count rates and the predicted count rates in three groups of LE detectors with three different orientations.

So far, *Insight*-HXMT has monitored more than 800 known sources (Fig. 4-4). Fig. 4-5 takes Swift J0243.6+6124 as an example, which shows the long-term monitoring light curves from the three detectors LE, ME and HE, respectively. More information on the monitored light curves and the source catalogue is available on the official website of *Insight*-HXMT. Besides monitoring the known sources, one of the scientific objectives of *Insight*-HXMT Galactic plane survey is to find new sources. Now some candidate sources are confirmed to be new sources that have just undergone outbursts. For example, for MAXI J1727–203, *Insight*-HXMT detected its outburst on the same day when MAXI discovered it: its flux is 49.4+/-1.5 mCrab with significance of 33.8σ (shown in Fig. 4-6). For *Insight*-HXMT publications on Galactic plan survey please refer to Sai et al. (2020), and the map with revised direct demodulation method (see Guan et al. 2020).

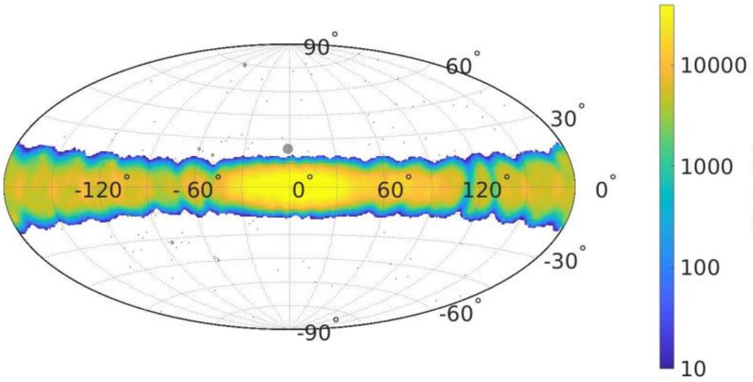

Fig. 4-2 Exposure map of the Galactic plane survey (Sai et al. 2020).

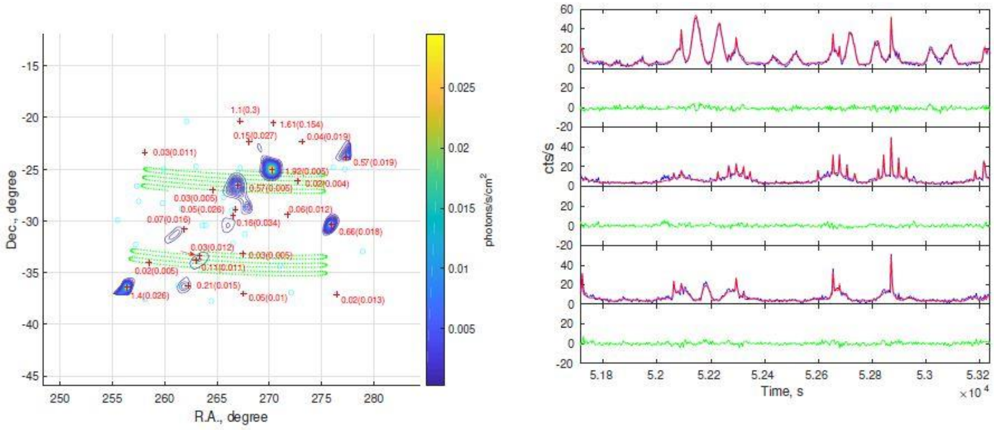

Fig. 4-3 Data processing result of an individual scanning observation with an improved direct demodulation method. The left one is the reconstructed sky map, while the right one is the comparison between the observed and predicted count rates in three groups of LE detectors with three different orientations (Guan et al. 2020).

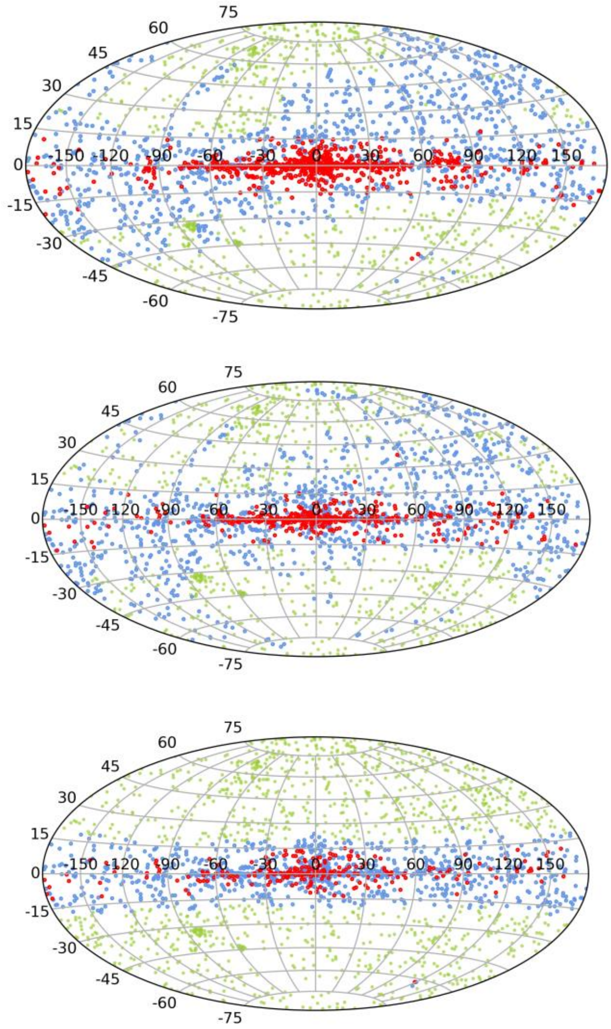

Fig. 4-4 Distribution of known sources monitored by *Insight*-HXMT in the galactic coordinate axis for LE, ME and HE, respectively. The red dots indicate SNR > 3, the blue dots indicate SNR <= 3, and the green dots indicate the catalog sources from *Swift* & *Integral* & *MAXI* (Sai et al. 2020).

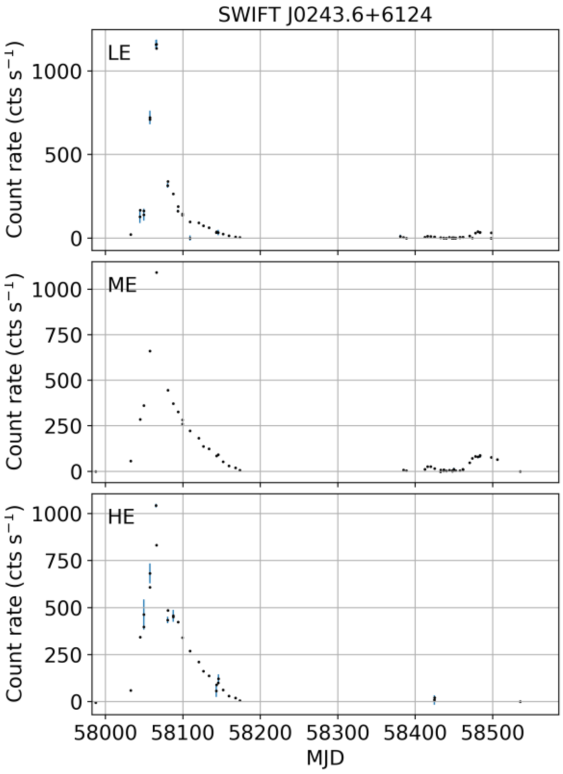

Fig. 4-5 Long-term monitoring light curves of Swift J0243.6+6124 (Sai et al. 2020).

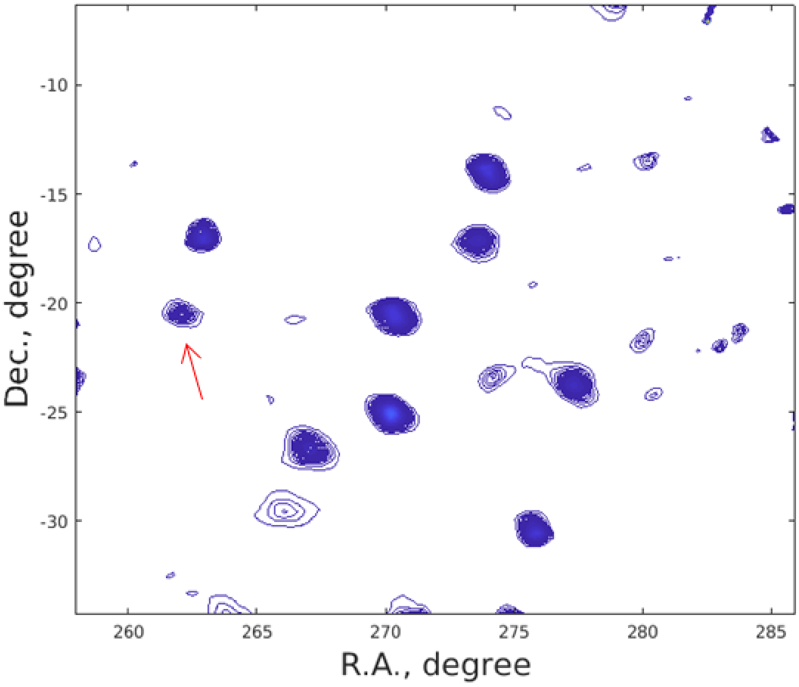

Fig. 4-6 *Insight*-HXMT detected the outburst of MAXI J1727–203: its flux is 49.4+/-1.5 mCrab with significance of 33.8σ.

4.2.1.4 In-orbit sensitivity

The sensitivity of *Insight*-HXMT can be measured in-orbit by studying all the scanning observations. Fig. 4-7 shows the correlation between the detected significance of signal and the exposure time of a single scanning observation. Such an investigation can reveal statistically the in-orbit sensitivity of *Insight*-HXMT: ~ 3 mCrab for LE, 20 mCrab for ME and 18 mCrab for HE.

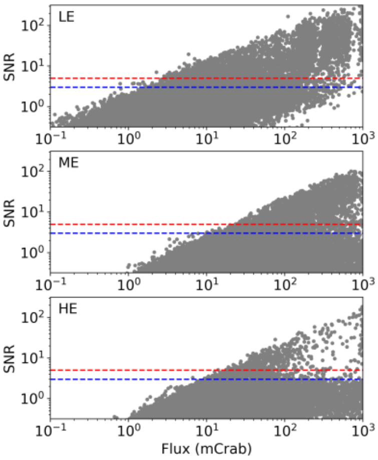

Fig. 4-7 Correlation between source significance and the exposure in single scanning observation (upper: LE, middle: ME, lower: HE).

4.2.1.5 Core proposals

The main scientific outputs of *Insight*-HXMT Galactic plane survey are: source light curves in different energy bands monitored by *Insight*-HXMT in long term; source catalogue; new outbursts on short time scales.

The primary mission of the core science group on the Galactic plane survey and monitoring scientific objectives are: to find the new activities of known sources, to organize multi-wavelength coordinated observations; to organize the follow-up identification and study for the newly discovered transient sources. The corresponding core proposals shall be focused on: (1) the details and feasibility for multi-wavelength observations and identification with other ground- and space- observatories. (2) the source catalogue with the light curves and energy spectra of some sources based on the Galactic plan survey.

4.2.2 High cadence monitoring of accreting BH and NS binaries

4.2.2.1 Introduction of scientific objectives

There are different types of activities taking place in BHs and NS, e.g., state transition. Some rotation-powered PSRs have shown long-term evolution of spin period. However, the mechanism of those long-term behavior and evolution remains unclear. Thus, long-term high cadence monitoring to BHs and NSs is necessary in order to obtain more observation samples.

4.2.2.2 Outburst evolution of BH Binaries

Different X-ray spectral states have been classified during an outburst of BH binaries, in which the low/hard state and the high/soft state are the most typical ones.

Low/hard state is dominated by the hard X-ray emission, which involves with the Comptonization of soft photons in a hot corona. During the low/hard state, the energy spectrum is hard and the soft X-ray is weak. Sometimes a reflection component of the corona from the accretion disk can be observed, accompanied by a Fe fluorescent structure. As to the fast variability (e.g. timing) characteristics, QPO signals and high rms related to the light curve are present. *Insight*-HXMT is able to measure the broad band spectrum in 1–250 keV in the low/hard state of a BH binary, which can give more accurate estimations of the source luminosity and accretion rate. Meanwhile, it has significantly increased the sample of the broad band spectra in the low/hard state.

Insight-HXMT also has advantages in studying the fast variability in the low/hard state. In particular, analyzing the time variability in frequency domain gives a better understanding on the physical properties of the accretion flow and jet near the BH. For instance, the basic geometric structure of disk-corona can be studied through the time lag spectrum from the reflection component in disk-corona. With observations in radio and other energy bands, the relation between the jet and QPOs in the low/hard state during the outburst can be explored. Further, a combined spectral-timing analysis in broad energy band allows us to study the basic radiation mechanism of the energy extraction of a BH.

A typical transient BH binary in outbursts evolves from the low/hard state through the intermediate state to the high/soft state. In the high/soft state, the radiation mainly comes from the blackbody radiation of the accretion disk, which is characterized by high accretion rate, small inner radius of accretion disk, weak hard X-ray emission and relatively steady flux (RMS has the minimum value). During the high/soft state, the accretion disk is relatively closer to the BH. Several measurements can be obtained by analyzing its energy spectrum and time variation, e.g., to attain the information of the innermost stable orbit and BH spin, to constrain the BH mass through the noise and cutoff frequency of its power spectra (McHardy et al. 2004), and to test the low frequency QPO signals corresponding to the anticipated GR precession (Ingram et al. 2010). *Insight*-HXMT has a modest area in soft X-ray band, which has no obvious advantage than other telescopes in operation. However, BH X-ray binaries are generally very luminous in the high/soft state of an outburst. The energy spectrum obtained with a focusing telescope usually suffers from severe pile-up effects in soft X-ray band below about 3 keV. The design of a focusing and imaging detector normally focuses on imaging capability of weak sources, which has relatively poor timing resolution that restricts on studying the light curve on short time scale. *RXTE* in 3–20 keV has more advantages (area and timing capability) than *Insight*-HXMT, yet stopped operation in 2012. Thus, for observations on BH binaries in high/soft states, the LE and ME onboard *Insight*-HXMT have good timing resolution and negligible pile-up effect, which gives advantages in energy spectrum measurements in soft X-ray and fast variability studies.

4.2.2.3 Outburst evolution of NS binaries

Depending on the mass of the companion star, NS X-ray binaries are divided into two types: low mass X-ray binary (LMXB, with companion mass less than 2 solar masses) and high mass X-ray binary (HMXB, with companion mass higher than 5 solar masses) (van den Heuvel 2009). They are also divided into persistent sources and transient sources. In LMXB, the companion transfers matter to the NS through Roche Lobe. Most of LMXBs behave as transients due to their unstable accretion disk and thermonuclear burst on the surface of NS (Frank et al. 2002). In HMXB, the companion is usually an O/B star or Be star. The NS captures the plasma from the stellar wind produced by the companion star. NSs with O, B stars are usually persistent sources with X-ray luminosity larger than ~10^{36} erg s^{-1}. While NSs with Be stars are usually transients with X-ray luminosity between ~10^{33} and 10^{37} erg s^{-1}. In addition, super giant stars as companions have also been found in some transient NSs recently (SFXT, Sguera et al. 2005).

The X-ray radiation and evolution in LMXB originate from the NS surface and its accretion disk. Therefore, studying the spectral and timing properties of NS binary provides valuable *Insight*s in understanding the strong gravitational field theory, GR theory and accretion disk structure and evolution.

In HMXB, when a magnetized neutron star accretes matter from a companion star via stellar wind, the accreted matter is finally funneled along the field lines onto the magnetic poles. Generally, the magnetic axis and the rotation axis are not aligned. The beam pattern shows structures that can be interpreted as pencil and fan-beam configurations. The appearance of beam patterns depends on the luminosity and energy (Meszaros et al. 1988). Thanks to the large effective area and the wide energy range of *Insight*-HXMT, the relationship between the luminosity and P/P_dot can be well studied. Cyclotron resonance line forms during the outbursts of the source, whose energy increases with the magnetic field strength. For the NS with magnetic field close to the typical value (~10^{12} G), the electric cyclotron resonance line may appear in hard X-ray energy band. Therefore, *Insight*-HXMT, with its broad energy band in 1–250 keV, is perfectly capable to study the cyclotron resonance line in high magnetic field, therefore can be used to measure the magnetic field of NS in HMXB.

4.2.2.4 Outburst evolution of magnetars

Magnetars are a special type of NSs, which have strong magnetic field, long spin period, short time scale and luminosity higher than that powered by rotation. There are two kinds of magnetars: anomalous X-ray Pulsars (AXPs) and soft Gamma Repeaters (SGRs) (Duncan & Thompson 1992). They have long spin period and large period derivative. The magnetic field might excess the critical value according to the deduction of dipole magnetic radiation. Magnetar has much higher X-ray luminosity than that powered by rotation, and has strong activity in X-ray energy band (giant flare, outburst and glitch). These dramatic actions contain plentiful information, which could help us to understand the energy origination of these phenomena, the outburst mechanism, and the state of dense matter.

In particular, observing the X-ray radiation of magnetars can help us to understand the following questions: (1) X-ray energy origination of magnetars, (2) whether the magnetic field of NS can exceed the supercritical value, (3) the magnetic field of magnetars are dominated by polar magnetic field or multi-pole magnetic field, (4) correlation between X-ray burst and fast radio burst (FRB). The long-time monitoring on the spin period of magnetars by *Insight*-HXMT can help us to find more diverse behaviors, thus hopefully to solve the mystery of energy origination of magnetars. For example, during the long-term monitoring on the spin period of magnetar, a glitch sometimes happens along with its spin-down, which refers to the spin frequency is higher than the predicted one. During the glitch, there always follows energy release in X-ray energy band. Anti-glitch of spin period accompanied by X-ray outburst was also observed in the AXP in 2013. The glitches of magnetars are related to its inner structure and surrounding stellar winds. More samples should be observed to study the emission mechanism of FRBs and X-ray bursts of magnetars.

4.2.2.5 Evolution of isolated NSs

The Crab pulsar and Vela pulsar have strong X-ray radiation, and Crab PSR is a valuable calibration source. With the observation of *Insight*-HXMT, the timing characteristics and pulse profiles of PSRs can be obtained, which allow us to study the radiation mechanism of PSRs and distinguish different magnetosphere models. In recent years, outbursts of Crab wind nebular in high energy band have been found. *Insight*-HXMT can help us to pursue research on possible outburst of Crab in hard X-ray energy band. Taking Crab as an example, several potential scientific objectives of isolated PSR with *Insight*-HXMT will be introduced.

The basic structure of magnetosphere of a PSR, especially the origin of high energy radiation, is one of the hottest topics in PSR research. Deducing the magnetosphere structure from the pulse profile of PSR only gives us an image in the line of sight. More precise description of the structure of magnetosphere can be obtained once multiple directions of sight are applied. If the magnetic axis is changing, it would be possible to get three-dimensional information of NS magnetosphere. *RXTE* observation suggests that the X-ray pulse profile of Crab is changing slowly, which embody slowly increasing of phase difference between two pulse peaks, decreasing of flux ratio and width of each pulse peak also suggests its spectrum evolve slowly. Those phenomena can be explained by the precession of NS magnetic axis (Lyne 2013; Zanazzi and Lai 2015; Ge et al. 2016). In addition, the pulse profile also evolves with the phase. Phase lag between X-ray and radio pulse has been found. Such phase lag not only explains the position relation among different radiation regions, but also is the main parameter to study the magnetosphere. With observation of *Insight*-HXMT, one can study pulse profile evolution of the Crab PSR in a broader energy band. Meanwhile, combining the existing observation, the systematic research of high energy radiation characteristic of the Crab PSR can be carried on in long time scale.

4.2.2.6 Observation strategy

The strategy is to conduct multiple pointing observations for one source, in order to obtain information of each photon from the source including arrival time and energy. The results can be used for high resolution timing and spectrum analysis in broad energy band. The observation mode belongs to regular pointing observation and target of opportunity observation. Trigger of the latter observation mode comes from monitoring results of broad FOV monitor onboard *Insight*-HXMT and all sky monitor from other X-ray satellites.

4.2.2.7 Simulation analysis and observation result

(1) Crab

Insight-HXMT can measure the pulse profile evolution of Crab PSR in a much broader energy band. Combined the existed data, systematically research on characteristic of high energy radiation of Crab pulsar on long time scale can be studied. Until now, the main X-ray satellites, that use to well measure Crab pulsar spectrum in 0.5-8 keV, are *XMM-Newton* and *Chandra*. The former only has 7% of effective time under Burst model, while the latter has problems in time system: when the source counts are high, its FIFO (first-in-first-out) buffer overflows which leads to many events lost. Since the telemetry data cannot record the information of all triggered events, the arrival time of many events are inaccurate (Tennant et al. 2001). However, LE in this energy band can work well to give more accurate results of phase-resolved spectrum. In high X-ray energy band (5–200 keV), *RXTE* and *INTEGRAL* have already performed long-term observation on Crab pulsar. However, considering that the X-ray radiation from Crab nebula may vary with time, it is important to study the high resolution phase-resolved hard X-ray spectrum. The observation of Crab pulsar from *RXTE*, *INTEGRAL* and *Fermi* suggest that the phase lag between X-ray and radio pulse is related to energy (Molkov et al. 2010; Ge et al 2012.

The result of the phase-resolved spectrum from *RXTE* is shown in Fig. 4-8. With the observation of *Insight*-HXMT, a precise phase-resolved spectrum of Crab is found (as shown in Fig. 4-8), which suggests that the power-law index evolves with energy at the same phase (Tuo et al. 2019). The evolution of the pulse profile with time by the result of *RXTE* is shown in Fig. 4-9 (Ge et al., 2012). *Insight*-HXMT observation mainly considers the time and energy evolution of the double peak flux ratio, while the analysis is in progress.

There is phase lag between the radio and X-ray pulse of Crab. In order to study the phase lags of Crab between X-ray and radio band, *Insight*-HXMT needs cooperation with simultaneously radio observation to eliminate the effect of the timing noise. The pulse profiles and timing results from *Insight*-HXMT and other wave bands are shown in Fig. 4-10, Fig. 4-11, and Fig. 4-12. It suggests that *Insight*-HXMT is capable to measure the phase lags precisely in different energy bands.

Glitches of the isolated pulsars have been investigated with *Insight*-HXMT and the broad band data archive (Ge et al. 2020a; Wang et al. 2020). Fig. 4-13 shows the observations of Crab glitch by *Insight*-HXMT (Ge et al. 2020a). The correlation between the power to pulsar wind nebula (PWN) and the pulsar glitch of PSR B0540-69 has been investigated partially based on *Insight*-HXMT observations. As shown in Fig. 4-14, the X-ray luminosity of PWN goes up at time 1000 days post spin-down rate transition (Wang et al. 2020).

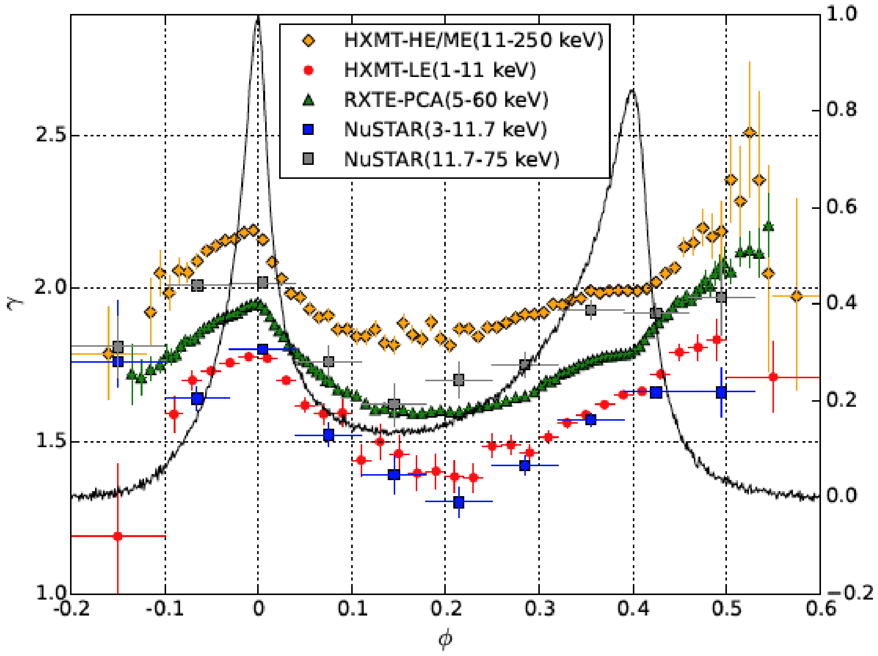

Fig. 4-8 Phase-resolved spectra of the Crab pulsar (observed result of *Insight*-HXMT compared

with that of RXTE/PCA and NuSTAR) (Tuo et al. 2019).

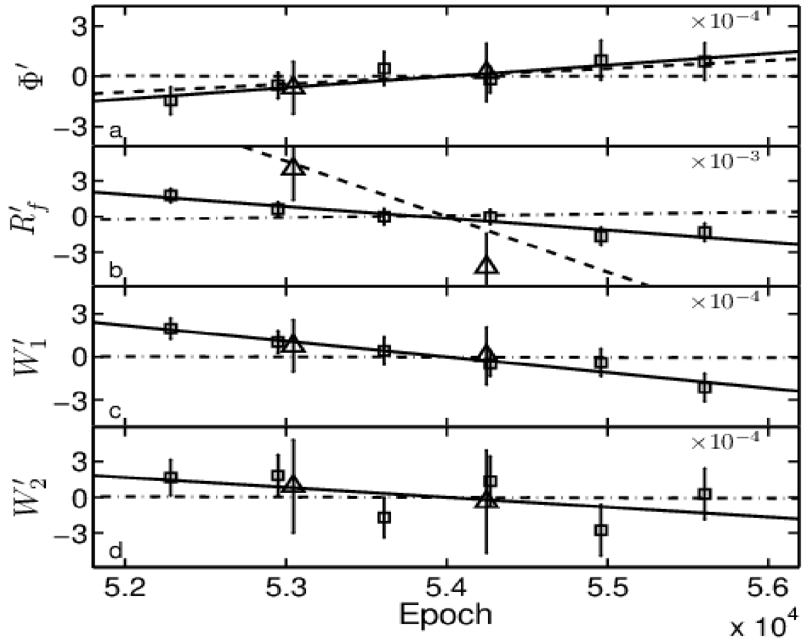

Fig. 4-9 Evolution of pulse shape of Crab observed by RXTE.

The square and triangle are the results from PCA and HEXTE, respectively. From upward to downward the panels are: peak separation, flux ratio, width of main peak and the second peak. All data are deduced their mean value. The solid line is the linear fitting result, dot line is the fitting result of response phase of detectors, and the dash line is the radio observed result (Ge et al. 2012).

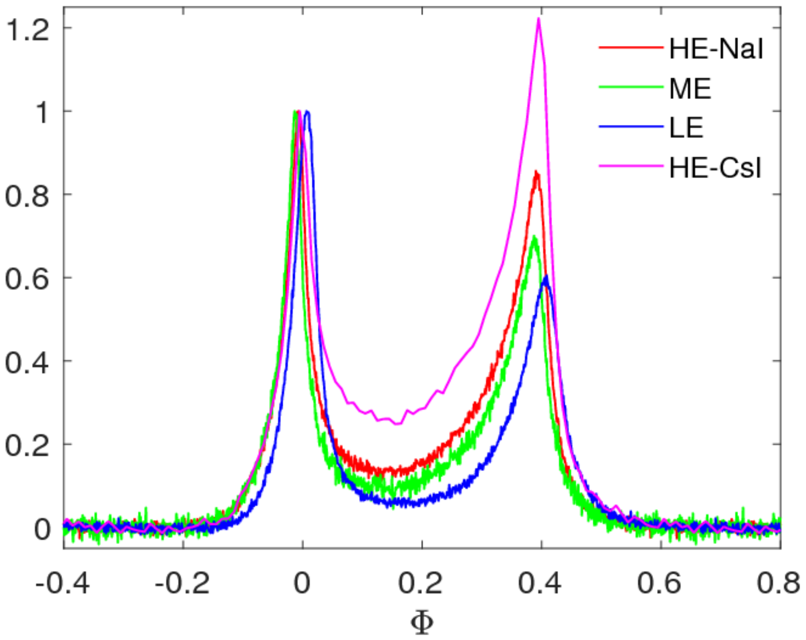

Fig. 4-10 Pulse profiles of the Crab pulsar observed by different detectors. The phase of LE has some differences to that of ME and others.

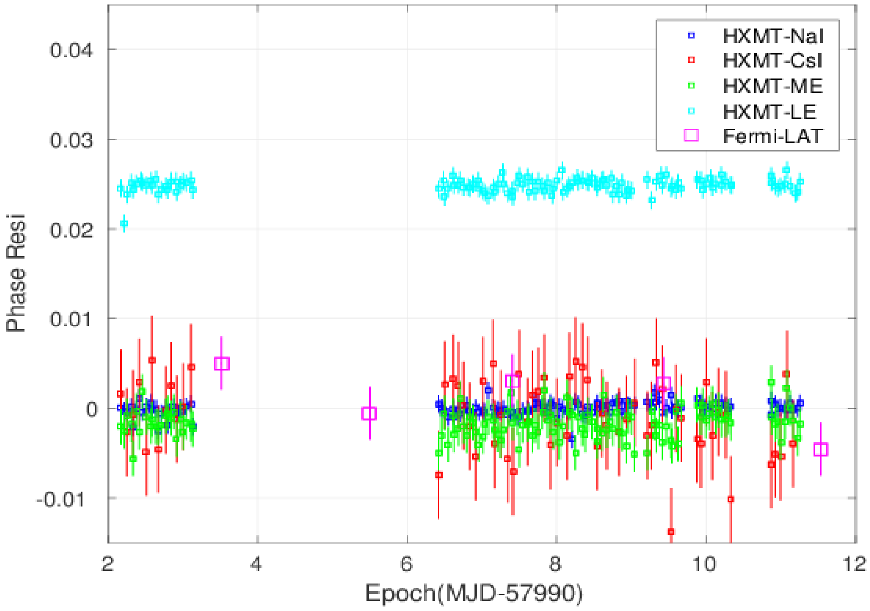

Fig. 4-11 Timing residuals of TOAs observed by different detectors compared to Fermi/LAT.

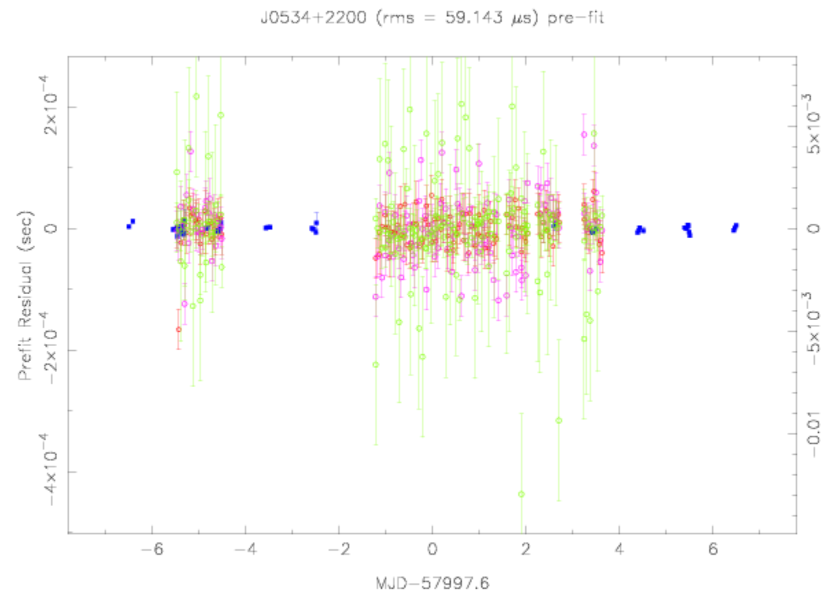

Fig. 4-12 Timing residuals of the Crab pulsar observed each detector compared to the radio observation (phase offset is deducted).

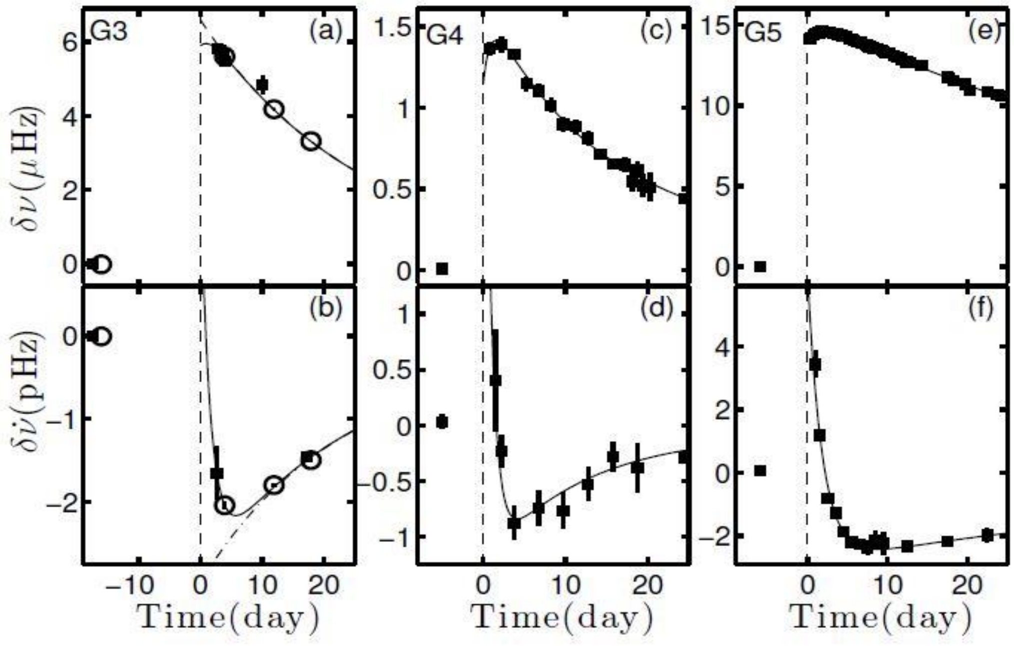

Fig. 4-13 *Insight*-HXMT observation of the Crab glitch (G5) (Ge et al. 2020a).

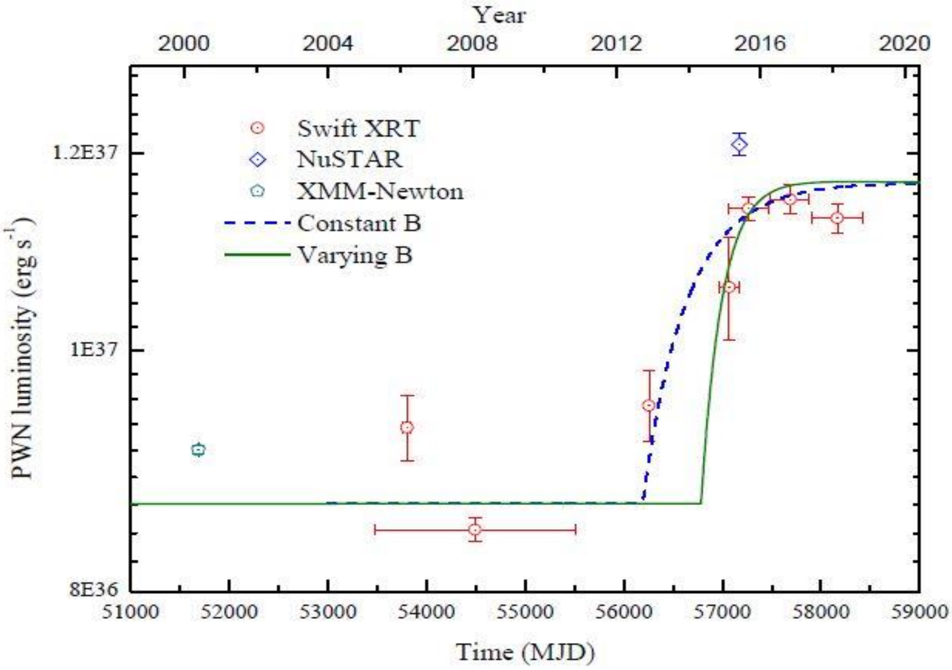

Fig. 4-14 The state transition of PSR B0540-69 (Wang et al. 2020).

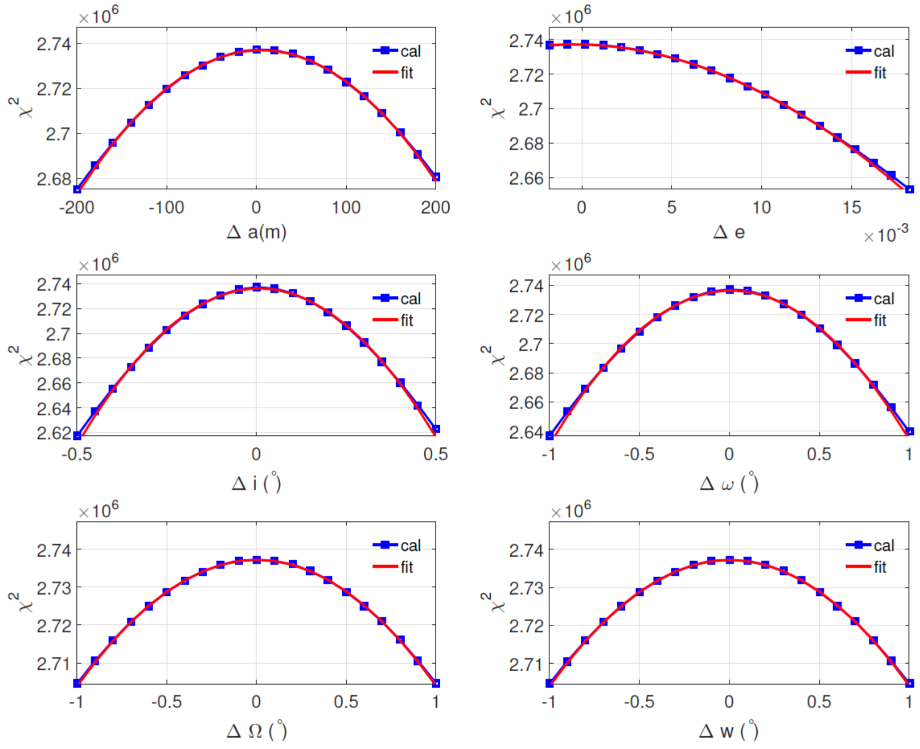

Fig. 4-15 Demonstration of capacity of *Insight*-HXMT in performance of pulsar navigation (Zheng et al. 2019).

As an application of isolated pulsar study, pulsar-based navigation is experimented with *Insight*-HXMT. As shown in Fig. 4-15, the orbital parameters can be measured with precision comparable to those reported by *NICER* (Zheng et al. 2019).

(2) QPO

Insight-HXMT has a wide energy range and is capable of detecting higher energy emissions beyond 30 keV, therefore is an ideal instrument to study the properties of QPOs and test the theories of their origin. A series of new and important scientific results on QPO have been obtained with *Insight*-HXMT. Fig. 4-16shows the rms of type-C QPO as a function of photon energy from the BH candidate MAXI J1535-571 observed by *Insight*-HXMT (Huang et al. 2018). It is the first time for *Insight*-HXMT to extend the rms-energy study to the 1-100 keV energy band, which is much broader than that of *RXTE*. A joint analysis of the QPO properties in both the time and energy domains shows residuals at hard X-rays, which may indicate additional component either intrinsic to QPO or to the energy spectrum (Fig. 4-17, Kong et al 2020a).

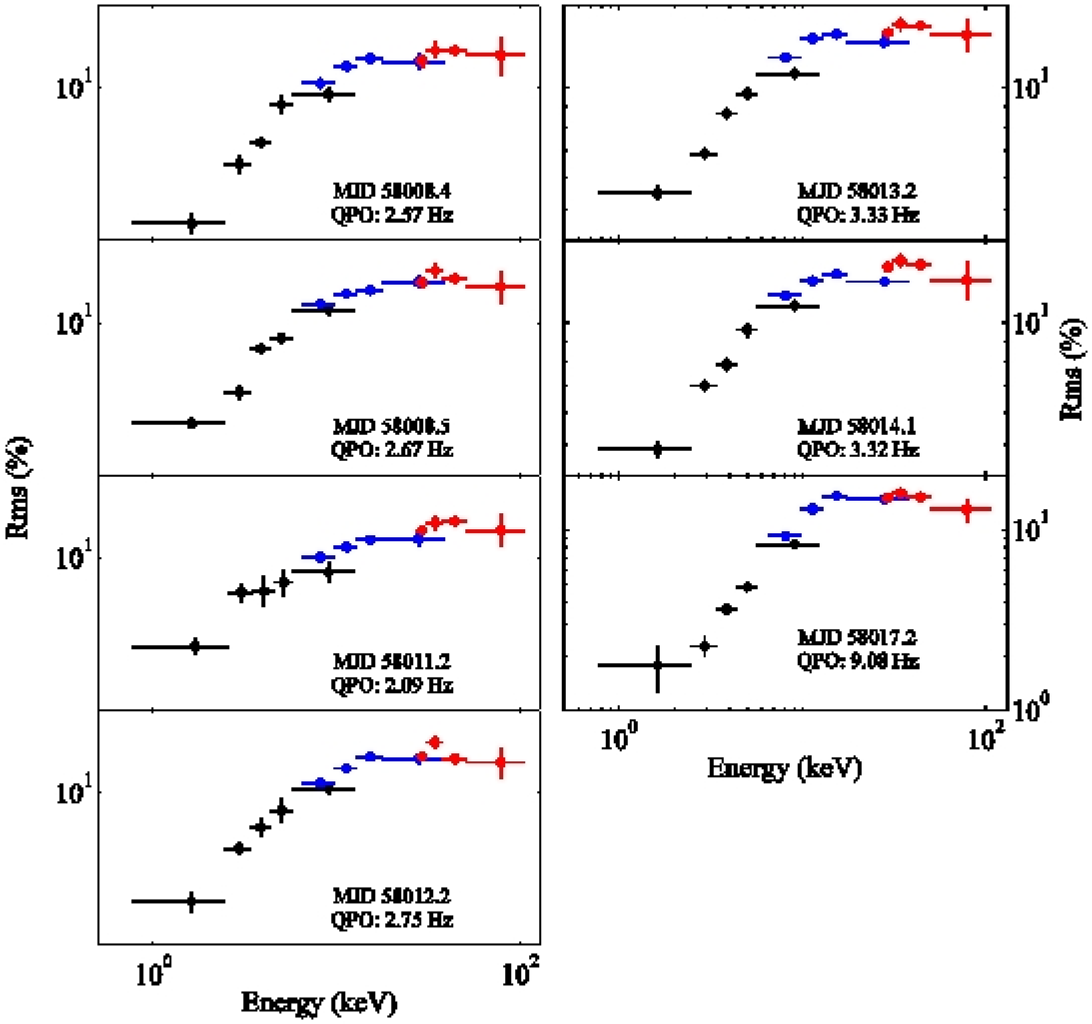

Fig. 4-16 the rms of type-C QPO as a function of photon energy of the BH candidate MAXI J1535-571 observed by *Insight*-HXMT. The results of LE, ME and HE are plot as black, blue and red dots, respectively (Huang et al. 2018).

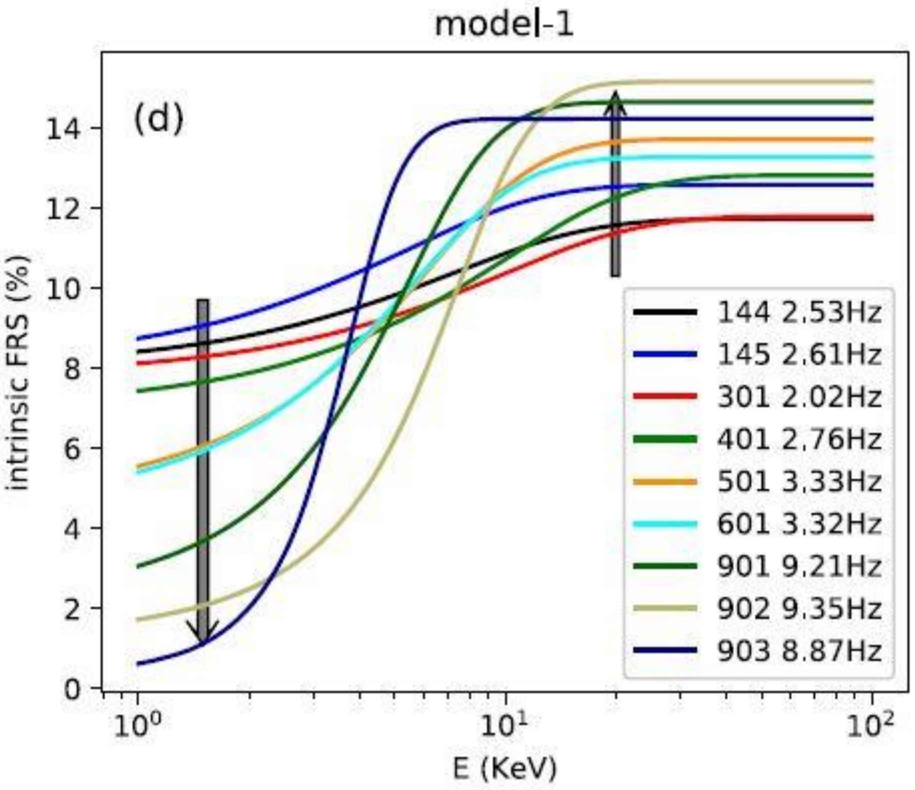

Fig. 4-17 the joint fit of QPO rms and energy spectrum of MAXIJ 1535-571 observed by *Insight*-HXMT shows that, the QPO rms becomes weaker and stronger as the source evolves towards soft intermediate state at soft and hard X-ray bands, respectively (Kong et al. 2020a).

The highest energy LFQPOs (above 200 keV) in the new black hole X-ray binary MAXI J1820+070 during the X-ray hard state are discovered with *Insight*-HXMT. The phase lag of the LFQPO is constant near zero below 30 keV, and becomes a soft lag above 30 keV. The soft lag gradually increases with energy and its maximum value is 1.3 s in the 150–200 keV band. The detection at high energies, the large soft lag and the energy dependent behaviors of the LFQPO pose a great challenge for most existing models. These findings suggest that the LFQPOs probably originate from the precession of a small-scale jet (Ma et al. 2021; see Fig. 4-18). Based on observations of NICER and *Insight*/HXMT, we find that the centroid frequency of the LFQPOs do not change significantly with energy, while the full width at half maximum (FWHM) and fractional rms show a complex evolution with energy (Ma et al. 2021). The LFQPO phase lags at high energies and low energies show consistent energy-dependence relations taking the ~ 2 keV as reference. Our results suggest that the LFQPOs from high energy come from the LT precession of the relativistic jet, while the low-energy radiation is mainly from the perpendicular innermost regions of the accretion disk (Fig. 4-19).

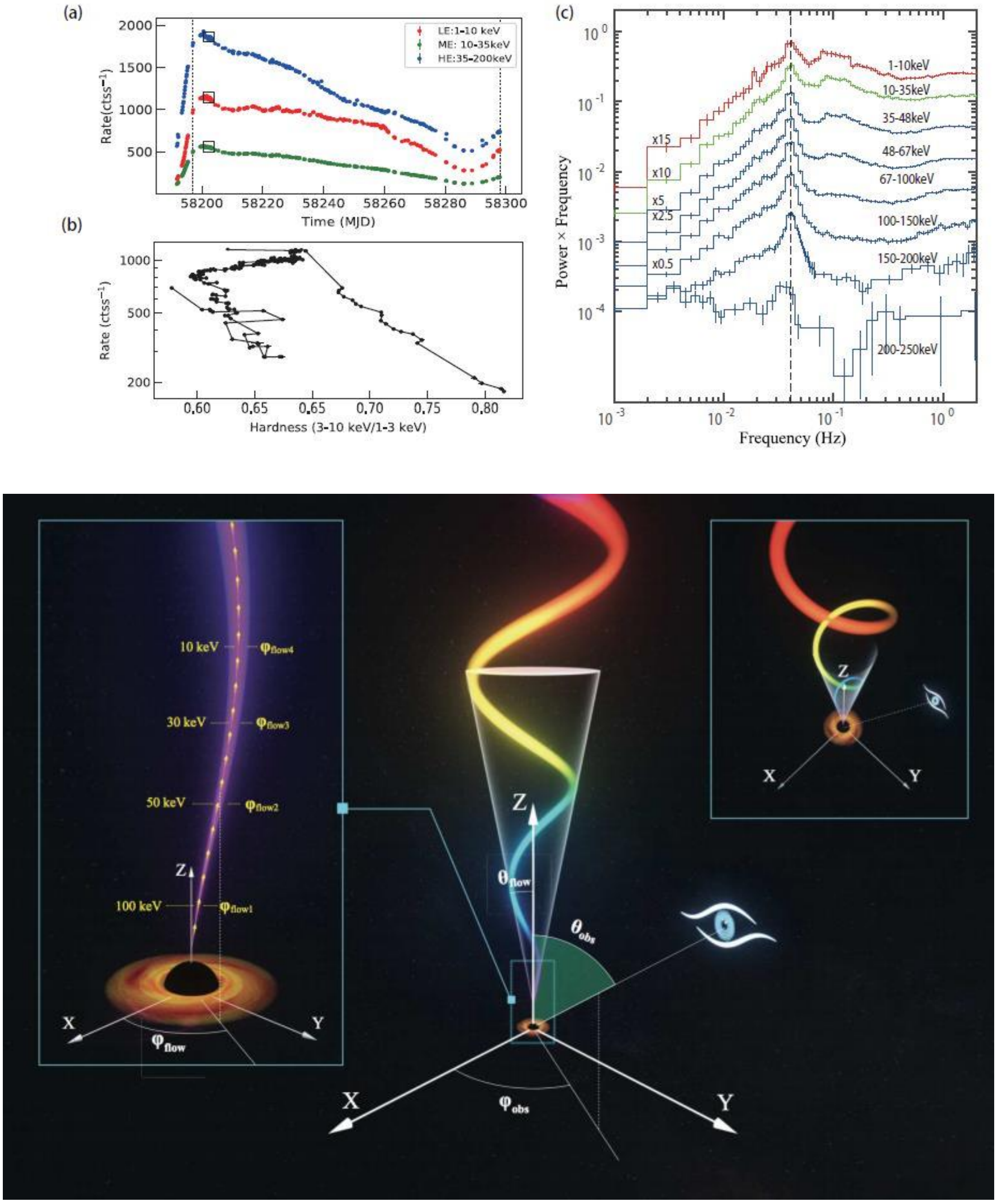

Fig. 4-18 the highest energy QPO discovered in MAXI J1820+070 (upper panel) and the model interpretation in a jet precession scenario (lower panel) (Ma et al. 2021).

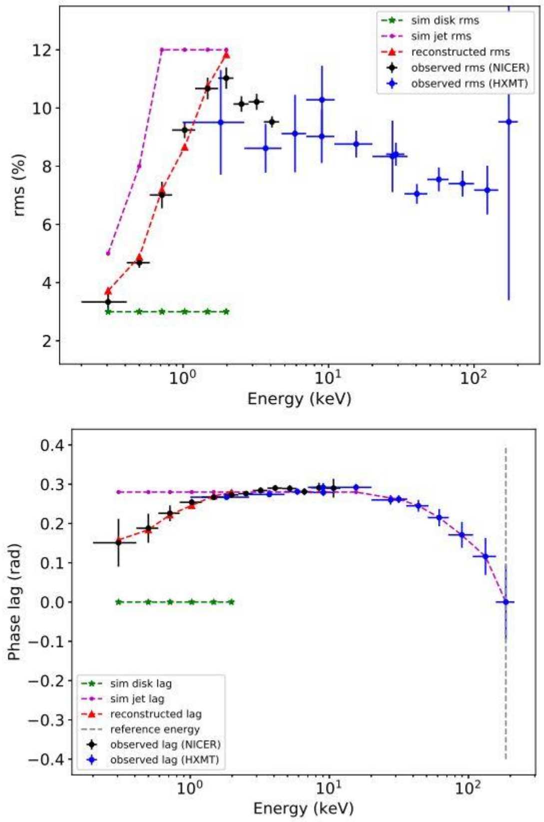

Fig. 4-19 Top: The comparison of observed rms and reconstructed rms. Bottom: The comparision of observed phase lags and reconstructed phase lags.

The blue dots and black dots represent the observation data of *Insight*-HXMT and NICER, respectively, and the reference energy band of phase lag is the highest energy band which is marked out in grey dashed line. The green stars are the rms and phase lag of disk component with the reference energy band. The timing and spectra properties of the QPO transitions observed in MAXI J1348–630 and the highest energy of the type-B QPO detected by *Insight*-HXMT. The spectral fitting results show that throughout the SIMS, the inner radius of the disk was very close to the ISCO, which is consistent with the results of Zhang et al. (2022) (Fig. 4-20). An additional xillver component is required in the modeling of the continuum of type-B QPO, while the reflection modeling also suggests a larger height of the corona. Combining these with other results, we suggest that type-B QPOs probably originate from the precession of the weak jet in a tilted disk-jet structure located relatively close to the BH. However, due to the Bardeen–Petterson effect, the misaligned inner disk in the high-spin BH system can tend to be parallel to the direction of the BH spin axis, which can explain the disappearance of type-B QPOs in the BHXBs. We can also explain the absence of type-B QPOs by the disappearance of small-scale jets bound by the magnetic flux tubes. In this source, *Insight*–HMXT observed a type-C/B transition that occurs within a very short timescale. It is still unclear whether type-C QPOs originate from the jet or the corona precession (Fig. 4-21).

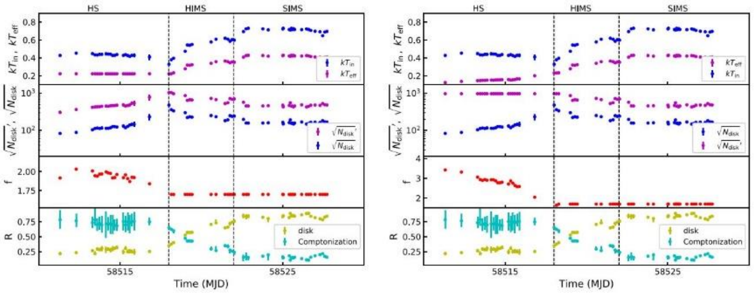

Fig. 4-20 *Insight*-HXMT observations on MAXI J1348-630: the peculiar hard-factor during the rising low/hard state of the initial outbursts. (Zhang et al. 2022, ApJ).

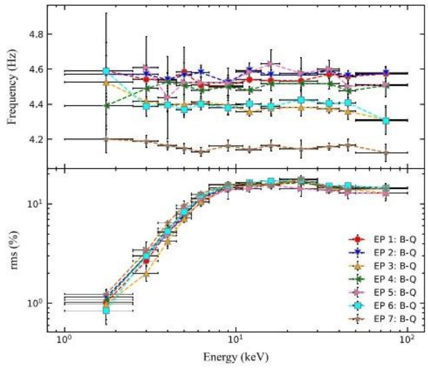

Fig. 4-21 The relationship between the type-B QPOs frequency/fractional rms and energy (Liu et al. 2022, ApJ).

Detailed timing and spectral analysis of type C QPOs and the secular mHz QRM in 4U 1630–47 as observed by *Insight*-HXMT during the 2021 outburst. Type C QPO in ~1.6–4.2 Hz and quasi-regular modulation (QRM) near 60 mHz are detected during the outburst. The mHz QRM has a fractional rms of ~10%–16% in the 8–35 keV energy band with a Q factor frequency/width) of ∼2–4, and even detected at 50 keV (Fig. 4-22). Benefiting from the broad energy band of *Insight*-HXMT, we study the energy dependence of the ∼60 mHz QRM in 1–100 keV for the first time. We find that the fractional rms of the mHz QRM increases with photon energy, while the time lags of the mHz QRM are soft and decrease with photon energy. Fast recurrence of the mHz QRM, in a timescale of less than 1 hr, has been observed during the outburst. During this period, the corresponding energy spectra moderately change when the source transitions from the QRM state to the non-QRM state. The QRM phenomenon also shows a dependence with the accretion rate. We suggest that the QRM could be caused by an unknown accretion instability aroused from the corona.

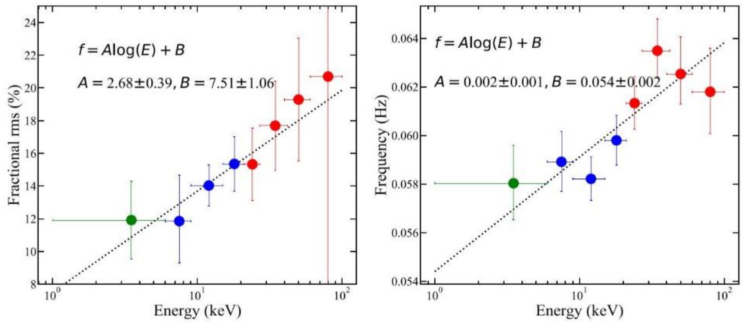

Fig. 4-22 The RMS spectra of the mHz QPO from 4U 1630-47 by *Insight*-HXMT (Yang et al. 2022, ApJ)

Insight-HXMT monitored the whole outburst of the new black hole transient, MAXI J1820+070, accumulating more than 140 observations. Using these data, we find that, in the hard state, the jet-like corona of the source gets closer to the black hole with the coronal material being outflowing faster (You et al. 2021, Fig. 4-23). Using the observations in the soft state and based on the continuum fitting method, the black hole spin is measured at a higher accuracy; the source is found to be a low spin system, which is consistent with the predictions of the timing and spectral analyses (Guan et al. 2021, Zhao et al. 2021, Fig. 4-24). By studying the evolution of broadband noise at different energy bands in the hard state, the time lag of the high-frequency noise is found to be significantly correlated to the photon index, indicating that the high-frequency time lags are produced by Comptonization in a jet (Wang et al. 2020, Fig. 4-25).

The spectral and temporal properties of the black hole X-ray transient binary MAXI J1820+070 during the 2018 outburst are studied systematically with *Insight*-HXMT observations. The outburst of MAXI J1820+070 can be divided into three intervals. For the two intervals of the outburst, we find that low-energy (below 140 keV) photons lag high-energy (140–170 keV) ones, while in the decay of the outburst, high-energy photons lag low-energy photons, both with a time-scale of the order of days. Based on these results, the canonical hysteresis effect of the ‘q’ shape in the hardness–intensity diagram can be reformed into a roughly linear shape by taking into account the lag corrections between different energy bands (Fig. 4-26). Time analysis shows that the high-frequency break of hard X-rays, derived from the power-density spectrum of the first interval of the outburst, is in general larger and more variable than that of soft X-rays. The spectral fitting shows that the coverage fraction of the hard X-rays drops sharply at the beginning of the outburst to about 0.5, and then increases slightly (Fig. 4-27). The coverage fraction drops to roughly zero once the source steps into soft state and increases gradually to unity when the source returns to low–hard state. We discussed the possible overall evolution scenario of corona hinted from these discoveries

(

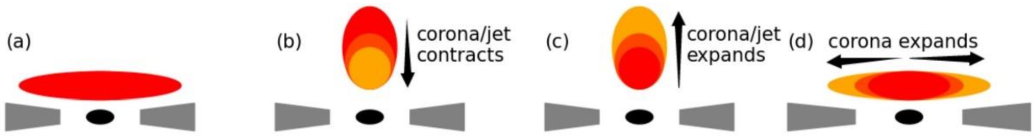

Fig. 4-28).

Further exploration of the Insight-HXMT data results in important progress upon the outburst of MAXI J1820+070. The joint Insight-HXMT, radio and optical observations show the unprecedented long-term time lags of the latter with respect to the X-rays. This reveals for the first time the observational evidence of magnetic transport within the accretion flow, and as well the whole process of forming a magnetic arrested disk (MAD). This serves as so far the most direct observational evidence of the existence for a MAD (You et al. 2023,**Fig. 4-29**). With non-traditional analysis technique HHT, the phase resolved QPO was first obtained from MAXI J1820+070. A series of spectral parameters are found to vary in step with flux modulation of the QPO signal (Shui et al., 2023,**Fig. 4-30**).

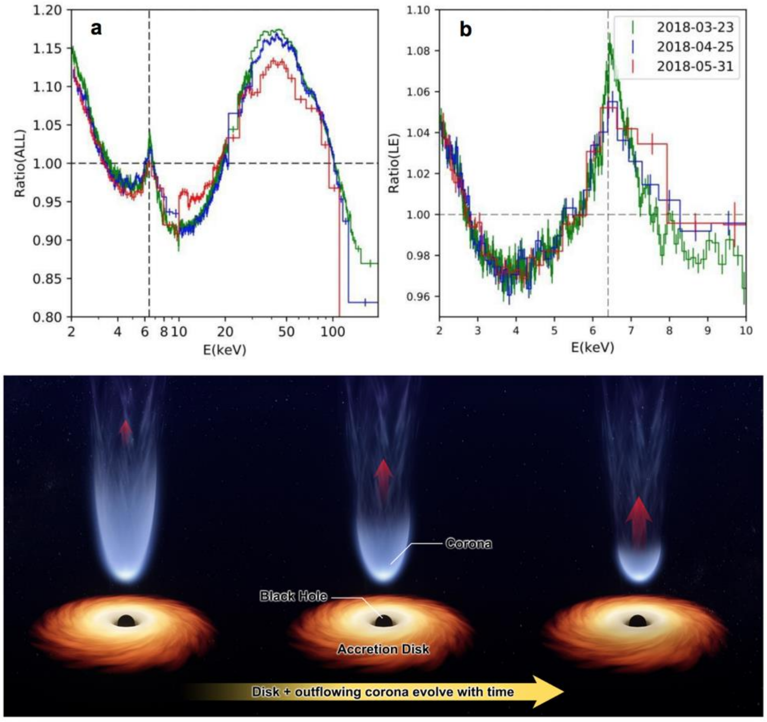

Fig. 4-23 Acceleration of the outflowing coronal material when the corona contracts towards the black hole with decreasing height (You et al. 2021)

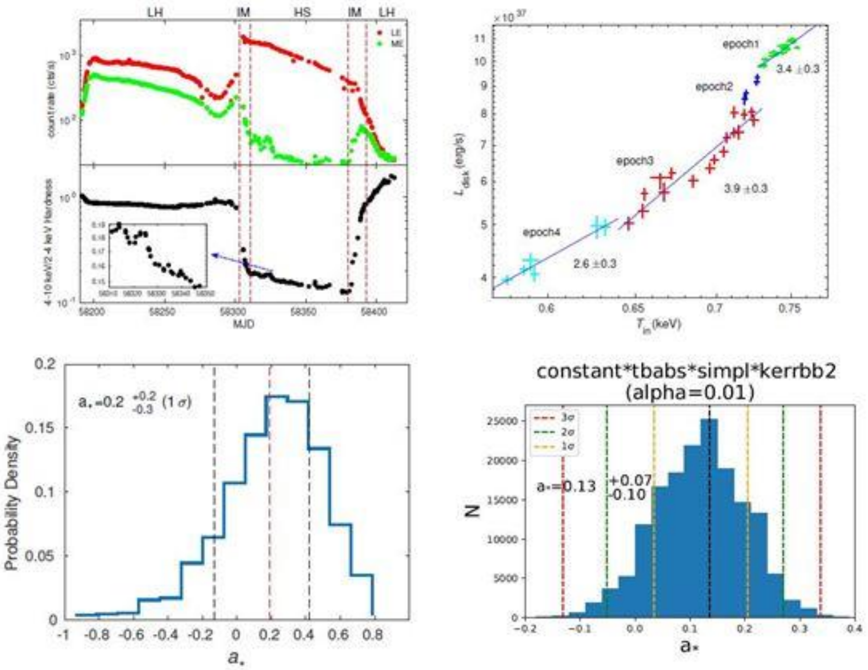

Fig. 4-24 Spin measurement of MAXI J1820+070 using the continuum fitting method (Guan et al. 2021; Zhao et al. 2021)

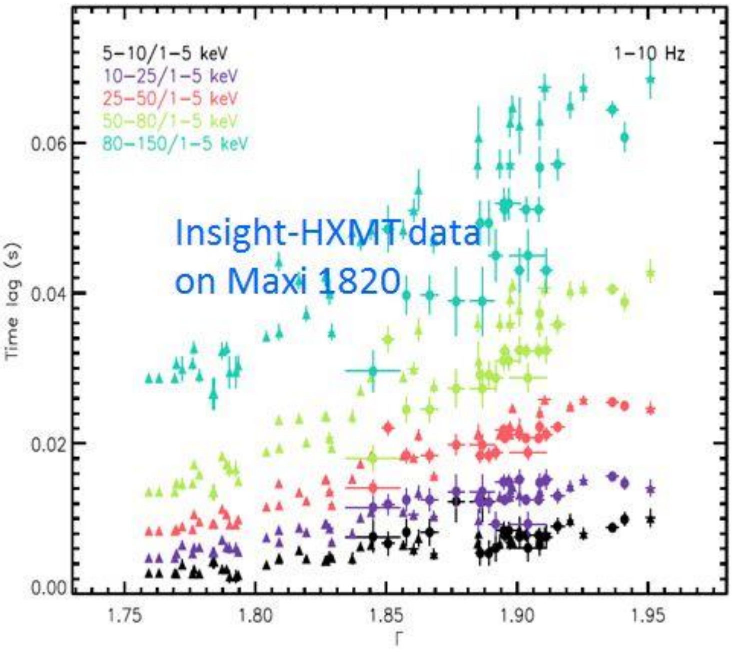

Fig. 4-25 Correlation of the noise time lag and the power-law index for MAXI J1820+070 (Wang et al. 2020)

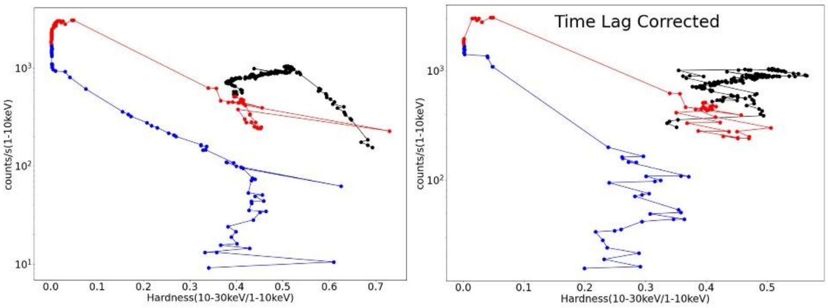

Fig. 4-26：The *Insight*-HXMT HID of MAXI J1820+070, and the HID by taking into account the time lag. (Peng et al., 2023, MNRAS)

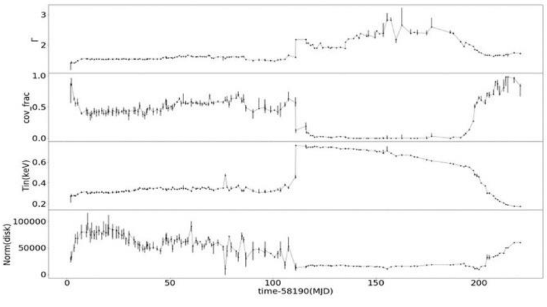

Fig. 4-27: The spectral evolution of MAXI J1820+070 observed by *Insight*-HXMT (Peng et al., 2023, MNRAS).

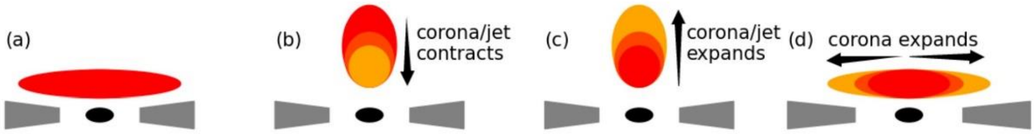

Fig. 4-28 Schematic figure illustrating the evolution of the corona and jet of MAXI J1820+070. (Peng et al., 2023, MNRAS)

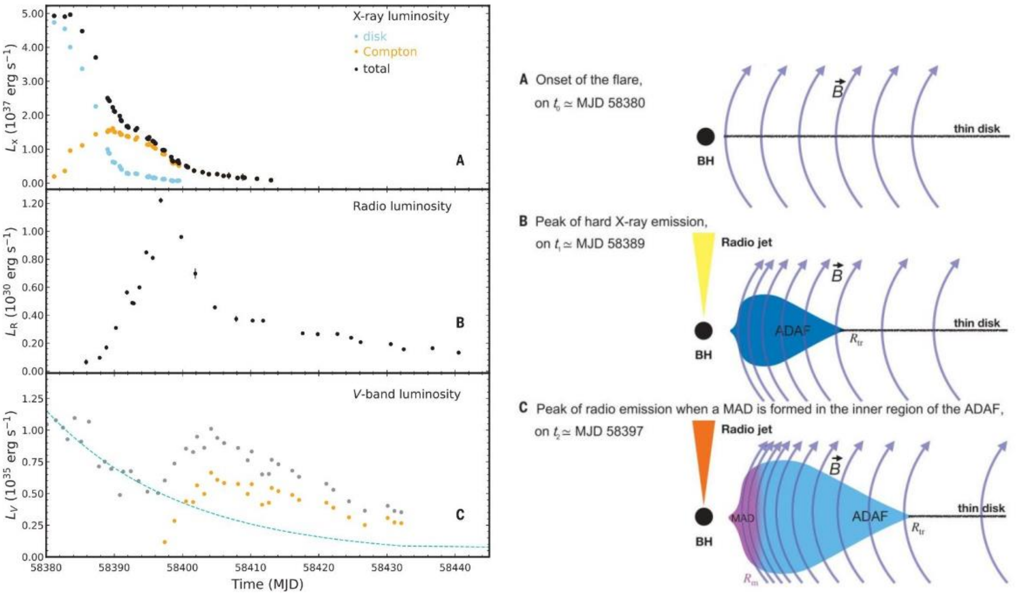

Fig. 4-29 The time lags observed by joint Insight-HXMT and the ground telescopes (left), and the formation of a MAD (right) (You et al. 2023).

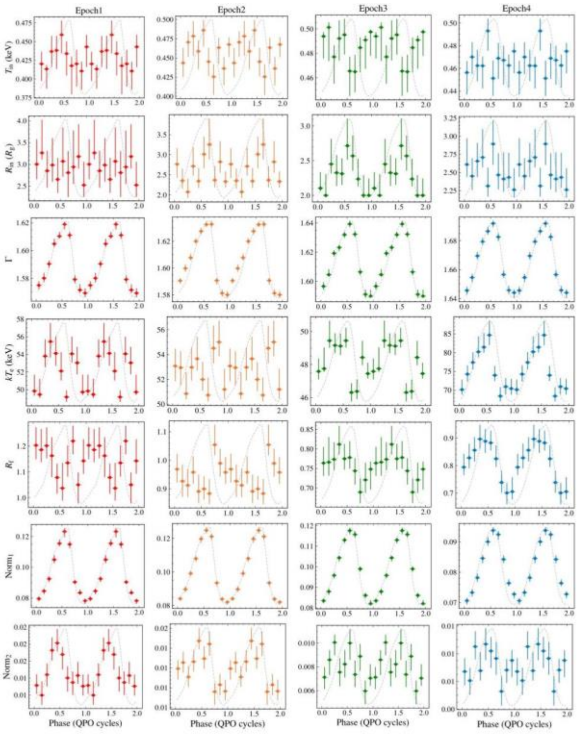

Fig. 4-30 During the outburst of MAXI J1820+070 observed by Insight-HXMT, with HHT technique the spectral parameters show modulations following the QPO phases (Shui et al. 2023).

The *Insight*-HXMT observations of the micro-quasar GRS 1915+105, during an unusual low-luminosity state, show that the source has experienced a possible transition from a jet-dominated state to a wind-dominated state in a timescale of 10^3 s (Kong et al. 2021, Fig. 4-31). Furthermore, for this source, based on the high statistic observations of *Insight*-HXMT, the tight positive correlation between the QPO frequency and mass accretion rate has been found in a large range of accretion rates (H. Liu et al. 2021, Fig. 4-32).

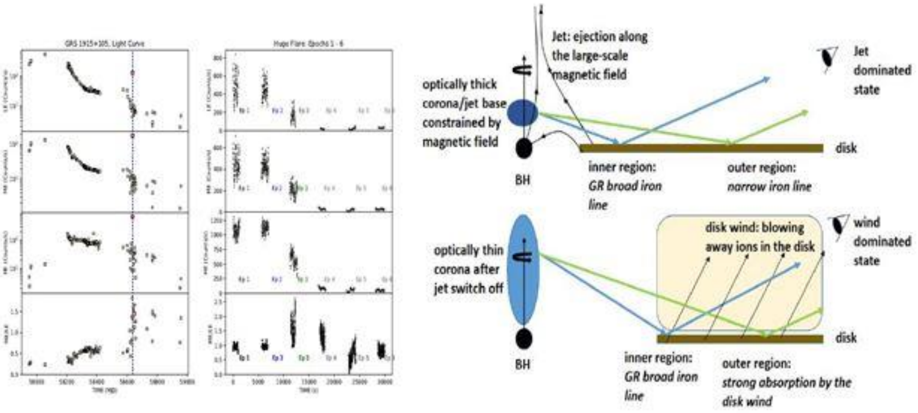

Fig. 4-31 Transition from a jet-dominated state to a wind-dominated state for the flare in GRS 1915+105 (Kong et al. 2021)

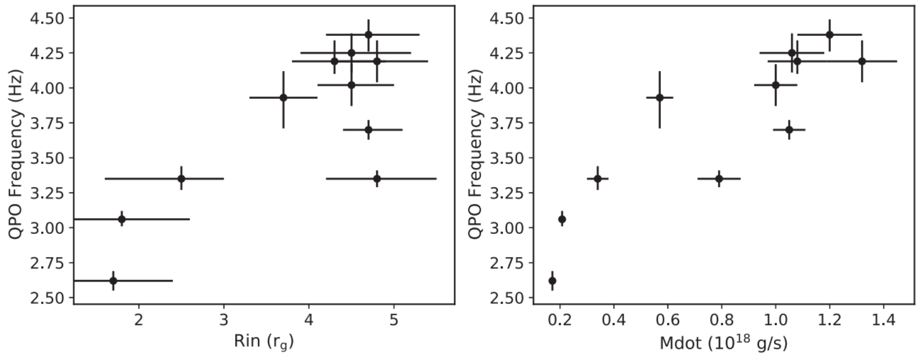

Fig. 4-32 Left: correlation between the QPO frequency and inner disk radius; Right: correlation between the QPO frequency and mass accretion rate (H. Liu et al. 2021)

Insight-HXMT has monitored the whole outburst of the black hole binary MAXI J1348-630, and provides the first observational evidence that the observed time-lag between radiations of the accretion disk and the corona leads naturally to the hysteresis effect and the "q"-diagram (Weng et al. 2021, Fig. 4-33). Moreover, this source shows a peculiar behavior in the hard state, which indicates that the inner disk was in the process of condensing from the hot, optically thin medium (Zhang et al. 2022, Fig. 4-34).

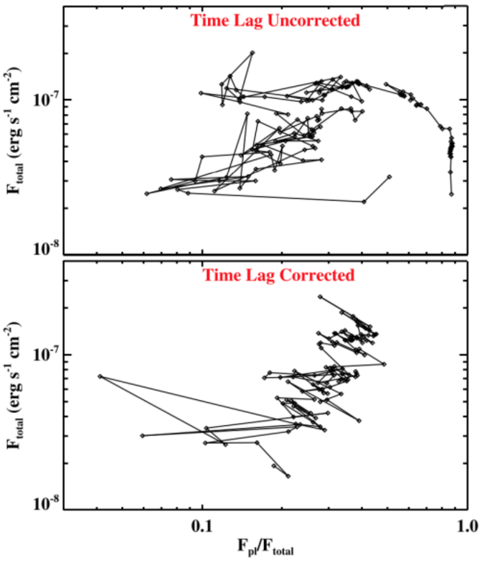

Fig. 4-33 Explanation of the hysteresis effect and the "q"-diagram (Weng et al. 2021)

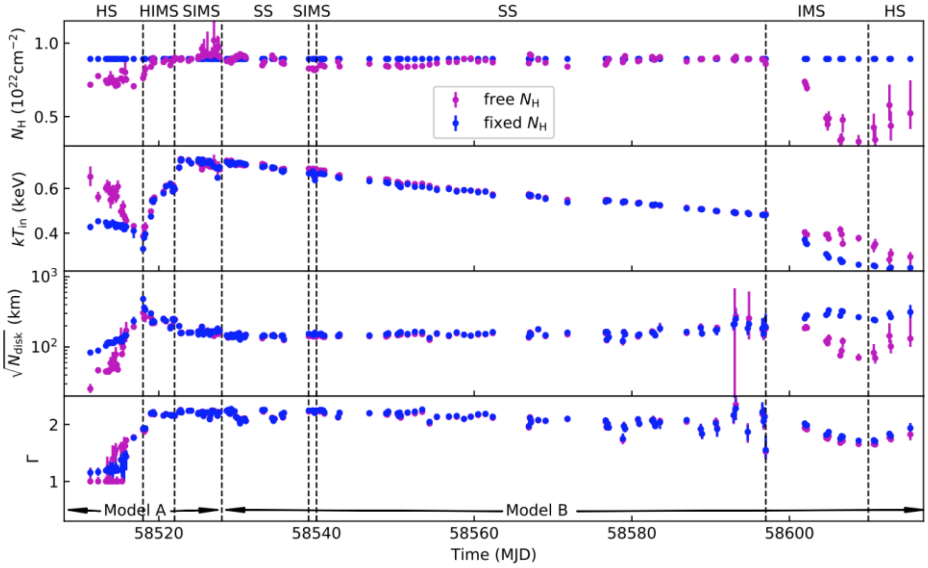

Fig. 4-34 Peculiar behavior of MAXI J1346-630 in the hard state (Zhang et al. 2022)

During the outburst of Swift J1727.8–1613 monitored in details by Insight-HXMT, the QPO was observed to have a systematical evolution at high energies: along with the outburst, the RMS of QPO shows firstly excess and then evolves to a plateau at high energies, indicating the co-existence and evolution of the balance between jet and corona (Yang et al., 2024,Fig. 4-35 The RMS RMS spectrum for QPO residing in each observational ID (Yang et al., 2024).). Peculiar outburst was caught by Insight-HXMT from SLX 1746–331: the temperature dependence of the disk flux follows Tin$^{3.98}$, and thus suggests that the inner disk reaches its innermost stable circular orbit and the system stays at a disk-dominated state during almost the entire outburst. Further evidences revealed in this outburst suggest that this system may have a tight orbit and harbors a tiny black hole (Peng et ail, 2024,Fig. 4-36 The correlation between disk flux and temperature during the whole outburst of SLX 1746–331 (Chen et al. 2024).).

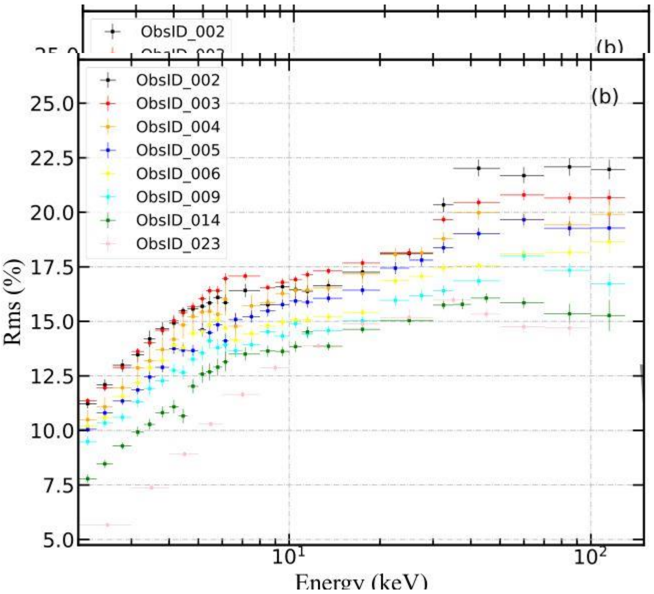

Fig. 4-35 The RMS RMS spectrum for QPO residing in each observational ID (Yang et al., 2024).

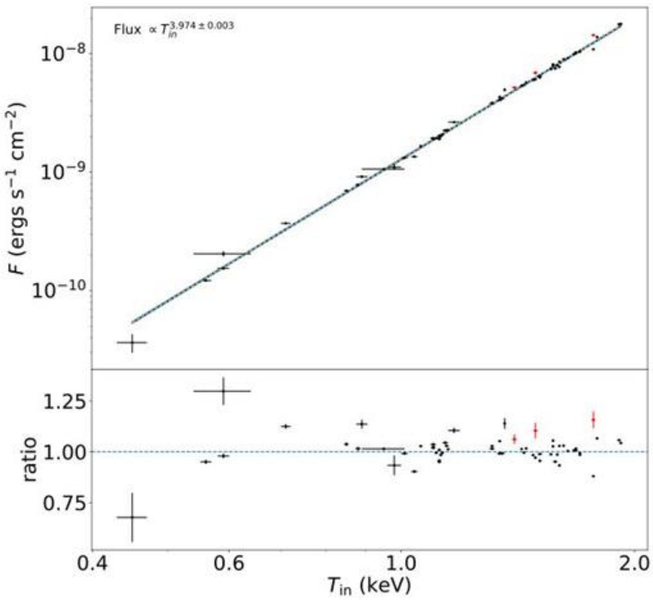

Fig. 4-36 The correlation between disk flux and temperature during the whole outburst of SLX 1746–331 (Chen et al. 2024).

The *Insight*-HXMT observations of other BHs have also revealed some import results: a new type of LFQPO is detected in the soft state of Cygnus X-1, which may be related to the local inhomogeneity of the accretion flow in the wind-fed accretion system (Yan et al. 2021,Fig. 4-37 A new type of LFQPO detected in the soft state of Cygnus X-1 (Yan et al. 2021)); the BH spin of MAXI J1535-571 and 4U 1630-472 have been measured, indicating that the two sources are high-spin BHs (Q. Liu et al. 2021, Fig. 4-38 Spin measurement of MAXI J1535-571 (Q. Liu et al. 2021)).

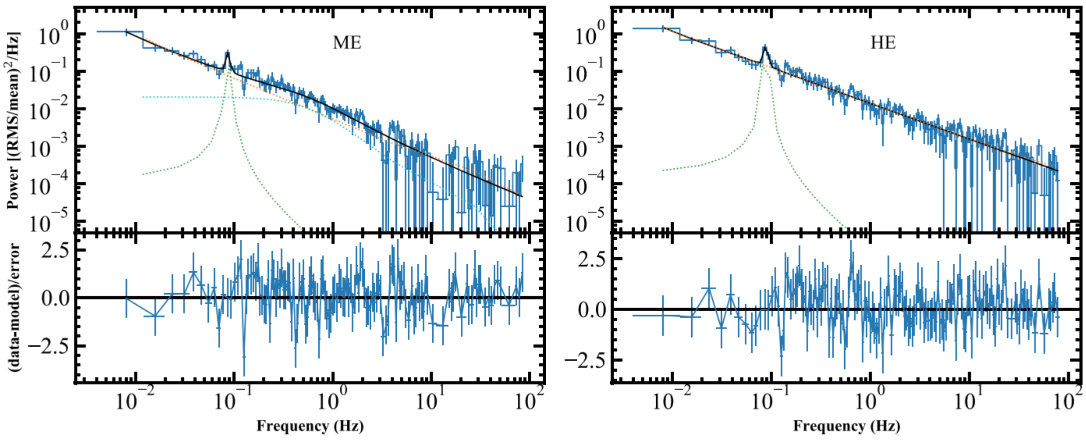

Fig. 4-37 A new type of LFQPO detected in the soft state of Cygnus X-1 (Yan et al. 2021)

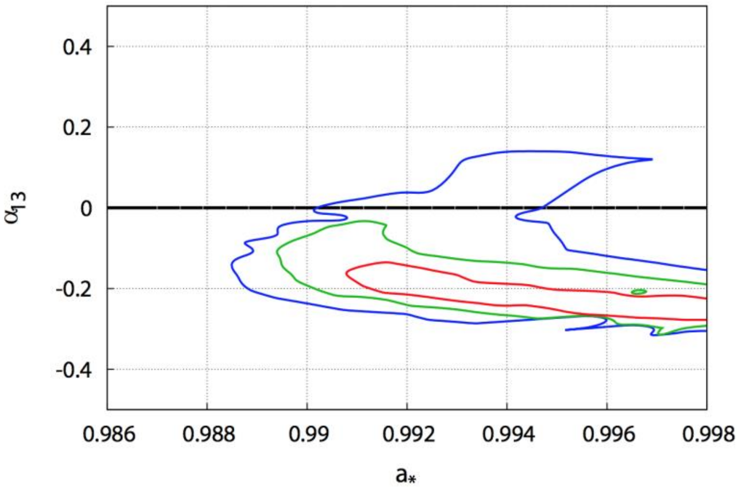

Fig. 4-38 Spin measurement of MAXI J1535-571 (Q. Liu et al. 2021)

Insight-HXMT observed thoroughly the outburst of the first Galactic ultra-luminous X-ray source (ULX), Swift J0243.6+6124. The accumulated high cadence and high statistic data allow for systematical study of the source property, especially on the NS accretion and spin evolution. These studies found that that the source experiences transitions in pulse profile, power spectrum and energy spectrum at two critical luminosities (Fig. 4-39 The outburst evolution of the Galactic ULX Swift J0243.6+6124 monitored by *Insight*-HXMT (Doroshenko et al. 2020)., Doroshenko et al. 2020; Zhang et al. 2019; Kong et al. 2020b; Wang et al. 2020b). The transition at higher critical luminosity denotes the transform of the disk accretion mode from gas pressure to radiation pressure dominated disk, which is consistent with the theoretical predication made half a century ago. Similar behavior was detected in the HMXB 2S 1417–624 (Ji et al. 2020). Besides, for Swift J0243.6+6124, *Insight*-HXMT has observed the first thorough accretion evolution of this source in the magnetic pole of NS (Kong et al. 2020b, Fig. 4-40 Spectral evolution of the Galactic ULX Swift J0243.6+6124 monitored by *Insight*-HXMT (Kong et al. 2020b)). Thanks to the high-cadence and high-statistic observations from *Insight*-HXMT, Swift J0243.6+6124 was observed with a third typical luminosity, around which the source was found to have pulse fraction evolution against luminosity that is different between the rising and decay phase (Wang et al. 2020, Fig. 4-41 Pulse fraction evolution of Swift J0243.6+6124 monitored by *Insight*-HXMT (Wang et al. 2020)).

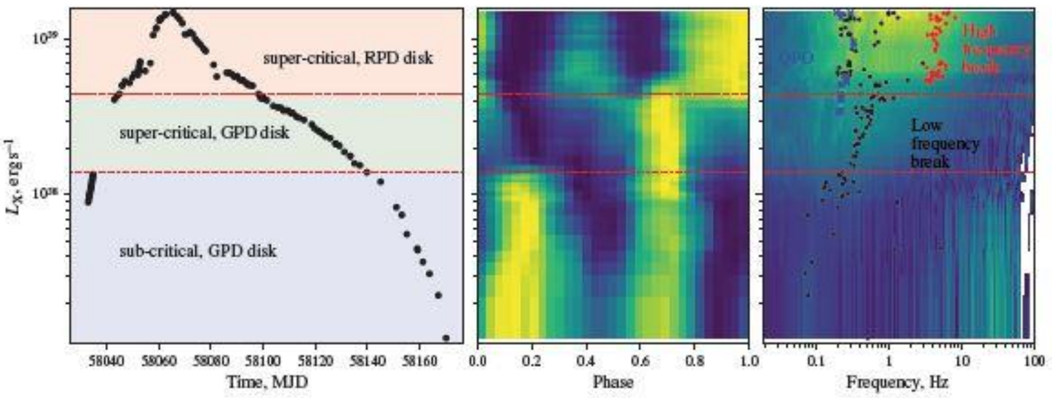

Fig. 4-39 The outburst evolution of the Galactic ULX Swift J0243.6+6124 monitored by *Insight*-HXMT (Doroshenko et al. 2020).

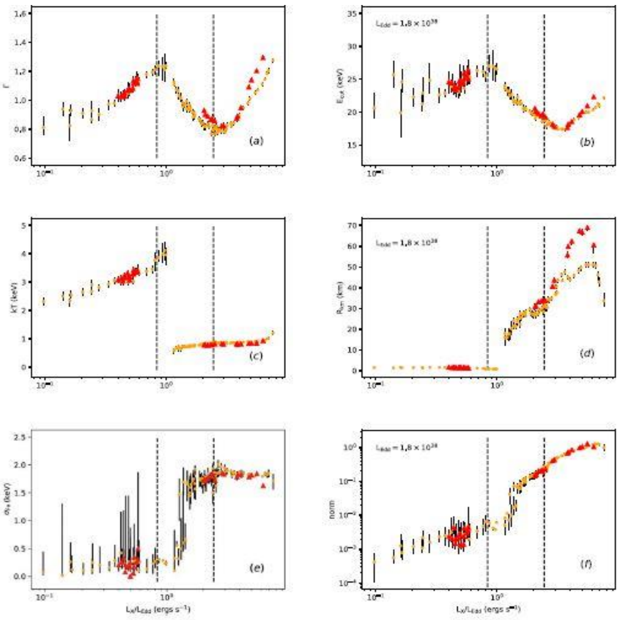

Fig. 4-40 Spectral evolution of the Galactic ULX Swift J0243.6+6124 monitored by *Insight*-HXMT (Kong et al. 2020b)

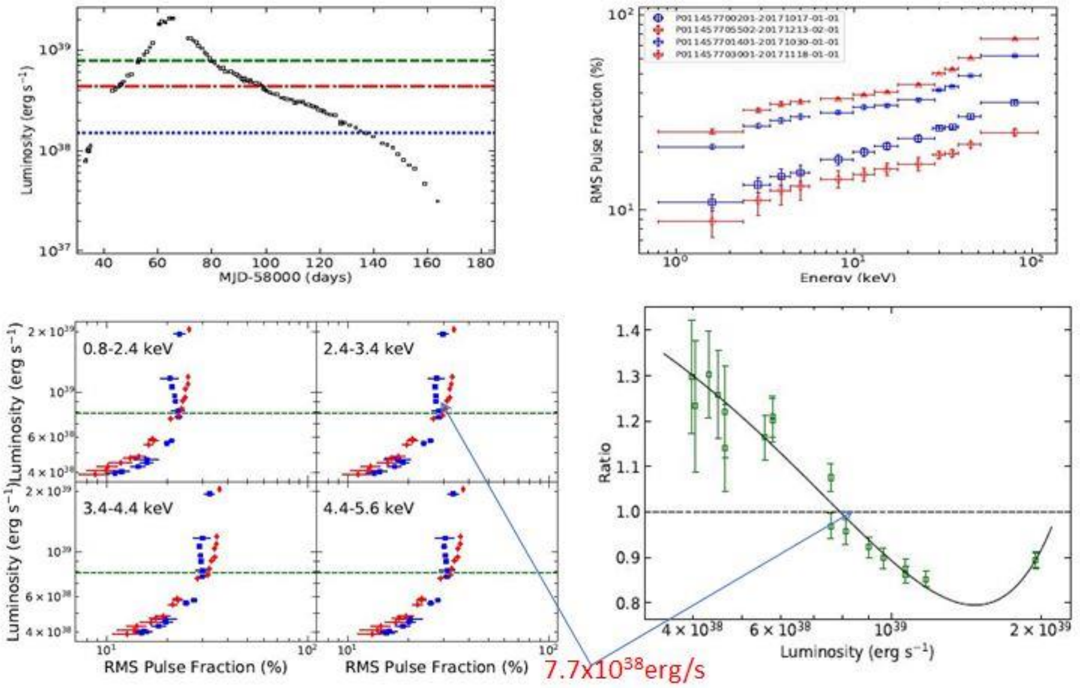

Fig. 4-41 Pulse fraction evolution of Swift J0243.6+6124 monitored by *Insight*-HXMT (Wang et al. 2020)

We studied the millihertz quasi-periodic oscillation (mHz QPO) in the 2020 outburst of the Be/X-ray binary 1A 0535 + 262 using *Insight*-HXMT data over a broad energy band. The mHz QPO is detected in the 27–120 keV energy band. The QPO centroid frequency is correlated with the source flux and evolves in the 35–95 mHz range during the outburst. The QPO is most significant in the 50–65 keV band, with a significance of ~8σ, but is hardly detectable (120 keV) energy bands. Notably, the detection of mHz QPO above 80 keV is the highest energy at which mHz QPOs have been detected so far. The fractional rms of the mHz QPO first increases and then decreases with energy, reaching the maximum amplitude at 50–65 keV. In addition, at the peak of the outburst, the mHz QPO shows a double-peak structure, with the difference between the two peaks being constant at ~0.02 Hz, twice the spin frequency of the neutron star in this system (Fig. 4-42 The double-peak structure and evolution in a typical PDS (MJD 59168) of 1A 0535 + 262by *Insight*-HXM (Ma et al., 2022, ApJ).). We discuss different scenarios explaining the generation of the mHz QPO, including the beat frequency model, the Keplerian frequency model, the model of two jets in opposite directions, and the precession of the neutron star, but find that none of them can explain the origin of the QPO well. We conclude that the variability of non-thermal radiation may account for the mHz QPO, but further theoretical studies are needed to reveal the physical mechanism.

We presented detailed timing and spectral analyses of the transient X-ray pulsar RX J0209.6-7427 in the Small Magellanic Cloud during its 2019 giant outburst. With a better known distance than most galactic X-ray pulsars, its peak luminosity is determined to be (1.11 ± 0.06) × 1039 erg s-1; it is thus a bona fide pulsating ultraluminous X-ray source (PULX). Owing to the broad energy band of *Insight*-HXMT, its pulsed X-ray emission was detected from 1 keV up to the 130-180 keV band, which is the highest energy emission detected from any PULXs outside the Milky Way. This allows us to conclude that its main pulsed X-ray emission is from the fan beam of the accretion column, and its luminosity is thus intrinsic. We also estimate its magnetic field of (4.8-8.6) × 10^{12} or (1.7-2.2) × 10^{13} G, from its spin evolution or transition in the accretion column structure during the outburst; we suggest that the two values of the magnetic field strength correspond to the dipole and multipole magnetic fields of the neutron star, similar to the recent discovery in the Galactic PULX Swift J0243.6+6124. Therefore, the nature of the neutron star and its ULX emission can be understood within the current theoretical frame of accreting neutron stars. This may have implications for understanding the nature of those farther away extragalactic PULXs. (Hou et al. 2022, ApJ)

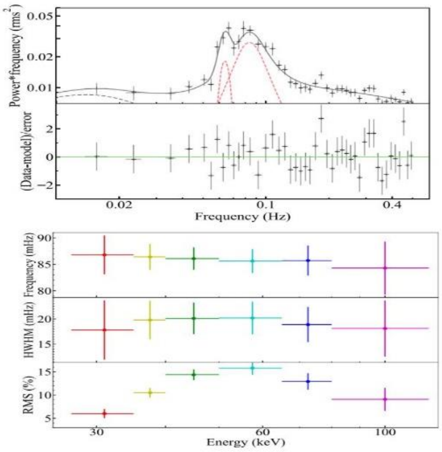

Fig. 4-42 The double-peak structure and evolution in a typical PDS (MJD 59168) of 1A 0535 + 262by *Insight*-HXM (Ma et al., 2022, ApJ).

4.2.2.8 Direction of proposal call

The observation mode applies to normal pointing or target of opportunity observations. The proposal needs to point out the explicit sources, state the detailed exposure time and observed frequency for each observation in order to achieve the scientific objective.

4.2.2.9 Observational results

(1) Spectral fitting results of Crab nebula

The *Insight*-HXMT spectra of Crab nebula are fitted with an absorbed power-law model (i.e., wabs*powerlaw). The effective exposure time is 982 s and the errors are estimated at 90% confidence level. The fitting parameters are compared with the results from XMM-Newton (Willingale et al. 2001). Fitting results are given in Table 4-1 and Fig. 4-43 Spectra of Crab nebula observed by *Insight*-HXMT in 982 s..

Table 4-1 Spectral fitting parameters of Crab nebula observed by *Insight*-HXMT and *XMM*-Newton

	n_H (10^{21} cm^{-2})	PhoIndex

Insight-HXMT	3.6	2.11
XMM	3.6	2.11

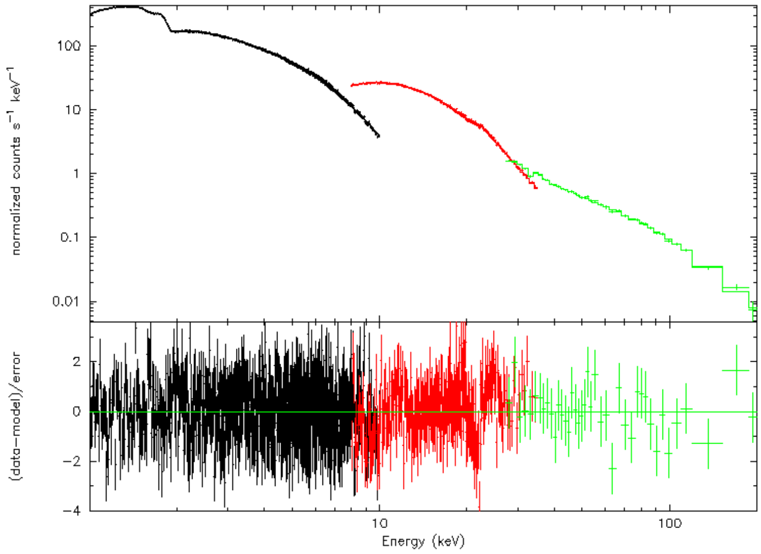

Fig. 4-43 Spectra of Crab nebula observed by *Insight*-HXMT in 982 s.

(2) Spectral fitting results of MAXI J1820+070

The *Insight*-HXMT spectral results of the low/hard state, intermediate state and high/soft state for MAXI J1820+070 are compared with the results of simultaneous/quasi-simultaneous NuSTAR observations. In the intermediate state, the used model is diskbb + bbody + relxillCp, and the effective exposure time of *Insight*-HXMT observation is 4.02 ks. The *Insight*-HXMT results are shown in Table 4-3 and Fig. 4-44 *Insight*-HXMT spectra of MAXI J1820+070 in the intermediate state, and the spectral results for a simultaneous NuSTAR observation (diskbb + bbody + cutoffpl, Fabian et al. 2020) are given in Table 4-2.

Table 4-2 Spectral results of MAXI J1820+070 in its intermediate state for *Insight*-HXMT and NuSTAR

Insight-	diskbb	bbody	relxillCp	

HXMT	Tin (keV)	norm	kT	norm	Gamma	kTe	Refl_frac
	0.680 ± 0.003	20700 ±500	1.16 ±0.01	0.144 ±0.007	1.84 ±0.04	400 ±900	0.34 ±0.13
NuSTAR	diskbb		bbody		cutoffpl		
	Tin (keV)	norm	kT	norm	Gamma		Ecut
	0.60 ±0.01	45000 ± 5000	1.12 ±0.01	0.177 ±0.004	1.6 ± 0.1		50±6

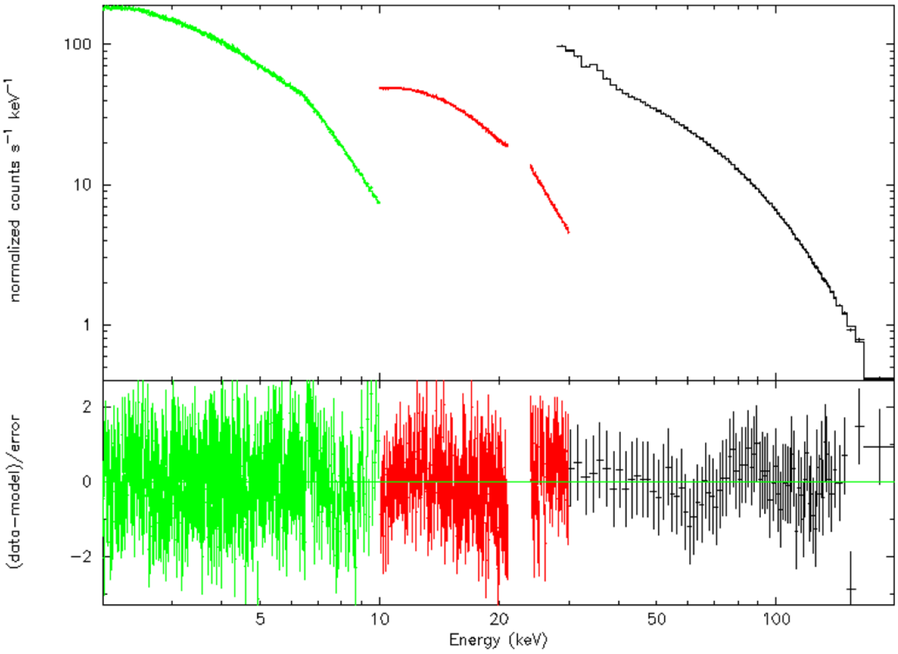

Fig. 4-44 *Insight*-HXMT spectra of MAXI J1820+070 in the intermediate state

The fitting model for high/soft state is (XSPEC) diskbb+bb+cutoffpl. The effective exposure time is 2.7 ks. The *Insight*-HXMT results are given in Table 4-4 and Fig. 4-45

Insight-HXMT spectra of MAXI J1820+70 in the high/soft state., and the results of a simultaneous NuSTAR observation (Fabian et al. 2020) are shown in Table 4-3.

Table 4-3 Spectral results of MAXI J1820+070 in its high/soft state for *Insight*-HXMT and NuSTAR.

	Tin(keV)	kT(keV)	Γ	Ecut (keV)
Insight-HXMT	0.68±0.03	0.97±0.06	1.54±0.09	172±53
NuSTAR	0.65±0.12	0.93±0.02	1.47±0.07	74^{+18}_{-12}

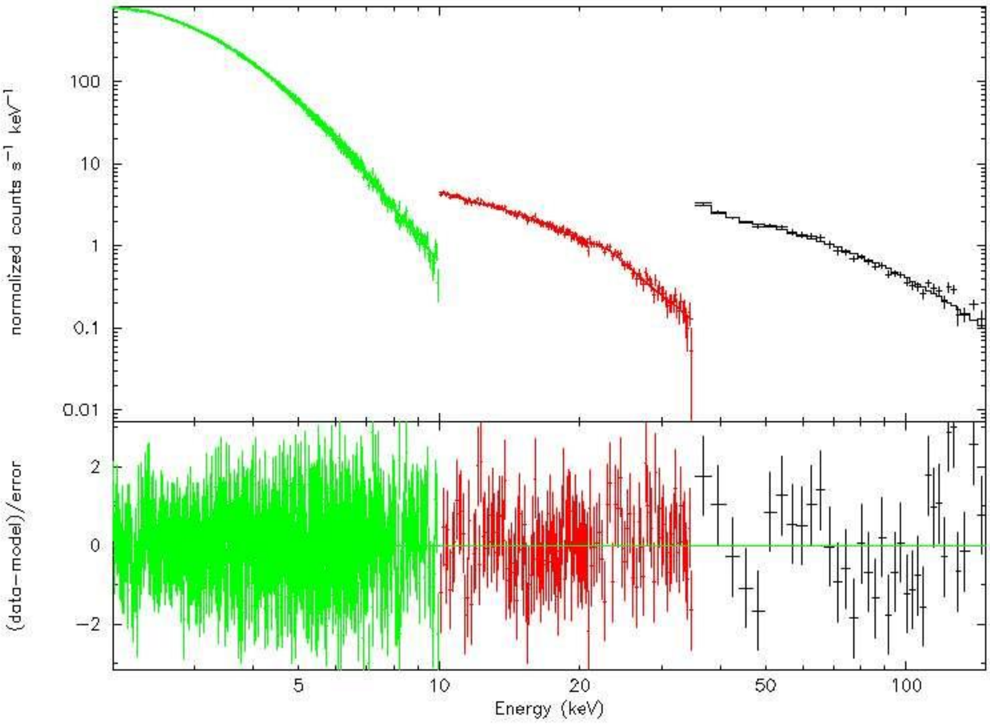

Fig. 4-45 *Insight*-HXMT spectra of MAXI J1820+70 in the high/soft state.

The fitting model for LHS is (XSPEC): diskbb + relxillCp + xillverCp. The effective exposure time is 4.40 ks. The spectral results are shown in Table 4-5 andFig. 4-46 *Insight*-HXMT spectra of MAXI J1820+070 in the low/hard state., and the results of a quasi-simultaneous NuSTAR observation are given in Table 4-4.

Table 4-4 Spectral results of MAXI J1820+070 in its low/hard state for *Insight*-HXMT and NuSTAR.

	T_{in} (keV)	Γ	Afe	kTe (keV)
Insight-HXMT	0.42 ± 0.02	1.560 ± 0.004	3.6 ± 0.2	58 ±2
NuSTAR	0.56 ± 0.05	1.65 ± 0.01	8 ± 3	80 ± 40

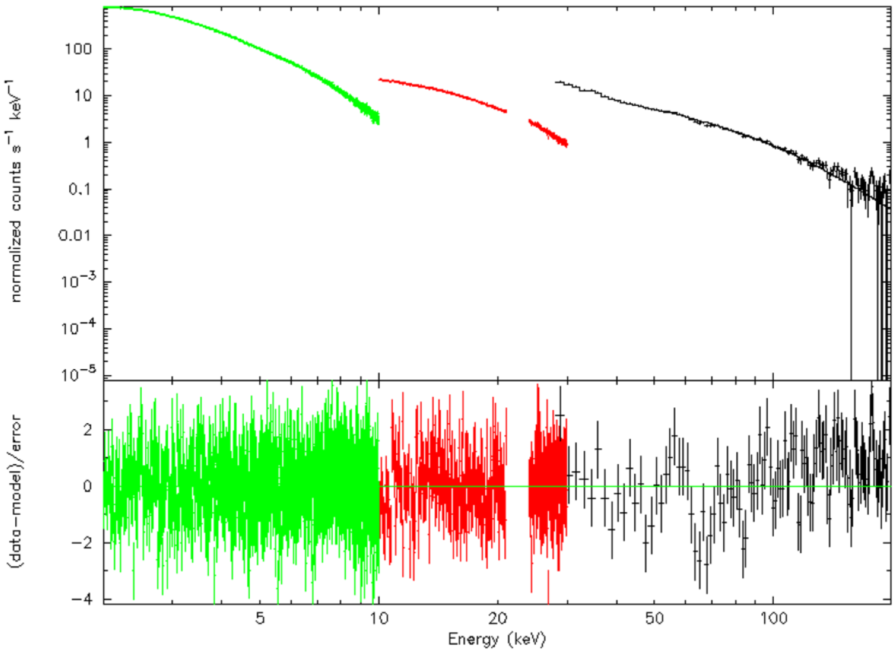

Fig. 4-46 *Insight*-HXMT spectra of MAXI J1820+070 in the low/hard state.

4.2.3 High statistic observation of BH and NS systems

4.2.3.1 Introduction to scientific objectives

Although tremendous of X-ray observations have been made to classic bright X-ray sources, some basic questions remain unclear due to the lack of the multi-wavelength, high statistic, high time resolution or high energy resolution observations. Thanks to the large effective area, broad band energy coverage and good energy resolution of *Insight*-HXMT, the new *Insight*-HXMT data will give us new opportunities to uncover the remaining questions for the classic bright X-ray sources (i.e., Cyg X–1, GRS 1915+105, GX 339–4, Aql X–1, Sco X–1, Her X–1 and et al.) and the newly discovered bright transient sources.

Although parts of the scientific objectives of high statistic observation of classic bright sources can be accomplished by the high cadence observation of variable sources, it is more convenient to arrange long-term observation for bright sources. the high statistic observations will focus on understanding the behaviors of the accretion disk near a BH, measuring the BH spin, studying the characteristic of magnetosphere, measuring the magnetic field of the NSs, studying the disk-corona geometry, understanding the characteristic of the jet, and studying the relationship and difference between the jet and corona.

14 brightest sources are listed in Table 4-5. High statistic observations will also be performed for other bright sources in the future.

Table 4-5 Radiation characteristics of the 14 brightest sources in soft and hard X-ray energy band (when estimating the averaged counts rate of the three X-ray telescopes, the power-law spectra from the Crab pulsar are applied for ME and HE with the source intensity measured by BAT, while the black body spectra at 1 keV are applied for LE with the source intensity measured by *RXTE*/ASM.).

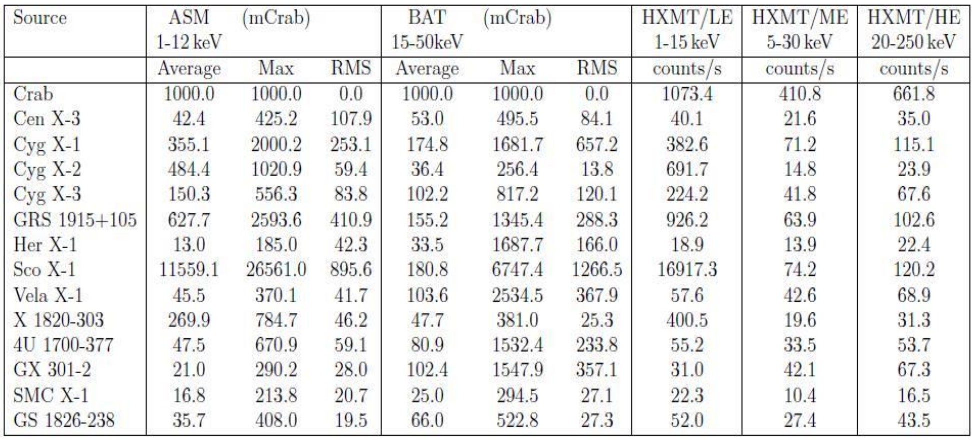

Source	ASM (mCrab) 1-12 keV			BAT (mCrab) 15-50keV			HXMT/LE 1-15 keV	HXMT/ME 5-30 keV	HXMT/HE 20-250 keV
	Average	Max	RMS	Average	Max	RMS	counts/s	counts/s	counts/s
Crab	1000.0	1000.0	0.0	1000.0	1000.0	0.0	1073.4	410.8	661.8
Cen X-3	42.4	425.2	107.9	53.0	495.5	84.1	40.1	21.6	35.0
Cyg X-1	355.1	2000.2	253.1	174.8	1681.7	657.2	382.6	71.2	115.1
Cyg X-2	484.4	1020.9	59.4	36.4	256.4	13.8	691.7	14.8	23.9
Cyg X-3	150.3	556.3	83.8	102.2	817.2	120.1	224.2	41.8	67.6
GRS 1915+105	627.7	2593.6	410.9	155.2	1345.4	288.3	926.2	63.9	102.6
Her X-1	13.0	185.0	42.3	33.5	1687.7	166.0	18.9	13.9	22.4
Sco X-1	11559.1	26561.0	895.6	180.8	6747.4	1266.5	16917.3	74.2	120.2
Vela X-1	45.5	370.1	41.7	103.6	2534.5	367.9	57.6	42.6	68.9
X 1820-303	269.9	784.7	46.2	47.7	381.0	25.3	400.5	19.6	31.3
4U 1700-377	47.5	670.9	59.1	80.9	1532.4	233.8	55.2	33.5	53.7
GX 301-2	21.0	290.2	28.0	102.4	1547.9	357.1	31.0	42.1	67.3
SMC X-1	16.8	213.8	20.7	25.0	294.5	27.1	22.3	10.4	16.5
GS 1826-238	35.7	408.0	19.5	66.0	522.8	27.3	52.0	27.4	43.5

4.2.3.2 Broad-band study of transient X-ray sources

Most of the transient sources radiate in the hard X-ray bands during the outbursts. For example, high energy tails above 100 keV have been observed in many X-ray sources by *INTEGRAL* (Woods & Thompson 2006), suggesting that the hard X-ray emission makes an important (sometimes could be dominant) contribution to the total energy release. Thus, observing the broad energy band in 1–250 keV might be the key to understanding the radiation mechanism of transient sources. Up to now, the sensitivities of the present X-ray telescopes are insufficient to produce simultaneously broad band energy spectra in 1–250 keV, let alone to study the timing and spectral variability in hard X-ray band. Therefore, the broad band analysis can be only done by combining observations from different telescopes. Nevertheless, there still lacks high statistic observation in 10–20 keV energy band.

4.2.3.3 NS X-ray Binary kHz QPO

kHz QPOs are the highest frequency signals ever detected in NS X-ray binaries (Morgan et al. 1997). Based on its extremely short time scale and relatively high amplitude, it can be confirmed that these signals come from the strong gravitational field region around NSs. It is widely accepted that the upper frequency of kHz QPO is related to the orbit movement of material in accretion disk. When the accretion material approaches to the innermost stable orbit, the rotation frequency reaches its maximum value and kHz QPO frequency reaches its saturation frequency. *RXTE* has detected kHz

QPO in about 30 LMXBs, whose highest frequency is ~1200–1300 Hz, which puts strongest constraints on the last stable orbit predicted by the GR and on the NS radius (Berger et al. 1996). However, the saturation of kHz QPO frequency has been only detected in few sources (Zhang et al. 1998; Kaaret et al. 1999). Moreover, *RXTE* observations suggest that the rms of kHz QPO increases with photon energy in 2–30 energy bands for LMXBs. The good sensitivity of *Insight*-HXMT in hard X-ray energy band brings advantages in exploring the physical mechanism under strong gravitational field and with ultra-dense matter. The improvement of detector sensitivity broadens the detectable frequency range of kHz QPO, thus allows us to investigate the saturation of kHz QPO frequency in more LMXBs. With the estimation of NS mass from other observed parameters, it can be used to test the existence of innermost stable orbit predicted by GR, and constrain the radius and state of matter of NS.

4.2.3.4 Thermonuclear burst probe

Using the thermonuclear burst on NS surface as a probe to study the structure and evolution of accreted disk and corona has drawn attention in recent years (Chen et al. 2012). A cooling corona X-ray binary catalogue has been established from previous studies, in which the hard X-ray emission of an accreting NS decreases during thermonuclear bursts. The recovering time scale of hard X-ray emission lags that of soft X-ray for 1–2 s. Since the signal is more significant above 30 keV, the large effective area of *Insight*-HXMT in hard X-ray band makes the study of thermonuclear burst an important scientific objective. The thermonuclear bursts as a probe of accretion disk can be further applied to: (1) constrain the geometry of the corona and compare with an extrapolation of the results from AGN Reverberation Mapping. (2) explore the impact on the accretion process in the inner region of accretion disk, which could obtain the burst feedback and relation with spectral state. (3) be a new method to measure the inner radius of accretion disk of a NS X-ray binary in the low/hard state.

4.2.3.5 Observing strategy

High statistic pointing observations will be performed on the known classic bright sources and new discovered bright transients. The number of observations depends on the scientific requirement. As the pointing observations do not rely heavily on the systematic errors from the background model, they can be carried out in the early stage of satellite operation and are used to do spectral and timing analyses. Their priority and exposure time are determined by core proposals.

(3) Observational results

So far, a great amount of research progresses has been derived to XRB outbursts and evolution, which will be introduced in the following sections. These studies include: basic properties of NS and BH; pulsar navigation; cyclotron resonant scattering feature (CRSF); propeller effect of high mass XRB (HMXB); emission mechanism in the magnetic pole of HMXB; probe of thermal nuclear burning on the surface of NS; evolution of Z and atoll sources; reflection component of BH XRB; quasi-periodic oscillation (QPO) and time lag in BH XRB outburst; joint spectral analysis in energy and time domains; evolution properties of the corona and jet in BH XRB outburst etc. Since 2020, many scientific papers had been published, submitted or in preparation in the above research fields.

Regarding to the NS XRB study, *Insight*-HXMT observed the recent outburst of GRO J1008-57 and detected a CRSF line at around 90 keV with a significance of more than 20 sigma (Fig. 4-47 CRSF around 90 keV detected in GRO J1008–57 with *Insight*-HXMT (Ge et al. 2020b)., Ge et al. 2020b). Such results have reported the highest centroid energy and the strongest magnetic field ever measured directly from the NS system. Her X-1 is the first NS system detected with CRSF in the last century. Its CRSF line energy previously showed a long-term decay, however, *Insight*-HXMT observations suggest that the long-term decaying trend of the CRSF centroid energy starts to flatten (Fig. 4-48 *Insight*-HXMT confirms that the long-term decaying trend of the Her X–1 CRSF centroid energy has stopped (Xiao et al. 2019)., Xiao et al. 2019). Better understanding of such phenomenon needs more *Insight*-HXMT observations. More CRSF features are detected as well with *Insight*-HXMT in other HMXB, e.g. in 4U 0115+63 one cyclotron line is around 18 keV. In the recent outburst of 1A 0535+26, it is the second source which shows the energy of CRSF shows anti correlation of its luminosity as shown in Fig. 4-49 Left panel: relation between energy of CRSF and luminosity. Right panel: evolution of energy of CRSF with time. (Kong et al. 2021).

By taking the P2P technique upon the Insight-HXMT observations, the detailed evolution of CRSF against luminosity is revealed (Fig. 4-50 The evolution of the CRSF centroid energy against luminosity, as revealed with a P2P technique upon the outburst of 1A 0535+262 observed by Insight-HXMT (Shui et al. 2024).). Apart from the correlation as found previously between CRSF centroid energy and the luminosity , new trend is discovered at even lower luminosity range (Shui et al., 2024). Since it is generally believed the site produces CRSF shall correspond to the major emission region of the accretion column at the magnetic pole, the continuous evolution of CRSF centroid energy against luminosity may suggest that the emission region of the accretion column shall also change smoothly during the transition between different emission modes. This in turn constrains strongly the emission models at work currently.

We report the phase-resolved analysis of the data of the first Galactic NS ULX Swift J0243.6+6124 observed by *Insight*HXMT during its 2017–2018 outburst. The 120 to 146 keV CRSF is robustly detected in a spin-phase region of 0.6–1.0 at a significance level of 6σ–18σ, when the source was at a luminosity of $\sim 2 \times 10^{39}$ erg s−1, far above its critical luminosity for the transition from a “pencil” to a “fan” emission pattern (Fig. 4-51 The spectral fittings and residuals for phase 0.2–0.3 (left) and 0.8–0.9 (right) on MJD 59171 from 1A0535+262(Kong et al., 2022, ApJ).). This serves as the first unambiguous measurement of a CRSF from ULXs and also the highest CRSF energy discovered so far from all NS X-ray binary systems. The measured surface magnetic field of $\sim 1.6 \times 10^{13}$ G for Swift J0243.6+6124 is the strongest for all known

NSs with detected electron CRSFs and also the strongest for all NS ULXs (Kong et al., 2022, ApJL). Furthermore, we also found the highest energy of the harmonic CRSF (first CRSF) at > 100 keV, from the accreting pulsar Swift J0243.6+6124 based on observations of *Insight*-HXMT during the 2020 type II outburst of the source (Kong et al., 2022, ApJ) (Fig. 4-52 The CRSF of Swift J0243.6+6124 @ 146keVdetected by *Insight*-HXMT (Kong et al., 2022, ApJL).).

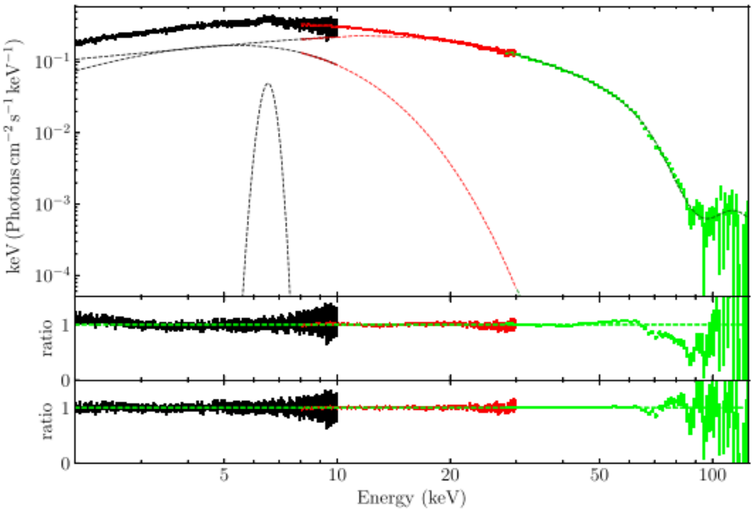

Fig. 4-47 CRSF around 90 keV detected in GRO J1008–57 with *Insight*-HXMT (Ge et al. 2020b).

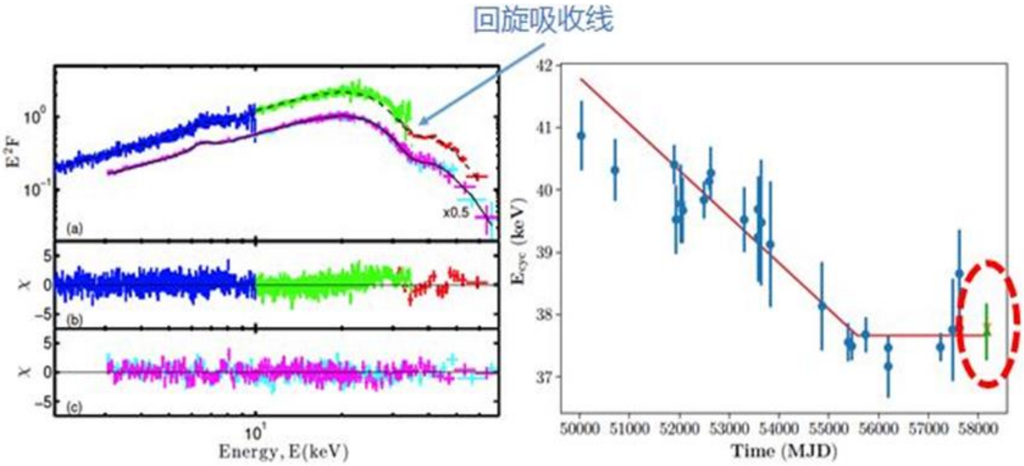

Fig. 4-48 *Insight*-HXMT confirms that the long-term decaying trend of the Her X–1 CRSF centroid energy has stopped (Xiao et al. 2019).

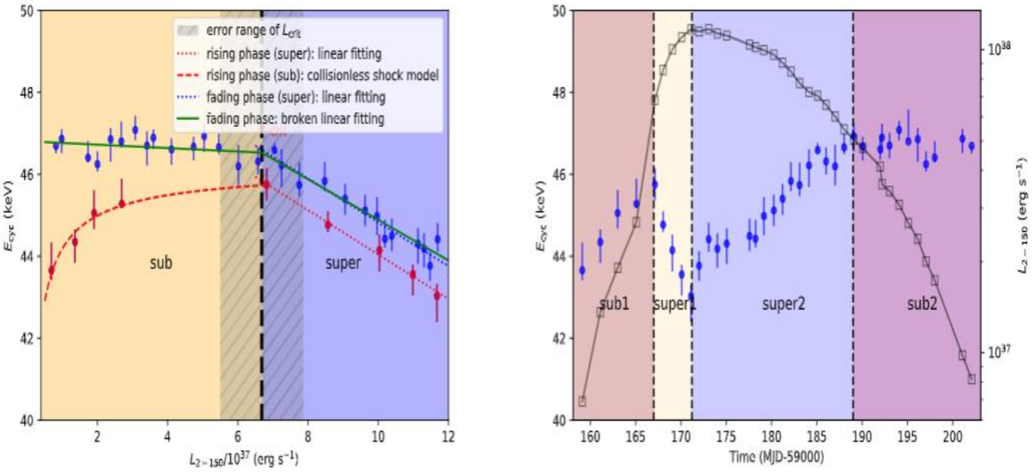

Fig. 4-49 Left panel: relation between energy of CRSF and luminosity. Right panel: evolution of energy of CRSF with time.

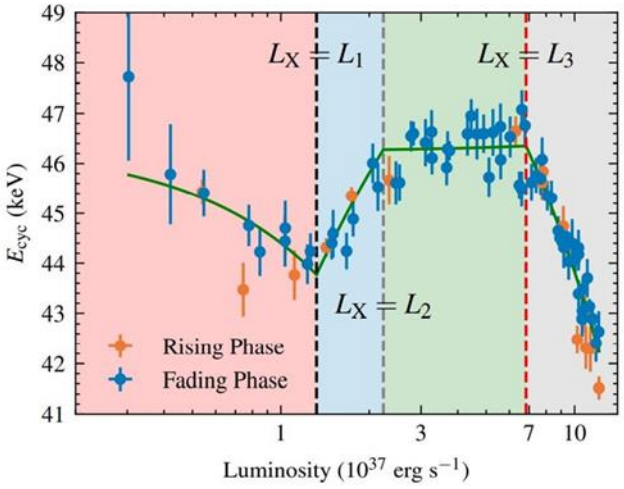

Fig. 4-50 The evolution of the CRSF centroid energy against luminosity, as revealed with a P2P technique upon the outburst of 1A 0535+262 observed by Insight-HXMT (Shui et al. 2024).

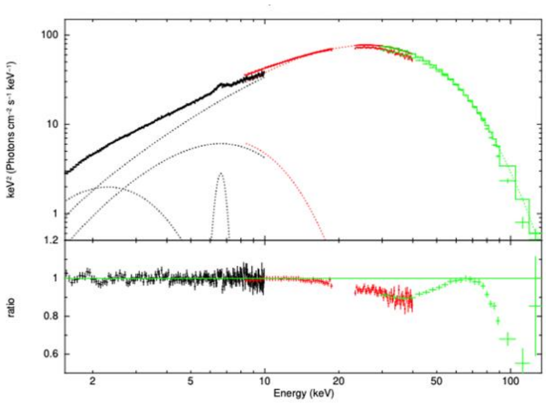

Fig. 4-51 The spectral fittings and residuals for phase 0.2–0.3 (left) and 0.8–0.9 (right) on MJD 59171 from 1A0535+262(Kong et al., 2022, ApJ).

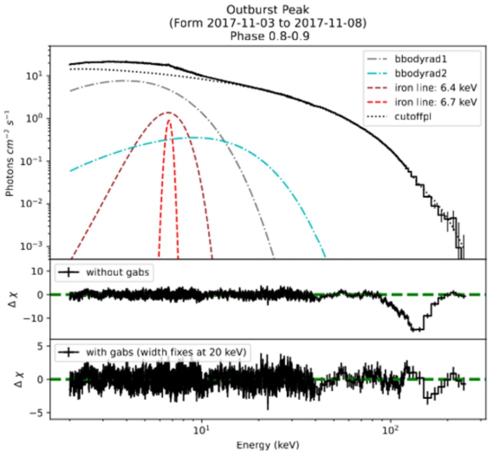

Fig. 4-52 The CRSF of Swift J0243.6+6124 @ 146keVdetected by *Insight*-HXMT (Kong et al., 2022, ApJL).

Type I X-ray bursts are thermonuclear explosions that occur on the surface of accreting NS binary systems, which usually lasts for dozens to hundreds of seconds. Type I bursts have a great effect on the accretion process, thus can be used as a probe in studying the accretion process of the NS X-ray binary. Previous results from other observatories had suggested a cooling corona during the thermonuclear bursts, based on the data combined by tens to hundreds of bursts (e.g., tens of bursts for RXTE/PCA and more than one hundred bursts for INTEGRAL). However, with *Insight*-HXMT observation, the cooling corona phenomenon had been found in a single burst of the NS X-ray binary 4U 1636–536, accompanied with significant improvement on the signal-to-noise ratio. It is also the first time that the decrease of hard X-ray emission has been found in the spectra of type I burst on a time scale of seconds, as shown inFig. 4-53 Spectra and light curves of Type-I X-ray burst of 4U 1636–536 (Chen et al. 2018). (Chen et al. 2018). Compared to other missions, *Insight*-HXMT has shown its advantage in studying such phenomena.

Supported by this capability and the data accumulated for type-I bursts by Insight-HXMT, the spectral property of the corona cooled by the shower of the type-I burst was investigated. The results show that for the millisecond pulsar MAXI J1816-195, the corona is cooled with special spectral structure at high energies, which suggest that there may have additional non-thermal emission (e.g. jet) which is hardly be cooled by the type-I burst at the magnetic pole. During the outburst of 4U 1608–52, the hard X-rays can only be cooled roughly 50% by the type-I burst at the high energies (Chen et al. 2024,Fig. 4-54 The energy spectrum of the deficit fraction of the corona detected by Insight-HXMT during the outburst of 4U 1608–52 (Chen et al. 2024).). Similar result was also found in 4U 1636-536 (Peng et al. 2024,Fig. 4-55 The energy spectrum of the deficit fraction of the corona detected by Insight-HXMT during the outburst of 4U 1636-536 (Peng et al. 2024).).

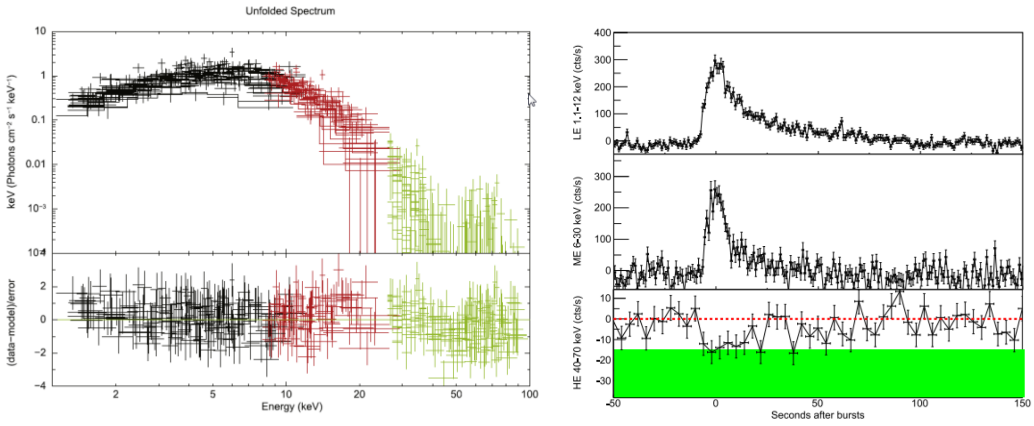

Fig. 4-53 Spectra and light curves of Type-I X-ray burst of 4U 1636–536 (Chen et al. 2018).

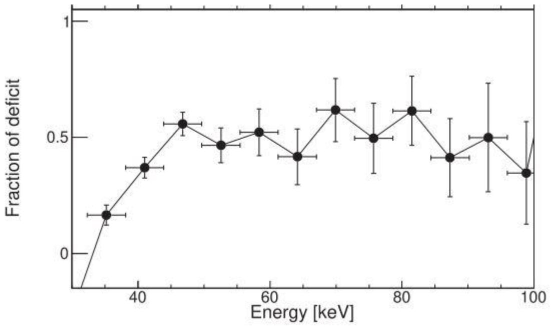

Fig. 4-54 The energy spectrum of the deficit fraction of the corona detected by Insight-HXMT during the outburst of 4U 1608–52 (Chen et al. 2024).

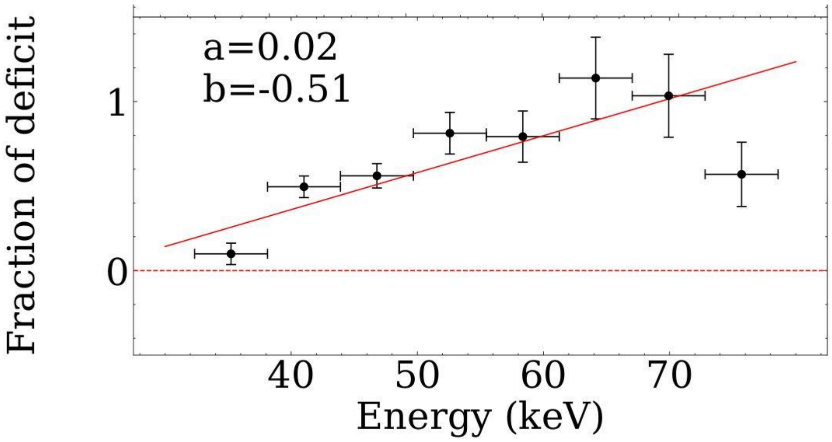

Figure

Fig. 4-55 The energy spectrum of the deficit fraction of the corona detected by Insight-HXMT during the outburst of 4U 1636-536 (Peng et al. 2024).

Insight-HMXT spectral study of 4U 1608–52 suggests the existence of an additional component besides the thermal component from the NS surface (Chen et al. 2019), as shown in Fig. 4-56 the merged spectra fitted with an absorbed black-body model (left) and the f_a model (right). The dotted lines represent the model components for the pre-burst emission (blackbody and nthcomp). (Chen et al. 2019). The flux of this component is positively correlated with the burst flux, and the spectrum is similar to that of the accretion radiation. It can be explained by the increase of accretion rate caused by the thermonuclear bursts. The burst of 4U 1608–52 has an emission radius larger than the NS radius, and its luminosity reaches the Eddington limit, thus the inner-disk radius is thought to be larger than the burst radius.

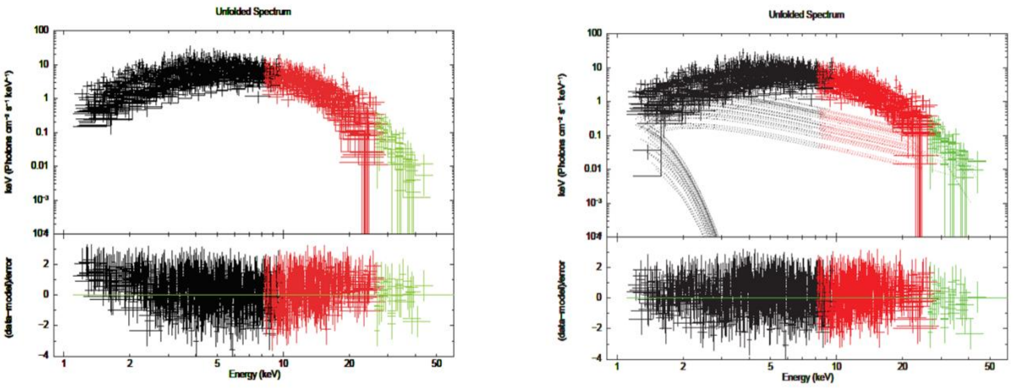

Fig. 4-56 the merged spectra fitted with an absorbed black-body model (left) and the f_a model (right). The dotted lines represent the model components for the pre-burst emission (blackbody and nthcomp). (Chen et al. 2019)

The obscuration by the disk of the burst emission from 4U 1730-22 detected by *Insight*-HXMT. Time-resolved spectroscopy reveals that the excess during bursts can be attributed to an enhanced preburst/persistent emission or the Comptonization of the burst emission by the corona. We find, the burst emission shows a rise until the photosphere touches down to the NS surface rather than the theoretical predicted constant Eddington luminosity. The shortage of the burst emission in the early rising phase is beyond the occlusion by the disk. We speculate that the findings above are due to that the obscured part (not only the lower part) of the NS surface is exposed to the line of sight due to the evaporation of the obscured material by the burst emission, or the burst emission is anisotropic ($\xi > 1$) in the burst early phase (

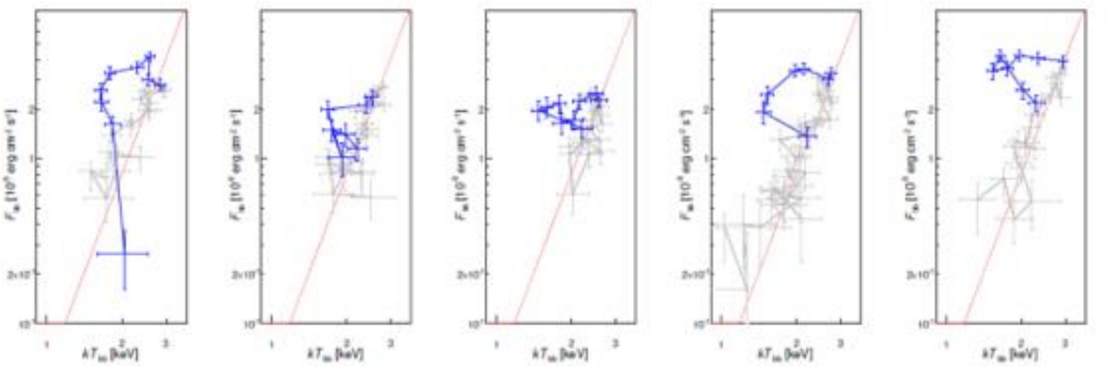

Fig. 4-57). In addition, based on the fluxes of PRE bursts at their touchdown times, we derive a distance estimation as 9.0–12.4 kpc. (Chen et al., 2022, ApJ)

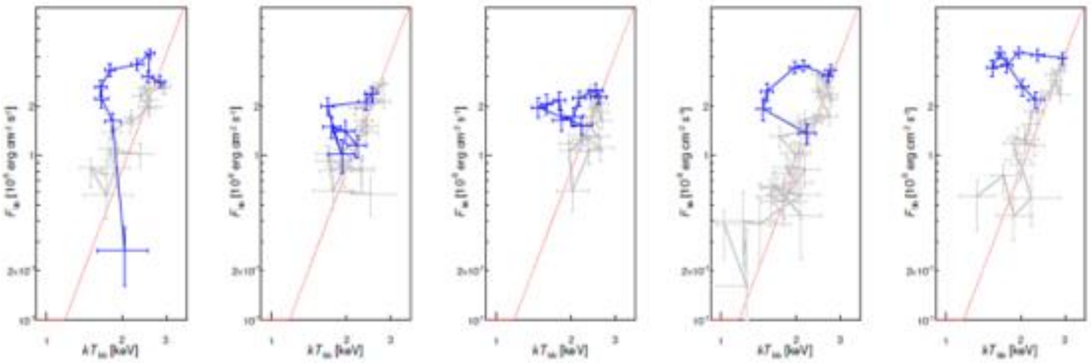

Fig. 4-57 The obscuration by the disk of the burst emission from 4U 1730-22 (Chen et al., 2022, ApJ).

Burst oscillations have also been found with *Insight*-HXMT in NS binary systems, which have provided more observational evidences in understanding the accretion process of NS X-ray binaries.

Although the kilohertz QPO (kHz QPO) has been observed in some Z- and atoll-sources, such as Sco X–1, its origin remains a puzzle in the last 20 years. Due to the limited observing energy bands, previous telescopes cannot detect kHz QPO at high energy and thus cannot fully test previous models. *Insight*-HXMT detected for the first time the kHz QPO from Sco X–1 at energy above 20 keV. Since X-rays at energy above 20 keV are not likely dominated by the disk emission, such detection challenges the current popular kHz QPO models (Fig. 4-58 High energy kHz QPOs in Sco X–1 observed with *Insight*-HXMT (Jia et al. 2020)., Jia et al. 2020).

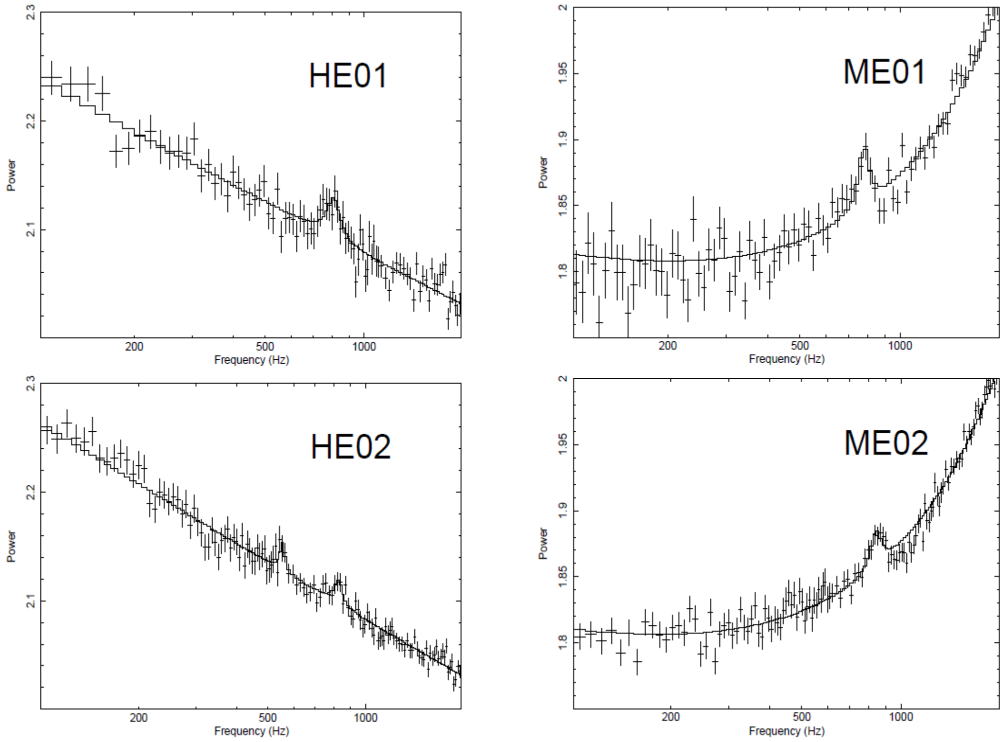

Fig. 4-58 High energy kHz QPOs in Sco X–1 observed with *Insight*-HXMT (Jia et al. 2020).

4.2.3.6 Direction of proposal call

The observation mode will be the normal pointing observation.

The proposal should be aimed at the following scientific objectives: (1) to understand the behaviors of accretion disk near BH and measure the BH spin, (2) to understand the characteristic of the NS magnetospheres and measure the strength of NS surface magnetic field, (3) to understand the coronal properties and measure the geometry, (4) to understand the properties of the jet and to study the relationship and difference between the jet and the corona.

4.2.4 Space- and ground-based coordination and follow-up observations

During the in-orbit operation of *Insight*-HMXT, there are more than 10 astronomical space observatories in operation. They cover X-ray and other energy bands (e.g., Gamma-ray). China's Gravitational wave high energy Electromagnetic

Counterpart All-sky Monitor (GECAM), launched in December 2020, is the newest member in this family. This is an exciting period for astronomy. These telescopes can find new or even new type of sources. With the operation of a series of multi-messenger detection instruments, more multi-messenger events will be detected. In particular, the ground-based gravitational wave observatories have detected the first gravitational wave event (Abbott et al. 2016) and the first gravitational wave event caused by NS merger (Abbott et al. 2017a). IceCube Neutrino Observatory has detected the first isotropic high energy neutrino flux (Aartsen et al. 2013, 2014). Based on the multi-wavelength follow-up observations, the electromagnetic counterparts to the NS merger (Abbott et al. 2017b) and to the high energy neutrinos (IceCube Collaboration et al. 2018) have been found respectively. Recently, the electromagnetic counterpart of fast radio burst has been observed for the first time, and *Insight*-HXMT provides key evidence in identifying its magnetar origin (Li et al. 2021). *Insight*-HXMT aims at finding new high energy transients via Galactic plane scanning survey, and detecting new activities from known sources via scanning survey. All of these will provide targets for coordination and multi-wavelength follow-up observations. The main research topics are listed below:

1) To participate in multi-wavelength follow-up observations, in order to search for and study the electromagnetic counterparts of gravitational wave events and high energy neutrinos. The electromagnetic counterpart for the first gravitational wave event from neutron-star merger has been found by multi-wavelength follow-up observations. *Insight*-HXMT has contributed the upper limit on the emission of the counterpart in MeV band (Li et al. 2018). Moreover, *Insight*-HXMT has joined the follow-up campaign of gravitational wave events through an agreement. The science operation center of *Insight*-HXMT will ensure the observation time of such follow-up observations. In addition, *Insight*-HXMT has also participated in searching for the electromagnetic counterpart of high energy neutrinos, which has provided constraints on the emission in MeV band.

2) To coordinate with ground-based optical telescopes. Optical telescopes with large FOV can perform high cadence multi-wavelength sky surveys. Once *Insight*-HXMT finds new sources, they can perform timely follow-up observations to identify and locate the optical counterparts, which allows us arrange further follow-up observations. Moreover, some high mass X-ray binaries are usually active in optical and other energy bands before going into outbursts in X-ray. Optical observations prior to X-ray outbursts can help us to better understand accretion physics.

3) To study radio, infrared, optical, ultraviolet and gamma-ray properties during X-ray state transitions, in order to study the relation between jets and spin of compact objects, the relation between state transition and jet power, and the relation between episodic jet sand spin of compact objects/non-stable accretion.

4) To study the origin and evolution of QPOs using multi-wavelength joint observations. QPOs have been observed in optical and X-ray bands of some sources. For example, X-ray and optical QPOs have been detected in the new black hole X-ray binary MAXI J1820+070 during its 2018 outburst. Multi-wavelength joint observations have been performed by *Insight*-HXMT and other telescopes.

5) To perform simultaneous observations in radio and gamma-ray bands for rotation-powered pulsars and gamma ray-binaries. For rotation-powered pulsars, we can study the radiation mechanism, the radiation region and the magnetospheres' properties in much broader energy band. For gamma-ray binaries, there are some flares when the sources pass their periastrons. We can measure the time lags between different wavelengths and explore their physical nature. Moreover, using joint observations of Crab between *Insight*-HXMT and Xinjiang Nanshan radio telescope, the timing calibration of *Insight*-HXMT can be applied. In addition, X-ray and radio joint observations can be used to measure the phase lags between X-ray and radio bands, and study the evolution of their phase lags, pulse profiles,

timing noises, glitches, and braking indices, which will constrain the physical properties of the magnetospheres of pulsars. Fruitful achievement has been made for Crab: using the coordinated observations from *Insight*-HXMT and other radio telescopes, we confirmed that the timing system of *Insight*-HXMT is very accurate; using the joint observations from *Insight*-HXMT and other X-ray telescopes, the pulse profiles of Crab are measured, which helps us to test and calibrate the response files; using the multi-wavelength observation of Crab, the delayed spin-up phenomenon is observed during the largest glitch of the Crab pulsar.

6) To monitor the optical spectrum and light curves of the optical counterparts of compact X-ray binaries using Lijiang and Xinglong optical telescopes. Using these observations, we can confirm the type of the companion star, measure the dynamical mass of the central object, and constrain the orbital inclination. Meanwhile, for some bright transients, the long-term observations can be used to study the evolution of accretion disk and accretion process.

7) To measure the spin of newly discovered BH X-ray binaries. Once the BH mass, distance and orbital inclination are measured by infrared and optical telescopes, we can use *Insight*-HXMT to produce the spectra in the high/soft state, further measure the spin via modelling the continuum.

8) To study the evolution of cyclotron line energy and its physical origin. For Her X-1, recently its cyclotron line energy shows flattening after its long-term gradual decrease (Staubert et al. 2021; Xiao et al. 2019.) Coordinated observations between *Insight*-HXMT and other telescopes can monitor and study the energy change of cyclotron line. *Insight*-HXMT performed several joint observations with *NuSTAR* and *INTEGRAL*, from which the flattening of its cyclotron line energy were confirmed.

9) To perform coordinated observations with GECAM and Fermi/GBM in order to study terrestrial gamma-ray flashes (TGFs). We can observe TGFs and terrestrial

electron beam events by combining high-energy astronomical satellites (*Insight*-HXMT, GECAM, Fermi/GBM, etc.) and lightning detection networks, in order to study their radiation mechanisms and the effects on the detection and identification of gamma-ray bursts and magnetar bursts.

10) To observe active magnetars with FAST and other radio telescopes. *Insight*-HXMT has discovered the first X-ray burst associated with a fast radio burst and identified it coming from the Galactic magnetar SGR J1935+2154. *Insight*-HXMT also found that the two pulses of the X-ray burst are coincident with the two peaks of the radio burst, as shown inFig. 4-59 Multiwavelength observations of *Insight*-HXMT and other telescopes for FRB 200428, which identified that the FRB originates from the magnetar SGR J1935+2154 (Li et al. 2021). (Li et al. 2021), which is key to identifying its magnetar origin. The radio emission is not detected in the simultaneous FAST observation, indicating that the physical process behind the magnetar-fast radio burst association is complicate and is worth exploring further. By performing coordinated observations with FAST and radio telescopes, we can study the flare and the evolution behaviors in a broad band with high time resolution, which is extremely important for us to understand the generation and the radiation mechanism of fast radio bursts.

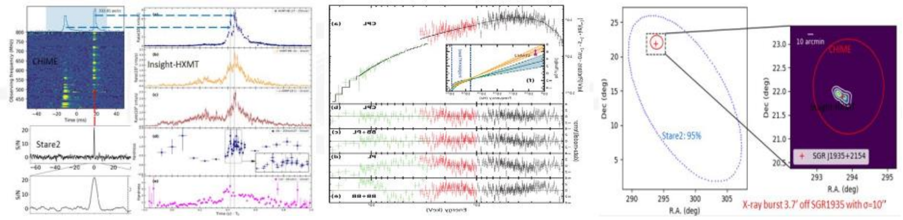

Fig. 4-59 Multiwavelength observations of *Insight*-HXMT and other telescopes for FRB 200428, which identified that the FRB originates from the magnetar SGR J1935+2154 (Li et al. 2021).

5 Observation Modes

5.1 Introduction

The solicited observation proposals in this AO cover two observation modes of *Insight*-HXMT. The switch between the two modes can be achieved by adjusting the satellite attitude.

(1) Pointing observation mode: the satellite points to a certain sky direction in the inertial space for specified duration. This mode is further divided into two types: on-axis pointing observation and off-axis pointing observation.

(2) Small sky area scan mode: The satellite completes the deep scanning observation of specific small sky areas to achieve a full coverage of the 7°~10° half cone sky area. This observation mode can be used to scan and monitor the Galactic plane and other sky areas.

5.2 Pointing observation mode

The pointing observation mode is implemented using three-axis stabilized inertial space orientation. In this mode, the X-axis (the optical axis) of the satellite points to the observation target, and the angle between the solar vector and the satellite Z-axis must be acute. During a pointing observation of a certain target, the attitude of the satellite remains unchanged, and the solar panel remains stable.

In pointing observation of regular sources, in order to meet the temperature control requirements of medium and low energy detectors, and to ensure the normal operation of the star sensor, the sun avoidance angle should be larger than 70°, namely, the angle between the satellite + X axis and the solar vector is 70°~180°. In order to prevent the sunlight from irradiating the detectors, it is also necessary to consider the situation where the sun light from the side to the detector, in addition to satisfying the sun avoidance angle. Therefore, the maximum duration for a pointing observation cannot be longer than 20 days.

Earth occultation is basically unavoidable during the observation of *Insight*-HXMT. Considering the radius of the Earth, the Earth albedo and the detector field of view, it may be considered that during the Earth occultation, sources in a region of radius of 83° centered at the center of the Earth are invisible. In the case of Moon occultation, sources within 15.5' of the Moon center are invisible.

5.3 Small sky area scan mode

The small sky area scan observation performs deep scanning observations on a circular area with an angular radius of *n* degrees ($7^\circ \le n \le 10^\circ$) in the inertial space, and requires a full coverage of the small sky area. Taking into account of the actual operability of the satellite control system, namely, each time only one single rotation around a certain axis of the satellite, the actual scanning range of the sky area can be expanded to a diamond-shaped area with the circle as an inscribed circle to achieve the full coverage of the required circular area.

In order to ensure the overlap rate of the sky scanning, the line-by-line scanning method has been adopted according to the actual capabilities of the satellite platform, as shown in Fig. 5-1. Point O is the center of the specified circular area to be scanned, the circle is the circular area to be observed, and the dotted lines with arrows are the scanning paths. When scanning along the horizontal direction shown in the figure, the available scanning rates are 0.01°/s, 0.03°/s and 0.06°/s. The time required to change the scanning direction is fixed, and the step between two adjacent scans is from 0.1° to 1° with an interval of 0.1°. The size of the scanned area is in the range of 14°×14° to 20°×20°. The duration of a small sky area scan is usually from 2.3 hours to 5 days, which should be specified in the observation plan.

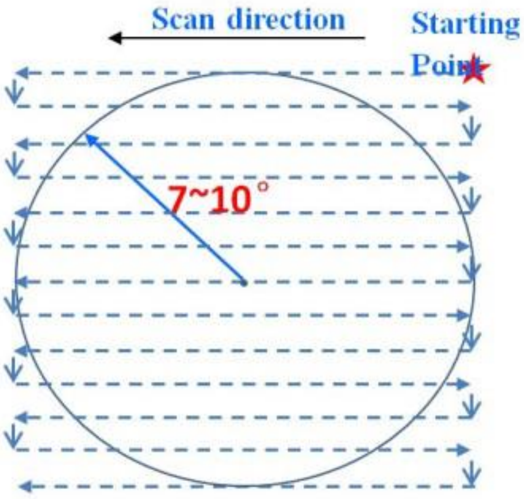

Fig. 5-1 Demonstration of small sky area scan with *Insight*-HXMT.

Different observation times for a certain sky area will result in different relative positions between the observation pointing direction and the solar vector, and the satellite inertial coordinate system will be different as well. Therefore, the tangent direction of the diamond-shaped area scanned by the satellite's principal axis to the circular area will be different. However, in all cases, the scanned diamond area can always completely cover the circular area to be observed.

This observation mode can be used to scan and monitor the Galactic plane and other sky areas.

6 Background

6.1 Background Estimation Method

Insight-HXMT carries blind detectors and combination of detectors with large and small fields of view (FOV). The background estimation can be achieved by combining the different FOVs, off-axis observation and background model with the blind detectors and other auxiliary detectors. The method of combining FOV can resolve the source intensity, particle background and diffuse background by comparing the results of the detectors with different FOVs (large, small, and blind). For the off-axis observation method, the target deviates from the FOV center and locates only in the FOV of several detectors. Since the detector FOV is divided into three groups with the orientation differ by 60° along the long side, some of the detectors can observe the background, while some of the detectors can observe the source during off-axis observations. The blind FOV detector is an innovative design of *Insight*-HXMT. Based on the relationship between the blind FOV detector and the background components of the source observation detectors, the background model can be constructed to perform the background estimation. Currently, the background estimation of *Insight*-HXMT is performed with the background model base on the blind detector. For details, please refer to section 6.4.

6.2 Background components

Insight-HXMT has three telescopes in different energy bands, i.e., HE (20–250 keV), ME (5–30 keV) and LE (0.7–13 keV). *Insight*-HXMT operates in a quasi-circular low-earth orbit with an attitude of ~550 km and an inclination of ~43°. During its in-orbit operation, it will interact with various space radiation components (particles, photons), thereby produces different background components. According to the time characteristics of the background, the background can be classified into delayed component and prompt component. The former arises from the decay of activated detector material, while the latter arises from the moment when space radiations interact with the detector. At this stage, there are mainly two types of delayed background components and four types of prompt background components. There are two types of delayed components, i.e., the delayed background as the satellite passing through the South Atlantic anomalous (SAA) and the delayed background caused by the high energy cosmic-ray protons (CRP_D). The four kinds of prompt components are: the prompt background caused by the high energy cosmic-ray protons (CRP_P), the albedo gamma-ray of the Earth's atmosphere (Albedo), the non-aperture incident cosmic X-ray background (CXB_N), and aperture incident cosmic X-ray Background (CXB_A).

Based on the mass model of *Insight*-HXMT, the Geant4 simulation software can be used to simulate the response of the detector to different incident components from different directions. Combined with the known space radiation environment (spectral shape and intensity) of the main components of the space radiation (protons, gamma rays, and X-rays), the background generated by different space radiation components on the detectors can be simulated. Current simulation can give the delayed and attenuated curves of two kinds of delayed components (SAA & CRP_D) and the backgrounds of four kinds of prompt components (CRP_P, CXB_N, CXB_A & Albedo) from different directions of incidence. The contributions of various backgrounds components of every payload are shown in Fig. 6-1. The LE background is mainly caused by CRP in the high-energy band and is dominated by CXB in the low-energy band and the ME background is dominated by CRP in the whole energy band. The main contributors to the HE background are SAA, CRP_D and Albedo.

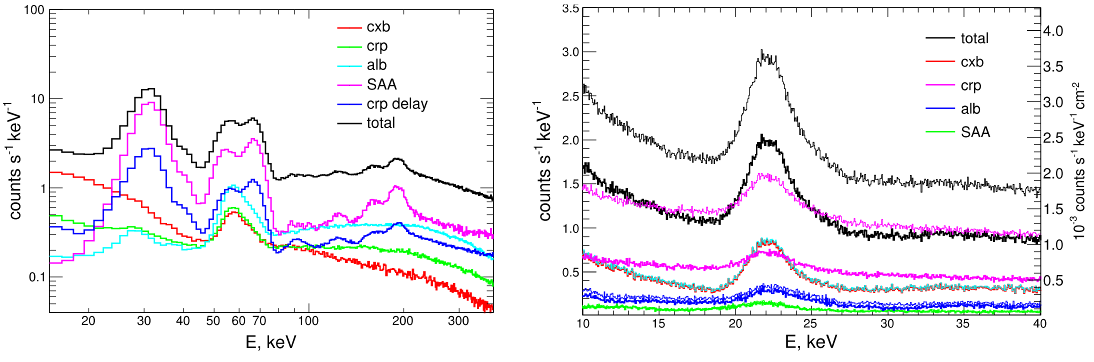

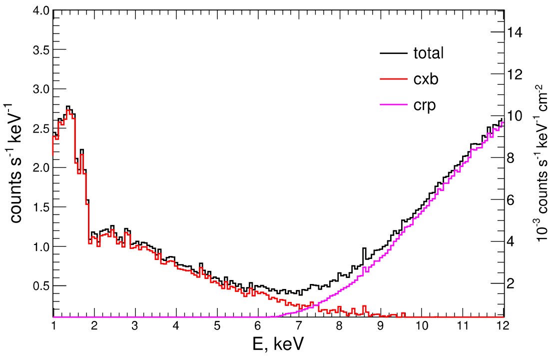

Fig. 6-1 Simulated background components of the three payloads (upper left: HE, upper right: ME, lower: LE) of *Insight*-HXMT (Zhang et al. 2020)

The basic background level of each detector at any time can be estimated, using these simulated response data of different background components and considering the effects of spatial anisotropy of incident particles, the Earth's periodic shielding of high energy protons and X-rays at different angles, the Earth’s periodic gamma-ray irradiation on the satellite at different directions, and the difference in the response of the detector to incident particles in different directions. The systematic error of the background estimation under different observation modes can then be estimated by constructing background models under different observation modes with a series of background model parameters and the time evolution characteristics of these model parameters.

The simulation shows that the background shape (the evolution of the background count rate over time) of the delayed background between the individual detector modules is similar. Therefore, the delayed background of each cell can be characterized by the scale factor relative to the blind detector. The HE detector has four prompt background components, namely CRP_P, Albedo, CXB_A, and CXB_N. When the Earth occultation effect and spatial anisotropy are not considered, only CRP_P is modulated with geographic coordinates and shows a periodic change, while the other three components remain constant. When the Earth occultation effect and spatial anisotropy are considered, due to the difference in the response of the detector to incident particles in different directions, each component exhibits periodic changes in each pointing observation. The solid angle coverage of the Earth for the satellite is about 1/3 of the whole sky. For Albedo, the Earth can be considered as a light source with uniform brightness, and the calculations show that its anisotropy as a surface light source can be ignored. For CXB_N, the effect caused by the spatial anisotropy can also be ignored.

Before launch, based on the Geant4 toolkit, we built a mass model and developed a simulation program for *Insight*-HXMT. Not only can it be used to estimate the background level of *Insight*-HXMT, but also the whole satellite mass model that can be used to do the analysis of the detection efficiency, PSF and response matrix for all the three payloads. These results can be used for GRB positioning, in-orbit ARF and RSP computation. In addition, the fluorescence lines in the background spectrum and the lines caused by material activation can also be used to analyze the in-orbit E-C (Energy-Channel) relationship and energy response.

The background level, background spectrum and background evolution with orbit motion and In-orbit operation time of the satellite can be obtained by Geant4 simulation for LE, ME and HE. For example, for HE, the initial delayed components of the satellite at ~30 keV and ~190 keV increase rapidly, and the level of activation lines of 50–70 keV increases slowly and tends to saturate after about one year. These results are very helpful for understanding the background data from the in-orbit measurements.

6.3 In-orbit background analysis

（1） Comparison of the in-orbit background with simulations:

Analysis of the in-orbit background data shows that the HE background level is roughly consistent to the on-ground simulation. The in-orbit background of ME and LE have become more complicated due to the light pollution and other problems. Therefore, in order to estimate the LE and ME background more accurately, more on-ground background simulations are needed to better understand the in-orbit background.

（2） Characteristics of the in-orbit background：

LE: The geomagnetic modulation is obvious, and the background of the low geomagnetic cut-off rigidity (COR) region is significantly higher than that of the high COR region. Due to the presence of a large number of low energy electrons and the scattering of the high energy protons, the blind detector background is not zero in the low energy band and is also subject to geomagnetic modulation. In low energy band, CXB dominates, and at high energy band, particle background dominates.

ME: The particle background dominates the ME background. There is one noise peak locating at the low energy band and another over-threshold signals at the high energy band. The background level is significantly affected by the geomagnetic modulation.

HE: The background of HE is mainly caused by the particle background that can be divided into delayed and prompt components. The delayed background has gradually increased and becomes saturated with the operation of the satellite. The prompt background is significantly affected by the geomagnetic modulation.

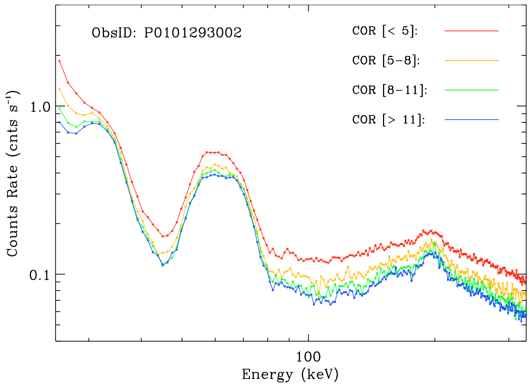

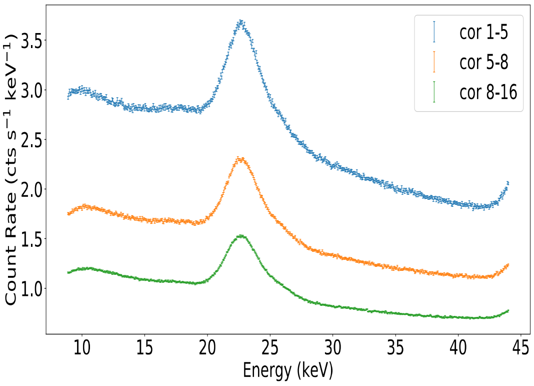

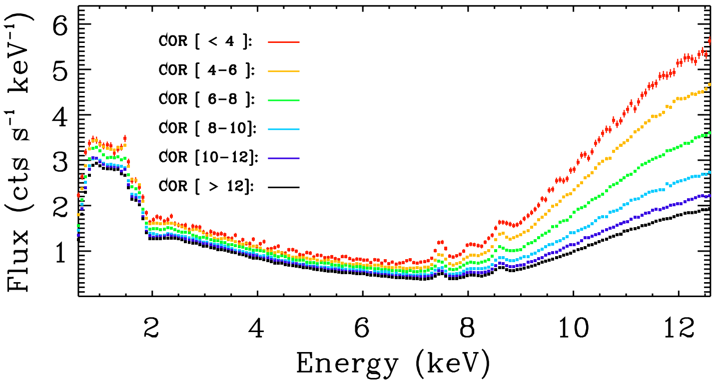

Fig. 6-2 Background spectra of the three payloads (upper left: HE, upper right: ME, lower: LE) in different COR range (Liao et al. 2020a, 2020b; Guo et al. 2020).

6.4 In-orbit background model

The low-energy telescopes, medium-energy telescopes and high-energy telescopes carried by *Insight*-HXMT belong to different types of detectors, so that they have different background characteristics as the satellite operate in orbit. Based on the different characteristics of each payload, we constructed the in-orbit background models of HE, ME and LE by the routine observations of the blank sky (~10 times per month and 3 ks for each time).

For the high-energy telescope, we first use the historical background database to obtain the time evolution function of the background of each detector for every channel and every geographic location, and then make a preliminary estimation of the background spectra. Finally, the real-time count rate of the blind detector is used to make a further modification. For the medium-energy telescope, the basic process of background estimation is similar to that of the high-energy telescopes, i.e., the estimated background spectrum is first obtained and corrected by busy detectors. However, due to the weak time evolution characteristic of the ME background, the preliminary estimated background spectra can be directly obtained from the background database. For the low-energy telescope, since the spectral shape of the particle background is basically consistent under different parameter combinations, the background model is more simplified than that of the medium-energy telescopes. We first obtain the particle background spectrum shape through the background database, and then use the blind detector to estimate the intensity. For the diffuse background in LE low-energy band, it can be estimated through the Galactic plane scanning survey and the pointing observations of the blank sky at high Galactic latitude.

Generally, *Insight*-HXMT performs the pointing observation with the on-axis observation mode (the target is located at the FOV center), and the blind detector is used as the background-monitoring detector to obtain or modify the intensity of the background energy spectra. For the off-axis observation mode (the target deviates from the FOV center and locates only in the FOV of several detectors), the detectors with no target in FOV are used as the background-monitoring detector. The background model can give the relation between the background monitoring detectors and the source observation detectors under various physical parameters (e.g., geographical location, space environment, detector status) in different observation periods. Under an exposure of 2 ks, the systematic error for HE background estimation (26-100 keV) is ~2.6%, and ~1.9% and ~3.2% for ME (8.9-44 keV) and LE (1-10 keV), respectively. Fig. 6-3, Fig. 6-4, and Fig. 6-5 are several examples of background estimation of HE, ME and LE under different exposures, respectively.

For more details in this chapter, please refer to Liao et al. (2020a,2020b), Guo et al. (2020).

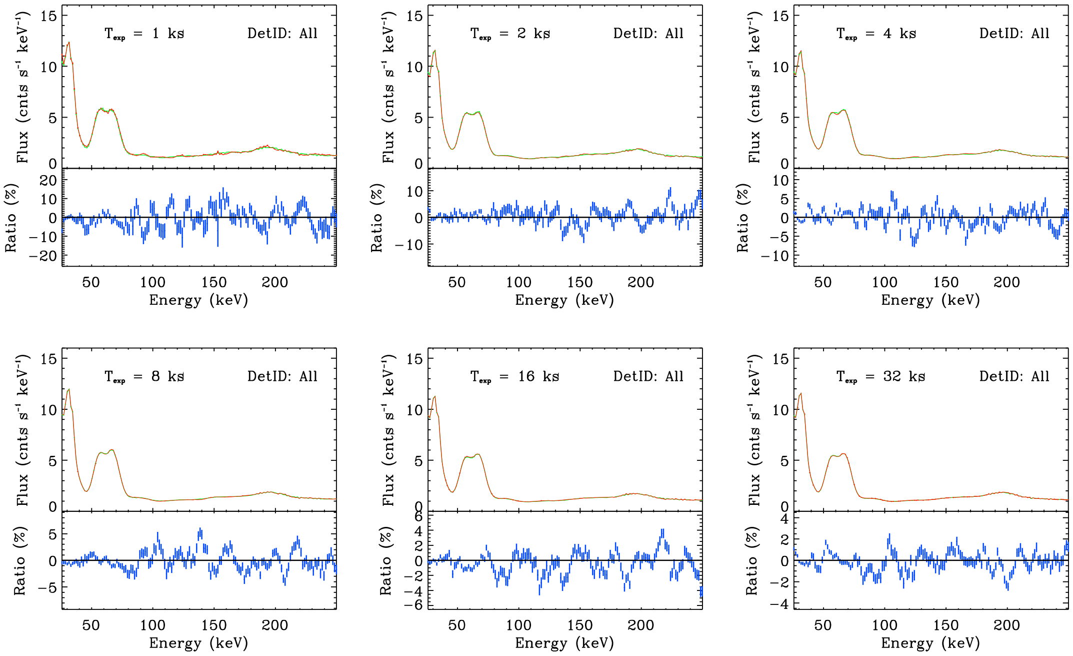

Fig. 6-3 Examples of the HE Background spectra estimation with the exposures 1 ks, 2 ks, 4 ks, 8 ks, 16 ks and 32 ks. Top: green is observational spectra and blue is estimation; bottom: Ratio of the residual and the data.

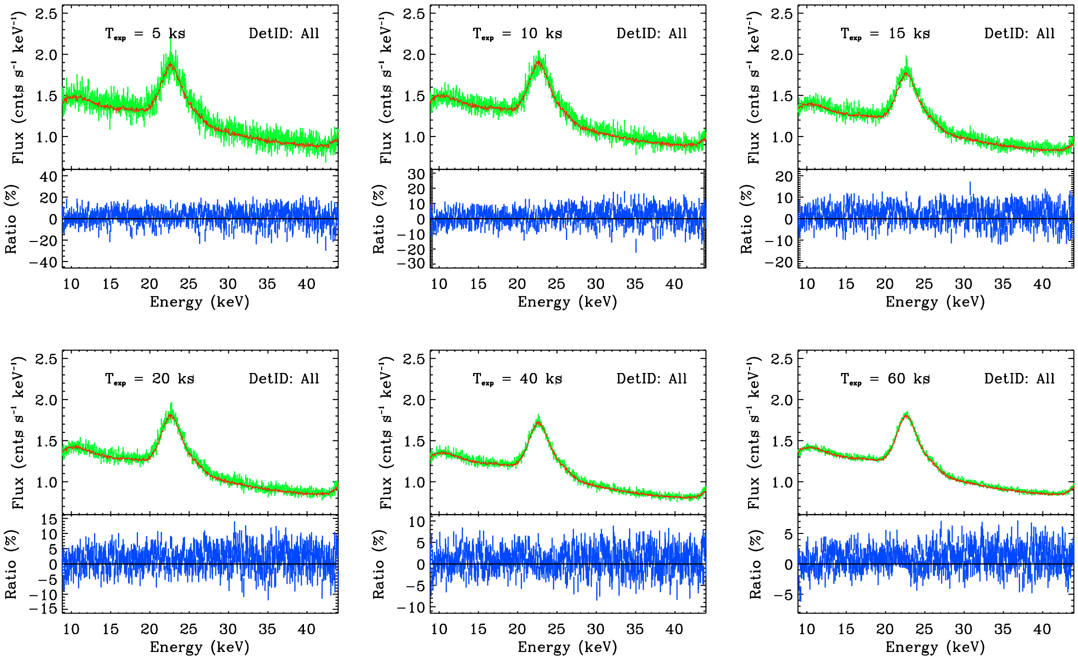

Fig. 6-4 Examples of the ME Background spectra estimation with the exposures 5 ks, 10 ks, 15 ks, 20 ks, 40 ks and 80 ks.. Top: green is observational spectra and blue is estimation; bottom: Ratio of the residual and the data.

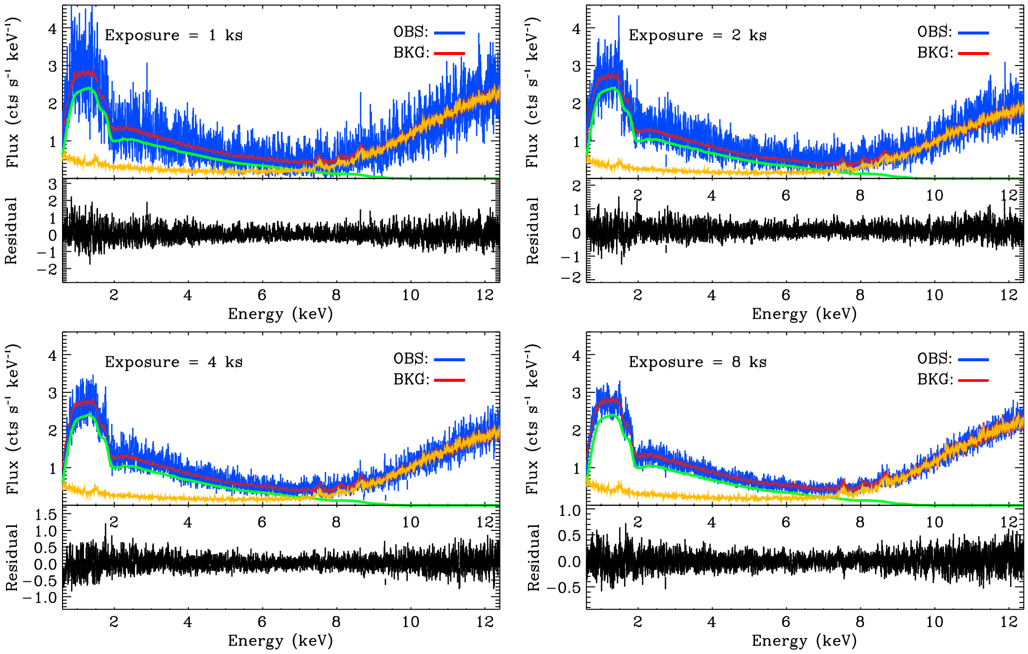

Fig. 6-5 Background spectra test with the exposures 1 ks, 2 ks, 4 ks and 8 ks. Top of each panel: blue is the observed spectrum of a blank sky; red is the estimated background spectrum that is composed of the CXB spectrum (green) and the particle background spectrum (yellow). Bottom of each panel: residual of the background spectra estimation.

7 Detector response

For the details of this chapter please refer to Li et al. (2020), Luo et al. (2020), Zhao et al. (2019), Xiao et al. (2020), Lu et al. (2020), Nang et al. (2020) and Tuo et al. (2022).

The operation of *Insight*-HXMT over the past five years has given us a better understanding of the evolution of the instrument performances, which can be found in three important papers on this evolution published in RDTM. Li et al. RDTM, 2023; Tan et al. RDTM, 2023; Li et al. RDTM, 2023.

7.1 In-orbit gain and energy resolution calibration

When the blank sky or the occulted area of the Earth is observed by the HE detectors, four lines will appear on the measured energy spectra, as shown in

Fig. 7-1. These lines are caused by the activation of the detector materials and can be used for the EC calibration. Because NaI(Tl) crystals are affected by deliquescence on the ground, the energy resolution of all detectors is worse than that during the ground calibration. The width of the 31 keV line is used to evaluate the in-orbit energy resolution of the HE detectors.

The peak centroid of 191 keV line and 59.5 keV line from the ^{241}Am source are utilized to monitor the energy scale of HE. The width of 59.5 keV line from ^{241}Am source are also used to monitor the energy resolution of HE as shown in Fig. 7-2 and Fig. 7-3.

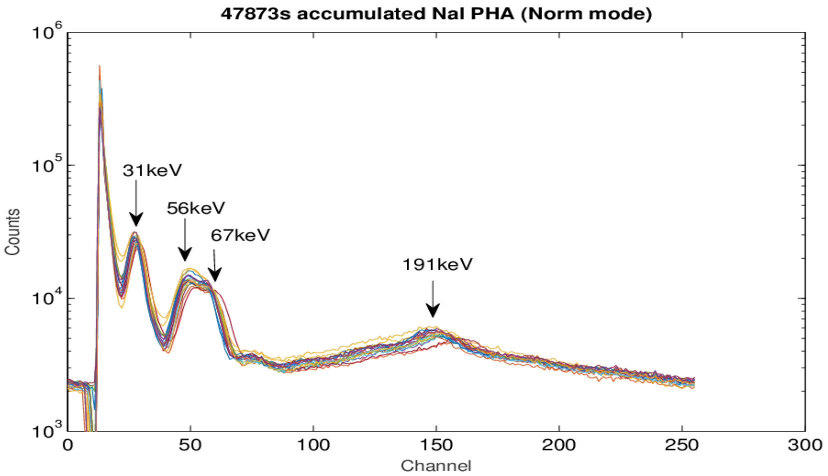

Fig. 7-1 Energy spectrum of 18 NaI(Tl) crystals measured by HE in the observation of blank sky. Four spectral lines are used to calibrate the in-orbit gain (Li et al. 2020).

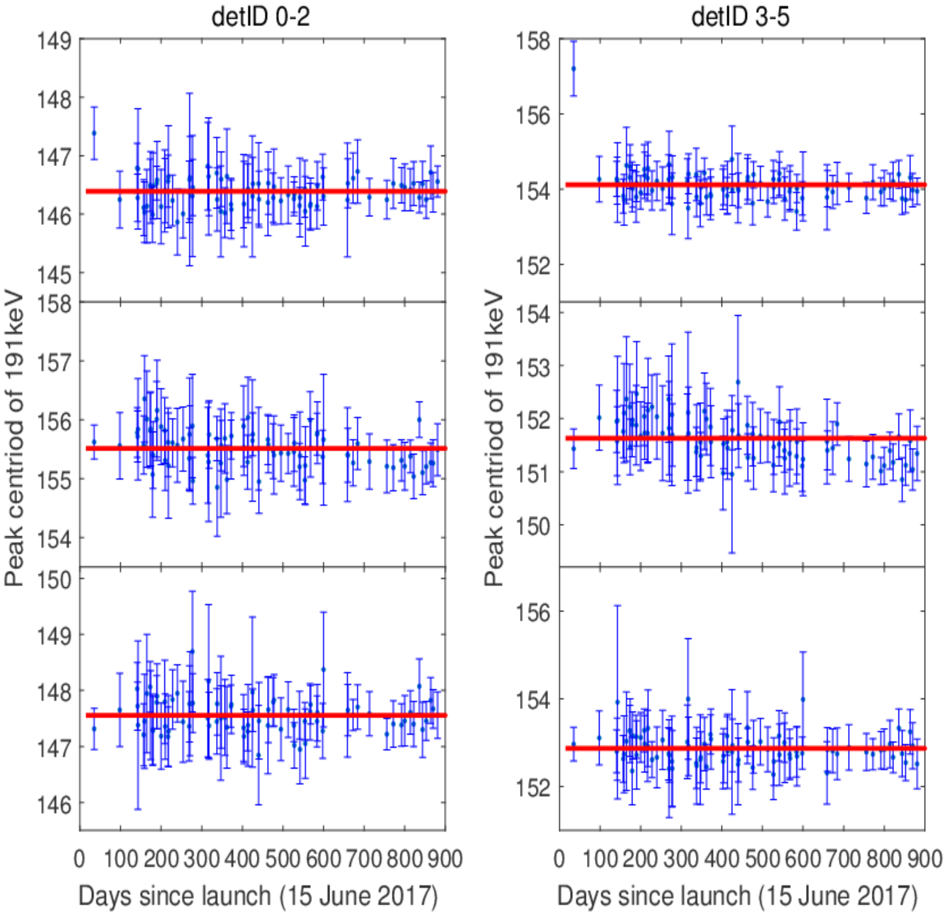

Fig. 7-2 the peak centroid of the 191 keV line versus time for detID 0–5 (Li et al. 2020).

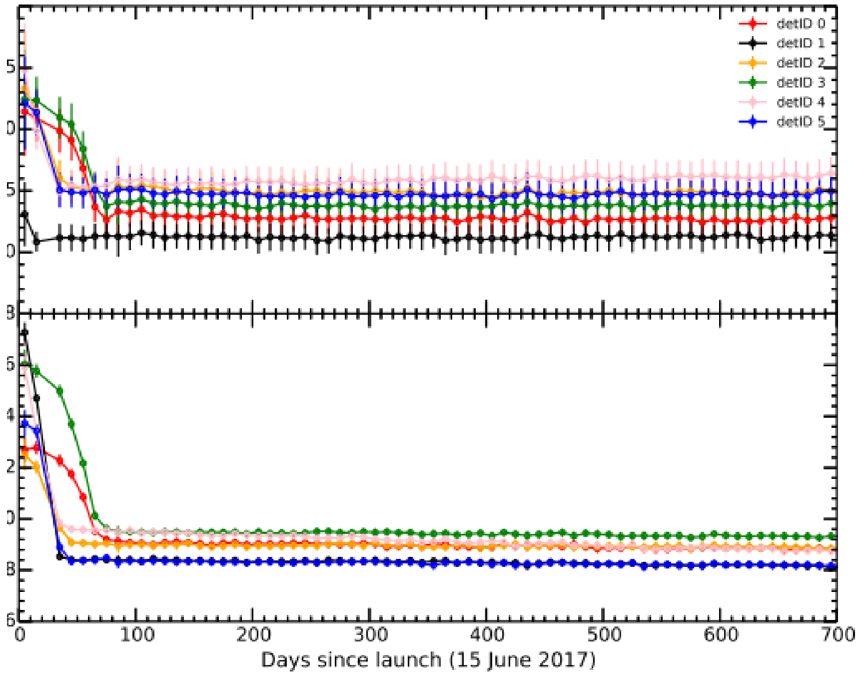

Fig. 7-3 The top panel shows the peak centroid of 59.5 keV from 241Am versus time for detID 0–5. The bottom panel shows the sigma of 59.5 keV from 241Am against time for detID 0–5. After about 90 days in-orbit, the peak centroids and sigma become stable at 0.01 channel and 0.02 channel, respectively (Li et al. 2020).

Each ME detector box contains two ^{241}Am sources which can continuously illuminate 8 Si-PIN pixels. The blank sky spectrum can be accumulated to obtain the peak centroids and widths of four radioactive lines from ^{241}Am source using the pre-launch EC. The spectrum of other pixels not illuminated with ^{241}Am sources are also generated from blank sky data to fit the Ag peak (22.5 keV). As shown in Fig. 7-4, the peak values of the five lines increase slowly with time. A linear function is used to fit the evolution of the five lines respectively. They increase by less than 1% till now. In the current status of software (HXMTDAS V2.04), this effect is not corrected in the gain for this small and slow change. But in the next software update, this effect will be added.

The FWHM of the ^{241}Am line is plotted as a function of time as shown in

Fig. 7-5. Although, there are some structures due to the effect of temperature, the change is very small. The resolution has increased by 0.5% till 700 days in orbit. Therefore, the resolution measured on ground can also be used for the in-orbit data for all the pixels.

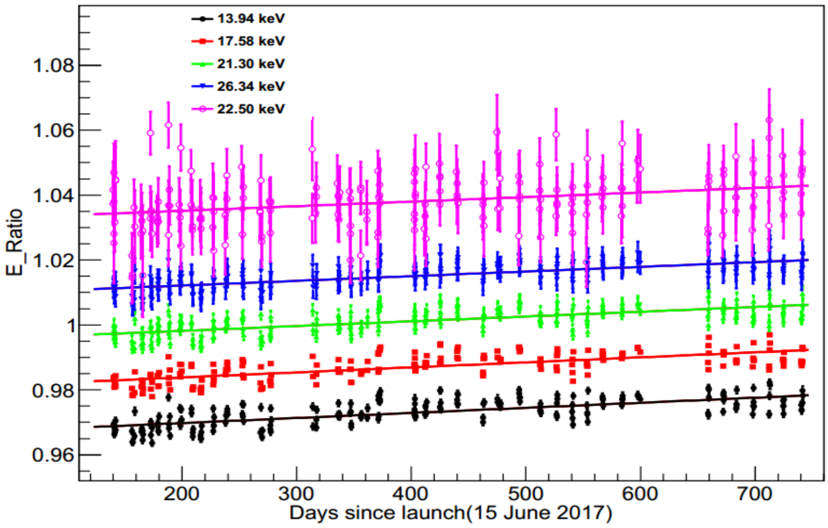

Fig. 7-4 Peak centroids of four lines form 241Am and Ag line versus time. The energy peak has scaled with a different constant. A linear fit is used to describe the evolution of the five lines (Li et al. 2020).

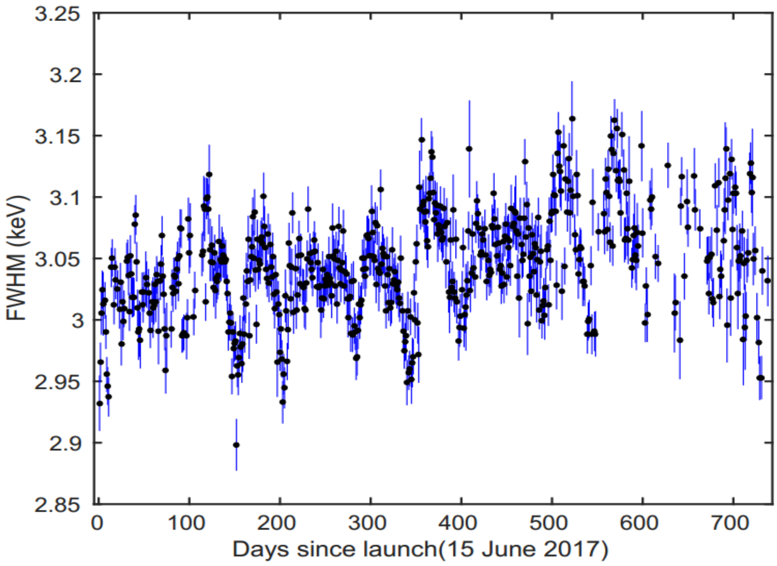

Fig. 7-5 the FWHM fit (with 1σ error bars) to the 241Am line in detector box0 versus time. The resolution has increased by 0.5% till 700 days after launch (Li et al. 2020).

LE uses the line peaks of supernova remnant Cas A and blank sky spectrum to check the EC relationship measured by ground calibration experiments of LE. Using *XMM*/MOS observation data of Cas A, the expected energy of each line is obtained. The difference between the expected peak energy of each line and the energy obtained from the ground EC relationship at different observation time is not linear, as shown in

Fig. 7-6. From Fig. 7-7, all the peaks of Cas A decrease gradually. In order to describe the evolution, a quadratic polynomial function is used to fit the change. From the fit result as shown in

Fig. 7-6, the peak values can be obtained on any day even when Cas A is invisible due to the observation constraints. According to the residual shape shown in

Fig. 7-6, a cubic function is used to describe the gain model of LE,as shown in Fig. 7-8.

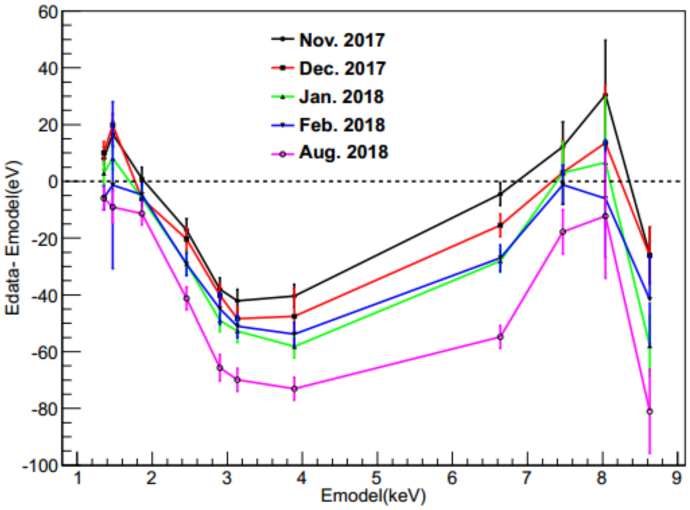

Fig. 7-6 the difference of the energy between data and model for Cas A lines (Li et al. 2020). The data energy is fitted by spectrum used the pre-launch EC of LE. Different color line means the fit result on different observation date.

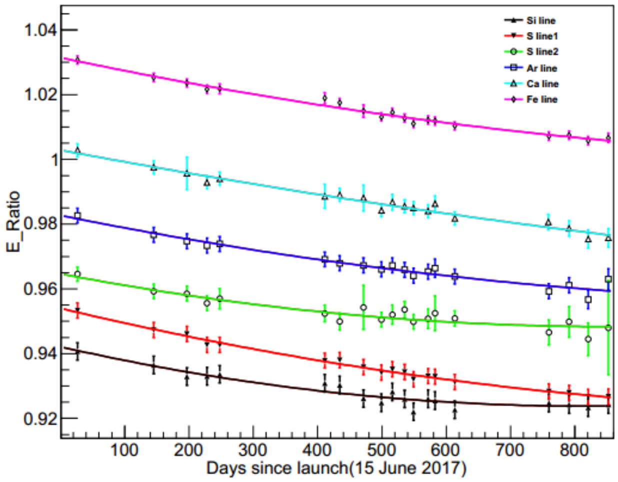

Fig. 7-7 Energy fit (with 1σ error bars) to Cas A. The peak of the lines decreased with time. A quadratic polynomial fit is used to describe the evolution (Li et al. 2020).

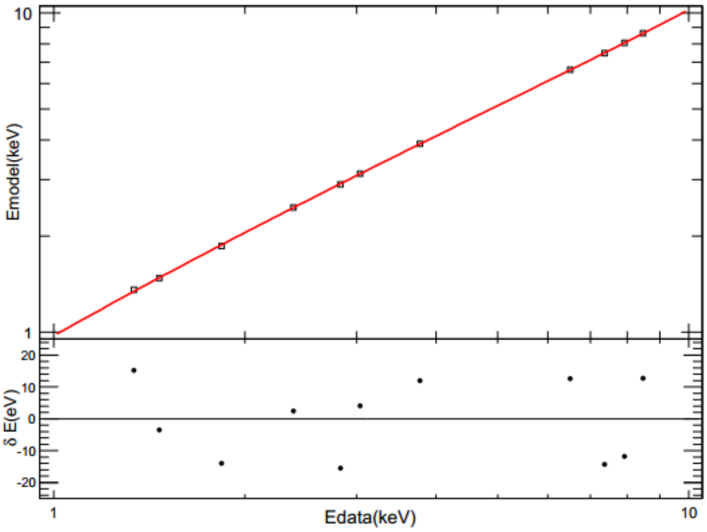

Fig. 7-8 A cubic function is used to fit the in-flight energy gain of LE. The x-axis is the line energy from the evolution fit as shown in Fig. 7-7. The y-axis is the corresponding model energy from XMM/MOS. The fit errors of the line energy peaks are small and thus ignored. The bottom panel shows the residuals of the fit result (Li et al. 2020).

The widths of Si, S and Fe using the pre-launch response file of LE are jointly fitted with data of *XMM*/MOS. If the energy resolution of LE remains the same as that measured on ground, the intrinsic width of Si, S and Fe will be same as the fit result of

XMM/MOS. Actually, the fitted intrinsic widths of Si, S and Fe for LE are larger than that of *XMM*/MOS, so the energy resolution has also changed, compared with the pre-launch calibration results. After subtracting the intrinsic widths of Si, S and Fe from the fit result of *XMM*/MOS, the extra broadening of the resolution of LE is obtained and it evolves with time and temperature. In order to parameterize the extra broadening of LE, we define the two-dimensional function as shown in

Fig. 7-9.

The function (Sigma (eV) = A × E + B) is used to describe the extra broadening in orbit as plotted in Fig. 7-10.

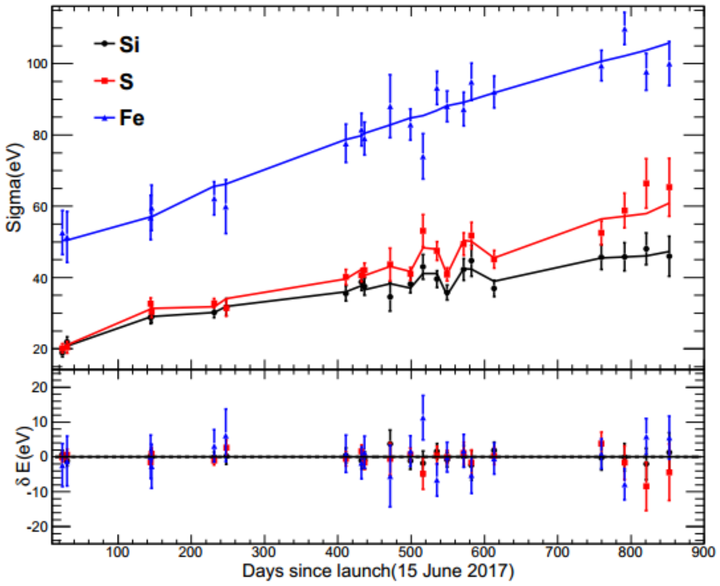

Fig. 7-9 Extra broadening of the widths of Si, S and Fe plotted against time at different observation temperature. In the lower panel, the residuals of the fit are plotted against time for the lines of Si, S and Fe respectively. The differences between data and model are less than 10 eV (Li et al. 2020).

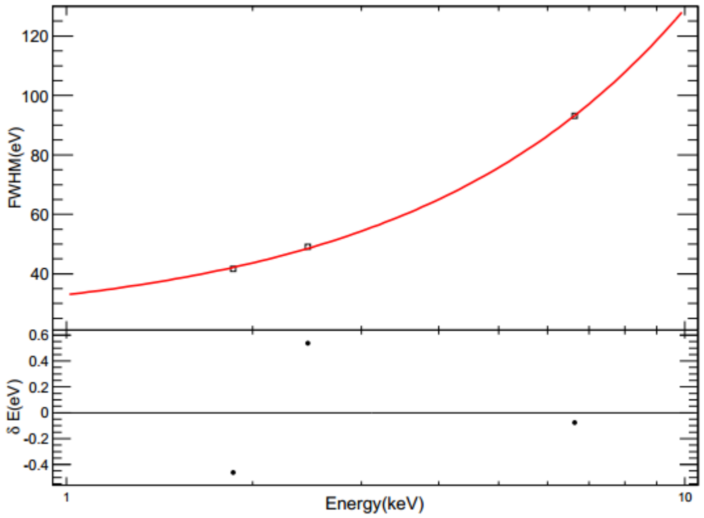

Fig. 7-10 A linear function is used to describe the extra energy broadening of LE at different energies. The fit errors of the extra broadening are small and thus ignored. The bottom panel shows the fit residuals (Li et al. 2020).

7.2 Calibration of the effective areas

The Crab has served as the primary calibration source for many hard X-ray instruments because of its brightness, relative stability, and simple power-law spectrum over the band from 1 to 100 keV (normalization factor is 8.76 keV^{-1} cm^{-2} s^{-1},photon index is 2.11, the neutral absorption parameter is 0.36×10^{22} cm^{-2}). As a collimated telescope, *Insight*-HXMT has a high background level and does not suffer from pile-up, the Crab therefore remains the best choice for its calibration in the X-ray band covered by its three telescopes.

After launch, when we use the new resolution to simulate the effective areas, there remain systematic residuals in the Crab spectrum. As plotted in panel (b) of Fig. 7-11, it shows the ratio of the net data to the Crab model. The ratio shows several features that indicate the inaccuracies in the simulation of the effective areas and the estimation of the background. The background levels of the three instruments are also plotted in panel (a) of Fig. 7-11. Finally, it is decided to use an empirical function f (E) to modify the simulated effective areas. We optimize the empirical function and make the residuals in an acceptable level as shown in panel (c) of Fig. 7-11. The residuals are typically less than 2% in most energy bands.

The systematic errors of HE, compared to the model of the Crab nebular, are less than 2% in 28–120 keV and 2%–10% above 120 keV. The systematic errors of ME are less than 1.5% in 10–35 keV. The systematic errors of LE are less than 1% in 1–7 keV except the Si K–edge (1.839 keV, up to 1.5%) and less than 2% in 7–10 keV.

On June 25, 2020, the LE threshold was adjusted to reduce the effect of detector noise, resulting in a very large variation of the effective area below 1.8 keV due to the temperature. Therefore, we recommend the effective energy band of LE is 2-10 keV after June 25, 2020.

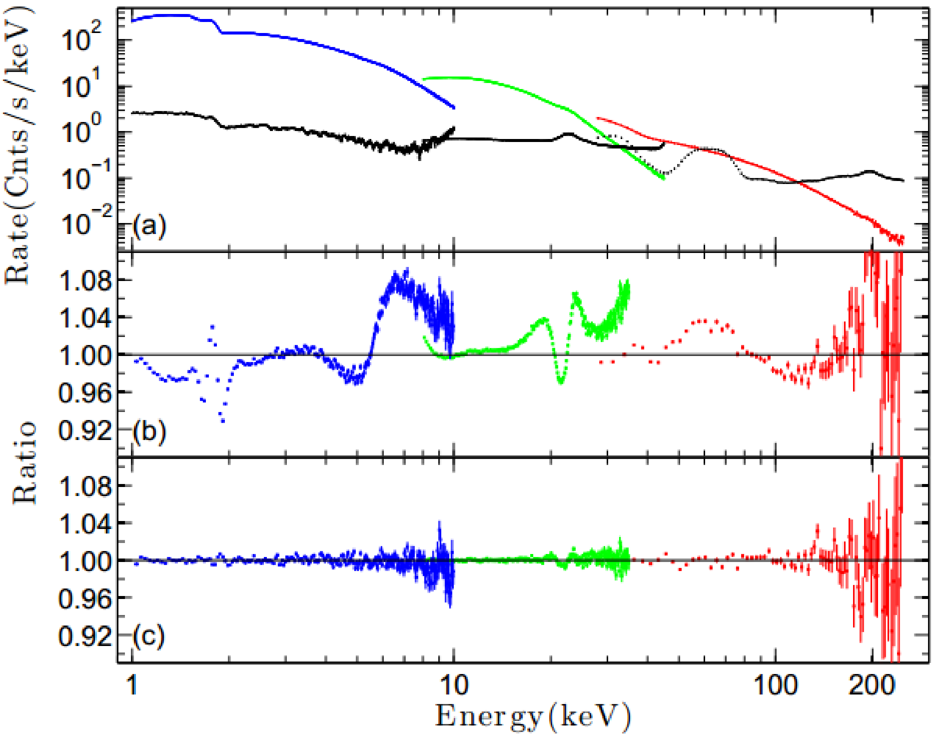

Fig. 7-11 Panel (a) are the background-subtracted Crab spectra measured by LE (Blue), ME (Green) and HE (Red, summed over 17 un-blinded detectors) and the black lines are the estimated background spectra for the three detectors. The lower panels (b) and (c) show the ratio of the data to the Crab model before and after the effective areas calibration (Li et al. 2020).

7.3 Calibration of PSF

The PSF calibration of HE, ME and LE is completed using the in-orbit data from the small-area scan of Crab. Using the new PSF results, the systematic errors of HE, ME, LE are reduced from 14.8%, 3.8% and 5.7% to 1.8% 1.6% and 2.7%, respectively (as shown in Fig. 7-12).

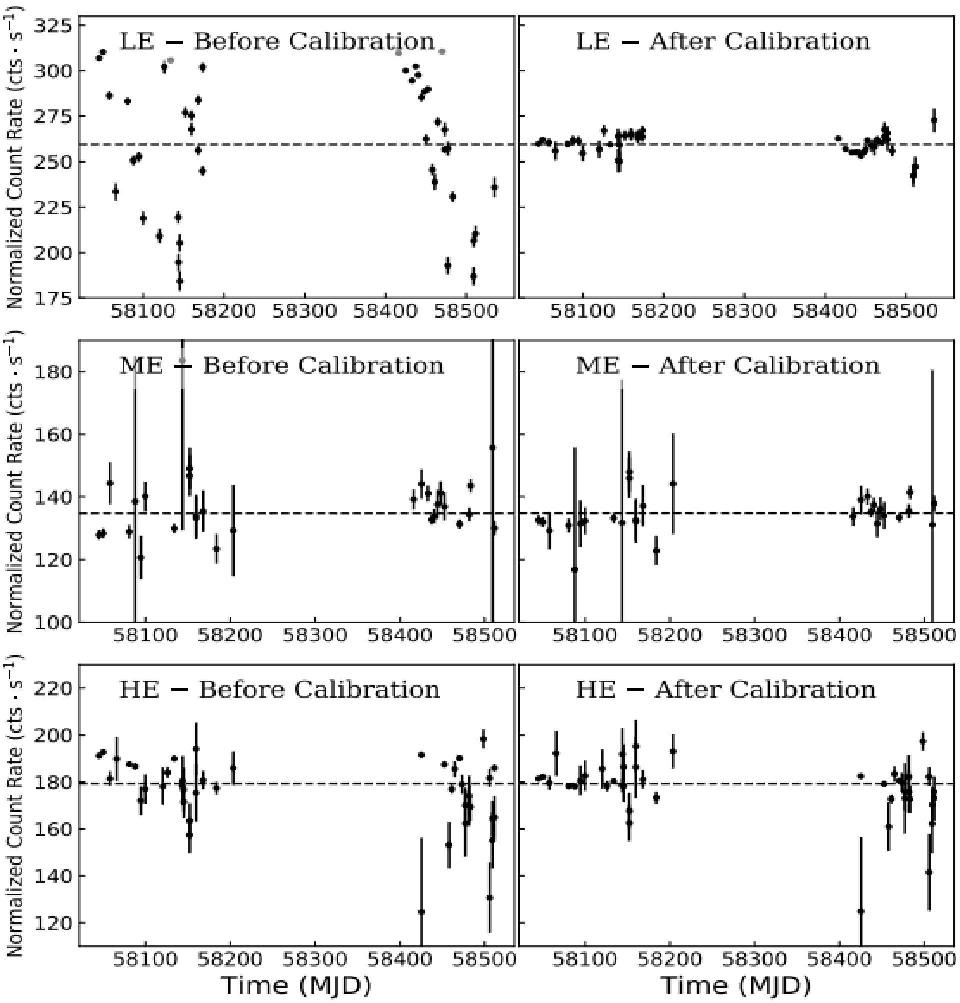

Fig. 7-12 Flux monitoring curves of Crab for the three instruments before and after the PSF calibration (Nang et al. 2020).

7.4 Calibration of the time accuracy

Based on the typical time response of the HXMT satellite hardware system, the offsets of time systems of the three payload are estimated as HE: 156 ns, ME: 334 ns, and LE: 864 µs, respectively. Through the simultaneous observation data of the Crab nebula with the NICER satellite, the ephemeris parameters of Crab during the synchronous observation period are confirmed, and HXMT use the ephemeris parameters to obtain the pulse profile of Crab in 12 observations. By comparing the arrival times and errors of the main pulses under different observations, we derive the systematic errors of the three payload time systems and the delays of different energy bands with respect to NICER as shown in Fig. 7-13. The delay of NICER relative to the radio is known, so the delay times of X-ray photons at different energies relative to the radio can be obtained as shown in Fig. 7-14 . Due to the large effective areas of HE, HXMT provides a high accuracy Crab main pulse arrival time with energy dependence of 0.26 ± 0.02 µs/keV (Tuo et al. 2022).

The Timing Errors of Insight-HXMT Payloads with Respect to NICER

Payloads	Mean Phase	Systematic Error (μs)	Statistic Error (μs)	Offset (μs)
NICER	0.999172	5.5	0.9	0
HE	0.999904	12.1	1.5	24.7
ME	0.999472	8.6	1.9	10.1
LE	1.02483	15.8	2.1	864.7

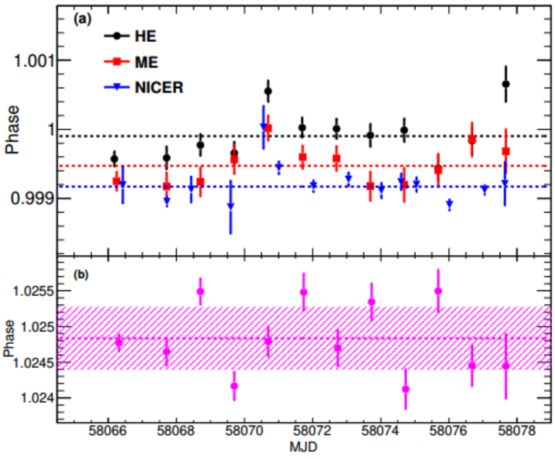

Fig. 7-13 The error of the time system of HXMT and the time delay relative to NICER are obtained by joint observations of the Crab nebula with NICER (Tuo et al. 2022).

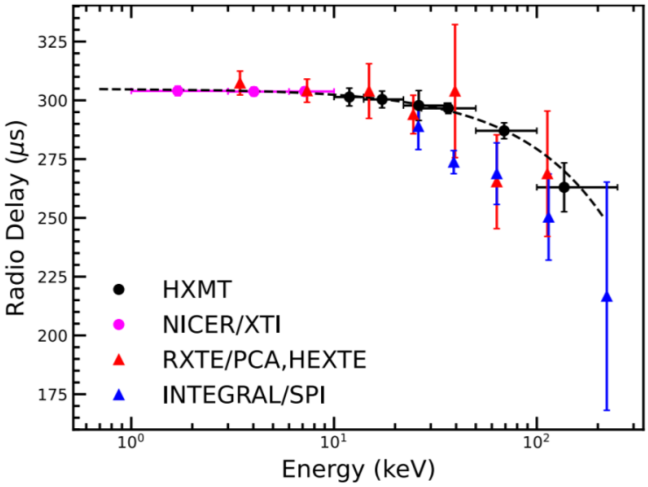

Fig. 7-14 The time delay of Crab's radio band with respect to X-ray photons at different energies. HXMT provides a high-precision dependence of the Crab nebula main pulse arrival time on energy: 0.26 ± 0.02 µs/keV (Tuo et al. 2022).

8 Ground Segment

8.1 Introduction

This section is taken from Jia et al. (2018), Zhang et al. (2018) and Zhang et al. (2020). The ground segment is one of the five major systems of the *Insight*-HXMT mission. It is divided into two branches: mission support branch and scientific application branch. The mission support branch includes: mission operation center, ground receiving center, data pre-processing and quick-look center, data archive management and release center, while the National Space Science Center of the Chinese Academy of Sciences is responsible for this branch. The scientific application branch includes: *Insight*-HXMT science operation center (HSOC), *Insight*-HXMT high level data production processing and calibration center (HDPC), *Insight*-HXMT science user center (HSUC) and *Insight*-HXMT science support center (HSSC), which are built and operated by the Institute of High Energy Physics, see Fig. 8-1.

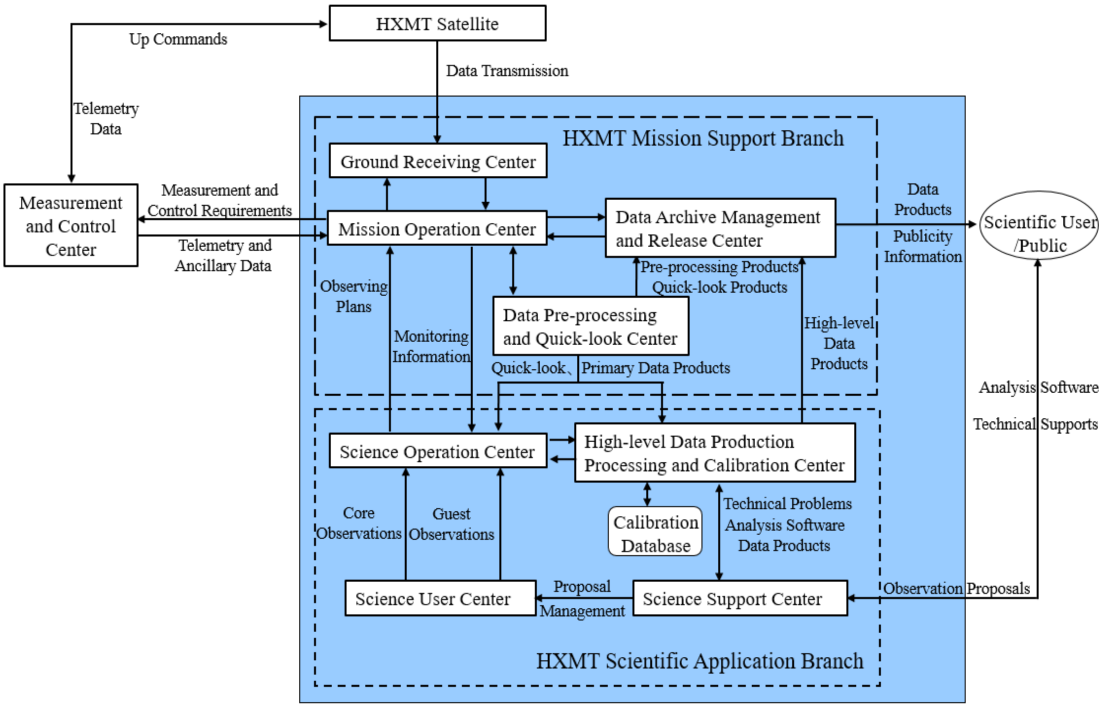

Fig. 8-1 the organization of *Insight*-HXMT's ground segment

The observation proposals (annual proposals and *ad hoc* proposals) are collected by HSUC, and the scientific assessment and technical feasibility assessment are done by HSSC and HSOC, respectively. In addition, HSOC makes long-term and short-term observation plans for the approved proposals. The plans will be converted to satellite instructions and submitted to TT&C system by the Mission Operation Center, further uploaded onto the satellite for execution.

After an observation is completed, the Ground Receiving Center is responsible for receiving data. After decoding, data will be sent to Mission Operation Center, the data pre-processing and quick-look center. The mission operation center monitors the working state of the satellite with the received data, and the data pre-processing and quick-look center generates primary data products. The satellite performance is analyzed and handled by HSOC. Then various types of data are integrated to generate advanced data products by HDPC who is also in charge of further data archive and release.

8.2 User Support and Service

The *Insight*-HXMT official website (http://www.hxmt.cn) regularly releases important notices or information about the ground segment, including:

(1) Proposals related information:

Call for proposals: including important timeline, notes, etc.

(http://proposal.ihep.ac.cn/proposal/index.jspx)

Proposal submission: registered users can submit proposals on the website below.

(http://proposal.ihep.ac.cn/proposal.jspx)

Auxiliary tools: Target Visibility Predictor, Observation Time Estimator, Bright source warning tool, and energy spectrum simulation and analysis tools.

(http://proposal.ihep.ac.cn/soft/soft.jspx)

(2) Tasks and plans:

Plan arrangement: long-term and short-term plans for observation tasks (http://hxmten.ihep.ac.cn/ObsPlan.jhtml).

(3) Data release:

Data downloading: includes data that have been publicly released or are still in proprietary period (http://archive.hxmt.cn/proposal).

(4) Software downloading: includes HXMTDAS downloading, instructions of installing and using (http://hxmten.ihep.ac.cn/analysis.jhtml).

(5) Help desk: includes frequently asked questions (FAQ), retrieve existing questions, and consult online (http://enghxmt.ihep.ac.cn/faq.jhtml).

8.3 Observation Planning

HSOC formulates long-term and short-term observation plans according to the target (observation) ranking, observation time and constraints of the observation tasks, and sends them to the task operation center in time.

(1) Long-term observation plan: based on the observation task and time allocation plan approved by the Scientific Committee, schedule all observations during the observing period.

(2) Short-term observation plan: detailed observation arrangements include: observation source information, satellite observation mode, payload working mode, satellite attitude requirements, maneuvering time, path planning, data storage and transmission arrangements, etc., with a period of less than one week.

HSOC regularly publishes the long-term and short-term observation plan information to the website: http://hxmten.ihep.ac.cn/ObsPlan.jhtml.

The scientific objectives of long-term and short-term observation plans mainly come from core proposals, guest proposals and *ad hoc* proposals.

9 Proposals Collection and Observation Plans

9.1 Proposal Classification

The *Insight*-HXMT proposals include annual proposals and *ad hoc* proposals as shown in Fig. 9-1. For annual proposals, it consists of core proposals, guest proposals and calibration proposals.

(1) Core proposals

The core proposals can ONLY be submitted by the core science groups. The proposals should focus on the core science of *Insight*-HXMT, make full use of the advantages of the telescope, and are expected to produce important scientific results. It can include the non-ToO observations and ToO observations.

(2) Guest proposals

The guest proposal is open to the whole international scientific community and thus guest proposals can be submitted by anyone (e.g., no restriction to nationality or affiliation), supplementing the core scientific program of *Insight*-HXMT. It also can include the non-ToO observations and ToO observations.

(3) Calibration proposals

Calibration proposals can ONLY be submitted by instrumental teams and calibration & background teams. It includes calibration observations and background observations.

(4) *Ad hoc* proposals

They are mainly in response to alerts of scientific opportunities discovered by the science quick-look center, the outburst sources reported in Atels or by other equipment, as well as unplanned but needed calibration observations, which are not pre-approved during the call for proposals.

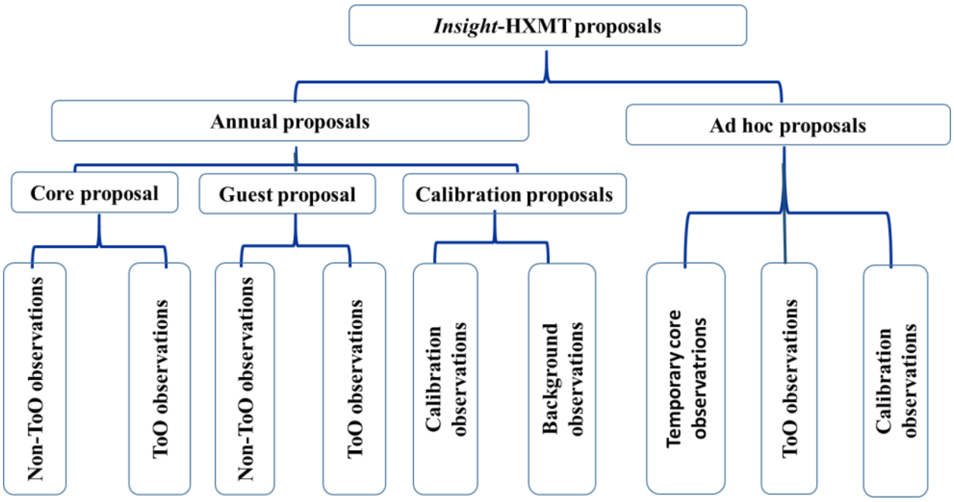

Fig. 9-1 HXMT proposal classification.

9.2 Proposal Collection

This AO is announced on the *Insight*-HXMT Website (http://www.hxmt.cn), and observation proposals will be collected through the proposal collection interface before the due time (http: //proposal.ihep .ac.cn/proposal/index.jspx).

After a proposal is submitted, the proposers can query the status of the proposal through the “Proposal list” on the application interface, including whether it has been submitted and passed the evaluation.

After the collection period is over, the science user center will transfer the observation proposals (proposal database) to the science research support center and carry out the following proposal evaluation work.

9.3 Proposal Evaluation

Proposal evaluation includes two processes: technical evaluation and scientific evaluation.

(1) Technical evaluation

The HSOC will organize technical evaluations. A technical evaluation report for each proposed observation in each proposal will be provided, including the visibility, effective observation time, various constraints, etc. For all proposed observations in all proposals, a comprehensive evaluation report (includes annual effective observation time, observation time required for the proposals, statistics on various proposals, proposals that may conflict with time requirements, etc.) will also be given.

(2) Scientific evaluation

Taking the results of the technical evaluation as reference, the scientific peer review panel evaluates the proposed observations and ranks them, focusing on the scientific value of the proposed observations. All accepted targets with observation requirements are ranked into A, B, C, and D grades. “A” will certainly be observed; “B” will most likely be observed; “C” might be observed depending on the available time allocation; and “D” will only be observed occasionally. If a conflict occurs, the observing priority will be assigned based on the ranking. Unobserved A targets will be automatically included in the observation plan of the next cycle. All unobserved B, C and D targets and untriggered ToO observations will not be automatically included in the observation program of the next cycle, but may be proposed again in the next cycle.

The science research support center will feedback the evaluation results to the proposers, as well as make the results publicly available. The approved targets with observation requirements will be sent to the HSOC for observation scheduling.

The processing flow for annual proposals is shown in Fig. 9-2, and the processing flow for ad hoc proposals is shown in Fig. 9-3.

The processing of *ad hoc* proposals is led by the HSOC, and scientific assessment is completed by the scientific committee.

After the annual proposal collection is over, only the *ad hoc* proposal collection interface will be open to the public. The processing flow of the *ad hoc* proposal is:

(1) ToO and other *ad hoc* proposals are submitted through the website;

(2) The reminder function of the *ad hoc* proposal database is set up. Once there is a new proposal, the relevant personnel of the HSOC will be notified by email and SMS;

(3) HSOC is responsible for the *ad hoc* proposal processing:

For each proposed observation, HSOC will determine whether it is a pre-approved ToO observation firstly. If the ToO observation is pre-approved and its technical assessment is passed, the center will start to formulate a temporary observation plan for this observation.

If it is not a pre-approved ToO observation, HSOC will carry out technical evaluation, and at the same time notify the scientific committee to carry out scientific assessment, and formulate a temporary observation plan after the proposed observation is approved, then feedback evaluation results to the proposer;

(4) When necessary, HSOC coordinates MOC and TT&C system for an emergency TT&C channel, and sends the formulated temporary observation plan to MOC;

(5) Post the temporary observation plan with relevant information to the website.

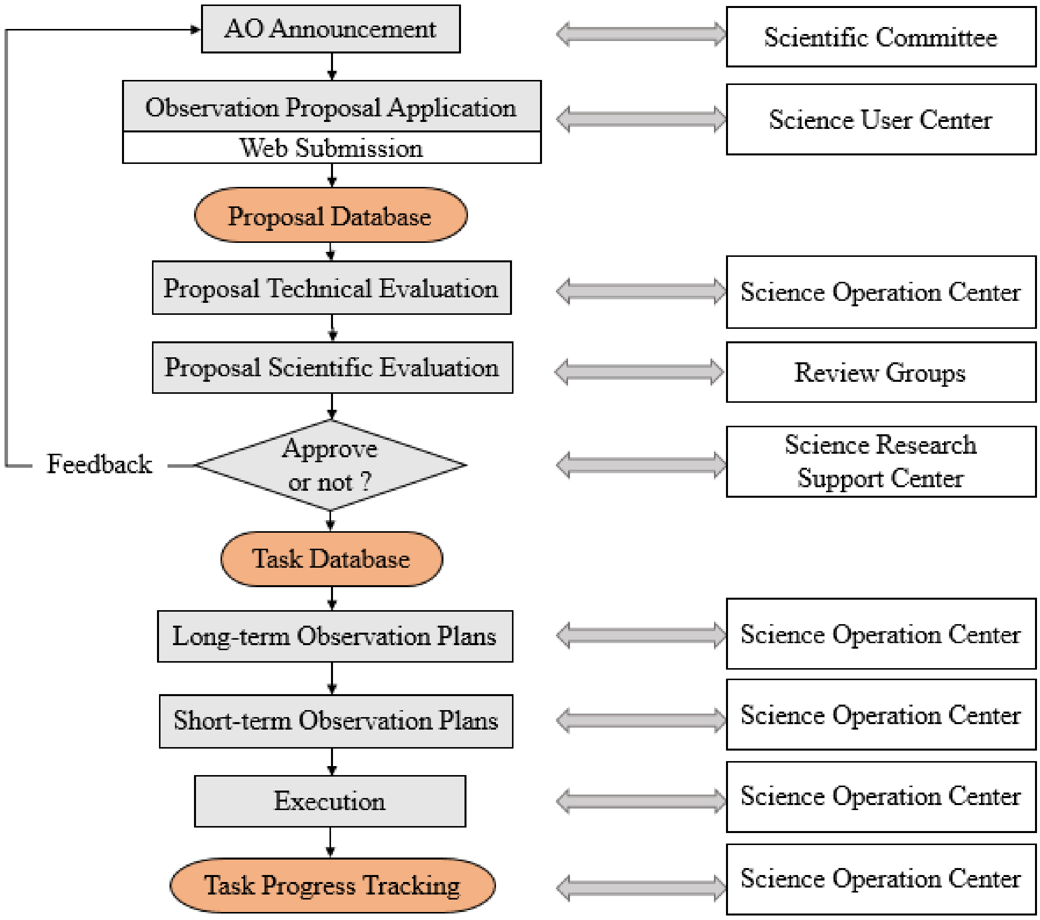

Fig. 9-2 the annual observation proposal processing flow.

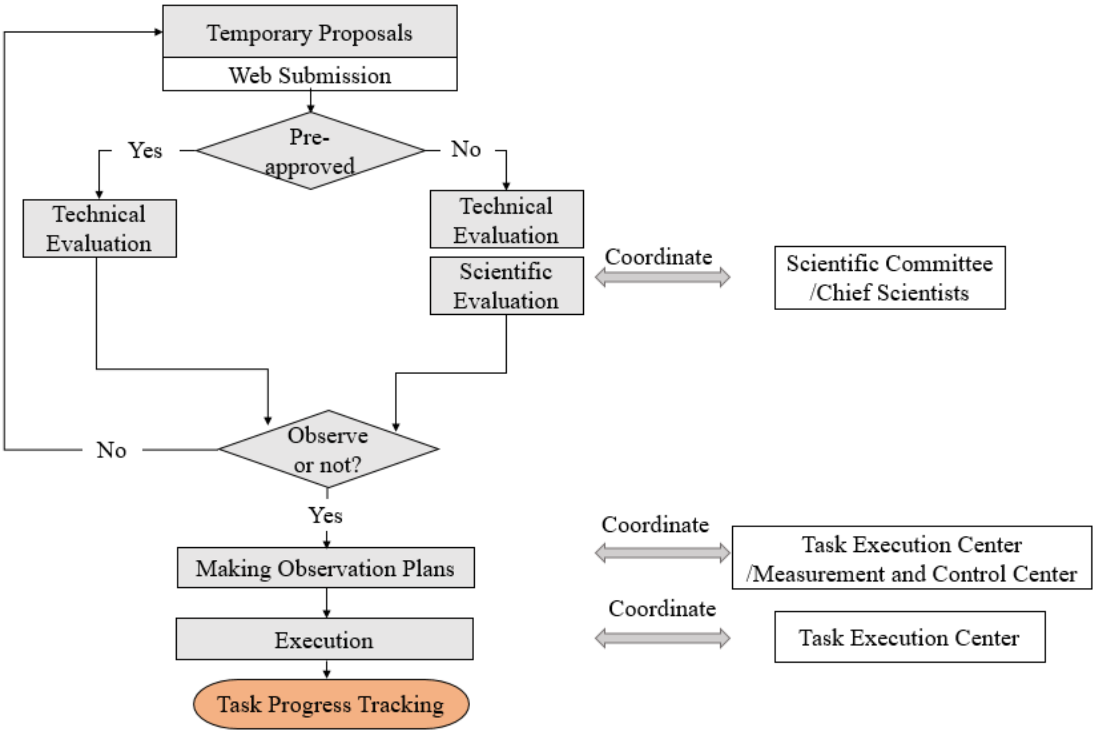

Fig. 9-3 the *ad hoc* proposal processing flow.

10 Proposal Tools

10.1 Basic requirements for *Insight*-HXMT observation proposals

An observation proposal needs to include the following sections.

(1) Title

(2) List of proposers and collaborators

(3) Author affiliation

(4) Abstract

(5) Observation request: it includes the observation mode (pointing or small area scan), the target information, the requirement of the exposure duration and observation constraints, et al.

(6) Feasibility analysis of the target

Upload the attachment of the feasibility analysis for EACH target. The template can be download here: http://enghxmt.ihep.ac.cn/doc/282.jhtml.

(7) Proposal form

Upload the attachment of the proposal. The template can be download here: http://enghxmt.ihep.ac.cn/doc/282.jhtml.

Note:

(1) The proposers should run the exposure estimation software to estimate the required exposure to reach certain detection significance.

(2) The energy spectrum simulation analysis tool shall be used to estimate the required exposure to obtain the required quality of the energy spectrum; all necessary figures and tables shall be included.

(3) It is necessary to analyze how the proposed observation makes use of which unique capability or advantage of *Insight*-HXMT, and make comparison with other X-ray telescopes currently in operation.

(4) It is necessary to explain on how to effectively use all the three telescopes, i.e., LE, ME and HE.

(5) For HE, the HV mode must be specified (the normal mode or low-gain mode, i.e., GRB mode).

10.2 Target Visibility Predictor

The Source Visibility Estimation Tool is provided for users to calculate the observation efficiency of *Insight*-HXMT, which can be accessed at: http://proposal.ihep.ac.cn/TargetVisibilityPredictor

This tool gives the time when a certain source can be observed in a selected time period. The development of this tool considers the following factors, which are described as follows:

(1) Sun avoidance angle

For *Insight*-HXMT, the sun avoidance angle is 70 to 180 degrees, that is, the angle between the direction of the HXMT and the sun must be greater than 70 degrees.

(2) South Atlantic Anomaly

When *Insight*-HXMT passes through the anomalous area of the South Atlantic, in order to avoid damage to the instrument, no scientific observation is performed during this period.

(3) Block from the Moon

The apparent angular diameter of the moon is 31′. Considering the field of view of *Insight*-HXMT, the avoidance angle of the moon is 6°; CXB and soft X-ray and visible light pollution are mainly considered.

A screenshot of this tool is shown in Fig. 10-1.

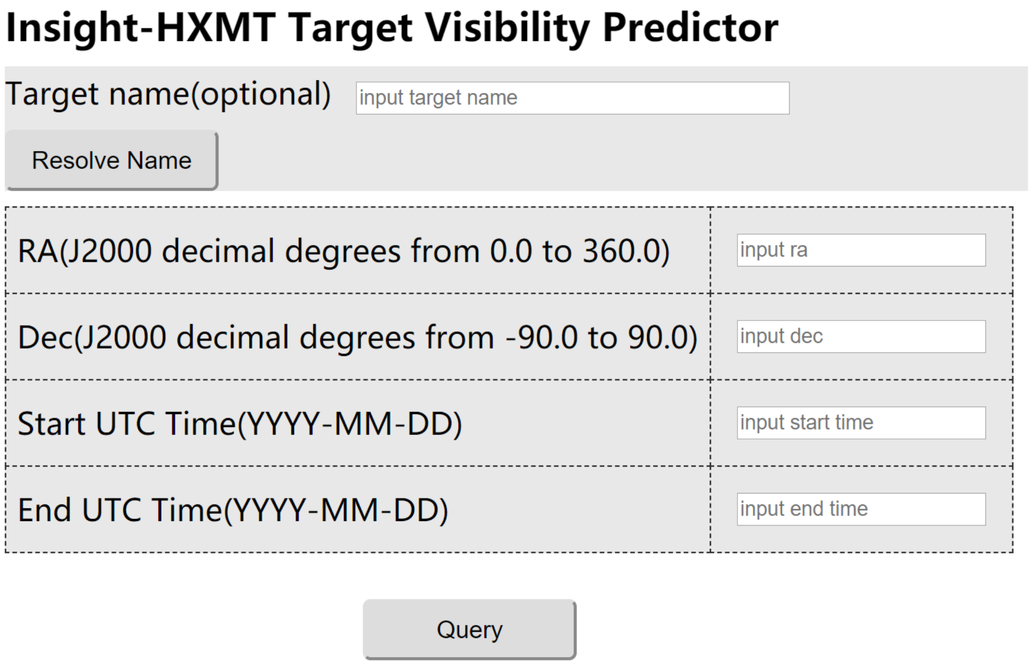

Insight-HXMT Target Visibility Predictor

Target name(optional) input target name

Resolve Name

RA(J2000 decimal degrees from 0.0 to 360.0)	input ra
Dec(J2000 decimal degrees from -90.0 to 90.0)	input dec
Start UTC Time(YYYY-MM-DD)	input start time
End UTC Time(YYYY-MM-DD)	input end time

Query

Fig. 10-1 Screenshot of Target Visibility Predictor Tool.

10.3 Observation Time Estimator

This tool is used to make a rough estimation of the exposure requirements for targets given the spectrum types and fluxes. The observation time estimator can be accessed at the following website: http://proposal.ihep.ac.cn/soft/soft.jspx.

The effective observation time is estimated based on the energy spectrum of the source, the effective area of the detector, and the estimated background. The observation times required to achieve a certain signal-to-noise ratio for the three detectors (HE, ME, LE) are obtained. There are currently two types of energy spectra supported: blackbody and power law. The output of this tool is the result of the conversion between exposure time and detection significance. It is used for the rough estimation of the exposure requirements in the preparation of the *Insight*-HXMT proposal. The detailed exposure estimation can be obtained by using the following spectrum simulation analysis tool. A screenshot of this tool is shown in Fig. 10-2.

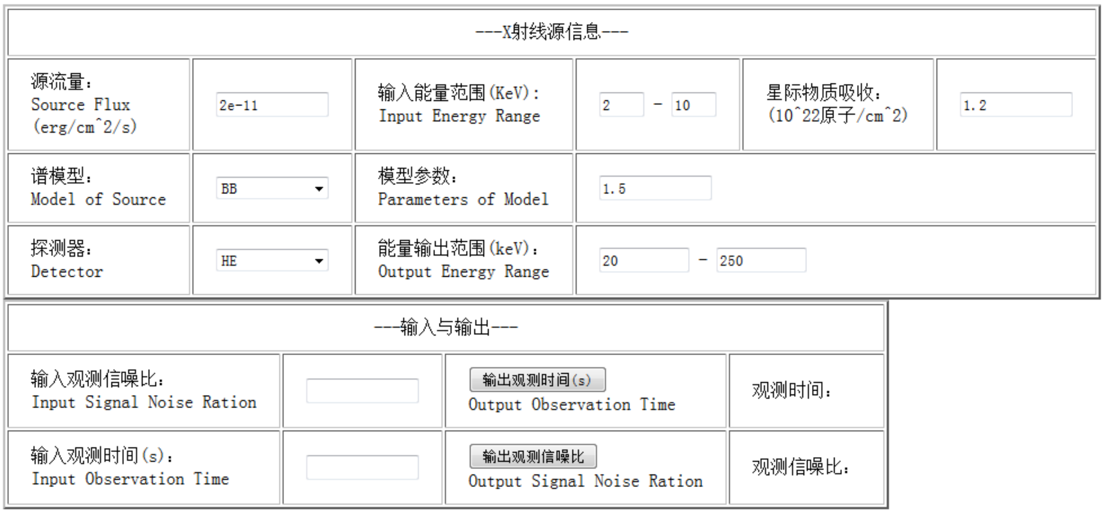

---X射线源信息---

源流量： Source Flux (erg/cm^2/s)	2e-11	输入能量范围(KeV)： Input Energy Range	2 – 10	星际物质吸收： (10^22原子/cm^2)	1.2
谱模型： Model of Source	BB	模型参数： Parameters of Model	1.5		
探测器： Detector	HE	能量输出范围(keV)： Output Energy Range	20 – 250		

---输入与输出---

输入观测信噪比： Input Signal Noise Ration		输出观测时间(s) Output Observation Time	观测时间：
输入观测时间(s)： Input Observation Time		输出观测信噪比 Output Signal Noise Ration	观测信噪比：

Fig. 10-2 the screenshot of the analysis tool for exposure estimation.

10.4 Bright source warning tool

This tool is used to estimate whether any source near the observation target has an impact on the observation, and this tool can be accessed at the following website: http://proposal.ihep.ac.cn/soft/soft2.jspx.

The input of the bright source warning tool is: location of the target source, flux, observation time, and the field of view of detectors. The satellite attitude at the observation time is determined by the solar direction vector at the observation time. The source table is mainly from the Integral reference source table (http://www.isdc.unige.ch/integral/science/catalogue#Reference). This tool only considers the situation of three sets of small fields of view at different orientations for each detector, corresponding to the fields of view 1, 2, and 3 in Fig. 10-3. For HE, only the field of view of 1.1°×5.7° is considered (see Chapter 3 for details). The tool calculates the ratio of the total counts of all other sources in field of view to the counts of the target source.

Only when the total interference source count / target source count is less than 1/3 for the three sets of fields of view at the same time, the “Auto Avoid” considers the period as observable, otherwise it is considered as affected. “View interference source information” can view the name of the source near the target source, and the count rate in the high, medium, and low energy detectors. In “Update Date”, you can move forward or backward by a few days to see if interference can be avoided. The number of days must be an integer.

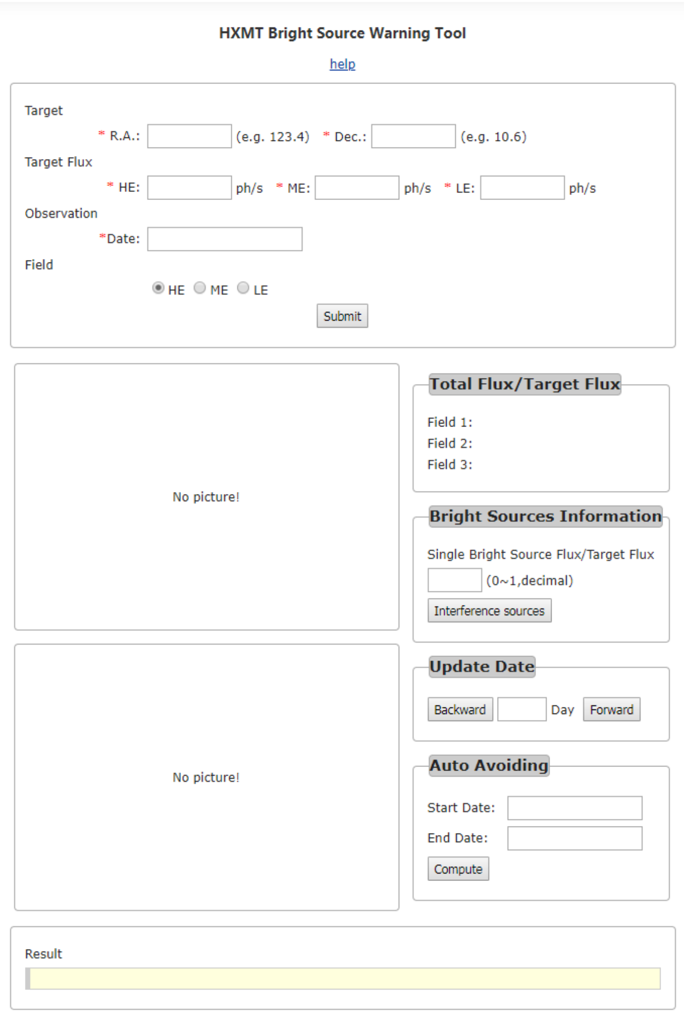

Fig. 10-3 the screenshot of the bright source warning tool.

10.5 Simulate the target source energy spectrum for given exposure time.

The energy bands are as follows: LE: 2–10 keV, ME: 10–35 keV, HE: 28–250 keV.

Note: the energy band of LE has a difference with the last version.

Warning: simulation should be made within the energy bands provided above.

The ‘fakeit’ command in XSPEC of HEASOFT is used for the simulation. The response and background files are packaged in ‘user_spec.zip’, the download website for which is “http://proposal.ihep.ac.cn/soft/soft.jspx”. Example scripts with the suffix ‘.tcl’ are provided in the ‘example’ directory in this package.

We now give an example on how to simulate an observational spectrum for ME. To simplify the example, we assume there is no other source inside the FOV (field of view) for the target source. We further assume the spectrum of the target source is described by a single power-law without interstellar absorption (the ‘powerlaw’ model in XSPEC with PhoIndex of 1.7 and norm of 10 photons keV^{-1} cm^{-2} s^{-1}@1 keV).

Step 0: copy the response and background files into the directory where the simulation will be made.

Those files for ME are in the directory named "ME" in the downloaded package. The file with the suffix ".fits" and contains "bg" in its name is the background spectrum. The files with the suffixes ".rsp" and ".arf" are the response files.

Step 1: run XSPEC and create the spectral model file.

Run XSPEC and enter ‘*mo po*’ to create the spectral model. Then enter the value of each parameter according to the prompt. Finally enter ‘save mo inputmodel.xcm’ to save the spectral model to a file named ‘inputmodel.xcm’. The process described above is shown in Fig. 10-4. Users can choose not to save the ‘inputmodel.xcm’ file, but to run fakeit next. The advantage of saving the ‘inputmodel.xcm’ file is that users need not create the spectral model every time when using it, but can simply enter ‘@inputmodel.xcm’ in XSPEC to load the spectral model easily.

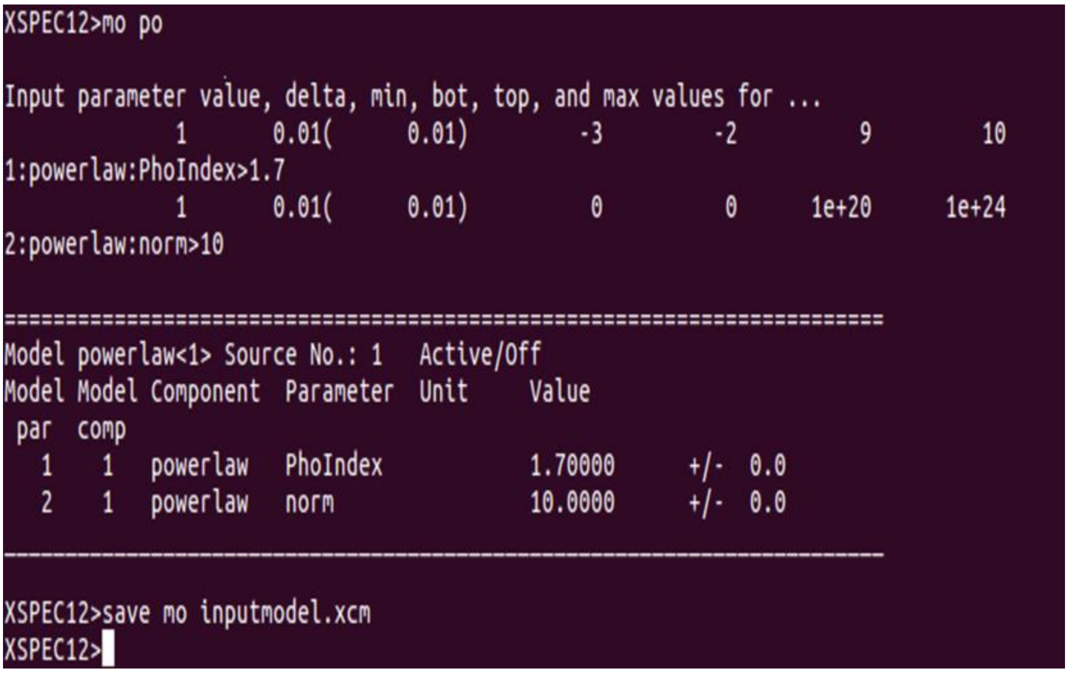

```
XSPEC12>mo po

Input parameter value, delta, min, bot, top, and max values for ...
              1      0.01(      0.01)        -3        -2         9        10
1:powerlaw:PhoIndex>1.7
              1      0.01(      0.01)         0         0     1e+20     1e+24
2:powerlaw:norm>10

========================================================================
Model powerlaw<1> Source No.: 1   Active/Off
Model Model Component  Parameter  Unit     Value
 par  comp
   1    1   powerlaw   PhoIndex            1.70000      +/-  0.0
   2    1   powerlaw   norm                10.0000      +/-  0.0
________________________________________________________________________

XSPEC12>save mo inputmodel.xcm
XSPEC12>
```

Fig. 10-4 the process of creating the spectral model file of the target source.

Since LE, ME, HE are slat-collimated instruments with large FOV (field of view), there might be other sources in the FOV for the target source. To estimate the effect of the nearby bright sources, please refer to Section 10.4. It should be noticed that the intensity of those sources might be variable. The response files provided here are for the case where the target source is located at the center of the field of view. Since interference sources are not at the center of the field of view, the effective areas for them are smaller.

Step 2: use ‘fakeit’ command to simulate the spectrum.

Taking ME for an example, if we want to simulate a spectrum with 10000 s net exposure, after step 1, we may enter the commands below in XSPEC (Note: commands below can be copied from the example script ‘ME.tcl’ in the directory named ‘example’ downloaded. However, they should not be copied directly from this document, because the mismatch of text formats may cause errors, even in the absence of a "warning" message).

First enter:

```
data none;
```

Then enter:

```
fakeit ME_bg.fits & ME_rsp.rsp & ME.arf & y & & ME_tot.fak & 10000,1,10000;
```

(Please note that entering “*data none;*” first can ensure that no spectrum has been loaded before running fakeit this time. Otherwise, if a spectrum has already been loaded in XSPEC, for example, a spectrum generated by running fakeit last time in this same XSPEC window is loaded automatically, fakeit will use the response files of that spectrum instead of those written as parameters in the current fakeit command.

In the above fakeit command, ME_bg.fits is the background spectrum, while ME_rsp.rsp and ME.arf are the response files for ME (the website for downloading them is already provided at the beginning of this section. Please note that the actual effective area is included in ME_rsp.rsp, while the effective area in ME.arf is written as 1 instead). The ‘y’ option means that counting statistics will be used in creating fake data (the corresponding prompt is ‘Use counting statistics in creating fake data?’). Usually we choose ‘y’ for this prompt, because real observations involve counting statistics.)

After running the above fakeit command, two simulated spectra are obtained. One is the total observed spectrum ‘ME_tot.fak’, which includes contributions from both the source and the background. The other is the estimated background spectrum ‘ME_tot_bkg.fak’, which is used to estimate the background in the total spectrum ‘ME_tot.fak’. Those two spectra are enough for users to do spectral analysis. They serve as the input total spectrum and the background spectrum when using XSPEC to fit the spectrum. (A friendly reminder: if the user uses XSPEC to do subsequent spectral fitting and chooses the χ^2 statistic, it is important to notice that the χ^2 statistic requires that the net count of each energy channel involved in the fitting follows a Gaussian distribution, where “net” means the background has been subtracted. In that case, the user may need to bin the spectrum to ensure that the count of each channel is large enough. This is because the count in each channel of the total spectrum generated by the above simulation follows a Poisson distribution. Only when the count is large enough can the Poisson distribution be approximately treated as a Gaussian distribution. The user can use the GRPPHA software to bin channels. For the selection of statistics used in the spectral fitting, please refer to the XSPEC users' guide.)

Please note: !!!When fitting the spectrum, please use the correct energy band, which is listed at the beginning of this section!!! For example, for ME, you can enter '*ig **-10.0 35.0-***', which will ignore the data below 10.0 keV and above 35.0 keV. Then the warning 'Chi-square may not be valid due to bins with zero variance in spectrum number(s): 1'will disappear. However, please do not write '*ig **-10 35-***', which will ignore the data below channel 10 and above channel 35.

In the above, we used ME to illustrate the simulation process. The simulation of HE or LE is similar to ME, except that their response and background files are different. In the previous version, for HE, the spectrum of each detector module was simulated separately (HE has 17 detector modules to observe the target source). Some users reported that this case caused inconvenience. Therefore, in this version, we have changed to simulate a total spectrum for HE, similar to the case of ME and LE. For the convenience of users, we provide example scripts for the simulation of HE, ME and LE, which are in the directory 'example' in 'user_spec.zip' mentioned at the beginning of this section. Users can choose whether to use them or not. The scripts are written in TCL language. They can be executed by using '@' in XSPEC. For example:

XSPEC12>@ inputmodel.xcm

XSPEC12>@HE.tcl

Note: There may be some differences between the simulated energy spectrum and the actually observed energy spectrum. For example, the background count rate of HE *varies with the position of the satellite on its orbit. Here, the averaged background spectrum between July 2023 and June 2024 is used. The number of good pixels of ME, which affects the effective area, may vary among different observations. Here, we use the value 800. In most observations, this value can be reached or exceeded. For LE, the Galactic diffuse X-ray background, which needs more complex treatment, is not taken into account here. For point sources which are not too faint (roughly >= 100 mCrab), its contribution is not important.*

(If there is any problem, please send an email to jjin@ihep.ac.cn)

10.6 Proposal Submission Tool

10.6.1 Proposal collection website

The "Proposal Call Announcement" will be published on the *Insight*-HXMT official Website (http://enghxmt.ihep.ac.cn/) and the proposals will be collected through the Proposal Collection Interface (http://proposal.ihep.ac.en/proposal/index.jspx) before due time.

10.6.2 Account management and permission

Any proposal submission is managed by a user account. Users in the Institute of High Energy Physics of the Chinese Academy of Sciences can log in directly with his/her email account and password in the institute. Users outside the institute need to register for an account, and log in through your account and complete the proposal submission following the instructions and requirements described above.

After the submission of a proposal, the proposers can check the proposal status through the "Proposal list" on the submission interface. Before the deadline, it can be modified or updated.

After the call period ends, the science user center transfers the observation proposal (proposal database) to the science research support center for proposal evaluation.

10.6.3 Proposal submission

(1) In default, a proposer is logged in as a user and the proposal cannot be modified after the deadline.

(2) Proposal information refers to the basic information of the proposal, including the title, abstract, target type, brief description of the scientific goal, and emergency level (for ToO). Target types are currently divided into six categories: active galaxy nuclei, X-ray binaries, pulsars, supernova remnants, diffuse sources, and other types.

(3) Observation targets can be observed in pointing or small sky scanning observation mode. Observation fields for pointing observations include source name, source description, Ra, Dec, target energy band, high energy estimated photon flux, medium-energy estimated photon flux, low-energy estimated photon flux, effective observation time, number of observations, minimum observation time, and special requirements, etc. The observation fields of the small sky observation include the scanning area, the target energy band, Ra and Dec of the scanning center, and the scanning radius.

(4) Upload the attachment of "template for feasibility analysis of each target" and the proposal form. The template can be download here:

http://enghxmt.ihep.ac.cn/doc/282.jhtml

Notices on the HE observation mode:

Please be aware of the following notices when you deal with the HE proposals:

(1) There are two gain modes in HE NaI/CsI detectors: Normal mode and Low Gain Mode. Gain mode will affect the measurement energy range of both NaI and CsI. Thus, which gain mode to be use should be explicitly specified and demonstrated.

(2) Only pointed and scan observation mode could be selected for HE proposals. The gamma-ray all-sky monitoring of HE CsI is not open for proposals.

As shown in section 3.2.2, gamma-ray all-sky monitoring can work no matter which observation mode (pointed or scan) HE works in, while the energy range of gamma-ray monitoring will be affected by the gain mode of HE NaI/CsI detectors (see 3.2.3). However, the gain mode is primary determined by the requirement of NaI pointed or scan observation, with which most core sciences have been done.

Data of GRBs that are found by the gamma-ray all-sky monitoring has been released routinely.

(3) By default, only NaI data is released for HE proposals, for both pointed observation and scan observation. If CsI data is needed, please explicitly demonstrate the necessity of CsI data in the proposal.

CsI has the same data format (i.e. event data) as NaI, but with a much larger data volume. It is strong recommended that users do not apply for CsI data unless they really need it.

11 References

Abbott, B.P., Abbott, R., Abbott, T.D., et al. 2016, Phy. Rev. Lett, 116, 061102

Abbott, B.P., Abbott, R., Abbott, T.D., et al. 2017a, Phy. Rev. Lett, 119, 161101

Abbott, B. P., Abbott, R., Abbott, T. D., et al. 2017b, ApJ, 848, L12

Aartsen, M. G., Abbasi, R., et al. (IceCube Collaboration), 2013, Science 342, 1242856

Aartsen, M.G., Abbasi, R., et al. (IceCube Collaboration), 2014, Phys. Rev. Lett. 113, 101101

Aartsen，M. G. & Ackermann, M., et al. (IceCube Collaboration), 2018, Science, 361, 1378

Baumgartner, W.H., Tueller, J., Markwardt, C. B., et al. 2013, ApJS, 207,19

Berger, M., van der Klis, M., van Paradijs, J., et al. 1996, ApJ, 469, 13

Bird, A.J., Bazzano, A., Malizia, A., et al. 2016, ApJS, 223, 15

Cai, C., Xiong, S.L., Li, C.K., et al. (*Insight*-HXMT team), 2021, MNRAS,508,3910

Cao, X.L., Jiang, W.C., Meng, B., et al. (*Insight*-HXMT team) 2020, Sci. China-Phys. Mech. Astron. 63, 249504

Buisson,D.J.K., Fabian, A.C., et al., 2019, MNRAS, 490, 1350

Chen, Y., Cui, W.W., Li, W., et al. (*Insight*-HXMT team) 2020, Sci. China-Phys. Mech. Astron. 63, 249505

Chen, Y.P., Zhang, S., Zhang, S.N., et al. (*Insight*-HXMT team) 2012, ApJL,752,34

Chen, Y.P., Zhang，S., Qu, J.L., et al. (*Insight*-HXMT team) 2018, ApJL,864, 30

Chen, Y. P., Zhang, S., Zhang, S. N., et al. (*Insight*-HXMT team) 2019, JHEAp, 24, 23

Chen Yu-Peng, et al. (*Insight*-HXMT team)2022, ApJ, 936, 46

Chen YuPeng et al., 2024, MNRAS, 531，1756

Doroshenko, V., Zhang, S.N., Santangelo, A., et al. (*Insight*-HXMT team) 2020, MNRAS,491, 1857

Duncan, R.C. & Thompson, C. 1992, ApJ, 392, 9

Fabian, A.C., Buisson, D.J.K., et al., 2020, MNRAS, 493, 5389

Frank, J., King, A., & Raine, D. J. 2002, Accretion Power in Astrophysics: Third Edition, ed. Frank, J., King, A., & Raine, D. J. (Cambridge University Press)

Ge, M.Y., Lu, F. J., Qu, J. L., et al. 2012, ApJS, 199, 32

Ge, M.Y., Yan, L. L., Lu, F. J., et al. 2016, ApJ, 818, 48

Ge, M.Y., Zhang, S.N., Lu, F.J., et al. (*Insight*-HXMT team) 2020a, ApJ, 896,55

Ge, M.Y.,Ji, L., Zhang, S.N., et al. (*Insight*-HXMT team) 2020b, ApJL, 899, 19

George, G., et al. 1999, NIM A, 428, 348

Gierlinsk, M. & Zdziarski, A.A. 2005, MNRAS, 363, 1349

Godet, O., Beardmore, A. P., Abbey, A. F., et al. 2009, A&A, 494, 775

Guan, J., Lu, F-J., Zhang, S., et al. (*Insight*-HXMT team) 2020, JHEAp, 26, 11

Guan, J., Tao, L., Qu, J.L., et al. (*Insight*-HXMT team) 2021, MNRAS, 504, 2168

Guo, C.C., Liao, J.Y., Zhang, S., et al. (*Insight*-HXMT team) 2020, JHEAp,27, 44

Huang, Y., Qu, J.L., Zhang, S.N., et al. (*Insight*-HXMT team) 2018, ApJ, 866, 122

IceCube Collaboration, Aartsen, M. G., Ackermann, M., et al. 2018, Science, 361, eaat1378

Ingram A. & Done, C. 2010, MNRAS, 405, 2447

Ji, L., Doroshenko, V., Santangelo, A., et al. (*Insight*-HXMT team) 2020, MNRAS, 491, 1851

Jia, S.M., Ma, X., Huang, Y., et al. (*Insight*-HXMT team) 2018, SPIE, 10704, 1

Jia, S. M., Bu, Q. C., Qu, J. L., et al. (*Insight*-HXMT team) 2020, JHEAp, 25,1

Kaaret, P., Piraino, S., Ford, E. C., et al. 1999, ApJ, 514, L31

Kong, L. D., Zhang, S., Chen, Y. P., et al. (*Insight*-HXMT team) 2020a, JHEAp, 25,29

Kong, L.D., Zhang, S., Chen, Y.P., et al. (*Insight*-HXMT team) 2020b, ApJ, 902, 18

Kong, L.D., Zhang, S., Chen, Y.P., et al. (*Insight*-HXMT team) 2021, ApJL, 906, 2

Kong Ling-Da, et al. (*Insight*-HXMT team)2022, ApJ, 933, 3

Li, C.K., Lin, L., Xiong, S.L., et al. (*Insight*-HXMT team) 2021, Nature Astronomy, 5, 378

Li, T.P., Xong, S.L., Zhang, S.N., et al. (*Insight*-HXMT team) 2018, Science China Physics, Mechanics, and Astronomy, 61, 031011

Li, X.B., Li, X-F., Tan, Y., et al. (*Insight*-HXMT team) 2020, JHEAp, 26,64

Li, X.F., Liu, C.Z., Chang, Z., et al. (*Insight*-HXMT team) 2019, JHEAp, 24,6

Liao, J.Y., Zhang, S., Chen, Y., et al. (*Insight*-HXMT team) 2020a, JHEAp, 27,24

Liao, J.Y., Zhang, S., Lu, X.F., et al. (*Insight*-HXMT team) 2020b, 27, 14

Liu, C.Z., Zhang, Y.F., Li, X.F., et al. (*Insight*-HXMT team) 2020, Sci. China-Phys. Mech. Astron. 63, 249503

Liu H.X, et al. (*Insight*-HXMT team) 2022, ApJ, 938, 108

Luo, Q., Liao, J.Y., Li, X.F., et al. (*Insight*-HXMT team) 2020, JHEAp, 27, 1

Lyne, A., Graham-Smith, F., Weltevrede, P., 2013, Science, 342, 598

Ma, X., Tao, L., Zhang, S.N.,et al. (*Insight*-HXMT team) 2021, Nature Astronomy, 5, 94

Magdziarz, P., & Zdziarski, A.A. 1995, MNRAS, 273, 837

McHardy, I.M., Papadakis, I. E., Uttley, P., et al. 2004, MNRAS, 348, 783

Meszaros, P., Novick, R., Szentgyorgyi, A.,et al. 1988, ApJ, 324, 1056

Molkov, S., Jourdain, E., Roques, J. P,.et al. 2010, ApJ, 708,403

Morgan, E.H., Remillard, R. A., Greiner, J. 1997, ApJ, 482, 993

Mukherjee, A. & Bhattacharyya, S. 2012 ApJ, 765, 55

Nang, Y., Liao, J., Sai, N.,et al. (*Insight*-HXMT team) 2020, JHEAp, 25, 39

Peng, J. Q, et al. (*Insight*-HXMT team) 2023, MNRAS, 518, 2521

Peng, J. Q, et al. (Insight-HXMT team) 2024, A&A, 685,71

Peng J.Q. et al., 2024, ApJL, 965,22

Revnivtsev, M., Gilfanov, M., Sunyaev, R., et al. 2003, A&A, 411, 329

Rodriguez, J., Grinberg, V., Laurent, P.,et al. 2015, ApJ, 807, 17

Sai, N., Liao, J-Y., Li, C., et al. (*Insight*-HXMT team) 2020, JHEAp, 26,1

Sguera, V., Barlow, E. J., Bird, A. J.et al. 2005, A&A, 444,221

Shui,Q.C., et al., 2023, ApJ, 957,84

Shui,Q.C., et al., 2024, MNRAS, 528,7320

Staubert, R., et al. 2021, in preparation

Tennant, A.F., Becker, W., Juda, M.,et al. 2001, ApJ, 554,173

Townsley, L.K., Broos, P. S., Nousek, J. A.,et al. 2002, NIMPA, 486, 751

Tuo, Y.L., Ge, M.Y., Song, L.M., et al. (*Insight*-HXMT team) 2019, RAA, 19, 87

Tuo, Y.L., Li, X.B., Ge M.Y., et al. (*Insight*-HXMT team) 2022, ApJS, 259, 14

van den Heuvel, E.P.J., 2009, Astrophysics and Space Science Library, 359,125

Wang, L.J., Ge, M.Y. et al. (*Insight*-HXMT team) 2020,MNRAS,494,1685

Wang, P.J., Kong, L.D., Zhang, S., et al. (*Insight*-HXMT team) 2020, MNRAS, 497, 5498

Wang, Y.N., Ji, L., Zhang, S.N., et al. (*Insight*-HXMT team) 2020, ApJ, 896, 33

Willingale, R., Aschenbach, B., Griffiths, R. G., et al. 2001, A&A, 365, 212

Woods, P. M. & Thompson, C. 2006, in Compact stellar X-ray sources, eds. W. H. G. Lewin & M. van der Klis (Cambridge University Press)

Xiao, G. C., Ji, L., Staubert, R., et al. (*Insight*-HXMT team) 2019, JHEAp, 23，29

Xiao, S., Xiong, S.L., Liu, C.Z., et al. (*Insight*-HXMT team) 2020,JHEAp, 26, 58

Yang Zi-Xu, et al. 2022, ApJ, 937, 33

Yang Zi-Xu et al., 2024, ApJL,970,33

You, B., Li, C.Z., Wang, W., et al. (*Insight*-HXMT team) 2021, Nature Communication,12,1025

Zanazzi, J.J. & Lai, D. 2015, MNRAS, 451, 695

Zhang, W. et al, (*Insight*-HXMT team) 2022,ApJ, 927,210

Zhang, S., Zhang, S.N., Lu, F.J., et al. (*Insight*-HXMT team) 2018, SPIE，10699,1

Zhang, S.N., Li, T.P., Lu, F.J., et al. (*Insight*-HXMT team) 2020, Sci. China-Phys. Mech.Astron., 63, 249502

Zhang, W., Smale, A. P., Strohmayer, T. E.,et al. 1998, ApJ, 500, 171

Zhang, Y., Ge, M.Y., Song, L.M., et al. (*Insight*-HXMT team) 2019, ApJ, 879, 61

Zhao, X.F., Zhu, Y.X., Han, D.W., et al. (*Insight*-HXMT team) 2019, JHEAp, 23,23

Zhao, X.S., Gou, L.J. Dong, Y.T., et al. (*Insight*-HXMT team) 2021, ApJ, 916, 108

Zheng, S.J., Zhang, S.N., Lu, F.J., et al. (*Insight*-HXMT team) 2019, ApJS, 244, 1

12 *Insight*-HXMT Publications

The papers (published, accepted and submitted) using Insight-HXMT data are listed here (updated on February, 2025). See below for further information on the web page: http://hxmten.ihep.ac.cn/papers.jhtml .

12.1 Published papers

1) Published papers A possible jet and corona configuration for Swift J1727.8–1613 during the hard state

   Peng JingQiang et al., 2025, JHEAp,45,316

2) The comprehensive studies of type I X-ray bursts in SRGA J144459.2–604207

   Tao Fu et al., 2025, ApJ, in press

3) Estimating the spin of MAXI J1348-630 from intermediate and soft states using Insight-HXMT data

   Guan Ju et al., 2025, ApJ,in press

4) NICER, NuSTAR and Insight-HXMT views to black hole X-ray binary SLX 1746–331

   Peng JiangQiang et al., 2024, ApJL,965,22

5) Insight-HXMT observations on thermonuclear X-ray bursts from 4U~1608--52 in the low/hard state: the energy-dependant hard X-ray shortage and cooling saturation of the corona

   Chen YuPeng et al., 2024, MNRAS,531,1756

6) Evidence for A Cyclotron Absorption Line and Spectral Transition in EXO 2030+375 During 2021 Giant Outburst

   Wen Yang et al., 2024, ApJ,969,107

7) Searching for the Highest Energy of Pulsation and Critical Luminosity of Swift J0243.6+6124 Observed by Insight-HXMT

   Zhao QingXia et al., 2024, RAA,24,5006

8) Energy dependence of the low-frequency quasi-periodic oscillations in Swift J1727.8-1613

   Zhu HaiFan et al., 2024, ApJ,974,303

9) Simultaneous detection of flare-associated kink oscillations and extreme-ultraviolet waves

   Li Dong et al., 2024, Science China Technological Sciences, 67, 1592

10) Periodic sampling and count rate correction of the low energy X-ray telescope on board the Insight- Hard X-ray modulation telescope

   Li Wei et al., 2024, Journal of Instrumentation, 19, P05013

11) The 2018 outburst of MAXI J1820+070 as seen by Insight-HXMT

   Fan NingYue et al., 2024, ApJ, 969，61

12) Evolution of QPOs in GX 339−4 and EXO 1846−031 with Insight-HXMT and NICER

   Zhang ZhuoBin et al., 2024,ApJ,971,148

13) The burst recurrence properties revealed with Insight-HXMT and NICER for the newly discovered accreting millisecond pulsar MAXI J1816—195

   Wang PengJu et al., 2024, A&A, 689,47

14) Measuring the Spin of Black Hole Transient 4U 1543-47 Using Insight-HXMT

   Yang Jun et al., 2024, MNRAS,532,1410

15) Temporal and Spectral Characteristics of Persistent Emission and Special Bursts of

Magnetar SGR J1935+2154 Based on Insight-HXMT

Lu XueFeng et al., 2024, RAA,24,6

16) Timing and Spectral Analysis of the Black Hole X-Ray Binary MAXI J1803-298 with Insight-HXMT Data

    Xu YinChen et al., 2024, RAA,24,6

17) A timing view of the additional high-energy spectral component discovered in the black hole candidate Swift J1727.8–1613

    Yang ZiXu et al., 2024, ApJL,970,33

18) Revisiting the dead time effects of Insight-HXMT/ME on timing analysis

    Tuo YouLi et al., 2024, MNRAS,532,431

19) Phase-resolved Spectroscopy of Low-frequency Quasi-periodic Oscillations from the Newly Discovered Black Hole X-ray Binary Swift J1727.8-1613

    Shui QingCang et al., 2024, ApJ,973,59

20) The Peculiar Precursor of a Gamma-Ray Burst from a Binary Merger Involving a Magnetar

    Xiao Shuo et al., 2024, ApJ,970, 6

21) The peculiar disk evolution of 4U 1630–472 observed by Insight-HXMT during the 2022 and 2023 outbursts

    Peng JingQiang et al., 2024, ApJ,975,4

22) AstroSat and Insight–HXMT observations of the long-period X-ray pulsar 4U 2206+54

    Prahlad R. Epili et al., 2024, ApJ,974,282

23) Insight-HXMT, NICER and NuSTAR views to the newly discovered black hole X-

ray binary SwiftJ151857.0-572147

Peng JingQiang et al., 2024, ApJ,975,4

24) Insight-HXMT Research Progress Since 2023

Zhang Shu, Zhang Shuang-Nan, 2024, Chin. J. Space Sci.,44,643

25) The bicoherence analysis of type C quasi-periodic oscillations in Swift J1727.8-1613

Zhu HaiFan et al., 2024, ApJ,974,303

26) A Revised Spin of the Black Hole in GRS 1716-249 with a New Distance

Zhao ShuJie, et al., 2024, A&A,691,192

27) Spectral evolution of RX J0440.9+4431 during the 2022–2023 giant outburst observed with Insight-HXM

Li PanPing et al., 2024, A&A 689,316

28) Wavelet analysis of low-frequency quasi-periodic oscillations in MAXI J1803-298 observed with Insight-HXMT and NICER

Jin Y.J. et al., 2024, MNRAS，535,207

29) Analysis of the drift of the South Atlantic Anomaly using particle monitors onboard Insight-HXMT

Zhao HaiSheng et al., 2024, JHEAp,44,187

30) The high-energy cyclotron line in 2S 1417-624 discovered with Insight-HXMT during the 2018 outburst

Liu Q. et al., 2024, A&A, 691,25

31) Broadband X-ray spectral and timing properties of the accreting millisecond X-ray pulsar IGR J17498−2921 during the 2023 outburst

Li ZhaoSheng et al., 2024, A&A,691,92

32) X-Raying Neutral Density Disturbances in the Mesosphere and Lower Thermosphere induced by the 2022 Hunga-Tonga Volcano Eruption-Explosion

Satoru Katsuda, 2024, GeoRL,5112025K

33) A Comprehensive Analysis of Insight-HXMT Gamma-Ray Burst Data. I. Power Density Spectrum

Zhou Zi-Min et al., 2024,ApJ,972,190

34) Scale-invariant Features of X-Ray Bursts from SGR J1935+2154 Detected by Insight-HXMT

Li XiuJuan et al., 2024, PASP,136,42

35) Insights from the Gaussian Process Method for the Fast Radio Burst–associated X-Ray Burst of SGR 1935+2154

Tang RuiJing et al., 2024, ApJ,971,26

36) Insight-HXMT View of the Black Hole Candidate Swift J1727.8–1613 during Its Outburst in 2023

Chatterjee, Kaushik et al., 2024, ApJ，977，148

37) Insight HXMT and GECAM joint observation of time domain astronomy from cosmic outbursts

Huang, Xinyue et al., 2024, J. Phys.: Conf. Ser. 2882 012057

38) Spin and spectral properties of Cygnus X-1 observed with Insight-HXMT

Zhu YiHao et al., 2024, JHEAp, 44, 381

39) Recovery of High-energy Low-frequency Quasi-periodic Oscillations from Black Hole X-ray Binary MAXI J1535-571 with a Hilbert-Huang Transform Method

Shui, QingCang et al. 2024, ApJL, 965, 7

40) The influence of thermonuclear bursts on polar caps of accreting X-ray millisecond pulsar MAXI J1816-195

    Ji, Long et al. 2024, ApJL,966， 3

41) Evidence for a nearly orthogonal rotator in GX 301--2 with phase-resolved cyclotron resonant scattering features

    Chen X. et al., 2024, MNRAS, 530, 3589

42) Efficiency of Non-Thermal Pulsed Emission from Eight MeV Pulsars

    Takata J., et al. 2024, ApJ, 965,126

43) Timing analysis of the newly discovered black hole candidate Swift J1727.8–1613 with Insight-HXMT

    Yu, Wei et al. 2024, MNRAS, 529, 4624

44) The bright black hole X-ray binary 4U 1543–47 during 2021 outburst: a thick accretion disk inflated by high luminosity

    Zhao, ShuJie et al. 2024, A&A, 685,42

45) New insight into the hard X-ray emission influenced by the type-I bursts observed by Insight-HXMT during outburst of 4U 1636–536

    Peng, JingQiang et al. 2024, A&A, 685,71

46) Distribution of number of peaks within a long gamma-ray burst

    Guidorzi C., et al. 2024, A&A, 685, 34

47) The double-peaked type I X-ray bursts with different mass accretion rate and fuel composition

    Song, Liyu et al. 2024, MNRAS, 529, 3103

48) The Post-quiescence Properties of Cir X -1 at Orbital Phase around Periastron Observed by NuSTAR and NICER

Yu, Zhuoli et al. 2024, MNRAS, 527, 8029

49) Insight-HXMT observations of thermonuclear X-ray bursts in 4U 1636-53

Yan, Zhe et al. 2024, MNRAS, 529, 1585

50) Broad-band noise and quasi-periodic oscillation characteristics of the X-ray pulsar RX J0440.9+4431

Li, Panping et al. 2024, MNRAS, 529, 1187

51) Pulsed Iron Line Emission from the First Galactic Ultraluminous X-Ray Pulsar Swift J0243.6+6124

Xiao, Yunxiang et al. 2024, ApJ, 965, 18

52) The bright black hole X-ray binary 4U 1543-47 during 2021 outburst. A clear state transition from super-Eddington to sub-Eddington accretion revealed by Insight-HXMT

Jin, Pei et al,. 2024, MNRAS, 530, 929

53) Type-I X-ray burst evolution of the new millisecond pulsar MAXI J1816-195 revealed by Insight-HXMT

Wang, Pengju et al. 2024, JHEAp, 41, 106

54) Studying the variations of the cyclotron line in Cen X-3 using Insight-HXMT

Liu, Qi et al. 2024, JHEAp, 41, 22

55) Timing and Spectral Analysis of HMXB 4U 1700-37 Observed with Insight-HXMT

Xiao, Hua et al. 2024, ApJ, 963, 18

56) Analysis of Bright Source Hardness Ratios in the 4 yr Insight-HXMT Galactic

Plane Scanning Survey Catalog

Wang, Chen et al. 2024, RAA, 24, 025013

57) Studies on the soft intermediate state X-ray flare of MAXI J1535-571 during its 2017 outburst

Ma, Ruican et al,. 2024, MNRAS, 528, 3864

58) Cyclotron line evolution revealed with pulse-to-pulse analysis in outburst of 1A 0535+262

Shui, Qingcang et al. 2024,,MNRAS, 528, 7320

59) The self-organized criticality behaviours of two new parameters in SGR J1935+2154

Xiao, Shuo et al. 2024, MNRAS, 528, 1388

60) Individual and averaged power density spectra of X-ray bursts from SGR J1935+2154: quasi-periodic oscillation search and slopes

Xiao, Shuo et al. 2024, MNRAS, 527, 11915

61) Insights into the phase-dependent cyclotron line feature in XTE J1946+274: an AstroSat and Insight-HXMT view

Devaraj, Ashwin et al. 2024, MNRAS, 527, 11015

62) Design and verification of the electric control box of the low energy x-ray telescope onboard the Insight-HXMT

Li, Wei et al. 2024, ExA, 57, 6

63) Observation of GRB 221009A Early Afterglow in X-Ray/Gamma-Ray Energy Bands

Zheng, Chao et al. 2024, ApJ, 962, 2

64) Rapid Dimming Followed by a State Transition: A Study of the Highly Variable Nuclear Transient AT 2019avd over 1000+ Days

Wang, Yanan et al. 2024, ApJ, 962, 78

65) Rms–Flux Slope in MAXI J1820+070: A Measure of Disk–Corona Coupling

Wang, Yanan et al. 2024, ApJ, 962, 53

66) Background experiment of the low energy x-ray telescope detectors on insight-HXMT

Li, Wei et al. 2024, AIPA, 14, 5252

67) The spin of a stellar black hole 4U 1543-47 determined by Insight-HXMT

Chen, Jiashi et al. 2024, MNRAS, 527, 238

68) Spectral and Jet Properties of the Quasi-thermal-dominated GRB 210121A, GRB 210610B, and GRB 221022B

Song, Xinying et al. 2024, ApJ, 961, 137

69) Highly Significant Detection of X-Ray Polarization from the Brightest Accreting Neutron Star Sco X-1

Fabio La Monaca et al. 2024, ApJL, 960, 11

70) NICER, NuSTAR and Insight-HXMT views to the newly discovered black hole X-ray binary Swift J1727.8-1613

Peng, JingQiang et al. 2024,ApJL, 960, 17

71) A Comparative Study of Two Contrasting Cosmic-Ray Events Caused by Solar Eruptions from NOAA AR 12673 in 2017 September

Yu, XiaoXia et al. 2024, ApJ, 960, 85

72) Subsecond periodic radio oscillations in a microquasar

Tian, Pengfu, et al. 2023, Nature, 621, 271

73) A radio pulsar phase from SGR J1935+2154 provides clues to the magnetar FRB mechanism

Zhu, Weiwei, et al. 2023, SciA, 9, 6198

74) The spin measurement of MAXI J1348-630 using the Insight-HXMT data

Song, Yujia et al. 2023, MNRAS, 526, 6041

75) Type-A quasi-periodic oscillation in the black hole transient MAXI J1348-630

Zhang, Liang et al. 2023, 526, 3944

76) Timing properties of the X-ray accreting pulsar RX J0440.9+4431 studied with Insight-HXMT and NICER

Li, Panping et al. 2023, MNRAS, 526, 3637

77) Broadband X-Ray Timing and Spectral Characteristics of the Accretion-powered Millisecond X-Ray Pulsar MAXIJ1816-195

Li, Zhaosheng et al. 2023, ApJ, 958, 177

78) Statistical Properties of X-Ray Bursts from SGR J1935+2154 Detected by Insight-HXMT

Zhang, Wenlong et al. 2023, RAA, 23, 115013

79) A Spectral-timing Study of the Inner Flow Geometry in MAXI J1535-571 with Insight-HXMT and NICER

Yu, wei, et al. 2023, ApJ, 953, 191

80) Insight-HXMT observations on thermonuclear X-ray bursts from 4U 1608-52 in 2022: The accretion rate dependent anisotropy of burst emission

Chen, Yupeng et al. 2023, JHEAp, 40, 76

81) A Phase-resolved View of the Low-frequency Quasiperiodic Oscillations from the Black Hole Binary MAXI J1820+070

Shui, Qingcang et al. 2023, ApJ, 957, 84

82) Global Energetics of Solar Powerful Events on 2017 September 6

Li, Dong et al. 2023,RAA, 23, 5017

83) GRB 221009A with an Unconventional Precursor: A Typical Two-stage Collapsar Scenario?

Song, XinYing et al. 2023, ApJ, 957, 31

84) Origin of FRB-associated X-ray burst: QED magnetic reconnection

Xie, Yu, et al. 2023, Science Bulletin, 68, 1857

85) Back to business: SLX 1746–331 after 13 years of silence

Peng, Jing Qiang et al. 2023, ApJ, 955, 96

86) A new variability pattern in GRS 1915+105 with NICER and Insight-HXMT observations

Shi, Zhihong et al. 2023, MNRAS 525, 1431

87) Simultaneous and panchromatic observations of the fast radio burst FRB 20180916B?

Trudu, M., et al. 2023, A&A, 676, A17

88) A moderate spin for the black hole in X-ray binary MAXI J1348−630 revealed by Insight-HXMT

Wu, HanJi et al. 2023, MNRAS 522, 4323

89) Quasi-periodic Oscillations in GX 339−4 during the 2021 Outburst Observed with Insight-HXMT

Jin, Y.J., et al. 2023, ApJ, 953, 33

90) Insight-HXMT Detections of Hard X-ray Tails in Scorpius X-1

Ding, G.Q., et al. 2023, ApJ, 950, 69

91) The Minimum Variation Timescales of X-Ray Bursts from SGR J1935+2154

Xiao, Shuo et al. 2023, ApJS, 268, 5

92) Spin measurement of 4U 1543–47 with Insight-HXMT and NICER from its 2021 outburst A test of accretion disk models at high luminosities

Yorgancioglu, E. S. et al. 2023, A&A, 677, 79

93) Localization method for the pointing observation with the Collimated Telescopes of Insight-HXMT

Luo, Qi et al. 2023, RAA, 23, 5004

94) Centaurus X-3 orbital ephemerides using Insight-HXMT, RXTE, Swift/BAT and NuSTAR observations

Moritz, Klawin et al. 2023, A&A, 675, 135

95) Hilbert-Huang Transform analysis of quasi-periodic oscillations in MAXI J1820+070

Yu, Wei et al. 2023, ApJ, 951, 130

96) Intermittent QPO properties of MAXI J1820+070 revealed by Insight-HXMT

Zhang, Peng et al. 2023, A&A, 677, 178

97) The hard to soft transition of gx 339–4 as seen by Insight-HXMT

Liu, Honghui et al. 2023, ApJ, 950, 5

98) Timing analysis of a new black hole candidate MAXI J1803-298 with Insight-HXMT and NICER

Zhu, haifan et al. 2023, MNRAS, 523, 4394

99) Measurements of spin and orbital parameters in Cen X-3 by Insight-HXMT

Liu, Qi et al. 2023,JHEAp, 38, 32

100) Paired quasi-periodic pulsations of hard X-ray emission in a solar flare

Zhao, HaiSheng et al. 2023, SCPMA, 6659611

101) Reanalysis of the X-ray burst associated FRB 200428 with Insight-HXMT observations

Ge, Mingyu et al. 2023, ApJ, 953, 67

102) Non-linear variability observed with Insight-HXMT in MAXI J1820+070 and MAXI J1535-571

Ding, Qi et al. 2023, RAA, 23, 5024

103) Observations of a black hole X-ray binary indicate formation of a magnetically arrested disk

You, Bei et al. 2023, Science, 381, 961

104) Detection of a strong ~2.5 Hz modulation in the Newly Discovered Millisecond Pulsar MAXI J1816-195

Li, PanPing et al. 2023, MNRAS, 525, 595

105) Fast On-orbit Pulse Phase Estimation of X-ray Crab Pulsar for XNAV Flight Experiments

Wang, Yidi et al. 2023, ITAES, 59, 3395

106) CATCH: chasing all transients constellation hunters space mission

Li, Panping et al. 2023, ExA, 55, 447

107) The 100-m X-ray test facility at IHEP

Wang, Yusa et al. 2023, ExA, 55, 427

108) Monte Carlo Simulations on Possible Collimation Effects of Outflows to Fan Beam Emission of Ultraluminous Accreting X-Ray Pulsars

Hou, X et al. 2023, ApJ, 941, 126

109) Discovery of the linear energy-dependence of the spectral lag of X-ray bursts from SGR J1935+2154

Xiao, Shuo et al. 2023, MNRAS, 521, 5308

110) The Long-term Monitoring Results of Insight-HXMT in the First 4 Yr Galactic Plane Scanning Survey

Wang, Chen et al. 2023, ApJS, 265, 52

111) A detailed view of low-frequency quasi-periodic oscillation in the broadband 0.2–200 keV with Insight-HXMT and NICER

Ma, Xiang et al. 2023, ApJ, 948, 116

112) Fast transitions of X-ray variability in the black hole transient GX 339–4: comparison with MAXI J1820+070 and MAXI J1348–630

Yang, Zixu et al. 2023, MNRAS, 521, 3570

113) Evolution of disc and corona in MAXI J1348-630 during the 2019 reflare: NICER and Insight-HXMT view

Dai, Xiaohang et al. 2023, MNRAS , 521, 2692

114) Beam pattern evolution of accreting X-ray pulsar 1A 0535+262 during its 2020 giant outburst

Hu, Yongfeng et al. 2023, ApJ, 945, 138

115) GRANDMA and HXMT Observations of GRB 221009A - the Standard-

Luminosity Afterglow of a Hyper-Luminous Gamma-Ray Burst

D.A. KANN et al. 2023, ApJS, 948, 12

116) GRB minimum variability timescale with Insight-HXMT and Swift:implications for progenitor models, dissipation physics and GRB classifications

A.E. Camisasca, et al. 2023, A&A, 671, 112

117) Type I X-ray burst spectra and fuel composition from the atoll and transient source 4U 1730-22

Lu, yongqi et al. 2023, A&A, 670, 87

118) X-ray Energy Spectra Study and Black Hole Spin Estimate of GRS 1915+105

Wang, Yuan et al. 2023, ChA&A, 47, 625

119) Timing analysis of EXO 2030+375 during its 2021 giant outburst observed with *Insight*-HXMT

Fu, Yucong et al. 2023, MNRAS, 521, 893

120) Low-frequency quasi-periodic oscillation in MAXI J1820+070: Revealing distinct Compton and reflection contributions

Gao, Chenxu et al. 2023, MNRAS, 520, 554

121) Burst Phase Distribution of SGR J1935+2154 Based on *Insight*-HXMT

Lu, Xuefeng et al. 2023, RAA, 23, 5007

122) Discovery of two cyclotron resonance scattering features in X-ray pulsar cen X-3 by *Insight*-HXMT

Yang, W et al. 2023, MNRAS, 519, 5402

123) MAXI J1820+070 X-ray spectral-timing reveals the nature of the accretion

flow in black hole binaries

Kawamura, et al. 2023, MNRAS, 519, 4434

124) Accretion disk wind during the outburst of the stellar-mass black hole MAXI J1348-630

Wu, Hanji et al. 2023, JHEAp, 37, 25

125) Deep Search for Gamma-Ray Emission from the Accreting X-Ray Pulsar 1A 0535+262

Hou, X et al. 2023, APJ, 944, 57

126) Tracing the Accretion Geometry of H1743-322 with Type C Quasiperiodic Oscillations in Multiple Outbursts

Shui, Qing C et al. 2023, APJ, 943, 165

127) A possible overall scenario for the outburst evolution of MAXI J1820+070 revealed by *Insight*-HXMT

Peng, J. Q et al. 2023, MNRAS, 518, 2521

128) Neutral Atmospheric Density Measurement Using *Insight*-HXMT Data by the Earth Occultation Technique

Xue, wangchen et al. 2023, APJS, 264, 5

129) Return of 4U 1730-22 after 49 yr Silence: The Peculiar Burst Properties of the 2021/2022 Outbursts Observed by *Insight*-HXMT

Chen, yupeng et al. 2023, APJ, 942, 97

130) In-orbit performance evolution of *Insight*-HXMT in the first five years

Lu Fangjun, 2023, RDTM, 2023, 7, 1

131) In-orbit performance of HE onboard *Insight*-HXMT in the first 5 years

Li Xufang et al. 2023, RDTM, 2023, 7, 3

132) In-orbit performance of ME onboard *Insight*-HXMT in the first 5 years

Tan Ying et al. 2023, RDTM, 2023, 7, 15

133) In-orbit performance of LE onboard *Insight*-HXMT in the first 5 years

Li, Xiaobo et al. 2023, RDTM, 2023, 7, 25

134) Five-year in-orbit background of *Insight*-HXMT

Liao, Jinyuan et al. 2023, RDTM, 2023, 7, 34

135) Long-term evolution of the X-ray flux of the Crab pulsar

Zhao, Haisheng et al. 2023, RDTM, 2023, 7, 48

136) Review of X-ray pulsar spacecraft autonomous navigation

Wang Yidi et al. 2023, ChJAn, 36, 44

137) The origin of the photospheric emission of GRB 220426A

Song, XinYing, et al. 2022, MNRAS, 517, 2088

138) Revisiting the fermionic dark matter absorption on electron target

Ge Shaofeng et al. 2022, JHEP, 05, 191

139) X-ray timing observation of navigation pulsars

Yan L.L, et al. 2022, Acta Aeronautica et Astronautica Sinica, 2023, 44, 526588

140) Revisit the periodicity of SGR J1935+2154 bursts with updated sample

Xie Shenglun et al. 2022, MNRAS, 517, 3854

141) Comparing the super-Eddington accretion of SMC X-3 and RX J0209.6-7427 with Swift J0243.6+6124

Liu Jiren et al. 2022, MNRAS, 517, 3354

142) High energy millihertz quasi-periodic oscillations in 1A 0535 + 262 with *Insight*-HXMT challenge current models,

Ma, Ruichan et al. 2022, MNRAS, 517, 1988

143) Spectral and Timing Analysis of the Black Hole Transient MAXI J1631-479 During its 2019 Outburst Observed with *Insight*-HXMT

Fu Yucong et al. 2022, RAA, 22, 5002

144) Wavelet analysis of the transient QPOs in MAXI J1535-571 with *Insight*-HXMT

Chen X et al. 2022, MNRAS, 517, 182

145) Detection of a quasi-periodic oscillation at 40 mHz in Cen X-3 with *Insight*-HXMT

Liu Q et al. 2022., MNRAS, 516, 5579

146) Fan-beamed X-Ray Emission from 1 to above 130 keV from the Ultraluminous X-Ray Pulsar RX J0209.6-7427 in the Small Magellanic Cloud

Hou. X et al. 2022, ApJ, 938, 149

147) Transitions and Origin of the Type-B Quasi-periodic Oscillations in the Black Hole X-Ray Binary MAXI J1348-630

Liu H.X, et al. 2022, ApJ, 938, 108

148) The spectral-timing analysis of Cygnus X-1 with *Insight*-HXMT

Zhou M, et al. 2022, A&A, 666, 172

149) A 2-hr binary period for the black hole transient MAXI J0637-430

Soria Roberto et al. 2022, MNRAS, 515, 3105

150) Determination of QPO properties in the presence of strong broad-band noise:

a case study on the data of MAXI J1820+070

Zhou Deng-Ke, et al. 2022, MNRAS, 515, 1914

151) An *Insight*-HXMT View of the mHz Quasi-regular Modulation Phenomenon in the Black Hole X-Ray Binary 4U 1630-47

Yang Zi-Xu, et al. 2022, ApJ, 937, 33

152) *Insight*-HXMT Observation of 4U 1608-52: Evidence of Interplay between a Thermonuclear Burst and Accretion Environment

Chen Yu-Peng, et al. 2022, ApJ, 936, 46

153) The peculiar spectral evolution of the new X-ray transient MAXI J0637-430

Ma R.C, et al. 2022, MNRAS, 514, 5238

154) Variations of cyclotron resonant scattering features in Vela X-1 revealed with *Insight*-HXMT

Liu Q, et al. 2022, MNRAS, 514, 2805

155) Energetic transients joint analysis system for multi-INstrument (ETJASMIN) for GECAM - I. Positional, temporal, and spectral analyses

Xiao Shuo, et al. 2022, MNRAS, 514, 2397

156) Analysis of the reflection spectra of MAXI J1535-571 in the hard and intermediate states

Dong Yanting, et al. 2022, MNRAS, 514, 1422

157) Wavelet analysis of MAXI J1535-571 with *Insight*-HXMT

Chen X, et al. 2022, MNRAS, 513, 4875

158) Rapidly alternating flux states of GX 339-4 during its 2021 outburst captured by *Insight*-HXMT

Liu Honghui, et al. 2022, MNRAS, 513, 4308

159) *Insight*-HXMT measurements of the diffuse X-ray background

Huang R, et al. 2022, MNRAS, 513, 4074

160) Evolution of Accretion Modes between Spectral States Inferred from Spectral and Timing Analysis of Cygnus X-1 with *Insight*-HXMT Observations

Feng M.Z, et al. 2022, ApJ, 934, 47

161) *Insight*-HXMT Discovery of the Highest-energy CRSF from the First Galactic Ultraluminous X-Ray Pulsar Swift J0243.6+6124

Kong Li-Da, et al. 2022, ApJ, 933, 3

162) The Disk Wind in GRS 1915+105 as Seen by *Insight*-Hard X-Ray Modulation Telescope

Liu Honghui, et al. 2022, ApJ, 933, 122

163) GRB 190530A: From Precursor, Prompt Emission to Afterglow all Originated from Synchrotron Radiation

Liu Hui-Ya, et al. 2022, RAA, 22, 5002

164) Synchronous X-ray/optical quasi-periodic oscillations from the black hole LMXB MAXI J1820+070

Thomas Jessymol K, et al. 2022, MNRAS, 513, 35

165) Super-Eddington accretion of the first Galactic ultra-luminous X-ray pulsar Swift J0243.6+6124

Liu Jiren, et al. 2022, MNRAS, 512, 5686

166) The removal method and generation mechanism of spikes in *Insight*-HXMT/HE telescope

Wu Baiyang, et al. 2022, ExA, 53.1037

167) An *Insight*-HXMT Dedicated 33 day Observation of SGR J1935+2154. II. Burst Spectral Catalog

Cai Ce, et al. 2022, ApJS, 260, 25

168) An *Insight*-HXMT Dedicated 33 day Observation of SGR J1935+2154. I. Burst Catalog

Cai Ce, et al. 2022, ApJS, 260, 24

169) Phase-dependent Evolution within the Large Luminosity Range of 1A 0535+262 Observed by *Insight*-HXMT during 2020 Giant Outburst

Kong Li-Da, et al. 2022, ApJ, 932, 106

170) *Insight*-HXMT Study of the Inner Accretion Disk in the Black Hole Candidate EXO 1846-031

Ren X.Q, et al. 2022, ApJ, 932, 66

171) Invariable X-Ray Profile and Flux of the Crab Pulsar during Its Two Glitches

Zhang Y.H, et al. 2022, ApJ, 932, 11

172) The Accretion Flow Geometry of MAXI J1820+070 through Broadband Noise Research with *Insight* Hard X-ray Modulation Telescope

Yang Zi-Xu, et al. 2022, ApJ, 932, 7

173) GRB 210121A: Observation of Photospheric Emissions from Different Regimes and the Evolution of the Outflow

Song Xin-Ying, et al. 2022, ApJ, 931, 112

174) X-Ray Fine Structure of a Limb Solar Flare Revealed by *Insight*-HXMT, RHESSI and Fermi

Zhang Ping, et al. 2022, RAA, 22, 5006

175) The 2018 failed outburst of H 1743 - 322: *Insight*-HXMT, NuSTAR, and NICER views

Wang P.J, et al. 2022, MNRAS, 512, 4541

176) The evolution of the corona in MAXI J1535-571 through type-C quasi-periodic oscillations with *Insight*-HXMT

Zhang Yuexin, et al. 2022, MNRAS, 512, 2686

177) The spins of the Galactic black holes in MAXI J1535-571 and 4U 1630-472 from *Insight*-HXMT

Liu, Qichun, et al. 2022, MNRAS, 512, 2082

178) Quasi-periodic Oscillations of the X-Ray Burst from the Magnetar SGR J1935-2154 and Associated with the Fast Radio Burst FRB 200428

Li Xiaobo, et al. 2022, ApJ, 931, 56

179) New method for Earth neutral atmospheric density retrieval based on energy spectrum fitting during occultation with LE/*Insight*-HXMT

Yu,Dao-Chun, et al. 2022, AdSpR, 69, 3426

180) Measurement of the vertical atmospheric density profile from the X-ray Earth occultation of the Crab Nebula with *Insight*-HXMT

Yu,Dao-Chun, et al. 2022, AMT, 15, 3141

181) Optical and X-Ray Observations of MAXI J1820+070 During the Early Outburst Phase in 2018: Zooming in the Low Frequency QPOs

Mao,Dong-Ming, et al. 2022, RAA, 22,5009

182) The First *Insight*-HXMT Gamma-Ray Burst Catalog: The First Four Years

Song Xin-Ying, et al. 2022, ApJS, 259,46

183) The Second Catalog of Interplanetary Network Localizations of Konus Short-duration Gamma-Ray Bursts

Svinkin, D.S, et al. 2022, ApJS, 259,34

184) A Study on the X-Ray Pulse Profile and Spectrum of the Crab Pulsar Using NICER and *Insight*-HXMT's Observations

Yan Lin-Li, et al. 2022, ApJ,,928,183

185) *Insight*-HXMT, NuSTAR, and INTEGRAL Data Show Disk Truncation in the Hard State of the Black Hole X-Ray Binary MAXI J1820+070

Zdziarski, Andrzej A, et al. 2022, ApJ, 928,11

186) Peculiar Disk Behaviors of the Black Hole Candidate MAXI J1348-630 in the Hard State Observed by *Insight*-HXMT and Swift

Zhang.W, et al, 2022,ApJ, 927,210

187) X-ray spectral-timing variability of 1A 0535+262 during the 2020 giant outburst

Reig,P, et al, 2022,A&A, 659,178

188) In-orbit timing calibration of the *Insight*-Hard X-ray Modulation Telescope,

Tuo,Youli, et al,2022, APJS, 259,14

189) Periodicity Search on X-Ray Bursts of SGR J1935+2154 Using 8.5 yr of Fermi/GBM Data

Zou, Jin-Hang, et al. 2021, ApJ, 923, 30

190) GRB 200716C: Evidence for a Short Burst Being Lensed

Wang Yun et al. 2021, ApJ, 918, 34

191) State transitions of GX 339-4 during its outburst rising phase

Shui, QingCang, et al. 2021, MNRAS, 508, 287

192) Bursts before Burst: A Comparative Study on FRB 200428-associated and FRB-absent X-Ray Bursts from SGR J1935+2154

Yang Yu-Han et al. 2021, ApJ, 906,12

193) Detection of a low frequency quasi-periodic oscillation in the soft state of Cygnus X-1 with *Insight*-HXMT

Yan, Zhen, et al. 2021, ApJ, 919, 46

194) On the Terrestrial Gamma-Ray Flashes Preceding Narrow Bipolar Events

Zhang, HongBo, et al. 2021, GRL, 48, 92160

195) Timing and spectral variability of the high-mass X-ray pulsar GX 301-2 over orbital phases observed by *Insight*-HXMT

Ding,Y.Z.,Wang,W., Epili,P.R., et al. 2021, MNRAS, 506, 2712

196) Broadband Variability Study of Maxi J1631-479 in Its Hard-intermediate State Observed with *Insight*-HXMT

Bu,Q.C., Zhang,S.N., Santangelo,A., et al. 2021, ApJ, 919, 92

197) Detection of Flare Multiperiodic Pulsations in Mid-ultraviolet Balmer Continuum, Lyα, Hard X-Ray, and Radio Emissions Simultaneously

Li,Dong, Ge,Mingyu, Dominique,Marie, et al. 2021, ApJ,921,179

198) Detection of two bright radio bursts from magnetar SGR 1935 + 2154

Kisten,F., Snelders,M.P., Jenkins,M., et al. 2021,NatAs,5,414

199) Estimating the Black Hole Spin for the X-Ray Binary MAXI J1820+070
Zhao,Xueshan, Gou,Lijun, Dong,Yanting, et al. 2021, ApJ,916,108

200) Discovery of Transition from Marginally Stable Burning to Unstable Burning after a Superburst in Aql X-1

Li,Zhaosheng, Pan,Yuanyue, Falanga,Maurizio, et al. 2021, ApJ,920,35

201) Test the growth models of black hole by jointing LIGO and *Insight*-HXMT observations

Yang,Rong-Jia, Guo,Zhiwei, Zheng, Yaoguang, et al. 2021, JHEAp,32,6

202) GRB 210121A: A Typical Fireball Burst Detected by Two Small Missions

Wang,Xiangyu Ivy, Zheng,Xutao, Xiao,Shuo, et al. 2021, ApJ,922,237

203) Calibration of the energy response matrix for X-ray detector CCD236

Zhu,Y.X., Lu,J.B., Li,X,B., et al. 2021, JINST,16,5016

204) Search for gamma-ray bursts and gravitational wave electromagnetic counterparts with High Energy X-ray Telescope of *Insight*-HXMT

Cai,C., Xiong,S.L., Li,C.K., et al. (*Insight*-HXMT team), 2021, MNRAS,508,3910

205) Broadband X-ray spectra and timing of the accreting millisecond pulsar Swift J1756.9-2508 during its 2018 and 2019 outbursts

Li,Z.S., Kuiper,L., Falanga, M ., et al. 2021, A&A, 649,76

206) Enhanced Localization of Transients Based on a Novel Cross-correlation Method Xiao,S., Xiong, S.L., Zhang,S.N., et al. 2021, ApJ, 920,43

207) Non-thermal Electron Energization During the Impulsive Phase of an X9.3 Flare Revealed by *Insight*-HXMT

Zhang,P., Wang,W., Su,Y., et al. 2021, ApJ, 918,42

208) Relation of Cyclotron Resonant Energy and Luminosity in a Strongly Magnetized Neutron Star GRO J1008-57 Observed by *Insight*-HXMT

Chen,X., Wang,W., Tang, Y.M., et al. 2021, ApJ, 919,33

209) A Parametric Model to Reproduce the Background of the *Insight*-HXMT/HE Blind Detector

You, Yuan,Liao, Jin-Yuan,Zhang, Shuang-Nan, et al.(*Insight*-HXMT team) 2021, ApJS, 256,47

210) New *Insight* into the Rapid Burster by *Insight*-HXMT

Chen, Y.P., Zhang, S., Zhang,S.N., et al. (*Insight*-HXMT team) 2021, ApJ, 913,150

211) Luminosity Dependence of the Cyclotron Line Energy in 1A 0535+262 Observed by *Insight*-HXMT during the 2020 Giant Outburst

Kong, L.D.,Zhang, S., Ji, L., et al. (*Insight*-HXMT team) 2021, TApJL, 917,38

212) Accretion torque reversals in GRO J1008-57 revealed by *Insight*-HXMT

Wang, W.,Tang, Y.M., Tuo, Y. L., et al. (*Insight*-HXMT team) 2021, Journal of High Energy Astrophysics,30,1

213) Study on the energy limits of kHz QPOs in Sco X-1 with RXTE and *Insight* -HXMT observations

Jia, S. M., Qu, J. L., Lu, F. J., et al. 2021, ApJ,913,119

214) Physical origin of the non-physical spin evolution of MAXI J1820+070

Guan, J., Tao, L.,Qu J., L., et al. 2021, MNRAS, 504,2168

215) Disk versus wind accretion in X-ray pulsar GX 301-2

Liu, Jiren, Ji, Long, et al. 2021, MNRAS, 504,2493

216) QPOs and Orbital elements of X-ray binary 4U 0115+63 during the 2017 outburst observed by *Insight*-HXMT

Ding,Y.Z., Wang, W., Zhang, P., et al. 2021, MNRAS,503,6405

217) Testing Evolution of LFQPOs with Mass Accretion Rate in GRS 1915+105 with *Insight*-HXMT

Liu, Honghui, Ji, Long, et al. 2021, ApJ, 909,63

218) Time-lag between disk and corona radiation leads to hysteresis effect observed in black-hole X-ray binary MAXI J1348-630

Weng, Shan-Shan, Cai, Zhen-Yi, Zhang, Shuang-Nan, et al. 2021, ApJ,915,15

219) Timing analysis of the black hole candidate EXO 1846–031 with *Insight*-HXMT monitoring

Liu, He-Xin, et al. (*Insight*-HXMT team) 2021, RAA, 21,70

220) HXMT identification of a non-thermal X-ray burst from SGR J1935+2154 and with FRB 200428

Li, C.K., Lin, L., Xiong, S.L., et al. (*Insight*-HXMT team) 2021, Nature Astronomy,5,378

221) *Insight*-HXMT observations of jet-like corona in a black hole X-ray binary MAXI J1820+070

You, B., Li, C.Z., Wang, W., et al. (*Insight*-HXMT team) 2021, Nature Communications, 12, 1025

222) Discovery of oscillations above 200 keV in a black hole X-ray binary with *Insight*-HXMT

Ma, X., Tao, L., Zhang, S.N., et al. (*Insight*-HXMT team) 2021, Nature Astronomy, 5, 94-102

223) X-ray reprocessing in accreting pulsar GX 301-2 observed with *Insight*-HXMT

Ji, L., V. Doroshenko, V. V. Suleimanov, V., et al. (*Insight*-HXMT team) 2021, MNRAS, 501,2,2522-2530

224) *Insight*-HXMT Observations of a Possible Fast Transition from the Jet- to Wind-dominated State during a Huge Flare of GRS 1915+105

Kong, L.D., Zhang, S., Chen, Y.P., et al. (*Insight*-HXMT team) 2021, ApJL, 906,2

225) A Variable Ionized Disk Wind in the Black-Hole Candidate EXO 1846-031

Wang, Y.N., Ji, L., Garcia, J.A., et al. (*Insight*-HXMT team) 2021, ApJ 906,11

226) The influence of the *Insight*-HXMT/LE time response on timing analysis

Zhou, D.K., Zheng, S.J., Song, L.M., et al. (*Insight*-HXMT team) 2021, RAA, 21,5

227) Spectral evolution of X-ray pulsar 4U 1901+03 during 2019 outburst based on *Insight*-HXMT and NuSTAR observations

Nabizadeh, Armin, Tsygankov, Sergey S., Ji, Long, et al. 2021, A&A,652,89

228) Switches between accretion structures during flares in 4U 1901+03

Ji, L., Ducci, L., Santangelo, A., et al. (*Insight*-HXMT team) 2020, MNRAS,493,5680

229) No pulsed radio emission during a bursting phase of a Galactic magnetar,

Lin, L., Zhang, C.F., et al. 2020, Nature, 587, 63-65

230) A search for prompt γ–ray counterparts to fast radio bursts in the *Insight*-HXMT data

Cuidorzi, C., Marongiu, M., Martone, R., et al. (*Insight*-HXMT team) 2020, A&A, 637, 69

231) Discovery of Delayed Spin-up Behavior Following Two Large Glitches in the Crab Pulsar, and the Statistics of Such Processes

Ge, M.Y., Zhang, S.N., Lu, F.J., et al. (*Insight*-HXMT team) 2020, ApJ, 896,55

232) The braking index of PSR B0540-69 and the associated pulsar wind nebula emission after spin-down rate transition

Wang,L.J.,Ge,M.Y. et al. (*Insight*-HXMT team) 2020,MNRAS,494,1865

233) Timing analysis of 2S 1417-624 observed with NICER and *Insight*-HXMT

Ji, L., Doroshenko, V., Santangelo, A., et al. (*Insight*-HXMT team) 2020, MNRAS, 491, 1851

234) *Insight*-HXMT observations of Swift J0243.6+6124: the evolution of RMS pulse fractions at super-Eddington luminosity

Wang, P.J., Kong, L.D., Zhang, S., et al. (*Insight*-HXMT team) 2020, MNRAS, 497, 5498

235) Two Complete Spectral Transitions of Swift J0243.6+6124 Observed by *Insight*-HXMT

Kong, L.D., Zhang, S., Chen, Y.P., et al. (*Insight*-HXMT team)2020, ApJ, 902,18

236) Hot disc of the Swift J0243.6+6124 revealed by *Insight*-HXMT,

Doroshenko, V., Zhang, S. N., Santangelo, A., et al. (*Insight*-HXMT team) 2020, MNRAS, 491, 1857

237) Constraining the transient high-energy activity of FRB 180916.J0158+65 with *Insight*-HXMT follow-up observations

Cristiano, C., Orlandini, M.; Frontera, F., et al. (*Insight*-HXMT team) 2020, A&A, 642, 160

238) Comparison of simulated backgrounds with in-orbit observations for HE, ME, and LE onboard *Insight*-HXMT

Zhang,J., Li, X.B., Ge, M.Y., et al. (*Insight*-HXMT team) 2020, Ap&SS, 365, 158

239) *Insight*-HXMT Firm Detection of the Highest-energy Fundamental Cyclotron

Resonance Scattering Feature in the Spectrum of GRO J1008-57

Ge, M.Y., Ji, L., Zhang, S.N., et al. (*Insight*-HXMT team) 2020, ApJL, 899, 19

240) The Evolution of the Broadband Temporal Features Observed in the Black-hole Transient MAXI J1820+070 with *Insight*-HXMT

Wang, Y.N., Ji, L., Zhang, S.N., et al. (*Insight*-HXMT team) 2020, ApJ, 896, 33

241) GRB 200415A: A Short Gamma-Ray Burst from a Magnetar Giant Flare?

Jun, Yang, Vikas, Chand et al.2020, ApJ, 899, 106

242) Overview to the Hard X-ray Modulation Telescope (*Insight*-HXMT) Satellite
Zhang, S.N., Li, T.P., Lu, F.J., et al. (*Insight*-HXMT team) 2020, Sci. China-Phys. Mech. Astron. 63, 249502

243) The High Energy X-ray telescope (HE) onboard the *Insight*-HXMT astronomy satellite

Liu, C.Z., Zhang, Y.F., Li, X.F., et al. (*Insight*-HXMT team) 2020, Sci. China-Phys. Mech. Astron. 63, 249503

244) The Medium Energy X-ray telescope (ME) onboard the *Insight*-HXMT astronomy satellite

Cao, X.L., Jiang, W.C., Meng, B., et al. (*Insight*-HXMT team) 2020, Sci. China-Phys. Mech. Astron. 63, 249504

245) The Low Energy X-ray telescope (LE) onboard the *Insight*-HXMT astronomy satellite

Chen, Y., Cui, W.W., Li, W., et al. (*Insight*-HXMT team) 2020, Sci. China-Phys. Mech. Astron. 63, 249505

246) An underlying clock in the extreme flip-flop state transitions of the black hole transient Swift J1658.2-4242

Bogensberger, D., Ponti, G., Jin, C., et al. 2020, A&A, 641, 101

247) Constraining the X-Ray-Infrared Spectral Index of Second-timescale Flares from SGR 1935+2154 with Palomar Gattini-IR

De, K., Ashley, M.C. B., Andreoni, I., et al. 2020, ApJL, 901, 7

248) Introducing a special collection of papers in the Journal of High Energy Astrophysics on the Early Results of China's 1st X-ray Astronomy Satellite: *Insight*-HXMT

Torres, Diego F., Zhang Shuang-Nan, 2020, JHEAp,27,51

249) A modified direct demodulation method applied to *Insight*-HXMT Galactic plane scanning survey

Guan, J., Lu, F-J., Zhang, S., et al. (*Insight*-HXMT team) 2020, JHEAp,26, 11

250) Diagnostic of the spectral properties of Aquila X-1 by *Insight*-HXMT snapshots during the early propeller phase

Gungor, C., Ge, M.Y, Zhang, S., et al. (*Insight*-HXMT team) 2020, JHEAp,25, 10

251) The background model of the medium energy X-ray telescope of *Insight*-HXMT

Guo, C.C., Liao, J.Y., Zhang, S., et al. (*Insight*-HXMT team) 2020, JHEAp,27, 44

252) *Insight*-HXMT study of the timing properties of ScoX-1

Jia, S.M, Bu, Q.C, Qu, J.L, et al. (*Insight*-HXMT team) 2020,JHEAp, 25, 1

253) Joint analysis of energy and RMS spectra from MAXI J1535-571 with *Insight*-HXMT

Kong, L.D., Zhang, S., Chen, Y.P., et al. (*Insight*-HXMT team) 2020, JHEAp, 25, 29

254) In-flight calibration of the *Insight*-Hard X-ray Modulation Telescope

Li, X.B., Li, X.-F., Tan, Y., et al. (*Insight*-HXMT team) 2020, JHEAp, 27,64

255) Background model for the Low-Energy Telescope of *Insight*-HXMT

Liao, J.Y., Zhang, S., Chen, Y., et al. (*Insight*-HXMT team) 2020a, JHEAp, 27,24

256) Background model for the high-energy telescope of *Insight*-HXMT

Liao, J.Y., Zhang, S., Lu, X.F., et al. (*Insight*-HXMT team) 2020b, JHEAp, 27, 14

257) Design and calibration of the high energy particle monitor onboard the *Insight*-HXMT

Liu, Congzhan., Lu, XueFeng., Li, Xiaobo., et al. (*Insight*-HXMT team) 2020, JHEAp, 26, 77

258) Calibration of the instrumental response of *Insight*-HXMT/HE CsI detectors for gamma-ray monitoring

Luo, Q., Liao, J.Y., Li, X.F., et al. (*Insight*-HXMT team) 2020, JHEAp, 27, 1

259) In-orbit calibration to the point-spread function of *Insight*-HXMT

Nang, Y., Liao, J.Y, Sai, N.,et al. (*Insight*-HXMT team) 2020, JHEAp, 25, 39

260) Methodology and performance of the two-year galactic plane scanning survey of *Insight*-HXMT

Sai, N., Liao, J-Y., Li, C-K., et al. (*Insight*-HXMT team) 2020, JHEAp, 26,1

261) *Insight*-HXMT *Insight* into switch of the accretion mode: the case of the X-ray pulsar 4U 1901+03

Tuo, Y.L., Ji, L., Tsygankov, S.S., et al. (*Insight*-HXMT team) 2020,JHEAp, 27, 38

262) Deadtime calculation method of the High Energy X-ray telescope (HE) onboard the *Insight*-HXMT satellite

Xiao, S., Xiong, S.L., Liu, C.Z., et al. (*Insight*-HXMT team) 2020, JHEAp, 26, 58

263) The observation of the South Atlantic Anomaly with the particle monitors onboard *Insight*-HXMT

Zhao, H.S, Liu, C.Z., Li, X.Q., et al. (*Insight*-HXMT team) 2020, JHEAp,26, 95

264) Confirming the spin parameter of the black hole in Cygnus X-1 using the *Insight*-HXMT

Zhao, X.S., Gou, L.J., Dong, Y.T., et al. (*Insight*-HXMT team) 2020, JHEAp,27,53

265) Super-Eddington Accretion onto the Galactic Ultraluminous X-Ray Pulsar Swift J0243.6+6124

Tao, L., Feng, H., Zhang, S.N. et al. (*Insight*-HXMT team) 2019, ApJ, 873, 19

266) In-orbit Demonstration of X-ray Pulsar Navigation with the *Insight*-HXMT Satellite

Zheng, S.J., Zhang, S.N., Lu, F.J., et al. (*Insight*-HXMT team) 2019, ApJS, 244, 1

267) *Insight*-HXMT Observations of Swift J0243.6+6124 during Its 2017-2018 Outburst,

Zhang, Y., Ge, M.Y., Song, L.M., et al. (*Insight*-HXMT team) 2019, ApJ, 879, 61

268) *Insight*-HXMT observations of the Crab pulsar

Tuo, Y.L., Ge, M.Y., Song, L.M., et al. (*Insight*-HXMT team) 2019, RAA, 19, 87

269) *Insight*-HXMT observation on 4U 1608－52: Evolving spectral properties of a bright type-I X-ray burst

Chen, Y.P., Zhang, S., Zhang, S.N., et al. (*Insight*-HXMT team) 2019, JHEAp, 24, 23

270) Ground-based calibration and characterization of the HE detectors for *Insight*-

HXMT

Li, X.F., Liu, C.Z., Chang, Z., et al. (*Insight*-HXMT team) 2019, JHEAp, 24, 6

271) Constant cyclotron line energy in Hercules X–1 - joint *Insight*-HXMT and NuSTAR observations

Xiao, G.C., Ji, L., Staubert, R., et al. (*Insight*-HXMT team) 2019a, JHEAp, 23, 29

272) Timing analysis of Swift J1658.2–4242's outburst in 2018 with *Insight*-HXMT, NICER and AstroSat

Xiao, G.C., Lu, Yu, Ma, X., et al. (*Insight*-HXMT team) 2019b, JHEAp, 24, 30

273) Studies on the time response distribution of *Insight*-HXMT/LE

Zhao, X.F., Zhu, Y.X., Han, D.W., et al. (*Insight*-HXMT team) 2019, JHEAp, 23, 23

274) *Insight*-HXMT Observations of 4U 1636-536: Corona Cooling Revealed with Single Short Type-I X-Ray Burst

Chen, Y.P., Zhang, S., Qu, J.L., et al. (*Insight*-HXMT team) 2018, ApJL, 864, 30

275) *INSIGHT*-HXMT Observations of the New Black Hole Candidate MAXI J1535-571: Timing Analysis

Huang, Y., Qu, J.L., Zhang, S.N., et al. (*Insight*-HXMT team) 2018, ApJ, 866, 122

276) *Insight*-HXMT observations of the first binary neutron star merger GW170817

Li,T.P., Xiong, S.L., Zhang, S.N., et al. (*Insight*-HXMT team) 2018, SCPMA, 61, 1011

277) The *Insight*-HXMT mission and its recent progresses

Zhang, S., Zhang, S.N., Lu, F.J., et al. (*Insight*-HXMT team) 2018, SPIE, 10699, 1

278) *Insight*-HXMT science operations

Jia, S.M., Ma, X., Huang, Y., et al. (*Insight*-HXMT team) 2018, SPIE, 10704, 1

279) In-orbit calibration status of the *Insight*-HXMT

Li, X.B., Song, L.M., Li, X.F., et al. (*Insight*-HXMT team) 2018, SPIE, 10699, 69

280) The readout design of Si-PIN detector in HXMT

Luo, T., Meng, B., Chen, Y., et al. (*Insight*-HXMT team) 2018, SPIE, 10709, 2

281) Design and applications of scientific ground segment for HXMT Satellite

Zheng, S.J., et al. (*Insight*-HXMT team) 2018, Spacecraft Engineering, 27, 162

282) Preliminary evaluation for scientific observations application of HXMT Satellite

Jia, S.M., Huang, Y., Ma, X., et al. (Insight-HXMT team) 2018, Spacecraft Engineering, 27, 168

283) In-orbit calibration data processing of HXMT Satellite

Li, X.B., Ge, M.Y., Li, X.F., et al. (*Insight*-HXMT team) 2018, Spacecraft Engineering, 27, 143

284) Multi-messenger Observations of a Binary Neutron Star Merger

Abbott, B.P., Abbott, R., Abbott, T. D., et al. (*Insight*-HXMT team) 2017, ApJL, 848, 12

12.2 Special Issue in SCPMA

1) Overview to the Hard X-ray Modulation Telescope (*Insight*-HXMT) Satellite

Zhang, S.N., Li, T.P., Lu, F.J., et al. (*Insight*-HXMT team) 2020, Sci. China-Phys. Mech. Astron. 63, 249502

2) The High Energy X-ray telescope (HE) onboard the *Insight*-HXMT astronomy satellite

Liu, C.Z., Zhang, Y.F., Li, X.F., et al. (*Insight*-HXMT team) 2020, Sci. China-Phys. Mech. Astron. 63, 249503

3) The Medium Energy X-ray telescope (ME) onboard the *Insight*-HXMT astronomy satellite

   Cao, X.L., Jiang, W.C., Meng, B., et al. (*Insight*-HXMT team) 2020, Sci. China-Phys. Mech. Astron. 63, 249504

4) The Low Energy X-ray telescope (LE) onboard the *Insight*-HXMT astronomy satellite

   Chen, Y., Cui, W.W., Li, W., et al. (*Insight*-HXMT team) 2020, Sci. China-Phys. Mech. Astron. 63, 249505

12.3 Special issue in JHEAp

1) *Insight*-HXMT observation on4U 1608 – 52: evolving spectral properties of a bright type-I X-ray burst

   Chen, Y.P., Zhang, S., Zhang, S.N., et al. (*Insight*-HXMT team) 2019, JHEAp, 24, 23

2) A modified direct demodulation method applied to *Insight*-HXMT Galactic plane scanning survey

   Guan, J., Lu, F-J., Zhang, S., et al. (*Insight*-HXMT team) 2020, JHEAp,26, 11

3) Diagnostic of the spectral properties of Aquila X-1 by *Insight*-HXMT snapshots during the early propeller phase

   Gungor, C., Ge, M., Zhang, S., et al. (*Insight*-HXMT team) 2020, JHEAp,25, 10

4) The background model of the medium energy X-ray telescope of *Insight*-HXMT
   Guo, C.C., Liao, J.Y., Zhang, S., et al. (*Insight*-HXMT team) 2020, JHEAp,27, 44

5) *Insight*-HXMT study of the timing properties of ScoX-1

Jia, S., Bu, Q., Qu, J., et al. (*Insight*-HXMT team) 2020,JHEAp, 25, 1

6) Joint analysis of energy and RMS spectrafrom MAXI J1535-571 with *Insight*-HXMT

   Kong, L.D., Zhang, S., Chen, Y.P., et al. (*Insight*-HXMT team) 2020, JHEAp, 25, 29

7) In-flight calibration of the *Insight*-Hard X-ray Modulation Telescope

   Li, X., Li, X-F., Tan, Y., et al. (*Insight*-HXMT team) 2020, JHEAp, 27,64

8) Ground-based calibration and characterization of the HE detectors for *Insight*-HXMT

   Li, X.F., Liu, C.Z., Chang, Z., et al. (*Insight*-HXMT team) 2019, JHEAp, 24, 6

9) Background model for the low-energy telescope of Insight-HXMT

   Liao, J.Y., Zhang, S., Chen, Y., et al. (*Insight*-HXMT team) 2020a, JHEAp, 27,24

10) Background model for the high-energy telescope of *Insight*-HXMT

    Liao, J.Y., Zhang, S., Lu, X.F., et al. (*Insight*-HXMT team) 2020b, 27, 14

11) Design and calibration of the high energy particle monitor onboard the *Insight*-HXMT

    Liu, C., Lu, X., Li, X., et al. (*Insight*-HXMT team) 2000, JHEAp, 26, 77

12) Calibration of the instrumental response of *Insight*-HXMT/HE CsI detectors for gamma-ray monitoring

    Luo, Q., Liao, J.Y., Li, X.F., et al. (*Insight*-HXMT team) 2020, JHEAp, 27, 1

13) In-orbit calibration to the point-spread function of *Insight*-HXMT

    Nang, Y., Liao, J., Sai, N.,et al. (*Insight*-HXMT team) 2020, JHEAp, 25, 39

14) Methodology and performance of the two-year Galactic plane scanning survey of

Insight-HXMT

Sai, N., Liao, J-Y., Li, C., et al. (*Insight*-HXMT team) 2020, JHEAp, 26,1

15) *Insight*-HXMT *Insight* into switch of the accretion mode: the case of the X-ray pulsar 4U 1901+03

    Tuo, Y.L., Ji, L., Tsygankov, S.S., et al. (*Insight*-HXMT team) 2020,JHEAp, 27, 38

16) Constant cyclotron line energy in Hercules X–1 - joint *Insight*-HXMT and NuSTAR observations

    Xiao, G.C., Ji, L., Staubert, R., et al. (*Insight*-HXMT team) 2019a, JHEAp,23, 29

17) Timing analysis of Swift J1658.2–4242's outburst in 2018 with *Insight*-HXMT, NICER and AstroSat

    Xiao, G.C., Lu, Yu, Ma, X., et al. (*Insight*-HXMT team) 2019b, JHEAp,24, 30

18) Deadtime calculation method of the High Energy X-ray telescope (HE) onboard the *Insight*-HXMT satellite

    Xiao, S., Xiong, S.L., Liu, C.Z., et al. (*Insight*-HXMT team) 2020,JHEAp, 26, 58

19) The observation of the South AtlanticAnomaly with the particle monitors onboard *Insight*-HXMT

    Zhao, H., Liu, C.Z., Li, X.Q., et al. (*Insight*-HXMT team) 2020, JHEAp,26, 95

20) Confirming the spin parameter of theblack hole in Cygnus X-1 using the *Insight*-HXMT

    Zhao, X.S., Gou, L.J., Dong, Y.T., et al. (*Insight*-HXMT team) 2020, JHEAp,26,53

21) Studies on the time response distribution of *Insight*-HXMT/LE

    Zhao, X.F., Zhu, Y.X., Han, D.W., et al. (*Insight*-HXMT team) 2019, JHEAp, 23, 23

22) Introducing a special collection of papers in the Journal of High Energy Astrophysics on the Early Results of China's 1st X-ray Astronomy Satellite: *Insight*-HXMT

    Torres, Diego F.; Zhang Shuang-Nan, 2020, JHEAp, 27, 51

12.4 Special issue in RDTM

1) In-orbit performance evolution of *Insight*-HXMT in the first five years

   Lu Fangjun, 2023, RDTM, 2023, 7,1

2) In-orbit performance of HE onboard *Insight*-HXMT in the first 5 years

   Li Xu-Fang, et al. 2023, RDTM, 2023, 7,3

3) In-orbit performance of ME onboard *Insight*-HXMT in the first 5 years

   Tan Ying, et al. 2023, RDTM, 2023, 7,15

4) In-orbit performance of LE onboard *Insight*-HXMT in the first 5 years

   Li Xiaobo, et al. 2023, RDTM, 2023, 7,25

5) Five-year in-orbit background of *Insight*-HXMT

   Liao Jinyuan, et al. 2023, RDTM, 2023, 7,34

6) Long-term evolution of the X-ray flux of the Crab pulsar

   Zhao Haisheng, et al. 2023, RDTM, 2023, 7,48

13 Summary of AO-07 Observations

In AO-07, the approved exposure durations for the non-ToO sources is about 7.92 Ms, including 22 grade-A observations with ~6.02 Ms, and the Galactic plane scan with about ~1.9 Ms. Till now, about 6.66 Ms observations have been carried out, and according to the long-term plan of *Insight*-HXMT, all the above observations can be finished by the end of AO-07. In special cases, if a grade-A observations cannot be fully finished, it will be automatically postponed to AO-08.

For the pre-approved ToO observations in AO-07, 8 of them have been triggered and observed by *Insight*-HXMT with 2.19 Ms exposure durations in total. *Insight*-HXMT also carried out 10 ad hoc ToO observations, with 0.86Ms exposure durations in total.

The observed sources by *Insight*-HXMT till Mar. 31st, 2025 is listed in the following table, and for more detailed information please visits the website, http://hxmten.ihep.ac.cn/ShortPlan.jhtml.

	No.	Source name	RA	DEC	Proposal ID	Approved time (ks)	Approved number	Observation time (ks)	Observation Number
normal sources	1-16	Blank sky	-	-	16 sources	1200	120	600	60
	17	4U_1820-303	18:23:40.800	-30:21:36.000	P0705928	800	40	340	17
	18	SGR_J1935+2154	19:34:55.598	21:53:47.760	P0705025	360	6	120	2
	19	Vela_Pulsar	08:35:21.600	-45:10:48.000	P0705873	2000	20	1700	25
	20	Cas A	23:23:28.800	58:48:36.000	P0702839	800	8	750	8
	21	Crab	05:34:31.973	22:00:48.000	P0702840	400	8	450	9
	22	Crab Scan	05:34:31.973	22:00:48.000	P0702838	460	20	500	22
	23-	Galaxy plane scan with EP	-	-	720 areas	1900	330	2200	383
						7920	**552**	**6660**	**526**
approved ToO	1	1E_1841-045	280.3306	-4.9364	P0704971	-	-	50	5
	2	Aql_X-1	287.82	0.58	P0704768			1160	33
	3	AT2019wey	68.8369	55.374	P0704024			360	16
	4	GX_339-04	255.71	-48.79	P0704831			180	8
	5	Her_X-1	254.46	35.34	P0704814			200	2
	6	IGR_J17511-3057	267.79	-30.96	P0704855			120	6
	7	Swift_J1818-1607	274.5009	-16.1312	P0704958			60	2
	8	XTE_1810-197	272.4629	-19.7311	P0704053			60	3
								2190	**75**
ad hoc ToO	1	Cyg X-3	308.11	40.96	P0614367	-	-	30	1
	2	4hr	62.5	-55	P0711101			40	6
	3	4U 1608-52	243.1792	-52.4239	P0714104			20	3
	4	Antia	157.5166	-35.3233	P0711099			30	6
	5	EP240904a	276.875	-9.9426	P0714098			200	6
	6	EXO 0748-676	117.14	-67.75	P0714102			180	3
	7	FRB 20250316A	182.476	58.8494	P0714107			60	3
	8	FRB010312A	81.725	-64.9386	P0711100			30	6
	9	GRB 250308	160.761	23.741	P0714106			30	1
	10	IGR J17091-3624	257.28	-36.41	P0714103			240	12
								860	**47**